UNIVERSIDADE FEDERAL DE MINAS GERAIS

Instituto de Geociências

Programa de Pós-Graduação em Geologia

Ramon de Oliveira Aranda

PETROGENESIS OF THE AFONSO CLÁUDIO INTRUSIVE COMPLEX:

implications for the post-collisional evolution of the Araçuaí-West Congo orogen

Belo Horizonte

2023

Ramon de Oliveira Aranda

PETROGENESIS OF THE AFONSO CLÁUDIO INTRUSIVE COMPLEX:
implications for the post-collisional evolution of the Araçuaí-West Congo orogen

Tese apresentada ao Programa de Pós-Graduação em Geologia da Universidade Federal de Minas Gerais como requisito parcial à obtenção do título de Doutor em Geologia.

Orientador: Alexandre de Oliveira Chaves

Coorientador: Adolf Heinrich Horn

Belo Horizonte

2023

UNIVERSIDADE FEDERAL DE MINAS GERAIS

PROGRAMA DE PÓS-GRADUAÇÃO EM GEOLOGIA DO IGC-UFMG
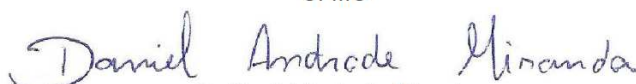
FOLHA DE APROVAÇÃO

Petrogenesis of the Afonso Cláudio Intrusive Complex: Implications for the post-collisional evolution of the Araçuaí-West Congo orogen

RAMON DE OLIVEIRA ARANDA

Tese submetida à Banca Examinadora designada pelo Colegiado do Programa de Pós-Graduação em GEOLOGIA do IGC-UFMG, como requisito parcial para obtenção do grau de Doutor(a) em GEOLOGIA, área de concentração GEOLOGIA REGIONAL, pelo Programa de Pós-graduação em Geologia do Instituto de Geociências da Universidade Federal de Minas Gerais.
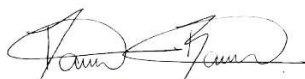
Aprovada em 27 de novembro de 2023, pela banca constituída pelos membros:

Prof. Dr. Alexandre de Oliveira Chaves – Orientador
UFMG

Dr. Daniel Andrade Miranda
Independente

Prof. Dr. Rodson de Abreu Marques
UFOP

Profa. Dra. Marcela Lopes Zanon
UFOP

Prof. Dr. Danilo Barbuena
UFVJM

Belo Horizonte, 27 de novembro de 2023.

Cada palavra deste trabalho é dedicada à minha família.

AGRADECIMENTOS

Ao Programa de Pós-Graduação em Geologia da Universidade Federal de Minas Gerais.

A todos técnicos do Centro de Pesquisas Professor Manoel Teixeira da Costa da Universidade Federal de Minas Gerais, em especial aos amigos Carlos, Jhonny e Denise.

Ao Marcelo e a Dalva, pelo suporte nestes anos de pós-graduação.

A todos os professores da Universidade Federal do Espírito Santo e da Universidade Federal de Minas Gerais, que grandemente contribuíram para a minha formação.

Todos os caminhos são mágicos se nos levam aos nossos sonhos (Paulo Coelho).

RESUMO

O Complexo Intrusivo Afonso Cláudio (CIAC) é uma típica intrusão pós-colisional do Orógeno Araçuaí-Congo Ocidental (OACO), que representa um importante segmento tectônico do sudeste do Brasil e do oeste da África. O CIAC é associado ao colapso orogênico do OACO, com as intrusões relacionadas a esta fase apresentando idades entre 530 a 480 Ma. Este pluton intrudiu gnaisses relacionados ao estágio pré-colisional do OACO e do Complexo Nova Venécia e é formado principalmente por dois núcleos compostos por monzogabro e monzodiorito indiferenciados circundados por quartzo monzonito, com intenso processo de mistura de magmas físico (*mingling*) e químico (*mixing*) entre ambos domínios. Xenólitos relacionados as rochas encaixantes são comuns no quartzo monzonito, enquanto ocorrem de maneira ocasional no monzogabro e no monzodiorito. Além destas feições, diques de sienogranito comumente cortam as rochas do CIAC. A química das fases minerais que compõem as principais rochas do CIAC e a investigação das condições de cristalização destas rochas revelaram que o CIAC é formado pela interação de magmas mantélicos e crustais que se cristalizaram entre crosta média e inferior. Os xenólitos hospedados pelo CIAC e as rochas encaixantes deste pluton apresentam semelhantes caraterísticas geoquímicas entre si, contudo ambos apresentam padrões geoquímicos diferentes das principais rochas do CIAC. Estes resultados sugerem que os xenólitos e as rochas encaixantes semelhantes são cogenéticos, contudo ambos não podem representar as principais fontes dos magmas que geraram as rochas do CIAC. Modelagem geoquímica de processos ígneos considerando os principais xenólitos e as rochas encaixantes como materiais assimilados sugere que processos de magma *mixing* foram responsáveis pelos padrões geoquímicos semelhantes entre as principais rochas do CIAC. A modelagem também indicou que cristalização fracionada com inexpressiva assimilação das rochas encaixantes controlou a evolução do monzogabro e do monzodiorito, que são relacionados a fusão parcial de um manto enriquecido, enquanto cristalização fracionada concomitante com assimilação das rochas encaixantes controlou a evolução do quartzo monzonito, que é associado a fusão de crosta inferior. Datação química de cristais de monazita encontrados em dois xenólitos provou que ambas rochas preservaram similares idades principais relacionadas a formação do CIAC. As idades mais velhas (478 e 477 Ma) são relacionadas a intrusão e cristalização do CIAC durante a fase pós-colisional do OACO, enquanto as idades mais novas (431 e 427 Ma) são possivelmente relacionadas as intrusões dos diques de sienogranito que cortam o CIAC, podendo representar uma extensão da fase pós-

colisional deste sistema orogênico ou um evento termal tardio não relacionado a esta fase orogênica. Devido as similaridades entre as típicas intrusões pós-colisionais do OACO, as descobertas relacionadas ao ACIC podem ser consideradas a outras intrusões semelhantes deste orógeno.

Palavras-Chave: petrogênese ígnea; geotermobarometria ígnea; modelagem geoquímica; magmatismo pós-colisional; mistura de magmas; Orógeno Araçuaí.

ABSTRACT

The Afonso Cláudio Intrusive Complex (ACIC) is a post-collisional intrusion from Araçuaí-West Congo orogen (AWCO), which represents an important tectonic segment from southeast Brazil and west Africa. The ACIC intrusion is associated to AWCO collapse stage, which ranges from 530 to 480 Ma. This pluton intruded gneisses from AWCO pre-collisional stage and Nova Venécia Complex and it is mainly composed of two off-centered monzogabbroic/monzodiorotic cores surrounded by quartz monzonite, with intense magma mingling and mixing widespread between these domains. Crustal xenoliths related to the enclosing country rocks occur widespread in the quartz monzonite domain, while are occasional in the monzogabbro/monzodiorite domain. In addition, syenogranite dykes commonly crosscut ACIC rocks. The typical AWCO post-collisional intrusions have been extensively studied, however the crystallization conditions of these intrusions have been occasionally investigated, while the commonly hosted crustal xenoliths have never been investigated in such detail. The examination of the chemistry of principal phases of the ACIC main rocks and the crystallization conditions of these rocks revealed that this pluton is formed by the interaction between mantle and crustal magmas which crystalized between middle to deep crustal levels. The commonly found xenoliths hosted by ACIC and enclosing country rocks show similar geochemical features, however both ones show different geochemical normalized patterns when compared to the ACIC main rocks. These results suggest that similar xenoliths and enclosing rocks are cogenetic, however both could not represent the main sources of magmas that generated the ACIC. Geochemical modeling of igneous processes of previous ACIC dataset considering investigated xenoliths and enclosing rocks as the main assimilant material suggests that mixing was responsible for the similar geochemical patterns between ACIC main rocks. The modeling also indicates that fractional crystallization with minor influence of assimilation from enclosing rocks controlled the magmatic evolution of monzogabbro and monzodiorite related to an enriched mantle source, while coupled assimilation and fractional crystallization ruled the evolution of quartz monzonite associated to lower crust magmas mainly contaminated by the enclosing rocks. Monazite dating of xenoliths showed that these ones preserved similar main ages related to different stages of ACIC evolution. The xenoliths showed main older ages of 478 and 477 Ma which are related to ACIC intrusion and crystallization during AWCO post-collisional stage, while younger ages of 431 and 427 Ma are probably related to the intrusion of syenogranite dykes, representing an extension of post-collisional magmatism or a later

unrelated thermal event. Due to the similarities between typical post-collisional intrusions, these insights could be considered to other similar intrusions from this orogenic system.

LIST OF FIGURES

LIST OF TABLES

SUMMARY

1. INTRODUCTION

The Araçuaí-West Congo orogen (AWCO) is a Neoproterozoic to Ordovician orogenic system formed by the collision of São Francisco and Congo cratons, which resulted in the West Gondwana amalgamation (Brito Neves and Cordani, 1991; Trompette, 1994; Pedrosa-Soares et al., 2001, 2008). This orogenic system remained linked until the South Atlantic opening, where all basic components required to characterize an orogen remained in the Brazilian domain, which is named Araçuaí orogen, whereas the African piece is named West Congo belt and inherited mainly the volcano-sedimentary to sedimentary orogenic successions (Porada, 1989; Alkmim et al., 2006, 2007; Pedrosa-Soares et al., 2007, 2008).

The Araçuaí orogen is located between the São Francisco craton and Atlantic margin of Brazil until latitude 21°S, where the N-S trend from Araçuaí orogen inflects to NE-SW trend from the Ribeira orogen (Almeida, 1977; Pedrosa-Soares and Wiedemann-Leonardos, 2000; Trouw et al., 2000). A long-lasting magmatic activity is a striking feature of the Brazilian AWCO segment, with this magmatism ranging from Early Ediacaran up to Cambro-Ordovician and associated to pre, sin, late and post-collisional stages of the tectonic evolution of this orogen (Pedrosa-Soares and Wiedemann-Leonardos, 2000; Pedrosa-Soares et al., 2001, 2011).

The focus of this thesis is the AWCO post-collisional magmatism, which is associated to the orogen collapse stage and ranges from 530 to 480 Ma (Pedrosa-Soares et al., 2001, 2011; Wiedemann et al., 2002; De Campos et al., 2016). This magmatism is mainly represented by circular to oval plutons ranging from 50 to 200 km^2 to large batholiths up to 1000 km^2 which intruded high grade rocks into weakness crustal zones such as regional shear zones, deep faults, fold hinges or contacts between two geological units (Paradella et al., 1978; Bayer et al., 1987; Wiedemann et al., 2002; De Campos et al., 2004, 2016).

Typical post-collisional intrusions have been intensely studied in the last years and are mainly composed of mafic to intermediate off-centered cores surrounded by intermediate to felsic rocks, with widespread mingling and mixing zones between these ones. In addition, some plutons show charnockitic rocks at borders and enclosing country rocks foliation generally concordant with the pluton borders foliation (Schmidt-Thome and Weber-Diefenbach, 1987; Bayer et al., 1987; Horn and Weber-Diefenbach, 1987; Ludka et al., 1998; Mendes et al., 1999, 2005; Medeiros et al., 2000, 2001; Ludka and Wiedemann-Leonardos, 2000; Wiedemann et al., 2002; De Campos et al., 2004, 2016; Mendes and De Campos, 2012; Zanon et al., 2015; Aranda et al., 2020; Araujo et al., 2020; Melo et al., 2020; Teixeira et al., 2020; Fernandes et al., 2021;

Lopes de Macêdo et al., 2022). Geochemical and isotopic studies have showed that these intrusions have evolution associated to interaction between previously enriched mantle magmas and crustal-derived magmas, with contamination by enclosing country rocks related (Ludka et al., 1998; Ludka and Wiedemann-Leonardos, 2000; Medeiros et al., 2000, 2001; Wiedemann et al., 2002; De Campos et al., 2004, 2016; Aranda et al., 2020).

Despite the extensive investigations concerning the AWCO post-collisional magmatism, few studies approached the crystallization conditions of these intrusions (Mendes et al., 1999; Ludka and Wiedemann-Leonardos, 2000; Medeiros et al., 2001; Wiedemann et al., 2002; Mendes and De Campos, 2012), while the widespread crustal xenoliths have never been examined in detail. The investigation of these topics could bring new and important insights for the post-collisional evolution and the role of crustal rocks in the post-collisional magmatism.

In spite of the local differences between the intrusions, these ones show a general pattern, allowing that a detailed study of one intrusion brings insights for the general AWCO post-collisional magmatism. Due to this, the focus of this investigation was the Afonso Cláudio Intrusive Complex (ACIC), a typical AWCO post-collisional intrusion located at homonymous town in Espírito Santo state which the detailed geological mapping, petrographic aspects, whole-rock geochemistry and zircon U-Pb geochronology and Lu-Hf isotopes were performed by Aranda et al. (2020).

In order to bring new insights for the ACIC and AWCO post-collisional magmatism evolution, we conducted an investigation focused on the mineral chemistry and geothermobarometry (crystallization conditions) of the igneous rocks from ACIC (paper 1) and a second study focused at whole-rock geochemistry and U-Pb-Th monazite geochronology of xenoliths hosted by ACIC and its main enclosing country rocks (paper 2).

1.1. Objectives

The main objectives of the thesis are:

- Understanding of the crystallization conditions of ACIC rocks;

- Understanding of the role of enclosing country rocks in ACIC evolution;

- Definition of the sources of ACIC magmas;

- Better understanding of the ACIC evolution;

- Bring new insights about the AWCO post-collisional magmatism;

1.2. Thesis structure

The thesis is organized on the following structure:

- Chapter 1: Introduction;

- Chapter 2: Geothermobarometry of igneous rocks from Afonso Cláudio Intrusive Complex (Espírito Santo state, Southeastern Brazil), Araçuaí-West Congo orogen: Further evidence for deep emplacement levels (paper published at Journal of South American Earth Sciences, v 110, 2021);

- Chapter 3: Petrography, geochemistry and monazite geochronology of crustal xenoliths hosted by Afonso Cláudio Intrusive Complex, Araçuaí-West Congo orogen (southeast Brazil): insights about contamination, magma sources and evolution of the post-collisional magmatism (paper submitted at Journal of South American Earth Sciences);

- Chapter 4: Conclusions;

1.3. References

Alkmim, F. F., Marshak, S., Pedrosa-Soares, A. C., Peres, G. G., Cruz, S. C. P., Whittington, A. (2006). Kinematic evolution of the Araçuaí-West Congo orogen in Brazil and Africa: Nutcracker tectonics during the Neoproterozoic assembly of Gondwana. *Precambrian Research* **149**, 43–64.

Alkmim, F. F., Pedrosa-soares, A. C., Noce, C. M., Cerqueira, S., Cruz, P. (2007). Sobre a Evolução Tectônica Do Orógeno Araçuaí-Congo Ocidental. *Geonomos* **15**, 25–43.

Almeida, F. F. M. (1977). O Cráton do São Francisco. *Revista Brasileira de Geociências* **7**, 349–364.

Aranda, R. O., Chaves, A. O., Medeiros Júnior, E. B., Venturini Junior, R. (2020). Petrology of the Afonso Cláudio Intrusive Complex: New insights for the Cambro-Ordovician post-collisional magmatism in the Araçuaí-West Congo Orogen, Southeast Brazil. *Journal of South American Earth Sciences* **98**, 1–19.

Araujo, C., Pedrosa-Soares, A., Lana, C., Dussin, I., Queiroga, G., Serrano, P., Medeiros-Júnior, E. (2020). Zircon in emplacement borders of post-collisional plutons compared to country rocks: A study on morphology, internal texture, U–Th–Pb geochronology and Hf isotopes (Araçuaí orogen, SE Brazil). *Lithos* **352–353**, 1–18.

Bayer, P., Schmidt-Thomé, R., Weber-Diefenbach, K., Horn, H. A. (1987). Complex concentric granitoid intrusions in the coastal mobile belt, Espírito Santo, Brazil: The Santa Angélica Pluton - an example. *Geologische Rundschau* **76**, 357–371.

Brito Neves, B., Cordani, U. (1991). Tectonic evolution of South America during the late Proterozoic. *Precambrian Research* **53**, 23–40.

De Campos, C. P., Cezar Mendes, J., Ludka, I. P., Medeiros, S. R., Moura, J. C., Wallfass, C. M. (2004). A review of the Brasiliano magmatism in southern Espírito Santo, Brazil, with emphasis on post-collisional magmatism. *Journal of the Virtual Explorer* **17**, 1–39.

De Campos, C. P., Medeiros, S. R., Mendes, J. C., Pedrosa-Soares, A. C., Dussin, I., Ludka, I. P., Dantas, E. L. (2016). Cambro-Ordovician magmatism in the Araçuaí Belt (SE Brazil): Snapshots from a post-collisional event. *Journal of South American Earth Sciences* **68**, 248–268.

Fernandes, C. M., Duffles Teixeira, P. A., Mendes, J. C. (2021). Constraining crystallization conditions during the Cambro-Ordovician post-collisional magmatism at Araçuaí belt (SE Brazil): Zircon as key petrologic witness. *Journal of South American Earth Sciences* **108**, 103235.

Horn, H. A., Weber-Diefenbach, W. (1987). Geochemical and genetic studies of three invers zoned intrusive bodies of both alkaline and calc-alkaline composition in the Ribeira Mobile Belt (Espírito Santo, Brazil). *Revista Brasileira de Geociências* **17**, 488–497.

Lopes de Macêdo, I. M., Geraldes, M. C., Marques, R. A., Melo, M. G., Tavares, A. D., Alves Martins, M. V., Oliveira, H. C., Rodrigues, R. D. (2022). New clues for magma-mixing processes using petrological and geochronological evidence from the Castelo Intrusive Complex, Araçuaí Orogen (SE Brazil). *Journal of South American Earth Sciences* **115**, 1–21.

Ludka, I. P., Wiedemann-Leonardos, C. M. (2000). Further Signs of an Enriched Mantle Source Under the Neoproterozoic Araçuaí-Ribeira Mobile Belt. *Revista Brasileira de Geociências* **30**, 95–98.

Ludka, I. P., Wiedemann, C. M., Töpfner, C. (1998). On the origin of incompatible element enrichment in the Venda Nova pluton, State of Espirito Santo, southeast Brazil. *Journal of South American Earth Sciences* **11**, 473–486.

Medeiros, S. R., Wiedeman-Leonardos, C. M., Mendes, J. C. (2000). Post-collisional multistage magmatism in the Ribeira mobile belt; geochemical and isotopic study of the Varzea Alegre Intrusive Complex, Espírito Santo, Brazil. *Revista Brasileira de Geociencias* **30**, 30–34.

Medeiros, S. R., Wiedemann-Leonardos, C. M., Vriend, S. (2001). Evidence of mingling between contrasting magmas in a deep plutonic environment: The example of Várzea Alegre, in the Ribeira Mobile Belt, Espírito Santo, Brazil. *Anais da Academia Brasileira de Ciencias* **73**, 99–119.

Melo, M. G., Lana, C., Stevens, G., Hartwig, M. E., Pimenta, M. S., Nalini, H. A. (2020). Deciphering the source of multiple U–Pb ages and complex Hf isotope composition in zircon from post-collisional charnockite-granite associations from the Araçuaí orogen (southeastern Brazil). *Journal of South American Earth Sciences* **103**, 1–22.

Mendes, J. C., De Campos, C. M. P. (2012). Norite and charnockites from the Venda Nova Pluton, SE Brazil: Intensive parameters and some petrogenetic constraints. *Geoscience Frontiers* **3**, 789–800.

Mendes, J. C., Medeiros, S. R., McReath, I., De Campos, C. M. P. (2005). Cambro-Ordovician magmatism in SE Brazil: U-Pb and Rb-Sr ages, combined with Sr and Nd isotopic data of Charnockitic rocks from the Varzea Alegre Complex. *Gondwana Research* **8**, 337–345.

Mendes, J. C., Wiedemann, C. M., McRearth, I. (1999). Conditions of Formation of Charnockitic Magmatic Rocks From the Várzea Alegre Massif, Espírito Santo, Southeastern Brazil. *Revista Brasileira de Geociências* **29**, 47–54.

Paradella, W. R., Liu, C. C., Meneses, P. R. (1978). Caracterização de maciços ácidos e diferenciados do sul do Espírito Santo através de técnicas de realces automáticos de dados do Landsat. *I Simpósio Brasileiro de Sensoriamento Remoto*. São José dos Campos: INPE, 582–596.

Pedrosa-Soares, A. C., De Campos, C.P., Noce, C., Silva, L.C., Novo, T., Roncato, J., Medeiros, S., Castañeda, C., Queiroga, G., Dantas, E., Dussin, I., Alkmim, F. (2011). Late Neoproterozoic – Cambrian granitic magmatism in the Araçuaí orogen (Brazil), the Eastern Brazilian Pegmatite Province and related mineral resources. *Geological Society, London, Special Publications* **350**, 25–51.

Pedrosa-Soares, A. C., Alkmim, F. F., Tack, L., Noce, C. M., Babinski, M., Silva, L. C., Martins-Neto, M. A. (2008). Similarities and differences between the Brazilian and African counterparts of the Neoproterozoic Araçuaí-West Congo orogen. *Geological Society, London, Special Publications* **294**, 153–172.

Pedrosa-Soares, A. C., Noce, C. M., Alkmim, F. F., da Silva, L. C., Babinski, M., Cordani, U., Castañeda, C. (2007). Orógeno Araçuaí : Síntese do conhecimento 30 anos após Almeida 1977. *Geonomos* **15**, 1–16.

Pedrosa-Soares, A. C., Noce, C. M., Wiedemann, C. M., Pinto, C. P. (2001). The Araçuaí-West-Congo Orogen in Brazil: An overview of a confined orogen formed during Gondwanaland assembly. *Precambrian Research* **110**, 307–323.

Pedrosa-Soares, A. C., Wiedemann-Leonardos, C. M. (2000). Evolution of Araçuaí Belt and its connection to the Ribeira Belt, eastern Brazil. In: Cordani, U. G., Milani, E. J., Filho, A. T., Campos, D. A. (eds) *Tectonic evolution of South America*. Rio de Janeiro: Sociedade Brasileira de Geologia, 265–285.

Porada, H. (1989). Pan-African rifting and orogenesis in southern to equatorial Africa and eastern Brazil. *Precambrian Research* **44**, 103–136.

Schmidt-Thome, R., Weber-Diefenbach, K. (1987). Evidence for "frozen-in" magma mixing in Brasiliano calc-alkaline intrusions: the Santa Angelica Pluton, southern Espirito Santo, Brazil. *Revista Brasileira de Geociencias* **17**, 498–506.

Teixeira, P. A. D., Fernandes, C. M., Mendes, J. C., Medeiros, S.R., Rocha, I. S. A. (2020). U-PB LA-ICP-MS and geochemical data of the Alto Chapéu Pluton: Contributions on bimodal post-collisional magmatism in the Araçuaí belt (SE Brazil). *Journal of South American Earth Sciences* **103**, 1–18.

Trompette, R. (1994). *Geology of western Gondwana (2000-500 Ma): Pan-African-Brasiliano aggregation of South America and Africa. Geology of western Gondwana (2000-500 Ma): Pan-African-Brasiliano aggregation of South America and Africa*. London: CRC Press.

Trouw, R. A., Heilbron, M., Ribeiro, A., Paciullo, F. V. P., Valeriano, C. M., Almeida, J. C. H., Tupinambá, M., Andreis, R. R. (2000). The Central Segment of the Ribeira Belt. *Tectonic Evolution of South America*, 287–310. Rio de Janeiro: 31st International Geological Congress.

Wiedemann, C. M., Medeiros, S. R., Ludka, I. P., Mendes, J. C., Costa-de-Moura, J. (2002). Architecture of Late Orogenic Plutons in the Araçuaí-Ribeira Fold Belt, Southeast Brazil. *Gondwana Research* **5**, 381–399.

Zanon, M. L., Chaves, A. O., Rangel, C. V. G. T., Gaburo, L., Pires, C. R. (2015). Os aspectos geológicos do Maciço Santa Angélica (ES): uma nova abordagem. *Brazilian Journal of Geology* **45**, 609–633.

2. GEOTHERMOBAROMETRY OF IGNEOUS ROCKS FROM AFONSO CLÁUDIO INTRUSIVE COMPLEX (ESPÍRITO SANTO STATE, SOUTHEASTERN BRAZIL), ARAÇUAÍ-WEST CONGO OROGEN: FURTHER EVIDENCE FOR DEEP EMPLACEMENT LEVELS

Ramon de Oliveira Aranda [a, b, *], Adolf Heinrich Horn [a], Edgar Batista de Medeiros Júnior [c], Ricardo Venturini Junior [d]

a - Universidade Federal de Minas Gerais, Programa de Pós-Graduação em Geologia, Instituto de Geociências - Centro de Pesquisa Professor Manoel Teixeira da Costa, Av. Antônio Carlos, 6627, 31270-901, Belo Horizonte, Minas Gerais, Brazil

b - Centro de Microscopia da Universidade Federal de Minas Gerais, Av. Antônio Carlos, 6627, 31270-901, Belo Horizonte, Minas Gerais, Brazil

c - Universidade Federal de Ouro Preto, Departamento de Geologia, Morro do Cruzeiro, s/n, 35400-000, Ouro Preto, Minas Gerais, Brazil

d - Universidade Federal do Espírito Santo, Programa de Pós-Graduação em Geografia, Av. Fernando Ferrari, 514, 29075-910, Vitória, Espírito Santo, Brazil

[*] Corresponding author: Universidade Federal de Minas Gerais, Programa de Pós-Graduação em Geologia, Instituto de Geociências, Centro de Pesquisas Professor Manoel Teixeira da Costa, Av. Antônio Carlos, 6627, 31270-901, Belo Horizonte, Minas Gerais, Brazil

[*] Corresponding author e-mail addresses: ramon-aranda@hotmail.com; ramonoaranda@gmail.com

2.1. Introduction

Geothermobarometry is a geologic tool broadly used to investigate the formation conditions of metamorphic rocks, but its use is not restricted to these ones. Some researchers have used this tool to unravel the cooling conditions of non- or slightly-deformed igneous plutons worldwide and the obtained results have agreed with the geological settings of these plutons (Hollister et al., 1987; Wilmart and Duchesne, 1987; Mendes and De Campos, 2012; Liu et al., 2013; Ma et al., 2017).

Igneous geothermobarometry methods are based on empirical calibration models, which consider the content of one or more elements present in stable minerals. This tool has been proven to be a suitable method to investigate pluton emplacement conditions, since the correct choice of the stable mineral phases and analyzed elements (Hollister et al., 1987; Putirka et al., 2003). However, the use of igneous geothermobarometry is still limited, mainly when compared with metamorphic geothermobarometry.

Many studies involving conventional and non-conventional metamorphic geothermobarometry have been conducted concerning Araçuaí West-Congo orogen (AWCO) rocks in the last years (Pedrosa-Soares et al., 2011; Peixoto et al., 2015; Richter et al., 2016; Serrano et al., 2018). On the other hand, igneous geothermobarometry studies have become scarce in these years (Mendes and De Campos, 2012).

The AWCO is an important orogenic system from Southeast Brazil and West Africa. A remarkable granite generation is a striking feature of this orogenic system, which shows different tectonic phases and granite generation stages (ca. 630 to 480 Ma) (Pedrosa-Soares and Wiedemann-Leonardos, 2000; Pedrosa-Soares et al., 2011; Gradim et al., 2014; De Campos et al., 2016). The Afonso Cláudio Intrusive Complex (ACIC) crops out in the Southern part of the Espírito Santo State, near the homonymous town (Figure 2.1), and belongs to the G5 Supersuite, which represents the post-collisional stage of the AWCO evolution (Wiedemann et al., 2002; Vieira, 2015; Aranda et al., 2020). The G5 plutons are made up of mafic cores surrounded by felsic rocks and their evolution is related to the interaction between mantle and crustal magmas which intruded in the AWCO crust between ca. 530 to 480 Ma (Bayer et al., 1987; Pedrosa-Soares and Wiedemann-Leonardos, 2000; Wiedemann et al., 2002; De Campos et al., 2004, 2016).

The AWCO post-collisional magmatism has been widely studied. However, these studies were mainly supported by petrographic features, mineral chemistry, whole-rock

geochemistry and isotopic investigations (mainly zircon U-Pb dating and Sm-Nd and Rb-Sr isotopes) (Bayer et al., 1987; Horn and Weber-Diefenbach, 1987; Ludka and Wiedemann-Leonardos, 2000; Medeiros et al., 2000, 2001; Wiedemann et al., 2002; Mendes et al., 2005; De Campos et al., 2004, 2016; Aranda et al., 2020; Araujo et al., 2020; Teixeira et al., 2020). Some of these studies dealt with the cooling conditions of the G5 Plutons, however, these investigations were mainly focused on the charnockitic and mafic rocks (Mendes et al., 1999; Ludka and Wiedemann-Leonardos, 2000; Medeiros et al., 2001; Wiedemann et al., 2002; Mendes and De Campos, 2012).

In order to investigate the cooling and emplacement conditions of the main rocks that make up the ACIC, we conducted a mineral chemistry and geothermobarometry study concerning these rocks and present here some regional inferences based on the results, which supported to a better understanding of the emplacement conditions of the AWCO post-collisional plutons.

2.2. Geological background

The Araçuaí orogen is an important tectonic segment from Southeast Brazil and together with its African counterpart, the West Congo belt, assembles the Araçuaí-West Congo orogen (AWCO), a confined orogenic system developed between the São Francisco and Congo cratons (Figure 2.1) (Pedrosa-Soares et al., 2001, 2008). These ones clashed during the Brasilian/Pan-African Orogeny and West-Gondwana assembly, between the Neoproterozoic and Ordovician (Pedrosa-Soares and Wiedemann-Leonardos, 2000; Alkmim et al., 2006; Pedrosa-Soares et al., 2008).

During that collision a remarkable granite generation took place, which shows clustering in five different stages based on petrologic, isotopic and geotectonic features (Figure 2.1) (Bayer et al., 1987; Pedrosa-Soares and Wiedemann-Leonardos, 2000; Wiedemann et al., 2002; Alkmim et al., 2006). The G1 Supersuite represents the pre-collisional magmatism (ca. 630 to 580 Ma), the Rio Doce Arc rocks being part of this magmatism. The metasedimentary rocks of the Nova Venécia Complex are also associated with this stage. During the collisional stage (ca. 580 to 560 Ma), the G2 Supersuite was generated, while the G3 Supersuite intruded during the late-collisional stage (ca. 560 to 530 Ma). The post-collisional stage (ca. 530 to 480 Ma) produced the G4 and G5 Supersuites and represents the AWCO collapse stage (Pedrosa-Soares and Wiedemann-Leonardos, 2000; Pedrosa-Soares et al., 2001; Wiedemann et al., 2002;

De Campos et al., 2004, 2016; Alkmim et al., 2006; Gradim et al., 2014; Richter et al., 2016; Tedeschi et al., 2016).
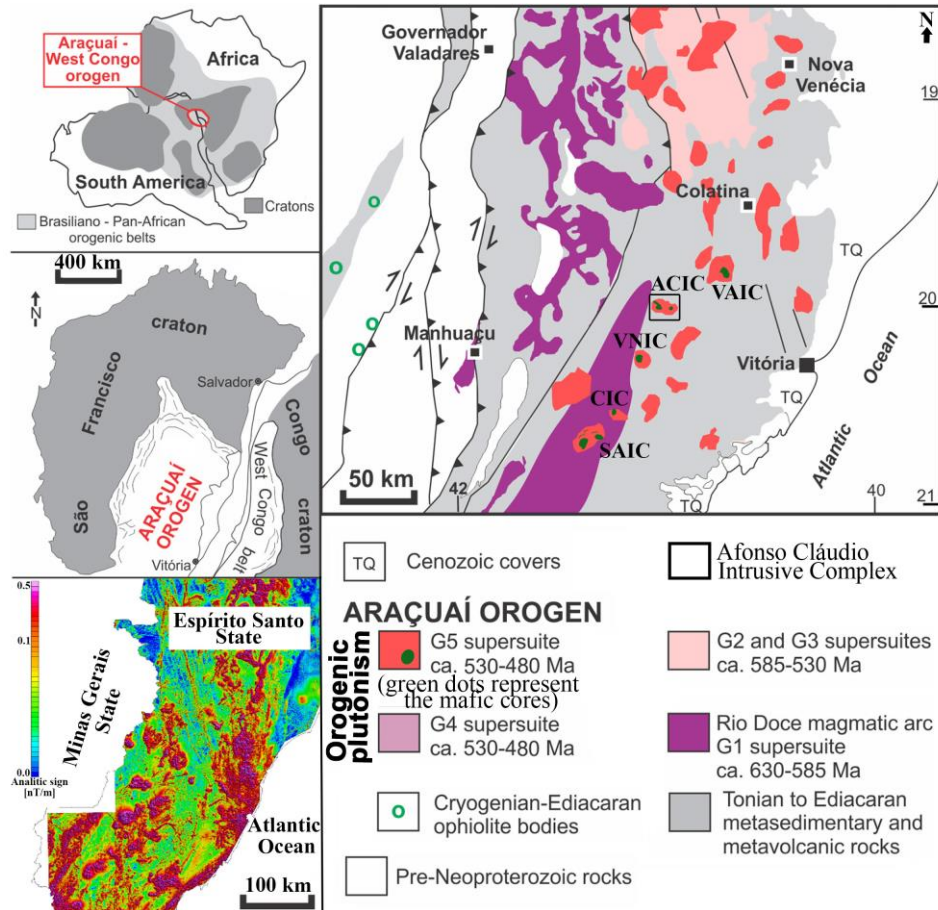
Figure 2.1: AWCO tectonic setting during West Gondwana amalgamation and geological map of the Southern part of the AWCO, showing the study area and some of the cited post-collisional plutons in this paper. Modified from: Alkmim et al., (2006); Pedrosa-Soares et al. (2008, 2011); Serrano et al. (2018). List of the abbreviations used in the figure are as follow: ACIC: Afonso Cláudio Intrusive Complex, VAIC: Várzea Alegre Intrusive Complex, SAIC: Santa Angélica Intrusive Complex, VNCI: Venda Nova Intrusive Complex; CIC: Castelo Intrusive Complex. On the left down side is showed the analytic signal amplitude magnetometric map of the Espírito Santo state. Modified from Vieira (2015).

The ACIC is part of the AWCO G5 plutons (Figure 2.1). These ones crop out over an area of about 50 to 200 km^2 and intruded vertical shear zones and fold axis, which developed on high-grade metamorphic rocks. These plutons show mafic to intermediate cores (ranging between gabbroic, dioritic and noritic compositions) surrounded by intermediate to felsic rocks

(from monzo-sienitic to granitic compositions). Some of these plutons present outer charnockitic rings, which show composition ranging from noritic to charnockitic (Bayer et al., 1987; Horn and Weber-Diefenbach, 1987; Ludka et al., 1998; Pedrosa-Soares and Wiedemann-Leonardos, 2000; Ludka and Wiedemann-Leonardos, 2000; Medeiros et al., 2001; Wiedemann et al., 2002; De Campos et al., 2004, 2016; Mendes et al., 2005; Pedrosa-Soares et al., 2011; Mendes and De Campos, 2012; Aranda et al., 2020; Teixeira et al., 2020; Melo et al., 2020).

Results of field and microscopic observations together with whole-rock geochemistry studies revealed mingling and mixing evidences. Furthermore, whole-rock geochemistry showed a post-collisional signature, I and A2-type granitoid correlation and clustering in three geochemical groups: tholeiitic, high-K calc-alkaline (90% of all plutons) and alkaline to peralkaline (Bayer et al., 1987; Wiedemann et al., 2002; De Campos et al., 2004, 2016).

The AWCO post-collisional stage is associated with the orogenic collapse (Pedrosa-Soares and Wiedemann-Leonardos, 2000; Wiedemann et al., 2002). At that time, the AWCO mantle became unstable and lithospheric mantle melting took place, producing mantle magmas. The associated decompression contributed to deep fault generation and crustal melting, which generated crustal magmas. Both magmas reached upper crustal levels through these deep faults and the different magmas interacted to generate the G5 rocks (Bayer et al., 1987; Horn and Weber-Diefenbach, 1987; Wiedemann et al., 2002; De Campos et al., 2004, 2016).

Crustal contamination process has been associated with the post-collisional magmatism. The ε_{nd}, ε_{sr} and ε_{hf} showed a crustal trend in the G5 evolution (Ludka and Wiedemann-Leonardos, 2000; Medeiros et al., 2001; Wiedemann et al., 2002; Mendes et al., 2005; De Campos et al., 2016; Aranda et al., 2020; Araujo et al., 2020; Melo et al., 2020). In addition, mafic rocks of the AWCO are enriched in some elements commonly abundant in crustal rocks, such as LILE and LREE (De Campos et al., 2004, 2016) and are not typical from mantle sources (Sparks, 1986).

Geothermobarometry studies pointed to crystallization pressure conditions from 5.5 to 6.6 kbars for the dioritic rocks from Várzea Alegre Intrusive Complex (Mendes et al., 1999). These dioritic rocks yielded plagioclase-amphibole crystallization temperatures of 750ºC (Medeiros et al., 2001). The gabbroic rocks from Várzea Alegre Intrusive Complex and other intrusions like Amparo, Itaoca and Jacutinga Plutons showed similar crystallization temperatures based on the clinopyroxene-orthopyroxene geothermometer, ranging from 700 to 970ºC (Ludka and Wiedemann-Leonardos, 2000; Medeiros et al., 2001). Concerning the G5 felsic rocks, Wiedemann et al. (2002) calculated pressures between 5.9 to 11.5 kbars in allanite

granite samples from the Santa Angélica Intrusive Complex based on hornblende geobarometers. Mendes et al. (2012) estimated similar emplacement conditions for charnockitic rocks from the outer ring of the Venda Nova Intrusive Complex. In addition to these, Serrano et al. (2018) and Araujo et al. (2020) calculated Zr saturation temperatures between 760 to 930 ºC to granitic rocks from some G5 Supersuite plutons. These investigations have pointed to middle and lower crust emplacement levels for AWCO post-collisional rocks (Medeiros et al., 2001; Mendes and De Campos, 2012).

2.2.1. Afonso Cláudio Intrusive Complex

The ACIC intruded paragneisses of the Nova Venécia Complex and orthogneisses of the G1 Supersuite and it is limited by two shear zones (Figure 2.2) (Signorelli et al., 1993; Vieira, 2015; Aranda et al., 2020). Aranda et al. (2020) mapped two lowered off-centered more mafic cores surrounded by marginal hills formed by felsic rocks (Figure 2.3a). Monzogabbro and monzodiorite (Figures 2.3b and 2.3c) predominate in the cores while quartz monzonite crops out surrounding these rocks (Figures 2.3a and 2.3d), representing the most abundant rock of the ACIC. Mingling and mixing zones occur between these domains (Figure 2.3e), where jotunite and quartz mangerite were locally mapped. In addition, syenogranite and quartz-feldspar rich dykes crop out the ACIC rocks (Figure 2.3c).

Host rock xenoliths were found all over the ACIC rocks. Allanite-bearing orthogneiss and paragneisses (garnet-cordierite-sillimanite-biotite gneiss and garnet-sillimanite-biotite gneiss) are the most common xenoliths (Figure 2.3f), representing the G1 Supersuite and Nova Venécia Complex, respectively. Some of these xenoliths showed melting evidences. Besides them, xenoliths of amphibolite, tonalite and calc-silicate rocks also occur (Aranda et al., 2020). Furthermore, quartz monzonite encloses enclaves of monzogabbro and monzodiorite, which were interpreted as mafic microgranular enclaves (mme) (Figures 2.3d and 2.3e) (Aranda et al., 2020).

The ACIC rocks are metaluminous with alkali-calcic signature and enriched in LREE and LILE. Linear trends can be observed in the binary diagrams (SiO$_2$ versus major and trace elements), with monzogabbro/monzodiorite and quartz monzonite as endmembers. Jotunite and quartz mangerite lie between the more mafic and felsic rocks in these diagrams (Aranda et al., 2020).

Zircon U-Pb dating yielded crystallization ages concordant with the AWCO post-collisional stage. The monzogabbro yielded a concordia age of 496 Ma, while the quartz monzonite showed a magmatic crystallization age of 480 Ma. In addition, the quartz monzonite showed post-collisional geochemical signature and I and A2 type granitoid correlation, which supports its affinity with AWCO post-collisional plutons (Pedrosa-Soares and Wiedemann-Leonardos, 2000; De Campos et al., 2016; Aranda et al., 2020). Lu-Hf zircon studies revealed ε_{hf} negative values between -12.93 and -8.84 to these rocks, which supports the crustal contamination (Aranda et al., 2020).
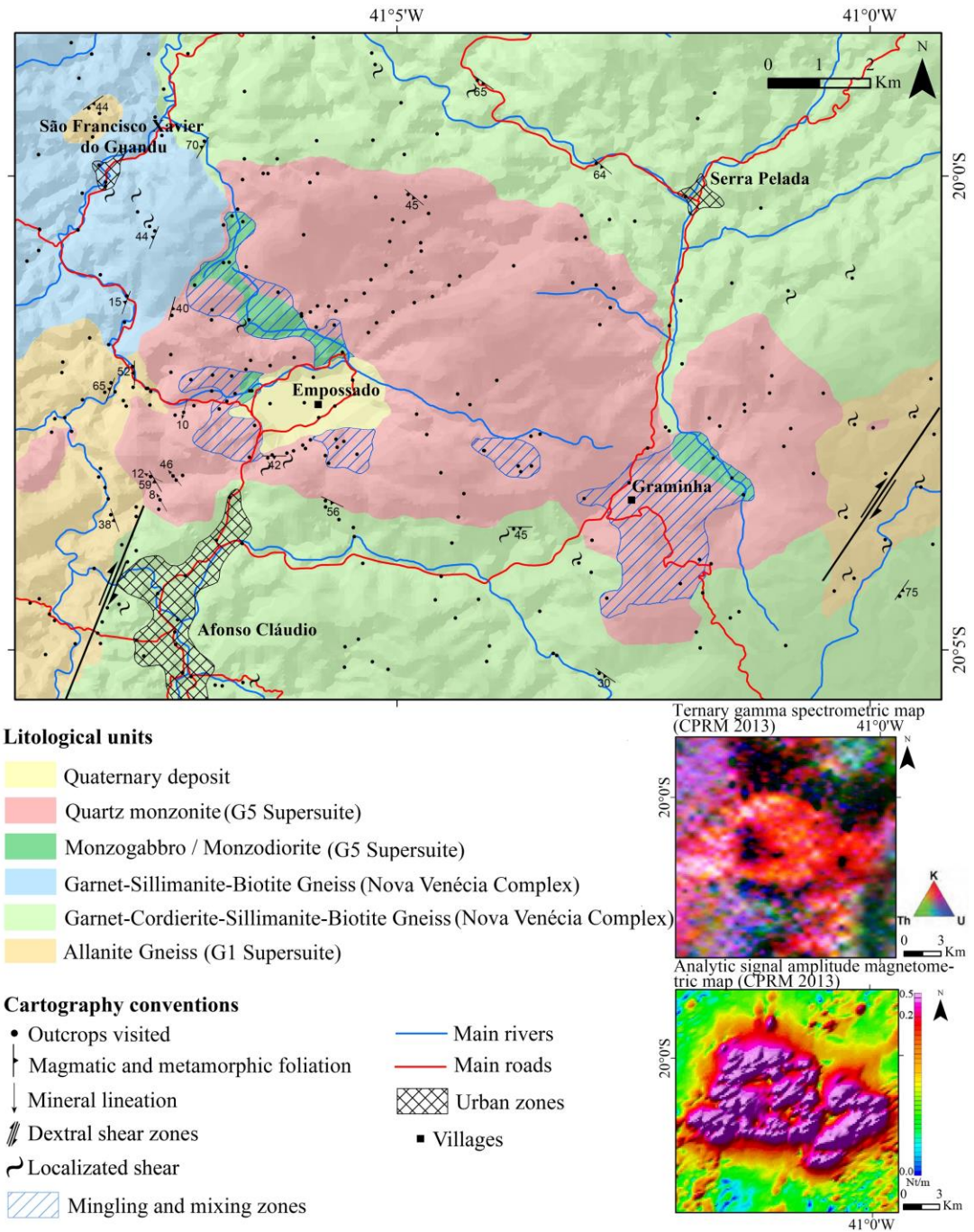
Figure 2.2: Geological map of the Afonso Cláudio Intrusive Complex (Aranda et al., 2020).
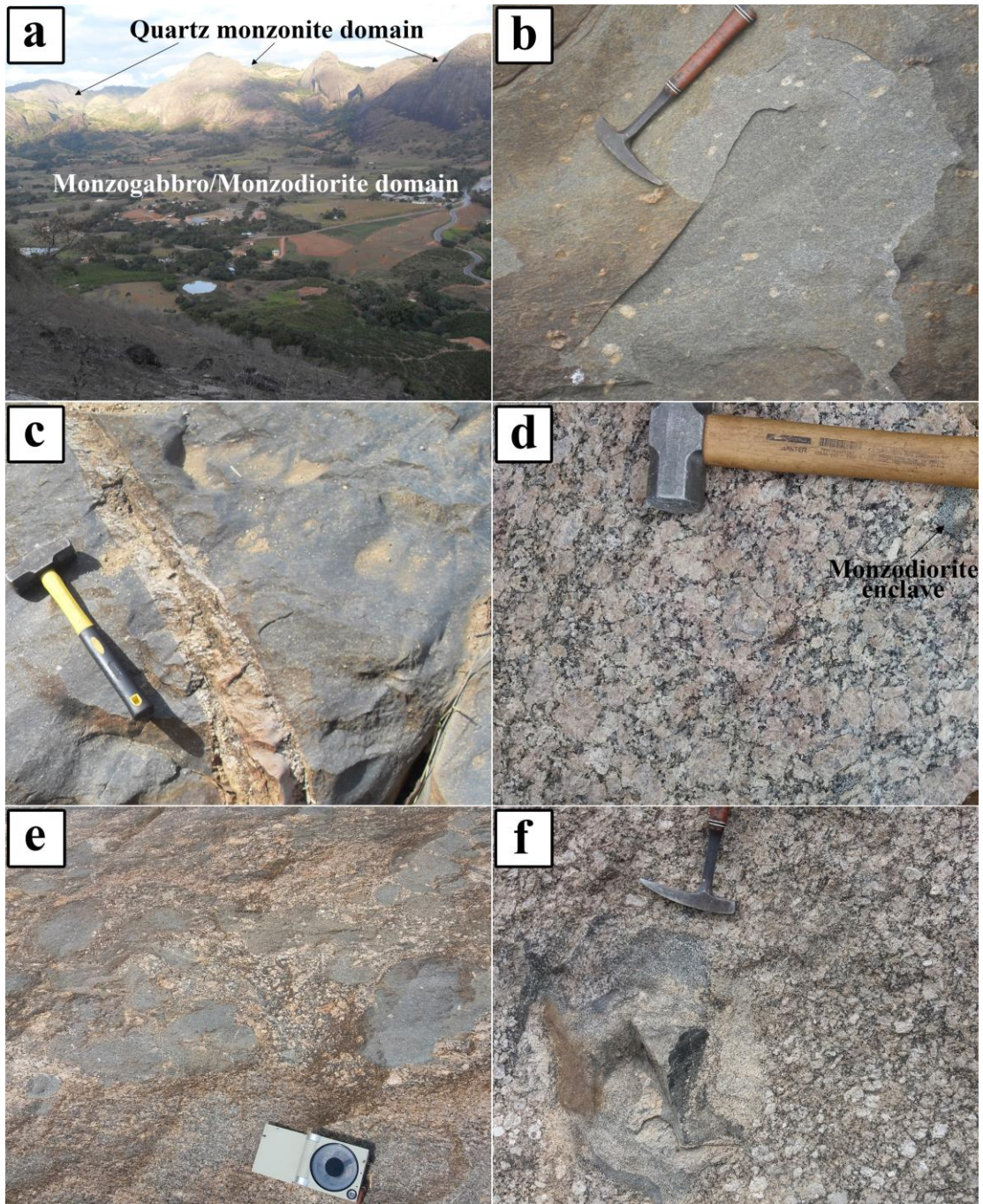
Figure 2.3: ACIC field aspects. (a): Typical monzogabbro/monzodiorite cores exposed in low topographic regions, near the Empossado village, surrounded by quartz monzonite hills. (b): Typical porphyritic monzogabbro. (c): Syenogranitic dyke crossing out the monzodiorite. (d): Typical quartz monzonite field aspect. Note the monzodiorite enclave (mme) enclosed by the quartz monzonite. (e): Monzodiorite and monzogabbro enclaves enclosed by quartz monzonite in mingling/mixing zone. (f): Allanite-bearing orthogneiss from G1 Supersuite enclosed by quartz monzonite.

2.3. Methodology

Thin sections of monzogabbro, monzodiorite and quartz monzonite were studied using an optical microscope Leica DM4500 P LED and an Electron Probe Microanalyzer (EPMA) JEOL - JXA 8900 RL at the Microscopy Center of the Federal University of Minas Gerais.

Feldspars, biotite, amphiboles, clinopyroxene, orthopyroxene, magnetite and ilmenite were analyzed by EPMA under the following conditions: acceleration voltage of 15 kV, current beam of 20 nA, diameter beam between 1 and 5 μm and peak counting time between 10 and 30 seconds. Natural and synthetic standards were used for calibration and ZAF matrix correction was carried out to obtain the final results. The total Fe was calculated as FeO. The full dataset of EPMA analyses is presented in the supplementary material 1. Compositional mapping and imaging were performed under analytical conditions similar to EPMA quantitative analyses.

The pressure conditions in the monzodiorite and quartz monzonite were obtained using Al-in-hornblende geobarometers (Anderson and Smith, 1978; Hollister et al., 1987; Schmidt, 1992). In addition, we used hornblende-plagioclase geothermometers (Blundy and Holland, 1990; Holland and Blundy, 1994) to estimate the crystallization temperatures of these rocks.

Clinopyroxene-orthopyroxene pairs were used to calculate monzogabbro crystallization temperatures by Wood and Banno (1973) and Putirka et al. (2008) methods. The temperature conditions were also obtained using the two-feldspars geothermometer (Putirka, 2008) for monzogabbro and quartz monzonite. The average pressures obtained by hornblende barometers were used on the thermometers which require pressure inputs. In these ones, we verified that these thermometers are insensitive to pressure variation.

Sub-solidus re-equilibration temperatures and oxygen fugacity (fO$_2$) were obtained through magnetite-ilmenite pairs using the models proposed by Andersen and Lindsley (1985).

In addition, zircon saturation thermometers (Watson and Harrison, 1983; Boehnke et al., 2013) were also used to estimate the crystallization temperatures of the ACIC felsic rocks. This geothermometer requires whole-rock geochemistry data, which was imported from Aranda et al. (2020).

2.4. Results

2.4.1. Petrography

Monzogabbro is a porphyritic fine-medium grained rock (Figure 2.3b). Plagioclase, biotite, clinopyroxene and K-feldspar are the major mineral phases, while quartz, opaque minerals (mainly magnetite and ilmenite), orthopyroxene, hornblende, apatite and zircon represent accessory minerals (Figures 2.4a, 2.4b and 2.4c). Plagioclase crystals show compositional zoning and are the principal phenocrysts, with their size ranging from 4 mm to 2 cm, while K-feldspar phenocrysts rarely occur. Some pyroxenes are found replaced by biotite and hornblende, which is also replaced by biotite. Coronitic texture with hornblende surrounding pyroxene crystals rarely occur. Occasionally, orthopyroxene crystals show clinopyroxene and magnetite inclusions (Figure 2.5a).

Monzodiorite is a fine-medium grained rock locally porphyritic, with phenocrysts larger than 6 mm (Figure 2.3c). Plagioclase, biotite, hornblende, clinopyroxene and K-feldspar constitute the main minerals. Quartz, opaque minerals (mainly magnetite and ilmenite), titanite and zircon are the minor mineral phases (Figures 2.4d and 2.4e). Plagioclase crystals represent the main phenocrysts and show compositional zoning (Figures 2.5b and 2.5c), while K-feldspar phenocrysts are scarce, occasionally showing poikilitic texture, with clinopyroxene, opaque minerals and biotite inclusions. Almost all clinopyroxene crystals are partially substituted by biotite and hornblende, which sometimes surrounds the pyroxene crystals (Figures 2.4e and 2.5d). Glomeroporphyritic texture rarely occur, with feldspar, biotite and clinopyroxene crystals larger than the matrix minerals. In addition, few biotite and hornblende crystals exhibit quartz symplectitic texture and some biotite crystals are replaced by chlorite. Titanite usually surrounds ilmenite and magnetite crystals.

The quartz monzonite is a porphyritic rock with fine- to coarse-grained matrix (Figures 2.3d and 2.3e). Microcline, plagioclase, quartz, biotite and hornblende are the main minerals (Figures 2.4f and 2.4g). The minor mineral phases are opaque minerals (mainly ilmenite and magnetite), titanite, apatite, allanite and zircon. Muscovite crystals were observed in few thin sections, showing association with feldspars. Microcline represents the main phenocryst (Figure 2.4f) and occasionally shows poikilitic texture, with predominant plagioclase inclusions. Many plagioclase phenocrysts (Figure 2.4f) and rare larger xenomorphic quartz crystals can also be observed. Plagioclase crystals normally show compositional zoning (Figure
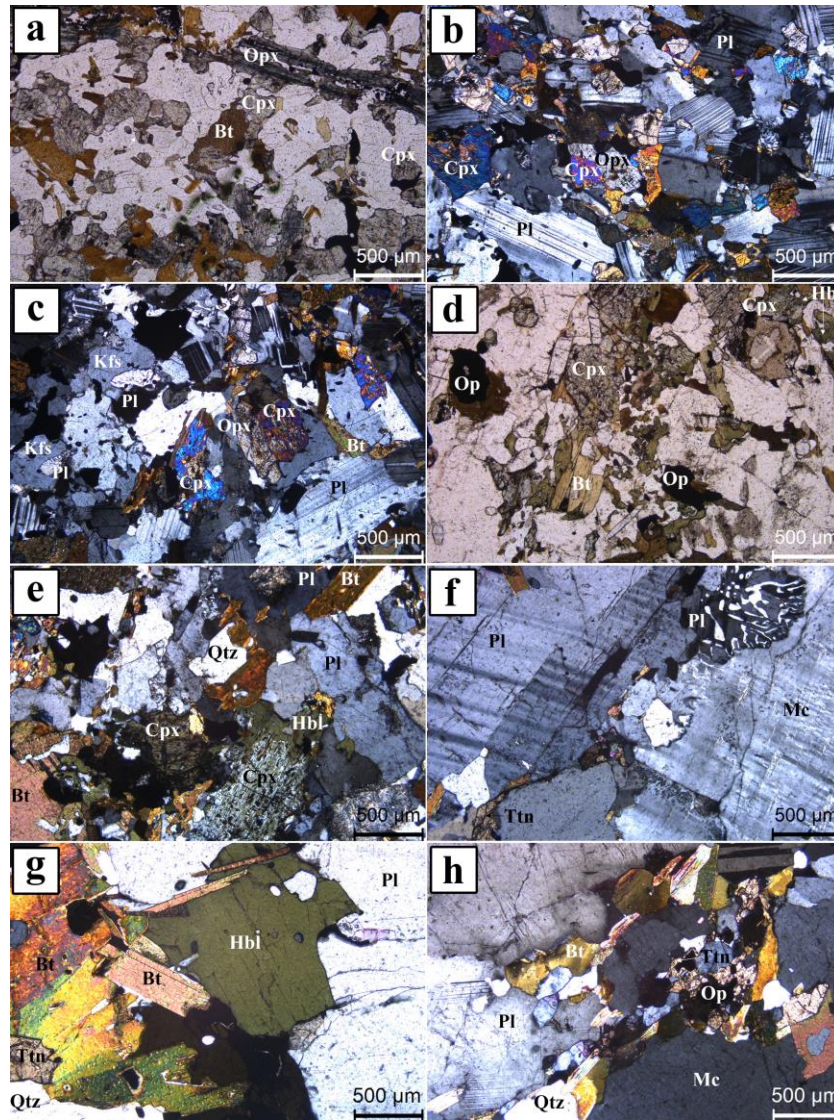
Figure 2.4: ACIC thin sections photographies. (a): Monzogabbro general texture and mineralogy (under plane polarized light). (b) and (c): Monzogabbro general texture showing the contacts between clino- and orthopyroxene crystals and plagioclase and K-feldspar crystals (under crossed polarized light). (d) and (e): Monzodiorite general texture showing the relations between plagioclase and hornblende crystals. Note the hornblende surrounding the clinopyroxene crystal (d is under plane polarized light and e is under crossed polarized light). (f), (g) and (f): General textures of the quartz monzonite. Note the contacts between the feldspar crystals and titanite surrounding magnetite and ilmenite crystals (f, g and h are under crossed polarized light). Mineral abbreviations: Bt: Biotite; Cpx: Clinopyroxene; Hbl: Hornblende; Kfs: K-feldspar; Mc: Microcline; Op: Opaque mineral (mainly magnetite and ilmenite); Opx: Orthopyroxene; Pl: Plagioclase; Qtz: Quartz; Ttn: Titanite.
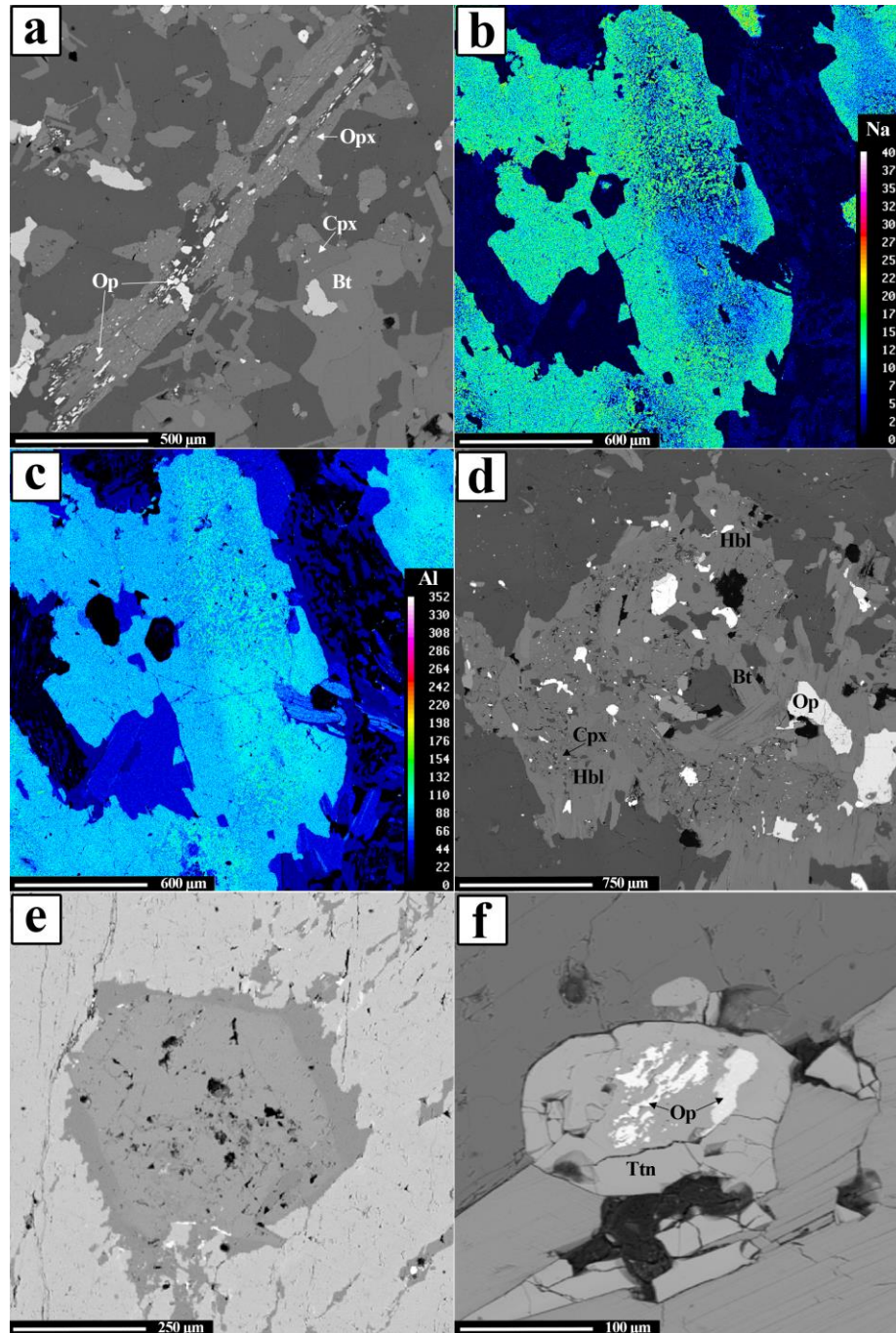
Figure 2.5: (a): Orthopyroxene crystal with magnetite inclusions (Backscattered Image). (b) and (c): Na and Al X-ray maps, respectively, of a zoned plagioclase crystal. The upper central portion of this plagioclase crystal shows alteration to sericite. The scale bar represents the number of X-ray counts. (d): Aggregate of clinopyroxene, hornblende and biotite crystals showing the hornblende crystals replacing clinopyroxene crystals (Backscattered Image). (e): Plagioclase crystal showing normal compositional zoning (Backscattered Image). (f): Opaque minerals (magnetite and ilmenite) surrounded by titanite crystal (Backscattered Image). The mineral abbreviations are the same as Figure 2.4.

2.5e) and hornblende crystals are partially replaced by biotite, that sometimes partially surrounds the hornblende crystals. Both biotite and hornblende present quartz symplectite texture and are sometimes replaced by chlorite. Magnetite and ilmenite crystals frequently have titanite coronas (Figures 2.4h and 2.5f).

These three lithotypes show some similar sub-solidus deformation features, such as undulose extinction, polygonal contacts and curved polysynthetic twinning in plagioclase and quartz crystals. In addition, rare stretched quartz crystals are present in the quartz monzonite located near the ACIC borders. The modal mineralogy of the studied rocks is reported in Table 2.1.

Table 2.1: Estimated modal mineralogy of the ACIC lithotypes studied in this work. The values in parenthesis represent the highest modal values of the lithotypes. Modified from: Aranda et al. (2020).

Lithotype / Mineral	Monzogabbro	Monzodiorite	Quartz monzonite
Quartz	2 - 4% (12%)	3 - 4% (17%)	(7%) 10 - 17%
Plagioclase	41 - 58% (64%)	43 - 58%	19 – 57% (43%)
K-Feldspar	(3%) 7 - 14 % (17%)	1 - 5% (18%)	19 - 43%
Hornblende	<1 - 2% (18%)	(2%) 8 - 23%	1 - 11%
Biotite	(3%) 8 - 14% (23%)	(4%) 10 - 32%	4 - 14%
Orthopyroxene	(1%) 3 - 7%	-	-
Clinopyroxene	(1%) 8 - 18%	1 - 15%	-
Titanite	-	<1 - 3%	0 - 3%
Zircon	<1 - 1%	<1 - 1%	<1 - 1%
Allanite	-	-	<1 - 1%
Opaque minerals	2 - 5%	1 - 4%	<1 - 3%
Apatite	<1 - 1%	1 - 2%	<1 - 1%
Sericite	<1 - 1%	<1 - 2%	<1 - 2%
Carbonate	<1 - 1%	<1 - 1%	<1 - 2%
Chlorite	-	<1 - 1%	< 1% - 1%
Muscovite	-	-	<1 - 1 %

2.4.2. Mineral Chemistry

2.4.2.1. K-feldspar

K-feldspar crystals show similar compositions over all analyzed rocks, showing compositions ranging from $Ab_{14}Or_{86}$ to Ab_7Or_{93} (Table 2.2 and Figure 2.6a). It is notable that K-feldspar crystals in the monzogabbroic and monzodioritic rocks have higher BaO contents (between 2.13 and 4.38 wt%) than those ones in the quartz monzonite (from 0.39 to 1.21 wt%). The porphyry and matrix K-feldspar crystals do not show distinct compositions.

2.4.2.2. Plagioclase

Plagioclase crystals show different compositions in the analyzed rocks (Table 2.2 and Figure 2.6a). However, the phenocryst and matrix crystals show similar compositions in each lithotype. The plagioclase commonly shows normal compositional zoning (phenocryst and matrix plagioclases) in the quartz monzonite, with core-rim compositions ranging from andesine ($An_{33}Ab_{65}Or_2$) to oligoclase ($An_{25.5}Ab_{74}Or_{0.5}$). Some plagioclase inclusions in microcline showed an albite composition ($An_2Ab_{97}Or_1$). In addition, one plagioclase crystal presented an andesine composition ($An_{38}Ab_{62}$), which is similar to the plagioclase compositions from the monzodiorite.

In monzodiorite, plagioclase shows a dominant andesine composition, with some of them showing a normal compositional zoning (Figures 2.5b and 2.5c), while others present an inverse compositional zoning. The crystals with normal zoning show core-rim composition ranging from $An_{34}Ab_{64}Or_2$ to $An_{30}Ab_{69}Or_1$. There are rare plagioclase cores with more anorthitic compositions, reaching a bytownite composition ($An_{84}Ab_{15.5}Or_{0.5}$). Plagioclase crystals with inverse zoning show core-rim compositions between $An_{32}Ab_{66}Or_2$ and $An_{45}Ab_{56}Or_2$. Among these inverse zoned crystals, some of them show cores with oligoclase compositions ($An_{18}Ab_{82}$). In addition, there are some crystals (phenocryst and matrix plagioclases) that showed an oscillatory compositional zoning, showing Ca-richer mantles than cores and rims ($An_{34}Ab_{65}Or_1$ cores, $An_{39}Ab_{60}Or_1$ mantles, and $An_{32}Ab_{67}Or_1$ rims).

Plagioclase crystals in the monzogabbro showed the least compositional variation. The largest part of the crystals shows a normal compositional zoning, ranging from labradorite cores ($An_{54}Ab_{45}Or_1$) to andesine rims ($An_{38}Ab_{60}Or_2$).

Table 2.2: Representative K-feldspar and plagioclase analyses.

Rock	Quartz Monzonite	Monzodiorite	Monzogabbro	Quartz monzonite		Monzodiorite		Monzogabbro	
Mineral	Microcline	K-Feldspar		Plagioclase		Plagioclase		Plagioclase	
Comment				Rim	Core	Rim	Core	Rim	Core
SiO₂	64.50	63.59	61.70	62.7	60.59	59.88	60.19	57.48	55.48
TiO₂	0.00	0.03	0.01	0.00	0.00	0.00	0.05	0.02	0.00
Al₂O₃	18.56	19.36	19.44	23.5	24.44	24.80	25.47	26.14	28.85
FeO	0.09	0.01	0.11	0.01	0.06	0.15	0.12	0.14	0.11
CaO	0.02	0.01	0.01	5.14	6.50	6.37	6.97	7.87	10.43
Na₂O	1.07	1.27	1.13	8.31	7.49	7.47	7.18	6.39	5.12
K₂O	15.15	13.99	14.20	0.08	0.13	0.25	0.16	0.31	0.18
BaO	0.97	3.23	2.14	0.00	0.08	0.04	0.03	0.00	0.17
SrO	0.05	0.03	0.00	0.00	0.06	0.12	0.18	0.07	0.08
MgO	0.00	0.02	0.02	0.02	0.00	0.01	0.00	0.01	0.00
MnO	0.05	0.03	0.00	0.00	0.01	0.03	0.00	0.01	0.00
Total	100.46	101.56	98.75	99.8	99.36	99.11	100.34	98.44	100.42
Oxygen number: 32									
Si	11.93	11.77	11.69	11.1	10.85	10.77	10.69	10.44	9.96
Ti	0.00	0.00	0.00	0.00	0.00	0.00	0.01	0.00	0.00
Al	4.05	4.22	4.34	4.91	5.16	5.26	5.33	5.60	6.10
Fe²⁺	0.01	0.00	0.02	0.00	0.01	0.02	0.02	0.02	0.02
Ca	0.00	0.00	0.00	0.98	1.25	1.23	1.33	1.53	2.01
Na	0.38	0.46	0.42	2.85	2.60	2.60	2.47	2.25	1.78
K	3.57	3.30	3.43	0.02	0.03	0.06	0.04	0.07	0.04
Ba	0.07	0.23	0.16	19.8	19.89	19.93	19.89	19.92	19.90
Endmembers									
An	0.08	0.06	0.04	25.3	32.18	31.55	34.57	39.74	52.38
Ab	9.65	12.11	10.82	74.1	67.08	67.00	64.47	58.40	46.55
Or	90.27	87.83	89.14	0.46	0.75	1.45	0.96	1.86	1.07

2.4.2.3. Clinopyroxene

Clinopyroxene crystals in monzogabbro have diopside compositions ($Wo_{46-47}En_{39}Fs_{14-15}$), with the exception of only one crystal showing augite composition ($Wo_{33}En_{45}Fs_{22}$) (Table 2.3 and Figure 2.6b). Otherwise, the clinopyroxenes in monzodiorite show two distinct compositions (Table 2.3 and Figure 2.6b). Some crystals show diopside composition ($Wo_{45-49}En_{37-39}Fs_{15-17}$) similar to the monzogabbro pyroxene crystals. This pyroxene type has more CaO contents, ranging from 22.10 to 24.10 wt%, than the second type. The second clinopyroxene group is composed of crystals with augite compositions ($Wo_{28-31}En_{44-51}Fs_{21-25}$) (Figure 2.6b). These ones have higher contents of FeO, MgO and Al_2O_3 (11.43-13.70, 13.65-16.46, and 3.50-5.98 wt%, respectively) than diopside crystals.

2.4.2.4. Orthopyroxene

Among the analyzed rocks, orthopyroxene crystals are only in the monzogabbro. These pyroxenes have an enstatite composition ($Wo_{1-6}En_{51-58}Fs_{40-48}$) (Table 2.3 and Figure 2.6b), with the MgO values ranging from 18.62 to 20.98 wt% and FeO compositions between 24.19 and 30.71 wt%.

Some crystals presented inclusions of clinopyroxene, maybe exsolutions, with diopside composition ($Wo_{33}En_{45}Fs_{22}$), and ilmenite and magnetite crystals (Figure 2.5a).

2.4.2.5. Biotite

Biotite crystals from monzogabbro, monzodiorite and quartz monzonite were classified as Mg-biotite (Table 2.4 and Figure 2.6c), with similar chemical compositions. The FeO_t, Al_2O_3 and MgO contents range from 14.0, 13.8 and 11.86 wt% to 19.5, 15.48 and 15.23 wt%, respectively. The MgO content in the monzogabbro biotite crystals is slighty higher than the other lithotypes. There are notable higher values of TiO_2 in biotite from monzogabbroic and monzodioritic rocks (4.0-5.5 wt%) than these ones in the quartz monzonite (1.4-2.7 wt%).

Table 2.3: Representative clinopyroxene and orthopyroxene analyses. *Fe^{2+} and Fe^{3+} calculated by stoichiometry.

Rock	Monzodiorite			Monzogabbro				
Mineral	Clinopyroxene			Clinopyroxene		Orthoyroxene		
Comment	In matrix (associated with hornblende and biotite)	Surrounded by hornblende	In matrix (associated with hornblende and biotite)	In matrix		In matrix		
SiO₂	50.32	53.00	54.66	50.66	51.86	47.6	51.01	52.98
TiO₂	0.70	0.14	0.04	0.09	0.08	0.09	0.13	0.11
Al₂O₃	5.98	0.67	1.27	2.89	1.68	0.93	0.92	1.04
FeO	13.70	9.67	8.96	13.04	8.76	29.1	27.18	26.30
MnO	0.43	0.57	0.41	0.22	0.28	0.89	0.79	0.79
MgO	13.95	13.57	13.70	15.15	13.70	19.3	20.93	20.98
CaO	13.74	22.86	23.36	15.31	22.55	2.29	0.49	0.54
Na₂O	0.79	0.39	0.52	0.19	0.40	0.04	0.03	0.05
K₂O	0.29	0.02	0.00	0.04	0.02	0.00	0.01	0.00
BaO	0.00	0.00	0.15	0.12	0.00	0.00	0.06	0.00
SrO	0.00	0.00	0.00	0.00	0.00	0.00	0.00	0.00
Total	99.90	100.90	103.07	97.69	99.34	100.	101.5	102.7
Oxygen number: 6								
Si	1.88	1.96	1.98	1.94	1.94	1.81	1.90	1.95
Ti	0.02	0.00	0.00	0.00	0.00	0.00	0.00	0.00
Al	0.26	0.03	0.05	0.13	0.07	0.04	0.04	0.04
Feᵗ	0.43	0.30	0.27	0.42	0.27	0.93	0.85	0.81
Mn	0.01	0.02	0.01	0.01	0.01	0.03	0.02	0.02
Mg	0.78	0.75	0.74	0.86	0.76	1.10	1.16	1.15
Ca	0.55	0.91	0.91	0.63	0.90	0.09	0.02	0.02
Na	0.06	0.03	0.04	0.01	0.03	0.00	0.00	0.00
K	0.01	0.00	0.00	0.00	0.00	0.00	0.00	0.00
Total	4.00	4.00	4.00	4.00	4.00	4.00	4.00	4.00
Fe²⁺*	0.42	0.23	0.25	0.41	0.21	0.59	0.69	0.75
Fe³⁺*	0.01	0.07	0.02	0.01	0.07	0.34	0.15	0.06
Endmembers								
Wo	31.10	46.00	46.98	32.76	46.38	4.39	0.96	1.06
En	43.95	37.99	38.34	45.11	39.19	51.8	56.90	57.48
Fs	24.95	16.01	14.68	22.13	14.43	43.8	42.14	41.46

Table 2.4: Representative biotite analyses. *Fe^{2+} calculated by stoichiometry.

Rock	Quartz monzonite		Monzodiorite		Monzogabbro	
SiO_2	37.39	36.51	35.86	37.92	36.39	37.46
TiO_2	2.10	1.79	4.89	4.56	5.06	4.41
Al_2O_3	14.43	13.88	14.07	14.81	14.04	15.06
FeO	19.35	18.75	18.29	17.95	16.08	15.14
MnO	0.51	0.55	0.09	0.07	0.09	0.03
MgO	12.37	12.83	12.75	13.06	13.89	15.23
CaO	0.04	0.03	0.74	0.02	0.05	0.07
Na_2O	0.08	0.10	0.17	0.09	0.05	0.03
K_2O	9.55	9.52	7.05	9.20	9.79	9.79
BaO	0.27	0.48	0.66	1.04	0.74	0.74
SrO	0.00	0.00	0.00	0.00	0.00	0.00
Total	96.09	94.43	94.58	98.71	96.17	97.95
Oxygen number: 22						
Si	5.68	5.67	5.49	5.58	5.49	5.50
Al^{iv}	2.32	2.33	2.51	2.42	2.50	2.50
Al^{vi}	0.27	0.21	0.02	0.15	0.00	0.10
Ti	0.24	0.21	0.56	0.51	0.57	0.49
Fe^{2+*}	2.46	2.43	2.34	2.21	2.03	1.86
Mn	0.07	0.07	0.01	0.01	0.01	0.00
Mg	2.80	2.97	2.91	2.87	3.13	3.33
Ca	0.01	0.01	0.12	0.00	0.01	0.01
Na	0.02	0.03	0.05	0.03	0.02	0.01
K	1.85	1.88	1.38	1.73	1.88	1.83
Total	15.72	15.81	15.39	15.50	15.63	15.63

2.4.2.6. Hornblende

The amphiboles in the monzogabbro are scarce and they were not found during the microprobe analysis. However, amphibole crystals in monzodiorite and quartz monzonite showed distinct compositions, but both belong to calcic amphibole group (Table 2.5).

In quartz monzonite, hornblende crystals have magnesio-hastingsite composition, with the exception of one crystal that showed a hastingsite composition (Figure 2.6d). The FeO (18.96-19.93 wt%), alkalis (2.87-3.21 wt%) and MnO (0.67-0.81 wt%) are higher than the monzodiorite hornblendes.

Monzodiorite hornblendes showed a larger range of varieties than these ones in the quartz monzonite (Figure 2.6d). The dominant hornblende type is magnesio-hornblende, which occurs as rock matrix and coronas in clinopyroxene crystals. There are zones where an accumulation of clinopyroxene, biotite and hornblende crystals occur (Figure 2.5d), where some hornblendes range in composition between magnesio-hornblende, edenite and tschermakite (Figure 2.6d). The variation in chemical composition of hornblende crystals in monzodiorite is slight, but these amphiboles have more SiO_2 and MgO (ranging from 43.65 and

11.37 wt% to 46.06 and 12.41wt%, respectively) when compared with hornblendes in the quartz monzonite.

Table 2.5: Representative hornblende analyses. *Fe^{2+} and Fe^{3+} calculated by stoichiometry.

Rock	Quartz monzonite		Monzodiorite			
Comment	In matrix		In matrix	Replacing clinopyroxene	Associated with biotite and clinopyroxene	Associated with biotite and clinopyroxene
SiO$_2$	41.91	41.76	45.38	45.75	44.23	44.27
TiO$_2$	0.87	0.79	1.24	1.51	1.61	1.56
Al$_2$O$_3$	10.13	11.42	9.66	9.56	10.05	9.72
FeO	19.93	19.88	16.18	16.35	16.48	15.87
MnO	0.67	0.81	0.34	0.46	0.32	0.26
MgO	9.37	8.50	11.70	11.96	11.51	11.97
CaO	11.86	11.89	12.09	12.28	12.14	12.40
Na$_2$O	1.50	1.53	1.04	1.13	1.34	1.25
K$_2$O	1.50	1.60	1.06	1.08	1.11	1.06
BaO	0.00	0.10	0.00	0.00	0.05	0.00
SrO	0.00	0.00	0.00	0.00	0.00	0.00
Total	97.75	98.26	98.70	100.08	98.84	98.36
Oxygen number: 23						
Si	6.36	6.33	6.63	6.61	6.50	6.52
Al^{iv}	1.64	1.67	1.37	1.39	1.50	1.48
T	8.00	8.00	8.00	8.00	8.00	8.00
Al^{vi}	0.17	0.37	0.29	0.23	0.24	0.21
Ti	0.10	0.09	0.14	0.16	0.18	0.17
Cr	0.00	0.00	0.00	0.00	0.00	0.00
Fe^{3+*}	0.69	0.51	0.53	0.52	0.50	0.45
Fe^{2+*}	1.84	2.01	1.45	1.45	1.53	1.50
Mn	0.09	0.10	0.04	0.06	0.04	0.03
Mg	2.12	1.92	2.55	2.57	2.52	2.63
C	5.00	5.00	5.00	5.00	5.00	5.00
Ca	1.93	1.93	1.89	1.90	1.91	1.96
Na	0.07	0.07	0.11	0.10	0.09	0.04
B	2.00	2.00	2.00	2.00	2.00	2.00
Na	0.37	0.38	0.19	0.22	0.29	0.31
K	0.29	0.31	0.20	0.20	0.21	0.20
A	0.66	0.69	0.38	0.42	0.50	0.51
Classification	Magnesio-hastingsite	Hastingsite	Magnesio-hornblende	Magnesio-hornblende	Tschermakite	Edenite

2.4.2.7. Opaque Minerals

Magnetite and ilmenite crystals show similar compositions in the analyzed rocks (Table 2.6). The analyzed magnetite grains showed FeO$_t$ contents, considering FeO as FeO$_t$, between 72.32 and 92.48. Magnetite grains surrounded by ilmenite crystals show progressive loss of FeO and enrichment in TiO$_2$ to borders, reaching over to 4.2 wt% of TiO$_2$. Ilmenite crystals have FeO and TiO$_2$ contents ranging from 41.32 wt% and 45.88 wt% to 53.98 and 51.57 wt%,

respectively, with ilmenite crystals in the monzogabbro and monzodiorite showing slightly higher values of FeO. Some magnetite and ilmenite crystals of the analyzed rocks showed elevated MnO values, mainly ilmenite crystals, reaching over to 7.06 wt%. It is notable that both magnetite and ilmenite crystals enclosed by pyroxene crystals show higher MgO, SiO_2 and Al_2O_3 contents. These crystals are smaller than matrix crystals and the high content of MgO, SiO_2 and Al_2O_3 can be due to analytical interference from the host orthopyroxene.

Table 2.6: Representative ilmenite and magnetite analyses. *Fe^{2+} and Fe^{3+} calculated by stoichiometry.

Rock	Quartz monzonite			Monzodiorite			Monzogabbro	
Comment	In matrix	Surrounded by titanite	Surrounded by titanite	In matrix	Associated with magnetit	Associated with ilmenite	Associated with ilmenite	Associated with magnetite
Mineral	Magnetite	Magnetite	Ilmenite	Ilmenite	Ilmenite	Magnetite	Magnetite	Ilmenite
SiO_2	0.02	0.03	0.03	0.05	0.14	0.10	0.07	0.02
TiO_2	0.01	0.31	47.66	47.84	51.46	0.21	0.32	50.02
Al_2O_3	0.13	0.23	0.01	0.00	0.03	0.16	0.26	0.03
FeO	91.60	90.68	46.74	49.04	47.87	94.05	91.30	49.11
MnO	0.20	0.15	3.93	2.02	2.67	0.07	0.00	0.65
MgO	0.00	0.04	0.03	0.06	0.04	0.00	0.05	0.58
CaO	0.03	0.21	0.31	0.00	0.21	0.01	0.00	0.00
K_2O	0.02	0.01	0.01	0.00	0.01	0.00	0.02	0.00
Na_2O	0.00	0.00	0.00	0.00	0.00	0.00	0.02	0.00
BaO	0.00	0.00	0.09	0.05	0.00	0.00	0.10	0.00
SrO	0.00	0.00	0.02	0.01	0.04	0.00	0.00	0.02
Total	92.01	91.65	98.82	99.07	102.47	94.60	92.14	100.43
Oxygene number	32	32	6	6	6	32	32	6
Si	0.01	0.01	0.00	0.00	0.01	0.03	0.02	0.00
Ti	0.00	0.07	1.82	1.83	1.90	0.05	0.08	1.88
Al	0.05	0.08	0.00	0.00	0.00	0.06	0.10	0.00
Fe^{3+*}	15.93	15.75	0.35	0.34	0.18	15.78	15.71	0.24
Fe^{2+*}	7.95	7.96	1.64	1.74	1.78	8.06	8.07	1.81
Mn	0.05	0.04	0.17	0.09	0.11	0.02	0.00	0.03
Mg	0.00	0.02	0.00	0.00	0.00	0.00	0.02	0.04
Ca	0.01	0.07	0.02	0.00	0.01	0.00	0.00	0.00
Total	24	24	4	4	4	24	24	4
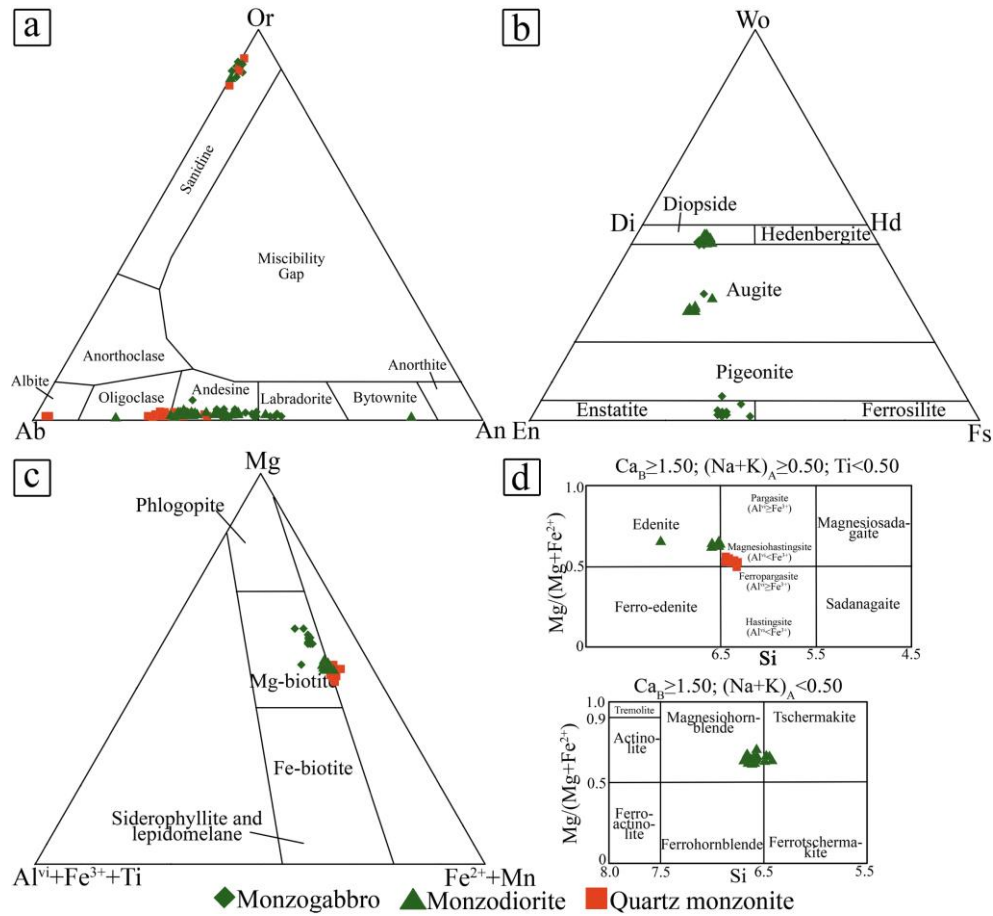
Figure 2.6: Compositional classification diagrams of the analyzed rocks. (a): Feldspar classification diagram. (b): Pyroxenes classification diagram (Morimoto et al., 1988). (c): Micas classification diagram (Foster, 1960). (d): Amphiboles classification diagram (Leake et al., 1978). *Fe^{2+} and Fe^{3+} calculated by stoichiometry.

2.4.3. Geothermobarometry

Hammarstrom and Zen (1986) Al-in-hornblende geobarometer revealed pressures ranging from 5 to 6.3 kbar for the quartz monzonite, while the monzodiorite showed crystallization pressures between 3.8 and 5.2 kbar. Hollister et al. (1987) and Schmidt (1992) Al-in-hornblende geobarometers showed similar pressures, the first one presented pressures from 5.3 to 6.7 kbar for quartz monzonite and pressures between 3.9 to 5.5 kbar for monzodiorite, while the last one produced pressures ranging from 5.5 to 6.7 kbar for quartz monzonite and pressures from 4.3 to 5.6 kbar for the monzodiorite.

Hornblende-Plagioclase geothermometer (Blundy and Holland 1990) showed temperatures ranging from 758 to 774 ºC for quartz monzonite and between 741 to 781 ºC for

monzodiorite, while Holland and Blundy (1994) geothermometer revealed temperatures between 719 to 733 ºC for quartz monzonite and ranging from 690 to 744 ºC for monzodiorite.

Clinopyroxene-orthopyroxene geothermometers (Wood and Banno, 1973; Putirka, 2008) revealed average crystallization temperatures of 904 ºC and 1060 ºC for the monzogabbro, respectively.

Two-feldspars geothermometer (Putirka, 2008) revealed average sub-solidus temperatures of 623 ºC for quartz monzonite and between 630 and 702 ºC for monzogabbro. In addition, ilmenite-magnetite pairs (Andersen and Lindsley, 1985) produced sub-solidus temperatures of 567 ºC for quartz monzonite and between 503 and 506 ºC for the monzodiorite, while the monzogabbro presented sub-solidus temperatures ranging from 510 to 574ºC. The fO2 for these rocks ranges from -18.50 to -23.06.

Zircon saturation thermometers were also used to estimate the crystallization temperatures of quartz monzonite. Watson and Harrison (1983) geothermometer produced temperatures between 846 and 909 ºC, while Boehnke et al. (2013) zircon saturation geothermometer estimated temperatures ranging from 793 to 867 ºC.

A summary of the calculated temperatures and pressures is presented in Table 2.7.

Table 2.7: Estimated temperatures and pressures from ACIC rocks.

Rock	Method	P (Kbars)	T (ºC)	Error
Monzodiorite	Al-in-hornblende (Hammarstrom and Zen, 1986)	3.8 to 5.2		± 3 kbar
Quartz monzonite		5 to 6.3		± 3 kbar
Monzodiorite	Al-in-hornblende (Hollister et al., 1987)	3.9 to 5.5		± 1 kbar
Quartz monzonite		5.3 to 6.7		± 1 kbar
Monzodiorite	Al-in-hornblende (Schmidt, 1992)	4.3 to 5.6		±0.6 kbar
Quartz monzonite		5.5 to 6.7		±0.6 kbar
Monzodiorite	Plagioclase-Hornblende (Holland and Blundy, 1994)		690 to 744	± 40 ºC
	Plagioclase-Hornblende (Blundy and Holland 1990)		741 to 781	± 75 ºC
Quartz monzonite	Plagioclase-Hornblende (Holland and Blundy, 1994)		719 to 733	± 40 ºC
	Plagioclase-Hornblende (Blundy and Holland 1990)		758 to 774	± 75 ºC
Monzogabbro	Clinopyroxene-Orthopyroxene (Putirka, 2008)		904	± 25 to 30
	Clinopyroxene-Orthopyroxene (Wood and Banno, 1973)		1060	± 25 to 30
Monzogabbro	Plagioclase-K-Feldspar (Putirka, 2008)		630 to 702	± 23 ºC
Quartz monzonite			623	± 23 ºC
Monzogabbro	Ilmenite-Magnetite (Andersen and Lindsley, 1985)		510 to 574	± 25 ºC
Monzodiorite			503 to 506	± 25 ºC
Quartz monzonite			567	± 25 ºC
Quartz monzonite	Zircon saturation (Watson et al. 1983)		846 to 909	-
	Zircon saturation (Boehnke et al. 2013)		793 to 867	± 40 to 45 ºC

2.5. Discussion

2.5.1. Emplacement conditions

Al-in-hornblende geobarometers have been applied as an effective tool to estimate crystallization pressures and emplacement depths of igneous plutons worldwide (Liu et al., 2013; Ma et al., 2017; Zhu et al., 2018; Babazadeh et al., 2019). Considering that the crustal

pressure increases 1 GPa each 37 km (Tulloch and Challis, 2000) and the pressures obtained by Al-in-hornblende barometers for ACIC rocks represent the final crystallization pressures, quartz monzonite would have crystallized between 20 and 24.8 km, while monzodiorite crystallization depth ranges from 15.8 to 20.9 km (Figure 2.7). The estimated pressures and intrusion depths of the ACIC are similar to those ones obtained by Medeiros et al. (2001) and Wiedemann et al. (2002) for gabbroic, dioritic, and granitic rocks from other G5 plutons. In addition, our results are also similar to pressures and depths obtained by Mendes and De Campos (2012) for the charnockitic rocks of the outer ring from Venda Nova Intrusive Complex.

In post-collisional environments, crystallization conditions of mafic rocks usually show similar or higher pressures than felsic rocks (Chen et al., 2016; Ma et al., 2017; Zhu et al., 2018), consequently, the intrusion depths should also be similar or higher. In ACIC, the monzodiorite showed in general lower pressures than the quartz monzonite (Figure 2.7). This is quite opposite to the expected results, which can be explained in two ways. If the shear zones that surround the west and east side of the ACIC were active until the end of the ACIC cooling, they could have introduced additional pressures and imprinted some strain in the ACIC rocks during a sub-solidus state. This is mainly supported by the shear evidences described in the quartz monzonite from ACIC edges by Aranda et al. (2020). The Al-content in the hornblende is sensitive to the pressure conditions (Anderson and Smith, 1978; Hammarstrom and Zen, 1986) and additional pressures could have been registered in Al contents of the hornblendes from the quartz monzonite. A metamorphic component and other deformational evidences in the AWCO post-collisional rocks were also found in other G5 plutons (Mendes et al., 1999; Medeiros et al., 2001; Mendes and De Campos, 2012; Teixeira et al., 2020).

On the other hand, during AWCO post-collisional stage, ACIC more mafic rocks could also have experienced decreasing pressures, which would be registered in Al-hornblende contents in the monzodiorite. If the more mafic rocks crystallized earlier than ACIC felsic rocks (Aranda et al., 2020), these latter could have crystallized in an advanced stage of the orogenic collapse, which would present higher and more stable pressures than the initial stages. This hypothesis is supported by ACIC petrogenetic model proposed by Aranda et al. (2020), which argues that the recently crystallized more mafic rocks could have melted due to decreasing pressures.
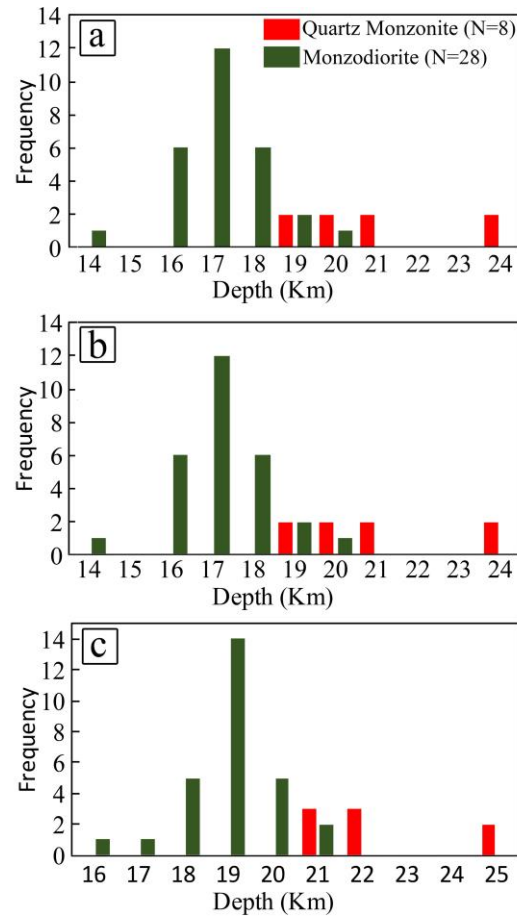
Figure 2.7: Histograms of quartz monzonite and monzodiorite emplacement depths based on Al-in-hornblende barometers. (a), (b) and (c): Pressures estimated using Hammarstrom and Zen (1986), Hollister et al. (1987) and Schmidt (1992) barometers, respectively.

The geothermobarometers used in this study estimated pressure and temperature conditions for ACIC rocks similar to other G5 Plutons. The hornblende-plagioclase temperatures yielded by quartz monzonite and monzodiorite from ACIC are similar to the results estimated by dioritic and gabbroic rocks from Várzea Alegre Intrusive Complex (Medeiros et al., 2001) and could be interpreted as an equilibrium temperature between hornblende and plagioclase. ACIC monzogabbro showed clinopyroxene-orthopyroxene temperatures similar to gabbroic rocks from Várzea Alegre Intrusive Complex (Medeiros et al., 2001) and gabbros from Amparo, Jacutinga and Itaoca Plutons (Ludka and Wiedemann-Leonardos, 2000). These temperatures possibly represent sub-solidus equilibrium temperatures (Lindsley and Munoz, 1969; Medeiros et al., 2001). Temperatures obtained by two-feldspar and ilmenite-magnetite geothermometers were interpreted as requilibrium sub-solidus temperatures in late stage and were similar to those obtained by Medeiros et al. (2001) for

similar rocks from Várzea Alegre Intrusive Complex. The zircon saturation temperatures showed by the quartz monzonite is lower than those obtained by Mendes et al. (1999) for charnockitic rocks from Várzea Alegre Intrusive Complex and similar to temperatures obtained by Serrano et al. (2018) and Araujo et al. (2020) to Medina Batolith and Vitória, Mestre Álvaro and Pedra Azul Intrusive Complexes and possibly represent the initial temperature of zircon crystallization in the melt (Watson and Harrison, 1983).

The $fO2$ values point to reduction conditions during ACIC cooling, which are also supported by low Mg/(Mg+Fe) ratios of the ACIC rocks (Aranda et al., 2020). Similar conditions were obtained by Mendes et al. (1999), Medeiros et al. (2001), and Mendes and De Campos (2012) for AWCO post-collisional rocks.

2.5.2. Petrogenetic constraints

Mantle and crustal magma mingling and mixing processes involving AWCO post-collisional plutons have been widely known (Medeiros et al., 2001; Wiedemann et al., 2002; De Campos et al., 2016; Aranda et al., 2020). The plagioclase crystals with inverse and oscillatory zoning in monzodiorite from ACIC is an evidence to support a mixing environment in the ACIC magmatic chamber. In addition, biotite and amphibole chemistry reveals a source involving mantle and crustal magmas (Figures 2.8a and 2.8b), which also supports the magma mixing hypothesis. Mantle and crustal magmas probably interacted between lower and middle crustal levels and ACIC magma chamber was probably recharged by mantle magmas during the crystallization of the first minerals, such as Ca-richer plagioclase crystals, which registered this process in the oscillatory and inverse compositional zoning. Mantle magmas late inputs in the post-collisional plutons were evidenced by Zanon et al. (2015) at the Santa Angélica Intrusive Complex. The amphibole crystals plotted near crustal and mantle field limits (Figure 2.8a) and these crystals should have been crystallized simultaneously with the plagioclase crystals showing oscillatory compositional zoning in the initial stages of magma mixing process. In more mafic rocks, many of these amphiboles can be formed by reequilibrium of the pyroxene crystals, which became unstable in a more evolved magma and were partially replaced by hornblende crystals. Otherwise, all analyzed biotite crystals plotted in the mantle-crustal magma source field (Figure 2.8b) and probably they were crystallized in a more advanced stage of the mixing process.

In addition to the field, petrographic and whole-rock lithochemistry evidences, mineral chemistry dataset presented here is a new evidence to support mixing in the ACIC evolution and due to similarities between post-collisional plutons, it is a new evidence to support a mixing environment during AWCO post-collisional evolution.

Affinity discrimination diagrams of amphiboles and pyroxenes (Figures 2.8c, 2.8d and 2.8e) revealed a subalkaline affinity, which is in agreement with whole-rock geochemical affinity diagrams that showed an alkali-calcic signature for ACIC rocks (Aranda et al., 2020). This mineral chemistry signature is an additional evidence to support ACIC relationship with the AWCO post-collisional rocks, which show similar chemical signatures (De Campos et al., 2016).

The biotite crystals from monzogabbroic and monzodioritic rocks revealed a primary genesis in the biotite genetic diagram (Figure 2.8f), typical of igneous rocks. Some samples plotted near the boundary between the primary and reequilibrated biotites. These last ones are biotite crystals associated with pyroxene and hornblende crystals, showing higher MgO values, and probably were formed when pyroxene and amphibole crystals became unstable in a more evolved mantle magma, afterward crystallization of the orthopyroxene, clinopyroxene and hornblende crystals. Otherwise, quartz monzonite biotite crystals plotted in the reequilibium biotite field (Figure 2.8f). This reequilibration process could have happened at the end of ACIC cooling, before the late fluids alteration process, which was responsible for some mineral replacements described by Aranda et al. (2020), such as replacement of biotite to chlorite and feldspars to sericite and carbonate. Quartz monzonite is younger than monzogabbroic and monzodioritic rocks (Aranda et al., 2020) and during this reequilibration process these last ones were probably almost fully crystallized, being less susceptible to this process than quartz monzonite.
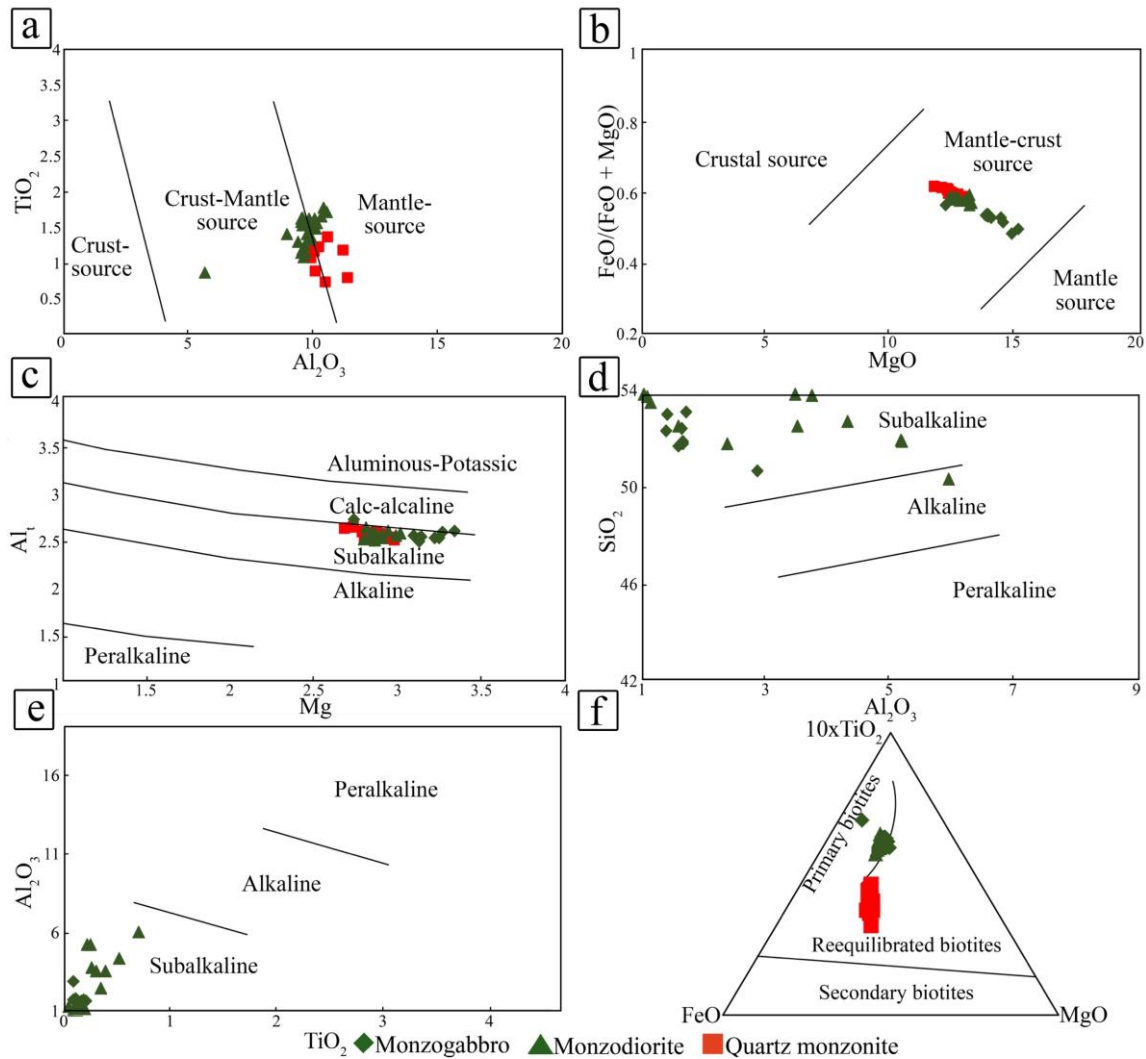
Figure 2.8: Chemical diagrams based on mineral chemical compositions. (a): $TiO_2 \times Al_2O_3$ binary diagram showing amphibole sources (Jiang and An, 1984). (b): $FeO/(FeO+MgO) \times MgO$ diagram showing the biotite sources (Zhou, 1986). (c): $Al^t \times Mg$ (apfu) binary diagram showing biotite magmatic series affinity (Nachit et al., 1985). (d) and (e): $SiO_2 \times Al_2O_3$ and $Al_2O_3 \times TiO_2$ binary diagrams, respectively, showing pyroxene magmatic series affinity (LeBas, 1962). (f): $(10 \times TiO_2) \times FeO \times MgO$ ternary diagram showing biotite sources (Nachit et al., 2005). Oxides values in wt%.

2.5.3. Host rock interactions

The crustal contamination in the G5 Plutons has been widely described and it is supported by whole-rock geochemistry and isotopic studies, mainly Nd, Sr and Hf isotopes (Bayer et al., 1987; Ludka and Wiedemann-Leonardos, 2000; Medeiros et al., 2001;

Wiedemann et al., 2002; De Campos et al., 2004, 2016; Mendes and De Campos, 2012; Aranda et al., 2020; Araujo et al., 2020). Host rock xenoliths mapped in the felsic and mafic rocks from G5 Plutons provide an additional evidence that some crustal contamination took place during AWCO post-collisional stage (Ludka et al., 1998; Ludka and Wiedemann-Leonardos, 2000; Medeiros et al., 2001; Wiedemann et al., 2002; De Campos et al., 2004, 2016; Aranda et al., 2020).

ACIC is hosted in paragneisses of the Nova Venécia Complex and orthogneisses of the G1 Supersuite. These rocks are the most common xenoliths enclosed by ACIC (Aranda et al., 2020) and these units have their evolution associated with middle and lower crust (Gradim et al., 2014; Richter et al., 2016; Tedeschi et al., 2016; Gonçalves et al., 2018). The emplacement depths estimated by Al-in-hornblende pressures in the ACIC rocks are also related to between middle and lower crust levels in AWCO under similar tectonic setting (Hacker et al., 2011; Huang et al., 2013; Rudnick and Gao, 2013). This is an evidence that ACIC rocks crystallized at similar depths to its main host rocks. In addition, it also supports that ACIC magmatic chamber could be installed nearby these rocks, which were possibly the main source of crustal magmas from ACIC crustal magmas and the main rocks responsible for crustal contamination of the ACIC mantle magmas. This hypothesis supports the petrogenetic model proposed by Aranda et al. (2020) for ACIC. In addition, melting evidences found in these xenoliths (Aranda et al., 2020) are also an evidence to this hypothesis.

AWCO G5 plutons show many similarities between them, such as the main lithotypes, petrographic aspects, emplacement conditions, lithogeochemistry and isotopic signatures (Wiedemann et al., 2002; De Campos et al., 2016). Due to these similarities, present work supports the hypothesis that AWCO post-collisional plutons crystallized between middle and lower crustal levels and the pluton's host rocks could be the main source of crustal magmas involved in the evolution of these plutons. Araujo et al. (2020) argued that the felsic borders of the post-collisional plutons were contaminated during its emplacement by country rocks, which is consistent with our results. In addition, Araujo et al. (2020) also argued that older and deeper rocks, maybe of the basement of the Ribeira Belt, could have contributed as sources to AWCO post-collisional magmas, which is in agreement with Aranda et al. (2020).

Differences between G5 plutons may be explained in terms of different host rocks, emplacement depths and contamination grades (Bayer et al., 1987; Horn and Weber-Diefenbach, 1987; Wiedemann et al., 2002; Aranda et al., 2020). However, more studies

involving gneiss xenoliths in the G5 Plutons are needed to determine their geological association and contribution as magma source.

2.6. Conclusions

Geothermobarometry is a powerful and suitable tool for investigating magmatic emplacement conditions since the correct choice of applied methods and analyzed minerals. An appropriate use of this tool may provide significant information about the emplacement conditions of igneous plutons worldwide.

AWCO post-collisional plutons have been widely studied and our investigation corroborated that the G5 Plutons intruded between middle and lower crustal levels. ACIC presents crystallization pressures corresponding to the middle and lower crust levels, which were similar to the estimated emplacement depths of other G5 plutons (Medeiros et al., 2001; Wiedemann et al., 2002; Mendes and De Campos, 2012). Mantle and crustal magmas probably interacted between these crustal levels, which is supported by the mixing evidences found on the chemical signatures of the hornblende and biotite crystals. The similarities between temperature and pressure values obtained from this study and the previous ones, in addition to the main lithotypes, petrographic features, lithogeochemical and isotopic signatures similarities between G5 plutons, support a similar emplacement level hypothesis between these plutons, with minor differences in the intrusions depths.

In addition, present work argues in favor of the intense host rocks influence in the post-collisional plutons during the AWCO collapse stage. Many host rock xenoliths of ACIC were mapped enclosed by ACIC main rocks, some of them showing melting evidences. These evidences, in addition to the similar depth levels between ACIC and its main host rocks, support the hypothesis that ACIC host rocks widely contributed to ACIC petrogenesis. Due to the similarities between AWCO post-collisional plutons, G5 plutons host rocks may have widely contributed as source of crustal magmas involving these plutons, which were the main sources of the contamination of mantle magmas involved in the AWCO post-collisional evolution. However, deeper rocks could also have contributed as magma source for the AWCO G5 plutons (Araujo et al., 2020). In order to a better understanding of the AWCO post-collisional magma sources, more studies concerning the xenoliths enclosed by G5 Plutons are needed.

2.7. Acknowledgments

We are grateful to the Microscopy Center of the UFMG for the laboratory facilities and Dr. Alexandre de Oliveira Chaves for the fruitful discussions. We are grateful to the Dr. Sebastian Grande and two anonymous reviewers, whose comments and suggestions significantly improved this paper. We are also grateful to the editor Franck Audemard, whose comments, suggestions and handling greatly improved this paper.

2.8. References

Alkmim, F. F., Marshak, S., Pedrosa-Soares, A. C., Peres, G. G., Cruz, S. C. P., Whittington, A. (2006). Kinematic evolution of the Araçuaí-West Congo orogen in Brazil and Africa: Nutcracker tectonics during the Neoproterozoic assembly of Gondwana. *Precambrian Research* **149**, 43–64.

Andersen, D. J., Lindsley, G. H. (1985). New (and final) models for the Ti-magnetite/ilmenite geothermometer and oxygen barometer. T*ransactions American Geophysical Union* **66** (18), 416.

Anderson, J. L., Smith, D. R. (1978). The effects of temperature and fo2 on the Al-in-hornblende barometer. *American Mineralogist* **561**, 549–559.

Aranda, R. O., Chaves, A. O., Medeiros Júnior, E. B., Venturini Junior, R. (2020). Petrology of the Afonso Cláudio Intrusive Complex: New insights for the Cambro-Ordovician post-collisional magmatism in the Araçuaí-West Congo Orogen, Southeast Brazil. *Journal of South American Earth Sciences* **98**, 1–19.

Araujo, C., Pedrosa-Soares, A., Lana, C., Dussin, I., Queiroga, G., Serrano, P., Medeiros-Júnior, E. (2020). Zircon in emplacement borders of post-collisional plutons compared to country rocks: A study on morphology, internal texture, U–Th–Pb geochronology and Hf isotopes (Araçuaí orogen, SE Brazil). *Lithos* **352**–**353**, 1–18.

Babazadeh, S., Furman, T., Cottle, J. M., Raeisi, D., Lima, I. (2019). Magma chamber evolution of the Ardestan pluton, Central Iran: evidence from mineral chemistry, zircon composition and crystal size distribution. *Mineralogical Magazine* **83**, 763–780.

Bayer, P., Schmidt-Thomé, R., Weber-Diefenbach, K., Horn, H. A. (1987). Complex concentric granitoid intrusions in the coastal mobile belt, Espírito Santo, Brazil: The Santa Angélica Pluton

- an example. *Geologische Rundschau* **76**, 357–371.

Blundy, J. D., Holland, T. J. B. (1990). Calcic amphibole equilibria and a new amphibole-plagioclase geothermometer. *Contributions to Mineralogy and Petrology* **104**, 208–224.

Boehnke, P., Watson, E. B., Trail, D., Harrison, T. M., Schmitt, A. K. (2013). Zircon saturation re-revisited. *Chemical Geology* **351**, 324–334.

Chen, M., Sun, M., Buslov, M. M., Cai, K., Zhao, G., Kulikova, A. V., Rubanova, E. S. (2016). Crustal melting and magma mixing in a continental arc setting: Evidence from the Yaloman intrusive complex in the Gorny Altai terrane, Central Asian Orogenic Belt. *Lithos* **252**–**253**, 76–91.

De Campos, C. P., Cezar Mendes, J., Ludka, I. P., Medeiros, S. R., Moura, J. C., Wallfass, C. M. (2004). A review of the Brasiliano magmatism in southern Espírito Santo, Brazil, with emphasis on post-collisional magmatism. *Journal of the Virtual Explorer* **17**, 1–39.

De Campos, C. P., Medeiros, S. R., Mendes, J. C., Pedrosa-Soares, A. C., Dussin, I., Ludka, I. P., Dantas, E. L. (2016). Cambro-Ordovician magmatism in the Araçuaí Belt (SE Brazil): Snapshots from a post-collisional event. *Journal of South American Earth Sciences* **68**, 248–268.

Foster, M. D. D. (1960). Interpretation of the composition of trioctahedral micas. *Geological Survey Professional Paper* **354**, 11–48.

Gonçalves, L., Alkmim, F. F., Pedrosa-Soares, A., Gonçalves, C. C., Vieira, V. (2018). From the plutonic root to the volcanic roof of a continental magmatic arc: a review of the Neoproterozoic Araçuaí orogen, southeastern Brazil. *International Journal of Earth Sciences* **107**, 337–358.

Gradim, C., Roncato, J., Pedrosa-Soares, A.P., Cordani, U., Dussin, I., Alkmim, F.F., Queirogra, G., Jacobsohn, T., Silva, L.C., Babinski. (2014). The hot back-arc zone of the Araçuaí orogen, Eastern Brazil: from sedimentation to granite generation. *Brazilian Journal of Geology* **44**, 155–180.

Hacker, B. R., Kelemen, P. B., Behn, M. D. (2011). Differentiation of the continental crust by relamination. *Earth and Planetary Science Letters* **307**, 501–516.

Hammarstrom, J. M., Zen, E. (1986). Aluminum in hornblende: An empirical igneous geobarometer. *American Mineralogist* **71**, 1297–1313.

Holland, T., Blundy, J. (1994). Non-ideal interactions in calcic amphiboles and their bearing on amphibole-plagioclase thermometry. *Contributions to Mineralogy and Petrology* **116**, 433–447.

Hollister, L. S., Grissom, G. C., Peters, E. K., Stowell, H. H., Sisson, V. B. (1987). Confirmation of the empirical correlation of Al in hornblende with pressure of solidification of calc-alkaline plutons. *American Mineralogist* **72**, 231–239.

Horn, H. A., Weber-Diefenbach, W. (1987). Geochemical and genetic studies of three invers zoned intrusive bodies of both alkaline and calc-alkaline composition in the Ribeira Mobile Belt (Espírito Santo, Brazil). *Revista Brasileira de Geociências* **17**, 488–497.

Huang, Y., Chubakov, V., Mantovani, F., Rudnick, R. L., McDonough, W. F. (2013). A reference Earth model for the heat-producing elements and associated geoneutrino flux. *Geochemistry, Geophysics, Geosystems* **14**, 2003–2029.

Jiang, C.Y., An, S.Y. (1984). On chemical characteristics of calcic amphiboles from igneous rocks and their petrogenesis significance. *Journal of Mineralogy and Petrology* **3**, 1–9.

Leake, B.E., Woolley, A.R., Arps, C.E.S., Birch, W.D., Gilbert, M.C., Grice, J.D., Hawthorne, F.C., Kato, A., Kisch, H.J., Krivovichev, V.G., Linthout, K., Laird, J., Mandarino, J., Maresch,W.V., Nickel, E.H., Schumacher, J.C., Smith, D.C., Stephenson, N.C.N., Ungaretti, L.,Whittaker, E.J.W., Youzhi, G. (1978). Nomenclature of amphiboles: report of the subcommittee on amphiboles of the International Mineralogical Association, Commission on New Minerals and Mineral Names. *The Canadian Mineralogist* **35**, 219–246.

LeBas, M. J. (1962). The role of aluminum in igneous clinopyroxenes with relation to their parentage. *American Journal of Science* **260**, 267–288.

Lindsley, D. H., Munoz, J. L. (1969). Subsolidus relations along the join hedenbergite-ferrosilite. *American Journal of Science* **267**, 295–324.

Liu, L., Qiu, J. S., Li, Z. (2013). Origin of mafic microgranular enclaves (MMEs) and their host quartz monzonites from the Muchen pluton in Zhejiang Province, Southeast China: Implications for magma mixing and crust-mantle interaction. *Lithos* **160**–**161**, 145–163.

Ludka, I. P., Wiedemann-Leonardos, C. M. (2000). Further Signs of an Enriched Mantle Source Under the Neoproterozoic Araçuaí-Ribeira Mobile Belt. *Revista Brasileira de Geociências* **30**, 95–98.

Ludka, I. P., Wiedemann, C. M., Töpfner, C. (1998). On the origin of incompatible element enrichment in the Venda Nova pluton, State of Espirito Santo, southeast Brazil. *Journal of South American Earth Sciences* **11**, 473–486.

Ma, X., Meert, J. G., Xu, Z., Zhao, Z. (2017). Evidence of magma mixing identified in the Early Eocene Caina pluton from the Gangdese Batholith, southern Tibet. *Lithos* **278**–**281**, 126–139.

Medeiros, S. R., Wiedeman-Leonardos, C. M., Mendes, J. C. (2000). Post-collisional

multistage magmatism in the Ribeira mobile belt; geochemical and isotopic study of the Varzea Alegre Intrusive Complex, Espírito Santo, Brazil. *Revista Brasileira de Geociencias* **30**, 30–34.

Medeiros, S. R., Wiedemann-Leonardos, C. M., Vriend, S. (2001). Evidence of mingling between contrasting magmas in a deep plutonic environment: The example of Várzea Alegre, in the Ribeira Mobile Belt, Espírito Santo, Brazil. *Anais da Academia Brasileira de Ciencias* **73**, 99–119.

Melo, M. G., Lana, C., Stevens, G., Hartwig, M. E., Pimenta, M. S., Nalini, H. A. (2020). Deciphering the source of multiple U–Pb ages and complex Hf isotope composition in zircon from post-collisional charnockite-granite associations from the Araçuaí orogen (southeastern Brazil). *Journal of South American Earth Sciences* **103**, 1–22.

Mendes, J. C., De Campos, C. M. P. (2012). Norite and charnockites from the Venda Nova Pluton, SE Brazil: Intensive parameters and some petrogenetic constraints. *Geoscience Frontiers* **3**, 789–800.

Mendes, J. C., Medeiros, S. R., McReath, I., De Campos, C. M. P. (2005). Cambro-Ordovician magmatism in SE Brazil: U-Pb and Rb-Sr ages, combined with Sr and Nd isotopic data of Charnockitic rocks from the Varzea Alegre Complex. *Gondwana Research* **8**, 337–345.

Mendes, J. C., Wiedemann, C. M., McRearth, I. (1999). Conditions of Formation of Charnockitic Magmatic Rocks From the Várzea Alegre Massif, Espírito Santo, Southeastern Brazil. *Revista Brasileira de Geociências* **29**, 47–54.

Morimoto, N., Fabries, J., Ferguson, A. K., Ginzburg, I. V., Ross, M., Seifert, F. A., Zussman, J. (1988). Nomenclature of pyroxenes. *American Mineralogist* **73**, 1123–1133.

Nachit, H., Ibhi, A., Abia, E. H., Ben Ohoud, M. (2005). Discrimation entre biotites magmatiques primaires, biotites rééquilibrées et biotites néoformées. *Comptes Rendus - Geoscience* **337**, 1415–1420.

Nachit, H., Razafimahefa, N., Stussi, J.M., Carron, J.P. (1985). Composition chimique des biotites et typologie magmatique des granitoides. *Comptes rendus de l'Académie des Sciences* **301**, 813-818.

Pedrosa-Soares, A. C., De Campos, C.P., Noce, C., Silva, L.C., Novo, T., Roncato, J., Medeiros, S., Castañeda, C., Queiroga, G., Dantas, E., Dussin, I., Alkmim, F. (2011). Late Neoproterozoic – Cambrian granitic magmatism in the Araçuaí orogen (Brazil), the Eastern Brazilian Pegmatite Province and related mineral resources. *Geological Society, London, Special Publications* **350**, 25–51.

Pedrosa-Soares, A. C., Alkmim, F. F., Tack, L., Noce, C. M., Babinski, M., Silva, L. C., Martins-Neto, M. A. (2008). Similarities and differences between the Brazilian and African counterparts of the Neoproterozoic Araçuaí-West Congo orogen. *Geological Society, London, Special Publications* **294**, 153–172.

Pedrosa-Soares, A. C., Noce, C. M., Wiedemann, C. M., Pinto, C. P. (2001). The Araçuaí-West-Congo Orogen in Brazil: An overview of a confined orogen formed during Gondwanaland assembly. *Precambrian Research* **110**, 307–323.

Pedrosa-Soares, A. C., Wiedemann-Leonardos, C. M. (2000). Evolution of Araçuaí Belt and its connection to the Ribeira Belt, eastern Brazil. In: Cordani, U. G., Milani, E. J., Filho, A. T., Campos, D. A. (eds) *Tectonic evolution of South America*. Rio de Janeiro: Sociedade Brasileira de Geologia, 265–285.

Peixoto, E., Pedrosa-Soares, A. C., Alkmim, F. F., Dussin, I. A. (2015). A suture-related accretionary wedge formed in the Neoproterozoic Araçuaí orogen (SE Brazil) during Western Gondwanaland assembly. *Gondwana Research* **27**, 878–896.

Putirka, K. D. (2008). Thermometers and Barometers for Volcanic Systems. *Reviews in Mineralogy and Geochemistry* **69**, 61–120.

Putirka, K. D., Mikaelian, H. M., Rerson, F., Shaw, H. (2003). New clinopyroxene-liquid thermobarometers for mafic, evolved, and volatile-bearing lava compositions, with applications to lavas from Tibet and the Snake River Plain, Idaho. *American Mineralogist* **88**, 1542–1554.

Richter, F., Lana, C., Stevens, G., Buick, I., Pedrosa-Soares, A. C., Alkmim, F. F., Cutts, K. (2016). Sedimentation, metamorphism and granite generation in a back-arc region: Records from the Ediacaran Nova Venécia Complex (Araçuaí Orogen, Southeastern Brazil). *Precambrian Research* **272**, 78–100.

Rudnick, R. L., Gao, S. (2013). Composition of the Continental Crust. *Treatise on Geochemistry: Second Edition*. Elsevier Ltd., 1–51.

Schmidt, M. W. (1992). Amphibole composition in tonalite as a function of pressure: an experimental calibration of the Al-in-hornblende barometer. *Contributions to Mineralogy and Petrology* **110**, 304–310.

Serrano, P., Pedrosa-Soares, A., Medeiros-Júnior, E., Fonte-Boa, T., Araujo, C., Dussin, I., Queiroga, G., Lana, C. (2018). A-type Medina batholith and post-collisional anatexis in the Araçuaí orogen (SE Brazil). *Lithos* **320–321**, 515–536.

Signorelli, N., Drumind, J. B. V., Raposo, F. O., Souza, E. C., Heineck, C. A. (1993). Afonso Cláudio, folha SF.24-V-A-II: estados do Espírito Santo e Minas Gerais. Escala: 1:100.000. In:

Signorelli, N. (ed.) *Afonso Cláudio, folha SF.24-V-A-II: estados do Espírito Santo e Minas Gerais. Escala: 1:100.000.* Brasília: DNPM/CPRM, 86–86.

Sparks, R. S. J. (1986). The role of crustal contamination in magma evolution through geological time. *Earth and Planetary Science Letters* **78**, 211–223.

Tedeschi, M., Novo, T., Pedrosa-Soares, A., Dussin, I., Tassinari, C., Silva, L.C., Gonçalves, L., Alkmim, F., Lana, C, Figueiredo, C., Dantas, E., Medeiros, S., De Campos, C., Corrales, F., Heilbron, M. (2016). The Ediacaran Rio Doce magmatic arc revisited (Araçuaí-Ribeira orogenic system, SE Brazil). *Journal of South American Earth Sciences* **68**, 167–186.

Teixeira, P. A. D., Fernandes, C. M., Mendes, J. C., Medeiros, S. R., Rocha, I. S. A. (2020). U-PB LA-ICP-MS and geochemical data of the Alto Chapéu Pluton: Contributions on bimodal post-collisional magmatism in the Araçuaí belt (SE Brazil). *Journal of South American Earth Sciences* **103**, 1–18.

Tulloch, A. J., Challis, G. A. (2000). Emplacement depths of Paleozoic-Mesozoic plutons from western New Zealand estimated by hornblende-Al geobarometry. *New Zealand Journal of Geology and Geophysics* **43**, 555–567.

Vieira, V. S. (2015). *Geologia e Recursos Minerais do Estado do Espírito Santo: texto explicativo do mapa geológico e de recursos minerais. Geologia e Recursos Minerais do Estado do Espírito Santo: texto explicativo do mapa geológico e de recursos minerais.* Belo Horizonte: CPRM.

Watson, E. B., Harrison, T. M. (1983). Zircon saturation revisited: temperature and composition effects in a variety of crustal magma types. *Earth and Planetary Science Letters* **64**, 295–304.

Wiedemann, C. M., Medeiros, S. R., Ludka, I. P., Mendes, J. C., Costa-de-Moura, J. (2002). Architecture of Late Orogenic Plutons in the Araçuaí-Ribeira Fold Belt, Southeast Brazil. *Gondwana Research* **5**, 381–399.

Wilmart, E., Duchesne, J. (1987). Geothermobarometry of igneous and metamorphic rocks around the Åna-Sira anorthosite massif: Implications for the depth of emplacement of the South Norwegian anorthosites. *Norsk Geologisk Tidsskrift* **67**, 185–196.

Wood, B. J., Banno, S. (1973). Garnet-Orthopyroxene and Orthopyroxene-Clinopyroxene Relationships in Simple and Complex Systems. *Contributions to Mineralogy and Petrology* **42**, 109–124.

Zanon, M. L., Chaves, A. O., Rangel, C. V. G. T., Gaburo, L., Pires, C. R. (2015). Os aspectos geológicos do Maciço Santa Angélica (ES): uma nova abordagem. *Brazilian Journal of Geology* **45**, 609–633.

Zhu, K. Y., Shen, Z. Y., Li, M. Y., Yu, Y. H. (2018). Interaction between mingling mafic and felsic magmas: Its roles in differentiation of a quartz monzonite and MMEs from eastern South China. *Lithos* **318**–**319**, 60–77.

3. PETROGRAPHY, GEOCHEMISTRY AND MONAZITE GEOCHRONOLOGY OF CRUSTAL XENOLITHS HOSTED BY AFONSO CLÁUDIO INTRUSIVE COMPLEX, ARAÇUAÍ-WEST CONGO OROGEN (SOUTHEAST BRAZIL): INSIGHTS ABOUT CONTAMINATION, MAGMA SOURCES AND EVOLUTION OF THE POST-COLLISIONAL MAGMATISM

Ramon de Oliveira Aranda [a, *]; Adolf Heinrich Horn [a], Edgar Batista de Medeiros Júnior [b], Pedro Leonardo Nicolau do Carmo Rossi Vieira [a], Ricardo Venturini Junior [c]

[a] Universidade Federal de Minas Gerais, Programa de Pós-Graduação em Geologia, Instituto de Geociências, Centro de Pesquisas Professor Manoel Teixeira da Costa, Av. Antônio Carlos, 6627, 31270-901, Belo Horizonte, Minas Gerais, Brazil

[b] Universidade Federal de Viçosa, Centro de Ciências Agrárias, Departamento de Solos, Av. P.H. Rolfs, S/N, 36571-900, Viçosa, Minas Gerais, Brazil

[c] Autonomous geologist, Rodovia do Sol, 808, 29102-020, Vila Velha, Espírito Santo, Brazil

[*] Corresponding author: Universidade Federal de Minas Gerais, Programa de Pós-Graduação em Geologia, Instituto de Geociências, Centro de Pesquisas Professor Manoel Teixeira da Costa, Av. Antônio Carlos, 6627, 31270-901, Belo Horizonte, Minas Gerais, Brazil

[*] Corresponding author e-mail address: ramonoaranda@gmail.com (R.O. Aranda)

3.1. Introduction

Igneous plutonic complexes are frequent and important pieces of orogenic systems worldwide and its investigation has been proved fundamental to the understanding of the large geological systems which comprise them (Janousek et al., 2000; Pedrosa-Soares and Wiedemann-Leonardos, 2000; Ratajeski et al., 2001; Sami et al., 2018; Babazadeh et al., 2019; Fourny et al., 2019; Lu et al., 2019; Wang et al., 2019). Mafic microgranular enclaves have been commonly found enclosed by plutonic complex worldwide and its usual investigation has successfully brought new insights about the host plutonic complexes and the related orogenic systems (Barbarin and Didier, 1992; Yang et al., 2015; Chen et al., 2016, 2017; Ma et al., 2017; Quek et al., 2017; Zhang and Zhao, 2017; Zhu et al., 2018). On the other hand, the also commonly found crustal xenoliths have been occasionally studied, even though its investigation also could bring fundamental insights about the genesis and evolution of the host magmatic rocks and associated geological systems (Zhang et al., 2016; Zhou et al., 2017; Lamarque et al., 2018; Thakurdin et al., 2019; Melekhova et al., 2022).

Mafic microgranular enclaves and crustal xenoliths have been commonly found enclosed by the magmatic rocks from Araçuaí-West Congo orogen (AWCO), a Neoproterozoic-Ordovician orogenic system located at southeast Brazil and west Africa with evolution associated to a complex and long-lasting magmatism (Pedrosa-Soares and Wiedemann-Leonardos, 2000; Pedrosa-Soares et al., 2001, 2007, 2011; Wiedemann et al., 2002; Alkmim et al., 2006, 2007; De Campos et al., 2016; Tedeschi et al., 2016; Serrano et al., 2018). This magmatism has been grouped in four different stages of evolution and the main rocks which compose these stages have been intensively investigated (Pedrosa-Soares and Wiedemann-Leonardos, 2000; Wiedemann et al., 2002; Gonçalves et al., 2014, 2016, 2018; Gradim et al., 2014; De Campos et al., 2016; Richter et al., 2016; Melo et al., 2017b, 2017a; Serrano et al., 2018; dos Santos Dias et al., 2019; Araujo et al., 2020; Wisniowski et al., 2021). On the other hand, enclaves and xenoliths commonly found enclosed by these rocks have hardly been investigated in such detail (Martins et al., 2004; Tedeschi et al., 2016; Serrano et al., 2018; Melo et al., 2020).

The post-collisional stage is the last great magmatic event related to AWCO tectonic evolution and it is mainly characterized by remarkable circular to elongated plutons to large batholiths with compositions ranging between gabbroic to granitic and charnockitic rocks which intruded between 530 to 480 Ma (Pedrosa-Soares et al., 1999; Pedrosa-Soares and

Wiedemann-Leonardos, 2000; De Campos et al., 2016). This magmatism has been broadly studied, with the investigations mainly focused on field aspects, petrography, mineral chemistry, whole-rock geochemistry, geochronology and isotopic features of the main rocks which compose the post-collisional intrusions (Ludka and Wiedemann-Leonardos, 2000; Medeiros et al., 2001; Wiedemann et al., 2002; Mendes and De Campos, 2012; De Campos et al., 2016; Serrano et al., 2018; Aranda et al., 2020; Araujo et al., 2020; Lopes de Macêdo et al., 2022). Despite the common occurrence, mafic microgranular enclaves have been occasionally investigated (Serrano et al., 2018; Aranda et al., 2020; Melo et al., 2020), while the crustal xenoliths also commonly found hosted by post-collisional intrusions have never been studied in such detail.

In order to bring new insights about the evolution of the AWCO post-collisional magmatism, we conducted an investigation focused on crustal xenoliths found hosted by Afonso Cláudio Intrusive Complex (ACIC), a typical AWCO post-collisional igneous complex located at homonymous town at Espírito Santo state, Brazil (Figure 3.1). This investigation focused on field aspects, petrography, whole-rock geochemistry and U-Th-Pb monazite geochronology of these crustal xenoliths. In addition, whole-rock geochemistry investigation of ACIC enclosing country rocks was also conducted in order to compare them with the crustal xenoliths and ACIC main rocks.

3.2. Geological setting

The Araçuaí-West Congo orogen (AWCO) is a Neoproterozoic-Ordovician orogenic system developed in a confined tectonic setting during São Francisco and Congo cratons clashing (Figure 3.1) (Brito Neves and Cordani, 1991; Pedrosa-Soares et al., 2001, 2008; Alkmim et al., 2006). This collision was accountable to the amalgamation of the West Gondwana, which was broken up during the South Atlantic opening in two fragments, the West Congo belt and the Araçuaí orogen, which respectively represent the AWCO African and Brazilian counterparts (Porada, 1989; Trompette, 1994; Alkmim et al., 2006; Pedrosa-Soares et al., 2007, 2008).

A striking and long-lasting magmatism ranging from Early Ediacaran to Ordovician is a remarkable feature of the AWCO and has been grouped in four main stages based on field, petrological, geochemical, geochronological and isotopic features (Pedrosa-Soares and Wiedemann-Leonardos, 2000). The pre-collisional magmatism is associated to G1 Supersuite

and ranges from 630 to 580 Ma, with the Rio Doce magmatic arc evolution and the deposition of Nova Venécia Complex precursors associated with this stage. The syn-collisional magmatism ranges from 580 to 560 Ma and is linked to G2 Supersuite, while the late-collisional magmatism is related to G3 Supersuite and shows evolution associated to the melting of the rocks from G2 Supersuite between 560 to 530 Ma. The metamorphic peak of the AWCO is associated with these stages and is accountable for the metamorphism and melting of Nova Venécia Complex rocks. The last great magmatic event associated with the AWCO tectonic evolution is the post-collisional magmatism, which ranges from 530 to 480 Ma and is associated to G4 and G5 Supersuites (Pedrosa-Soares and Wiedemann-Leonardos, 2000; Pedrosa-Soares et al., 2001, 2008; Wiedemann et al., 2002; Gradim et al., 2014; De Campos et al., 2016; Richter et al., 2016; Tedeschi et al., 2016).

The Afonso Cláudio Intrusive Complex (ACIC) is part of the G5 Supersuite post-collisional intrusions (Figure 3.1), which generally intruded weakness crustal zones, such as deep faults, regional shear zones, fold hinges and contact between two geological units and have evolution associated with crustal and mantle magmas (Paradella et al., 1978; Bayer et al., 1987; Wiedemann et al., 2002; De Campos et al., 2004, 2016). In the northern sector of the AWCO, these magmas intruded into shallow levels as large batholiths up to 1000 km^2 composed of an association between granitic (ranging between monzo- to syenogranite) and charnockitic rocks with minor mafic rocks related, these last ones mainly as mafic microgranular enclaves with dioritic composition (Pedrosa-Soares et al., 2001; De Campos et al., 2016; Serrano et al., 2018; Melo et al., 2020). Otherwise, the typical post-collisional intrusions are associated to mid to deep crustal levels and mostly outcrops at AWCO southern sector as circular to elongated plutons up to 200 km^2 intruding high-grade metasedimentar and metaigneous rocks, which locally melted due to the G5 intrusions and show foliation concordant with the pluton border foliation near the intrusions. These typical post-collisional intrusions are generally composed of mafic to intermediate off-centered cores (which range between gabbroic, dioritic and noritic compositions) surrounded by intermediate to felsic rocks (from monzo-syenitic to granitic compositions), with some plutons showing outer chanockitic rings, which show composition ranging from noritic to charnockitic (Schmidt-Thome and Weber-Diefenbach, 1987; Bayer et al., 1987; Horn and Weber-Diefenbach, 1987; Ludka et al., 1998; Mendes et al., 1999, 2005; Pedrosa-Soares and Wiedemann-Leonardos, 2000; Medeiros et al., 2000, 2001; Wiedemann et al., 2002; De Campos et al., 2004, 2016; Pedrosa-Soares et al., 2011; Mendes and De Campos, 2012; Zanon et al., 2015; Aranda et al., 2020, 2021; Teixeira

et al., 2020; Lopes de Macêdo et al., 2022). Some aspects of several post-collisional plutons are listed in table 1.

The post-collisional intrusions show typical post-collisional geochemical signature, LREE and LILE enrichment patterns, I and A2-type granitoid correlation and they are grouped in three main chemical groups: tholeiitic, high-K calc-alkaline (most of the plutons), and alkaline to peralkaline (Bayer et al., 1987; Horn and Weber-Diefenbach, 1987; Wiedemann et al., 2002; De Campos et al., 2004, 2016). In addition to the characteristic geochemical signatures, Potratz et al. (2021) recently found at transition zone between Araçuaí and Ribeira orogens a strongly S-type peraluminous pluton with an age associated with the AWCO post-collisional plutons, which diverges from the typical metaluminous to weak peraluminous character of these plutons (Wiedemann et al., 2002; De Campos et al., 2004). Geochemical studies supported by isotopic investigations have also pointed crustal contamination in post-collisional mantle magmas since Neoproterozoic to Ordovician times (Ludka et al., 1998; Ludka and Wiedemann-Leonardos, 2000; Medeiros et al., 2001; Wiedemann et al., 2002; Mendes et al., 2005; De Campos et al., 2016; Aranda et al., 2020, 2021; Araujo et al., 2020; Teixeira et al., 2020). The crustal contamination is also supported by occasional to common occurrence of crustal xenoliths enclosed by intermediate to felsic rocks near the borders of post-collisional plutons. These xenoliths have been associated to the enclosing country rocks and ranges since small single ones to large slabs, roof pedants and xenoliths swarms sometimes showing melting and assimilation reactions with the host magma (Wiedemann et al., 2002; De Campos et al., 2004, 2016; Aranda et al., 2020; Lopes de Macêdo et al., 2022).

The AWCO post-collisional magmatism has evolution associated to the AWCO collapse stage, where unstable previously enriched lithospheric mantle melted and uplifted by deep faults generated in this stage. These mantle magmas interacted with magmas originated from partial melting of crustal rocks, which reached higher crustal levels through these deep faults, crystalizing from lower to shallow crustal levels (Bayer et al., 1987; Medeiros et al., 2001; Wiedemann et al., 2002; De Campos et al., 2004, 2016; Serrano et al., 2018; Aranda et al., 2021; Temporim et al., 2022). The interaction between mantle and crustal magmas is better registered in the deeper plutons, which show off amazing magma mingling and mixing evidences supported by field, petrographic, geochemical and isotopic features (Wiedemann et al., 2002; De Campos et al., 2004, 2016).
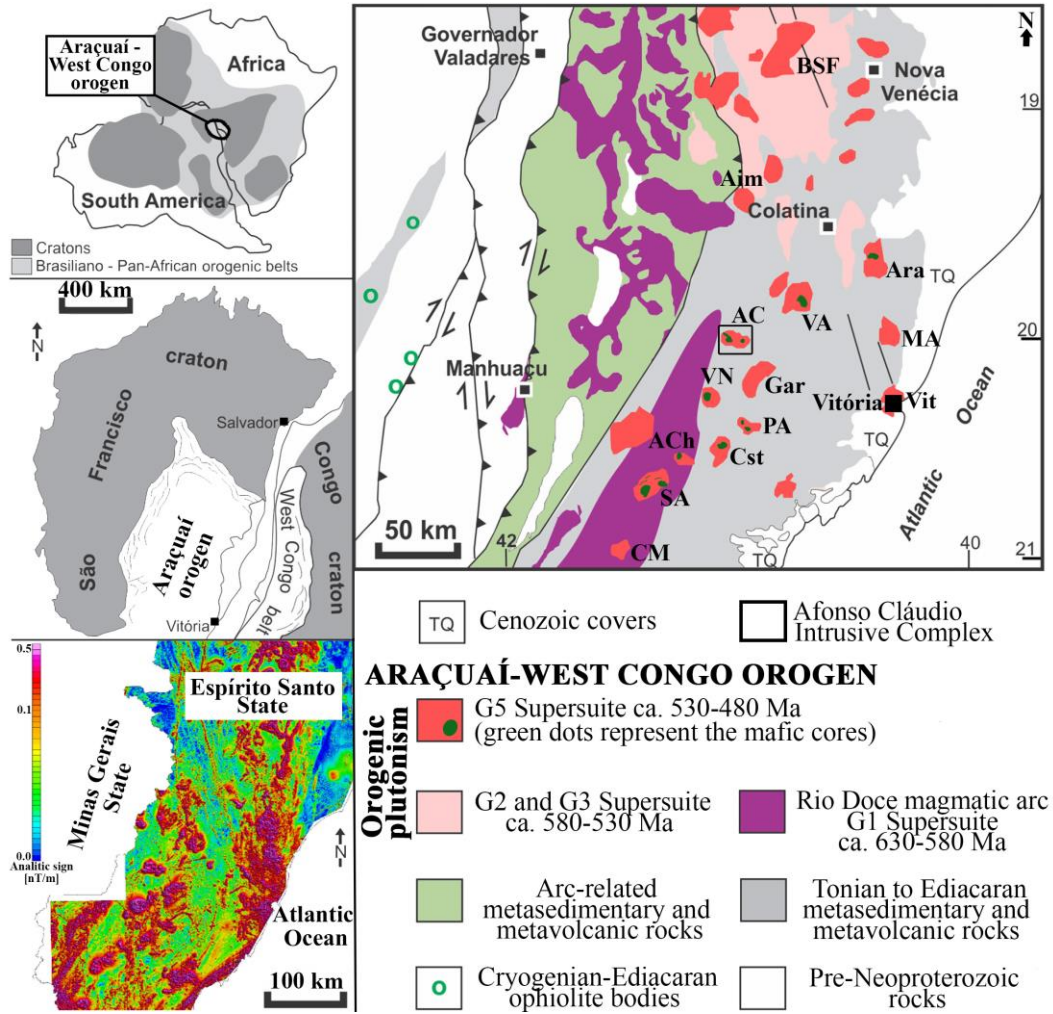
Figure 3.1: AWCO tectonic setting during West Gondwana amalgamation and a simplified geotectonic map of part of southern AWCO. Modified from Alkmim et al. (2006), Pedrosa-Soares et al. (2011, 2008), and Serrano et al. (2018). On the left down side is showed the analytic signal amplitude magnetometric map of the Espírito Santo state for comparison. Modified from Vieira (2015). The abbreviations of the intrusions assumed in the geotectonic map are: AC: Afonso Cláudio; ACh: Alto Chápeu; Aim: Aimorés; Ara: Aracruz; BSF: Barra de São Francisco; Cst: Castelo; CM: Conceição do Muqui; Gar: Garrafão; MA: Mestre Álvaro; PA: Pedra Azul; SA: Santa Angélica; VA: Várzea Alegre; VN: Venda Nova; Vit: Vitória.

Table 3.1: Summary of some aspects about several AWCO post-collisional intrusions (Horn and Weber-Diefenbach, 1987; Schmidt-Thome and Weber-Diefenbach, 1987; Bayer et al., 1987; Ludka et al., 1998; Mendes et al., 1999, 2005; Ludka and Wiedemann-Leonardos, 2000; Medeiros et al., 2000, 2001; Wiedemann et al., 2002; De Campos et al., 2004, 2016; De Mello et al., 2011; Mendes and De Campos, 2012; Gradim et al., 2014; Vieira, 2015; Zanon et al., 2015; Serrano et al., 2018; Aranda et al., 2020, 2021; Melo et al., 2020; Araujo et al., 2020; Teixeira et al., 2020; Wisniowski et al., 2021; Fernandes et al., 2021; Lopes de Macêdo et al., 2022; Potratz et al., 2022; Bellon et al., 2022; and references therein).

Post-collisional igneous complex/	C.a. area (km²)	Main lithotypes	Main enclosing country rocks	Hosted enclaves and xenoliths	Zircon U-Pb ages (Ma)	$\varepsilon Nd_{(t)}$ values	$\varepsilon Sr_{(t)}$ values	$\varepsilon Hf_{(t)}$ values	T_{DM} (Ga) (Hf)
Aimorés (Aimorés)	150	Monzodiorite, charnockite, granodiorite and granite	Nova Venécia Complex, Pocrane Complex, and G2 and	Mafic Microgranular Enclaves	498 (charnockite)	-7.77 (monzodiorite); -7.05 (charnockite); -6.58 (granodiorite);	Unknown	Unknown	Unknown
Afonso Cláudio	73	Monzogabbro (ranging to quartz monzogabbro), monzodiorite (ranging to quartz monzodiorite), hybrid rocks (quartz	Nova Venécia Complex and G1 Supersuite	Mafic Microgranular Enclaves and orthogneiss (G1 Supersuite)	496 (monzogabbro); 480 (quartz monzonite)	Unknown	Unknown	-11.89 to -8.84 (monzogabbro; -12.93 to -10.66 (quartz monzonite)	1.81 to 1.67 (monzogabbro; 1.84 to 1.73 (quartz monzonite)
Alto Chapéu	52	Monzodiorite (ranging to diorite), quartz syenite, and syenogranite	G1 Supersuite	Mafic Microgranular Enclaves	531 (syenogranite)	Unknown	Unknown	Unknown	Unknown
Aracruz	Not defined	Diorite, norite, charnockite, and granite	Nova Venécia Complex and Cenozoic	Paragneiss xenoliths	Unknown	Unknown	Unknown	Unknown	Unknown
Barra do São Francisco	Not defined	Charnockite and granite	G2 and G3 Supersuite	Mafic Microgranular Enclaves and paragneiss	528 to 509 (granite); 524 to 498 (charnockite)	-14.44 (granite); -8.20 (charnockite)	130.80 (granite); 111.06 (charnockite)	-9.3 to -5.9 (granite); -7.4 to -0.5 (charnockite)	1.68 to 1.49 (granite); 1.58 to 1.21 (charnockite)
Caladão (Aimorés)	Not defined	Granite (ranging to granodiorite, syenite and tonalite)	G2 and G3 Supersuite and Nova Vencia	Mafic Microgranular Enclaves and schist	Unknown	Unknown	Unknown	Unknown	Unknown
Castelo	100	Diorite (ranging to quartz monzodiorite), hybrid rocks (granodiorite), and monzogranite	G1 Supersuite and Italva Group	Mafic Microgranular Enclaves and orthoneiss and	486 Ma (quartz monzodiorite); 524 to 499 (monzogranite)	Unknown	Unknown	-22.7 to 12.5 (quartz monzodiorite); -24 to +12.6 (monzogranite)	2.64 to 0.65 (quartz monzodiorite); 2.71 to 0.64 (monzogranite)
Conceição do Muqui	50	Diorite, monzodiorite, monzonite, and monzogranite	Bom Jesus do Itabapoana Group and	Mafic Microgranular Enclaves and	Unknown	Unknown	Unknown	Unknown	Unknown
Cotaché	Not defined	Granite and charnockite	G2 and G3 Supersuite	Unknown	503 (granite)	-7.31 to -6.04 (granite)	99.22 to 127.82	Unknown	Unknown
Fundão	Not defined	Norite, granite, and charnockite	Nova Venécia Complex, G2 Supersuite,	Unknown	Unknown	Unknown	Unknown	Unknown	Unknown

Garrafão	Not defined	Granite, quartz diorite, and enderbite	Nova Venécia Complex and G1	Orthogneiss, paragneiss, and quartzite xenoliths	Unknown	Unknown	Unknown	Unknown	Unknown
Ibituba	Not defined	Diorite, granite, and charnockite	Nova Venécia Complex and G1 Supersuite	Paragneiss (Nova Venécia Complex), orthogneiss and	Unknown	Unknown	Unknown	Unknown	Unknown
Iconha (Alfredo Chaves and Iconha Intrusions	100	Diorite (ranging to monzonite), granodiorite (ranging to quartz monzonite), and granite	Nova Venécia Complex, G1 Supersuite, and	Unknown	Unknown	Unknown	Unknown	Unknown	Unknown
Itaoca	11	Gabbronorite (ranging to pyroxenite)	G1 Supersuite and Italva	Unknown	Unknown	-8.05 to -3.83 (gabbronorite)	15.31 to 30.24 (gabbronorite)	Unknown	Unknown
Itapina	Not defined	Diorite, granite, and charnockite	Nova Venécia Complex, G1 Supersuite, and G2 and	Unidentified xenoliths	Unknown	Unknown	Unknown	Unknown	Unknown
Lagoa Preta	Not defined	Gabbro, diorite, charnockite, anorthosite, and granite	Nova Venécia Complex and G1	Unknown	585 (charnockite)	Unknown	Unknown	Unknown	Unknown
Lajinha do Mutum	Not defined	Diorite and granite (ranging to granodiorite)	Rio Doce Group and Ipanema	Mafic Microgranular Enclaves	Unknown	Unknown	Unknown	Unknown	Unknown
Medina	1000	Monzogranite and syenogranite	G2 and G3 Supersuite	Mafic Microgranular Enclaves	501 (granite)	Unknown	Unknown	Unknown	Unknown
Mestre Álvaro	Not defined	Diorite, tonalite and granite	Nova Venécia Complex and	Unknown	526 (tonalite)	Unknown	Unknown	-8.8 to -5.7 (tonalite)	1.66 to 1.49 (tonalite)
Mimoso do Sul (Jacutinga	14	Gabbronorite	G1 Supersuite	Unknown	Unknown	-14.10 to -10.39 (gabbronorite)	45.56 to 59.94 (gabbronorite)	Unknown	Unknown
Mimoso do Sul (Torre Intrusion)	80	Diorite (ranging to monzodiorite), monzonite, quartz monzonite, and	Italva Group, São Fidelis Group, and	Unknown	498 (monzonite); 480 (granite)	-14.58 to -12.20 (monzonite)	39.89 to 41.23 (monzonite)	Unknown	Unknown
Padre Paraíso (Aimorés)	Not defined	Charnockite, enderbite, jotunite, mangerite, and opdalite	G2 and G3 Supersuites	Schist, paragneiss (Nova Venécia Complex),	513 to 502 (charnockite)	Unknown	Unknown	Unknown	Unknown
Pedra Azul (Aracê)	200	Diorite, tonalite, granodiorite (the last two maybe hybrid rocks), monzogranite, and syenogranite	Nova Venécia Complex	Mafic Microgranular Enclaves and quartzites and	522 (granite)	Unknown	Unknown	-23.8 to -21.3 (granite)	2.47 to 2.34 (granite)
Pedra do Elefante	Not defined	Charnockite and granite	Nova Venécia Complex and G2 and	Mafic Microgranular Enclaves	487 (charnockite); 531 (granite)	-9.32 (charnockite); -10.67 (granite)	72.21 (charnockite); 79.17 (granite)	Unknown	Unknown

Rio Novo do Sul	80	Quartz diorite (ranging to quartz gabbro), quartz monzodiorite (ranging to quartz monzogabbro), quartz monzonite (ranging to	São Fidélis Group, Nova Venécia Complex, G1 Supersuite, and Cenozoic	Mafic Microgranular Enclaves and paragneiss and orthogneiss xenoliths	Unknown	Unknown	Unknown	Unknown	Unknown
Santa Angélica	200	Gabbrodiorite (ranging to monzogabbrodiorite), hybrid rocks, and granites (allanite-bearing and titanite-	G1 Supersuite and Bom Jesus do Itabapoana Group	Mafic Microgranular Enclaves and orthogneiss (possibly	501 to 498 (gabbrodiorite); 515 to 510 (hybrid rocks); 513 to 492 (granite)	-13.55 to -12.40 (gabbrodiorite); -13.42 to -12.18 (granite)	43.73 to 47.52 (gabbrodiorite); 184.28 (granite)	-31.45 to 12.44 (gabbrodiorite); -28.39 to 13.09 (hybrid rocks); -35.28	3.09 to 0.64 (gabbrodiorite); 2.93 to 0.59 (hybrid rocks); 3.32 to 2.71 (granite)
São Gabriel da Baunilha	Not defined	Norite	Nova Venécia Complex and G2 and G3	Possibly metagranite (G2 and G3 Supersuite) xenoliths	524 (norite)	Unknown	Unknown	Unknown	Unknown
Várzea Alegre	150	Gabbronorite (ranging to monzograbbro and diorite), hybrid rocks (quartz diorite, quartz monzodiorite and	G1 Supersuite, Nova Venécia Complex and G2 and G3	Mafic Microgranular Enclaves and gneiss xenoliths	507 (granite); 498 (charnockite)	-6.09 to -4.73 (gabbronorite); -7.90 to -7.31 (hybrid rocks); -7.93 to -7.91 (granite); -10.10 to -6.51	36.41 to 48.50 (gabbronorite); 38.12 to 47.62 (hybrid rocks); 19.56 to 64.84 (granite); 55.51 to	Unknown	Unknown
Venda Nova	75	Alkali gabbronorite (ranging to olivine gabbronorite), hybrid rocks (monzodiorite), syeno-monzonites (ranging to quartz monzonites), granite	G1 Supersuite, Nova Venécia Complex, Italva Group, and G2 and G3	Mafic Microgranular Enclaves	500 (alkali gabbronorite); 497 (syeno-monzonite); 483 (charnockite)	-10.49 to -9.28 (alkali gabbronite); -11.28 to -7.33 (charnockite)	37.43 (alkali gabbronorite); 29.22 to 51.47 (charnockite	Unknown	Unknown
Viana	Not defined	Granite and charnockites	Nova Venécia Complex and	Unknown	Unknown	Unknown	Unknown	Unknown	Unknown
Vitória	Not defined	Granite	Nova Venécia Complex and	Mafic Microgranular Enclaves	505 (granite)	Unknown	Unknown	-10.3 to -7.4 (granite)	1.71 to 1.58 (granite)

3.2.1. Afonso Cláudio Intrusive Complex review

The ACIC is an elliptic shape igneous body outcropping an area of 73 km^2 (Signorelli et al., 1993; Aranda et al., 2020). This pluton intruded by one dextral regional shear zone into high-grade allanite-bearing orthogneisses from AWCO pre-collisional stage (G1 Supersuite) and cordierite-bearing to cordierite-free garnet-sillimanite-biotite paragneisses from Nova Venécia Complex, which locally melted due to ACIC intrusion (Figure 3.2) (Signorelli et al., 1993; Vieira, 2015; Aranda et al., 2020). Aranda et al. (2020) investigated the ACIC in detail and mapped two lowered off-centered cores composed of monzogabbro and monzodiorite surrounded by quartz monzonite high hills (Figures 3.3a, 3.3b and 3.3c), with intense magma mingling and mixing between these domains (Figure 3.3d), where jotunite and quartz mangerite

were locally found (Figure 3.2). Furthermore, syenogranite and quartz-feldspar rich dykes crosscut the ACIC and mafic microgranular enclaves and crustal xenoliths are widespread by the quartz monzonite domain.

The ACIC rocks show typical post-collisional signature and LREE and LILE enrichment patterns, in addition to a metaluminous character, alkali-calc signature and a typical linear trend between monzogabbro and monzodiorite to quartz monzonite in Harker diagrams (Aranda et al., 2020). The ACIC rocks are associated to mid to lower crustal levels and show magmatic crystallization ages of 480 Ma for quartz monzonite and 496 Ma for monzogabbro, both rocks types showing negative ƐHf values ranging from -12.93 to - 8.84, which are concordant with the typical post-collisional plutons from AWCO (De Campos et al., 2016; Aranda et al., 2020, 2021; Araujo et al., 2020).
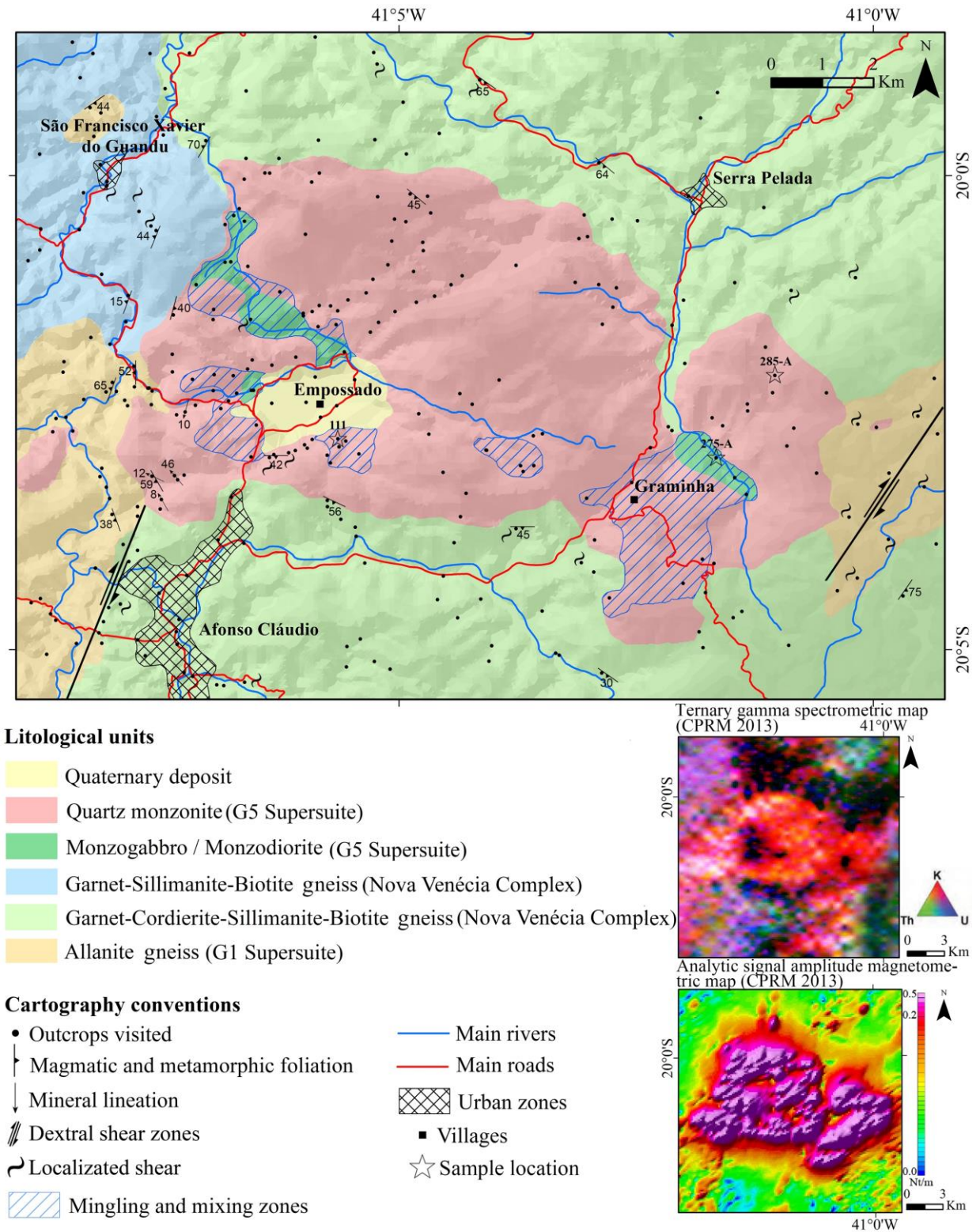
Figure 3.2: Afonso Cláudio Intrusive Complex geological map (Aranda et al., 2020).
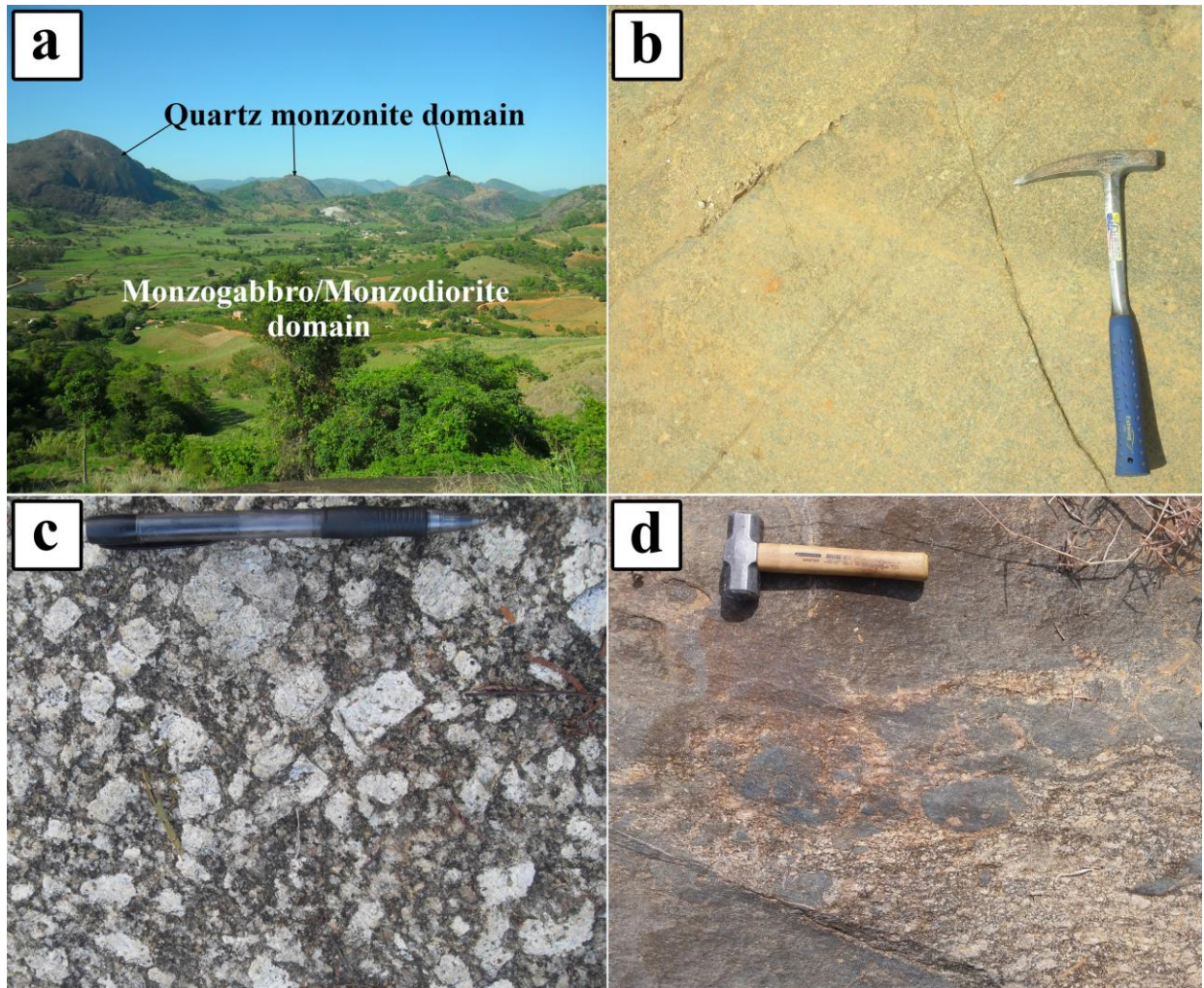
Figure 3.3: General aspects of the ACIC. (a): General view of the monzodiorite and monzogabbro lower regions surrounded by higher quartz monzonite hills. (b): General aspect of the monzodiorite. (c): General aspect of the quartz monzonite. (d): Monzogabbro/monzodiorite as mafic microgranular enclaves hosted by quartz monzonite in a mingling and mixing zone.

3.3. Methodology

The samples were collected from outcrops previously visited and described by Aranda et al. (2020) in which crustal xenoliths were found. Three xenoliths without visual host magma interactions were selected to petrography, whole-rock geochemistry (major and trace elements) and U-Th-Pb monazite geochronology. These xenoliths were classified as allanite-bearing orthogneiss (samples P111 and P285-A) from AWCO pre-collisional stage and paragneiss (sample P275-A) from Nova Venécia Complex.

The petrography and photomicrography acquisition were conducted with a Zeiss Axioplan at Arkad Laboratory facilities, while the whole-rock geochemical analyses were performed at SGS Labs facilities. In addition to the three xenoliths, six samples from enclosing country rocks previously collected by Aranda et al. (2020) were also analyzed, which comprise three allanite-bearing orthogneisses from AWCO pre-collisional stage (samples P52, P89, and P268) and three paragneisses from Nova Venécia Complex (cordierite-bearing to cordierite-free garnet-sillimanite-biotite paragneisses, samples P23, P117, and P274-A). All samples were washed to remove superficial contaminants, dried at 105 °C, crushed to 3 mm in crusher machine, homogenized, quartered, crushed to 150 mesh in agate ball mill and melted with lithium metaborate. After sample preparation, major and some trace elements concentrations were analyzed by Inductively Coupled Plasma Optical Emission Spectroscopy (ICP-OES), while the most trace and rare-earth elements (REE) concentrations were measured by Inductively Coupled Plasma Mass Spectroscopy (ICP-MS). The LOI was calculated by weight difference after 1000°C heating. The Igpet software (Carr and Gazel, 2017) was used to treat and interpret the whole-rock geochemical analyses.

The U-Th-Pb monazite geochronology was conducted with an Electron Probe Microanalyzer (EPMA) model JEOL JXA 8900-RL at Microcopy Center of Federal University of Minas Gerais (CM-UFMG) following the methodology of Chaves et al. (2013). The thin sections from the three selected xenoliths were first carbon coated and analyzed under 25kV, 50nA and probe diameter ranging from 1 to 5 μm to search and image monazite crystals. Backscattered imaging from all analyzed monazite crystals and chemical distribution maps (Ce, P, Pb, Th, U and Y) of one monazite crystal from each sample were performed to support the analyses of the two thin sections where monazite crystals were found (P111 and P275-A). The software EPMA dating (Pommier et al., 2004) was used to calculate the chemical U-Th-Pb ages and associated errors, while the average ages were calculated using Isoplot (Ludwig, 2003).

3.4. Results

3.4.1. Field aspects

Xenoliths from crustal rocks were found widespread in the quartz monzonite domain, while in the monzogabbro/monzodiorite domain were occasional. The xenoliths were clustered in two main groups, allanite-bearing orthogneisses and paragneisses, which were respectively

interpreted as rocks from enclosing AWCO pre-collisional stage and Nova Venécia Complex (Figures 3.4a and 3.4b). The xenoliths from both groups are morphologically similar, ranging in shape from angular to spheroidal, oval or irregular and in size from millimetric to metric scale, sometimes higher than 1 meter (Figures 3.4a, 3.4b, 3.4c and 3.4d). Allanite-bearing orthogneiss xenoliths higher than 100 meters were occasionally found, with these larger xenoliths interpreted as roof pendants. These ones were mainly situated enclosed by the quartz monzonite near the ACIC borders, however one large xenolith was found hosted by the quartz monzonite near the monzogabbro/monzodiorite core. The xenoliths for both groups and the host rocks (mainly the quartz monzonite) show contacts from sharp to irregular or diffuse (Figures 3.4a, 3.4c, 3.4d, 3.4e and 3.4f). It is frequently possible to note melting aspects and reworking of the xenoliths, where some of them show large feldspar crystals and deformational evidences such as strong folding of the internal foliation (Figure 3.4a). It is also possible to note that these xenoliths are often consumed by the quartz monzonite, where the paragneisses became darker or evanescent, the allanite-bearing orthogneisses became richer in large feldspar crystals and both show quartz monzonite injections (Figures 3.4b, 3.4e, 3.4f, 3.4g and 3.4h). In addition, some oriented xenoliths and mafic microgranular enclaves (monzogabbro and monzodiorite) occur grouped in the quartz monzonite domain near the mingling/mixing zones, which may be interpreted as enclave swarm.

The collected crustal xenolith samples characterize two large allanite-bearing orthogneiss xenoliths hosted by quartz monzonite, one larger than 100 meters near the monzogabbro/monzodiorite core (P111) and one larger than 1 meter near the ACIC border (P285-A), and one small paragneiss xenolith hosted by monzogabbro/monzodiorite in the mingling/mixing zone with the quartz monzonite (P275-A) (Figure 3.2).
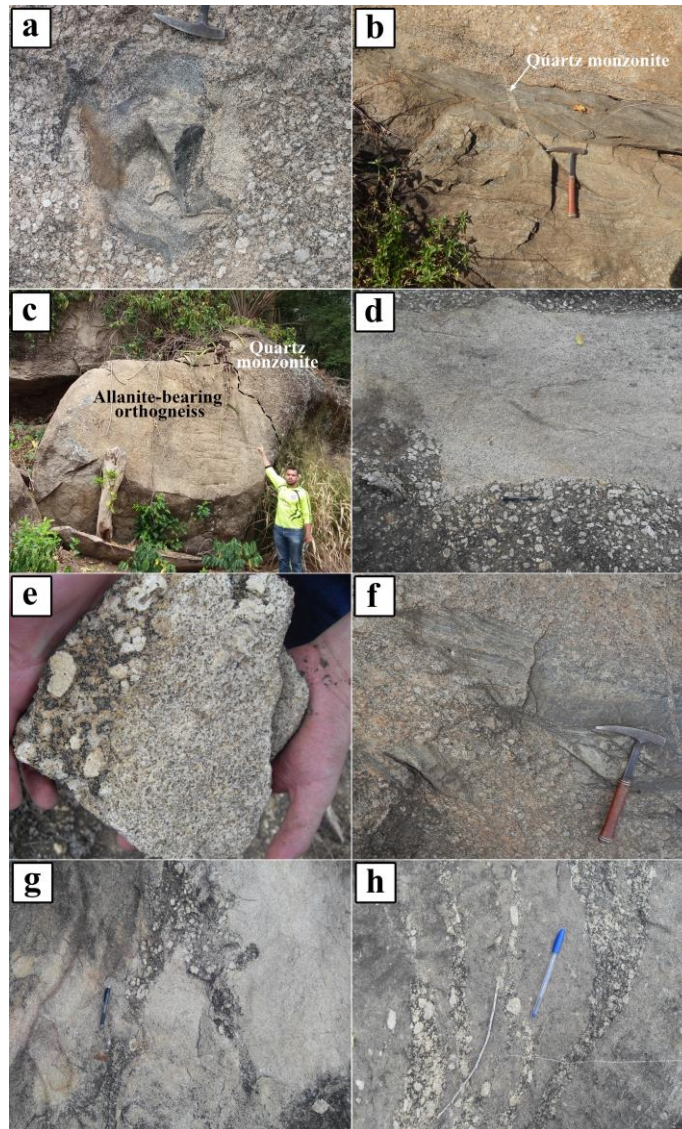
Figure 3.4: General field aspects of the crustal xenoliths hosted by ACIC rocks. (a): Allanite-bearing orthogneiss xenolith showing a spheroidal aspect, irregular contacts with the host quartz monzonite and reworking of the previous metamorphic structure due to the partial melting and deformation. Photography from Aranda et al. (2021). (b): Paragneiss xenolith showing angular shape, darker color and injections of quartz monzonite into the xenolith. (c): Larger than 1 meter allanite-bearing orthogneiss xenolith showing a spheroidal aspect and sharp contact with the host quartz monzonite. (d): Allanite-bearing orthogneiss showing an irregular shape and sharp to irregular contact with the host quartz monzonite. (e): Irregular contact between allanite-bearing orthogneiss xenolith and the host quartz monzonite. In addition, it is possible to note large feldspar crystals into allanite-bearing orthogneiss. (f): Paragneiss xenolith showing irregular contact and evidences of assimilation by the host quart monzonite. (g) and (h): Allanite-bearing orthogneiss xenoliths showing injections of quartz monzonite and large feldspar crystals.

3.4.2. Petrography

Three xenolith samples were selected to petrographic investigation, two allanite-bearing orthogneisses (P111 and P285-A) and one paragneiss (P275-A).

The sample P111 was classified as an allanite-bearing orthogneiss. This rock is mainly composed of quartz (40%), microcline (40%) and plagioclase (15%), while biotite (3%), allanite (<1%), opaque minerals (1%) and occasional hornblende and zircon (both <1%) are the accessory phases. It is a blastoporphyritic rock showing plagioclase and microcline recrystallized blastophenocrysts ranging from 3 to 4.5 mm set in crystals smaller than 3 mm (Figures 3.5a and 3.5b). The quartz crystals are in general smaller than 3 mm and exhibit deformational aspects, showing typical undulose extinction and frequent subgrain generation, occasionally oriented and stretched up to 3.5 mm (Figure 3.5a). Microcline is also abundant in this rock and occurs in crystals generally smaller than 1.25 mm, however some are up to 3 mm, which were classified as blastophenocrysts (Figure 3.5a). Both types show occasional pertites and commonly exhibit tartan twinning. Plagioclase is less abundant than quartz and microcline, however also occurs as blastophenocrysts ranging in size between 3 and 4.5 mm and as crystals smaller than 3 mm (Figure 3.5b). Both ones show typical features, such as frequent twining and compositional zonation, and myrmequite is formed when in contact with microcline. Both feldspars show a weak orientation and are locally replaced by sericite crystals (Figure 3.5b), while quartz, microcline and plagioclase show grain boundaries ranging from interlobate to polygonal. Biotite is the main accessory phase and occurs up to 1 mm as brown oriented crystals showing a subtle grouping, indicating an incipient metamorphic banding (Figure 3.5c). Magnetite and ilmenite (main opaque phases) are up to 0.5 mm and occur normally associated to biotite crystals in the incipient mafic bands (Figure 3.5c). Allanite is up to 0.15 mm and it is frequent, showing typical metamict texture, which is well noted in hand sample, while zircon can only be noted in microscopic observation as crystals up to 0.25 mm. Typical green hornblende occasionally occurs up to 0.25 mm.

The sample P285-A was also classified as allanite-bearing orthogneiss, however this rock is locally blastoporphyritic with microcline recrystallized blastophenocrysts ranging from 3 to 3.5 mm set in crystals smaller than 3 mm (Figures 3.5d and 3.5e). Plagioclase (38%), microcline (34%), quartz (15%) and biotite (8%) are the main mineral phases, while allanite (<1%), zircon (<1%), opaque minerals (2%) and occasional hornblende (1%) and apatite (1%) are the accessory phases. Plagioclase is the main phase occurring as crystals up to 3 mm

showing compositional zonation, occasional twinnings and undulose extinction, in addition to a rare antipertitic aspect. Microcline occurs as occasional blastophenocrysts ranging from 3 to 3.5 mm and as crystals smaller than 3 mm. Both are typical crystals showing occasional pertites and tartan twinning. Some occasional large crystals show plagioclase inclusions and could be classified as blastopoikilitic. Myrmequite is generated when both feldspars are in contact. In addition, both feldspars are replaced to sericite, while quartz, plagioclase and microcline show polygonal to interlobate grain boundaries. Quartz is up to 3 mm and normally shows undulose extinction and subgrain formation, in addition to occasional stretching. Biotite crystals are up to 1.2 mm showing a typical brown color, orientation and grouping with magnetite, ilmenite (both up to 0.5 mm) and occasional green hornblende (up to 0.75 mm) characterizing an incipient metamorphic banding (Figures 3.5e and 3.5f). Allanite is a common accessory phase, occurring as metamitized crystals up to 0.25 mm easily identified in hand sample (Figure 3.5f), while zircon and apatite are accessory phases up to 0.25 mm only identified in microscopic investigation.

The sample P 275-A is an inequigranular rock classified as paragneiss showing a poorly defined metamorphic banding. This rock is mainly composed of quartz (38%), plagioclase (34%), microcline (15%) and biotite (6%), while muscovite (3%), garnet (<1%), opaque minerals (1%), zircon (1%), allanite (<1%), sillimanite (<1%), and occasional apatite (1%), hercynite (<1%), epidote s.s. (1%) and titanite (<1%) are the accessory phases. The plagioclase crystals are up to 2 mm and show common twining and occasional compositional zonation. It is possible to note some well-formed crystals which could be interpreted as from magmatic origin (Figures 3.5g and 3.5h). Microcline is up to 3 mm and occurs as typical twinned crystals occasionally pertitic and myrmequite texture is generated when in contact with plagioclase. Occasional plagioclase, quartz and apatite inclusions occurs. Both feldspars are replaced by sericite crystals and show interlobate grain boundaries. Quartz is up to 3 mm normally showing undulose extinction, occasional subgrain generation and interlobate grain boundaries, while biotite occurs as oriented crystals up to 2 mm. Muscovite is the main accessory phase and occurs as oriented crystals up to 2.5 mm. It is possible to note some aggregates of muscovite with fine inclusions of sillimanite crystals (Figure 3.5h), which also occur as oriented crystals up to 2 mm widespread by the rock. Magnetite, ilmenite, garnet, apatite, zircon, allanite, epidote s.s., hercynite and titanite are the other accessory phases and occur generally smaller than 0.5 mm disseminated in the rock.

Monazite crystals were only found during microprobe investigation in samples P111 and P275-A, while sample P285-A did not show monazite crystals. The monazite crystals are better described in the "U-Th-Pb monazite geochronology" section.
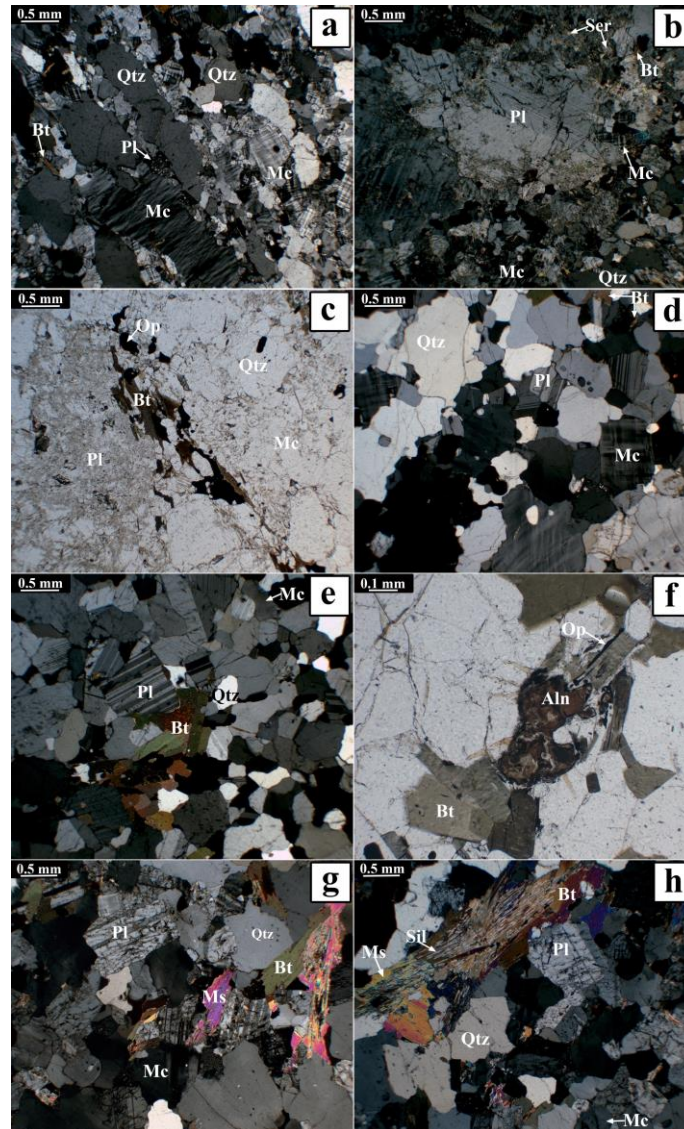
Figure 3.5: General microscopic aspect of the investigated xenoliths. (a): General aspect of allanite-bearing orthogneiss (sample P111), where it is possible to note microcline recrystallized blastophenocryst and stretched quartz crystals (crossed polarized light). (b): Plagioclase recrystallized blastophenocryst locally replaced by sericite crystals (crossed polarized light). (c): General aspect of the foliation and the incipient metamorphic banding (plane polarized light). (d): General aspect of allanite-bearing orthogneiss (sample P285-A) (crossed polarized lights). (e): General aspect of the incipient metamorphic banding (crossed polarized light). (f): Aspect of the metamict allanite crystals (plane polarized light). (g): General aspect of the paragneiss (sample P275-A), where it is possible to note well-formed plagioclase crystals (crossed polarized light). (h): Inclusions of fine and oriented sillimanite crystals in muscovite and well-formed plagioclase crystals (crossed polarized light). Labels: Aln: Allanite, Bt: Biotite, Mc: Microcline, Ms: Muscovite; Pl: Plagioclase, Sil: Sillimanite; Op: Opaque Minerals; Qtz: Quartz; Ser: Sericite.

3.4.3. Whole-rock major and trace geochemistry

Nine samples were selected for whole-rock geochemistry analyses (major and trace elements), which comprise two allanite-bearing orthogneiss xenoliths (samples P111 and P285-A), one paragneiss xenolith (sample P275-A), three allanite-bearing orthogneisses from enclosing country rocks (AWCO pre-collisional stage, samples P52, P89 and P268), and three paragneisses from enclosing country rocks (Nova Venécia Complex, samples P23, P117, and P274-A). The results are presented in supplementary material 2, in addition to the whole-rock database of ACIC main rocks from Aranda et al. (2020).

The allanite-bearing orthogneiss xenoliths show silica values ranging from 68.11 to 75.45 wt%, alkali (Na_2O+K_2O) content from 6.72 to 8.18 wt%, and plot in the granite field in the Total Alkali x Silica diagram (TAS diagram), showing concordance with petrographic investigation (Figure 3.6a). These rocks are metaluminous to weakly peraluminous with alumina saturation index (ASI, molar [Al_2O_3/K_2O+Na_2O+CaO]) ranging from 0.96 to 1.02 and plot in the calc-alkaline series field at AFM and $Na_2O+K_2O-CaOxSiO_2$ diagrams (Figures 3.6b, 3.6c and 3.6d), in addition to a ferroan to magnesian and volcanic arc granite signatures (Figures 3.6e and 3.6f). Chondrite-normalized Rare Earth Element (REE) patterns of the analyzed allanite-bearing orthogneiss xenoliths showed enrichment in Light Rare Earth Elements (LREE) relative to Heavy Rare Earth Elements (HREE) (La_N/Yb_N=158.06 to 12.14) and Eu positive anomalies (Eu/Eu*=1.43-1.73) (Figure 3.7a). It is possible to note that the sample P285-A showed LREE patterns similar to the host quartz monzonite (quartz monzonite, La_N/Sm_N=2.95-9.17; P111, La_N/Sm_N=9.18). Primitive mantle-normalized trace element patterns show enrichment in Large Ion Lithophile Elements (LILE) relative to High Field Strength Elements (HFSE) with Nb, P, Ti and Zr negative anomalies in both samples, while only sample P111 showed Th and Sr negative anomalies (Figure 3.7b). P and Zr were lower than the limit detection in the sample P111, while Ta and Pb were lower than limit detection in all analyzed samples.

The samples of enclosing allanite-bearing orthogneiss present silica content from 67.74 up to 74.47 wt%, which are similar to silica content from allanite-bearing orthogneiss xenoliths, alkali content from 4.51 to 7.37 wt%, and plot in the granodiorite to granite fields in TAS diagram (Figure 3.6a). These rocks present ASI values from 1.04 to 1.06 showing a weakly peraluminous signature (Figure 3.6b) and plot in the calc-alkaline series field in the AFM diagram and between calc-alkaline to calcic series fields in the $Na_2O+K_2O-CaOxSiO_2$ diagram

(Figures 3.6c and 3.6d). These samples also show ferroan to magnesian and volcanic arc granite signatures (Figures 3.6e and 3.6f), such as the allanite-bearing orthogneiss xenoliths. In the chondrite-normalized REE patterns it is possible to note LREE enrichment relative to HREE (La_N/Yb_N= 5.12-34.99), with the sample P268 showing higher REE depletion (La_N/Yb_N=34.99) than samples P89 and P52 (La_N/Yb_N=5.12-11.11) (Figure 3.7c). These samples showed Eu negative (P268) to positive (P89 and P52) anomalies (Eu/Eu*=0.31-2.33) (Figure 3.7c). In the primitive mantle-normalized diagram it is possible to note enrichment in LILE relative to HFSE and Nb, P and Ti negative anomalies in all analyzed samples, while Ba and Sr negative anomalies were only noted in the sample P89 (Figure 3.7d). P is lower than limit detection in the sample P89, while Ta is lower than limit detection in all analyzed samples.

The investigated paragneiss xenolith sample showed silica content of 70.3 wt% and alkali contents of 6.2 wt%, while the analyzed samples of enclosing paragneisses showed silica content from 71.31 to 79.93 wt% and alkali values from 1.6 to 8.09 wt%. Both xenolith and enclosing country rocks showed similar chondrite-normalized REE patterns with relative enrichment in LREE relative to HFSE (La_N/Yb_N= 5.38-32.31), with LREE depletion similar in all samples (La_N/Sm_N= 3.59-4.45), while HFSE depletion ranges from depleted (samples P275-A and P274; Gd_N/Yb_N= 4.30-4.31) to almost flat patterns (P117 and P23; Gd_N/Yb_N= 1.09-1.71) (Figures 3.7e and 3.7g). Eu negative anomaly (Eu/Eu*=0.51-0.75) is omnipresent in all samples (Figures 3.7e and 3.7g). LILE enrichment relative to HFSE and Nb, P and Sr negative anomalies are noted in all samples in the primitive mantle-normalized diagram, while only sample P117 does not show Ti negative anomaly and sample P274 does not show Ba negative anomaly (Figures 3.7f and 3.7h). Only sample P117 has Ta above the detection limit.
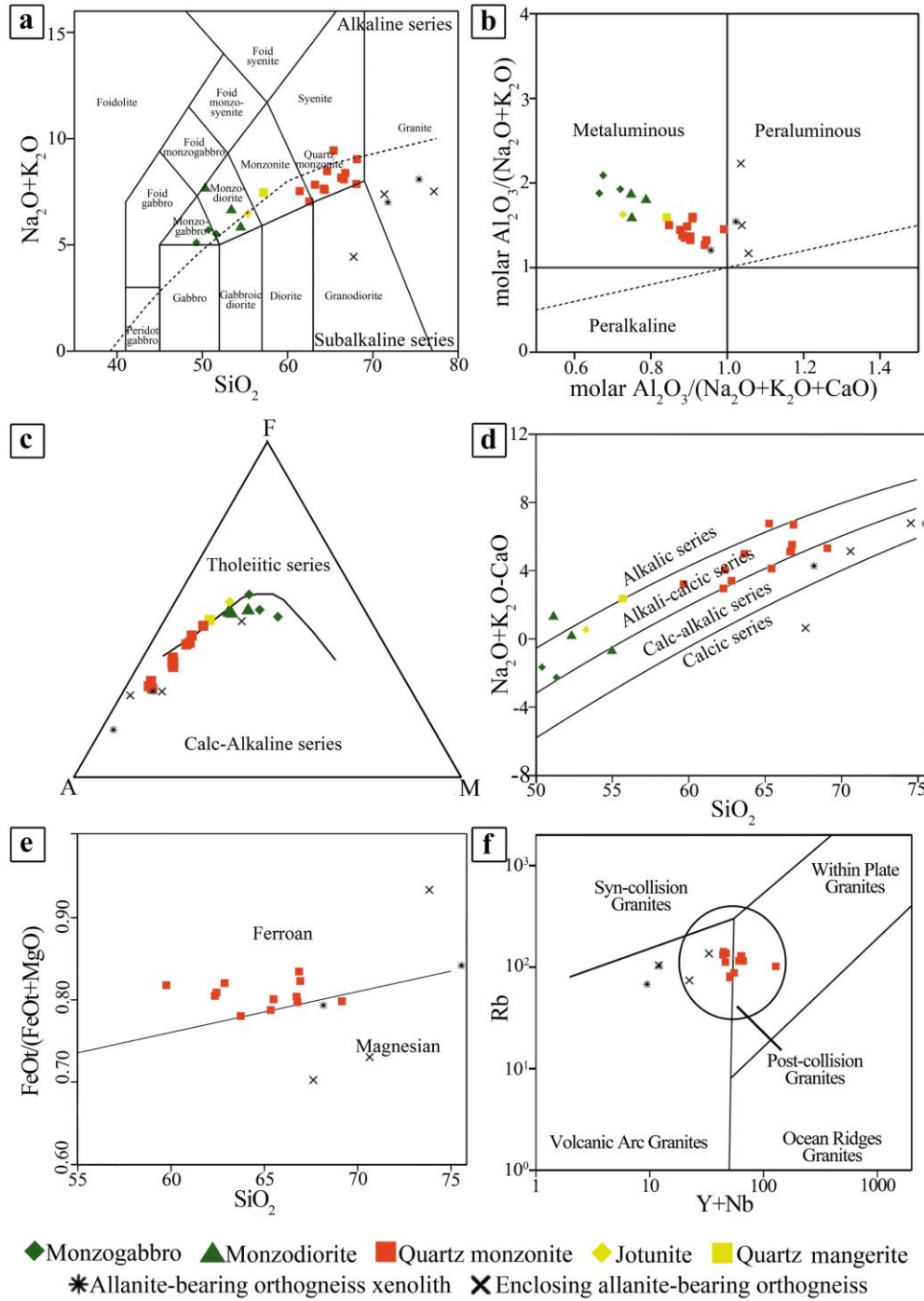
Figure 3.6: Geochemistry aspects of the investigated rocks and the main ACIC rocks. (a): Na_2O+K_2OxSiO_2 (wt%) diagram (Le Bas et al., 1986 adapted by Middlemost, 1994). (b): Molar A/NKxA/CNK diagram (Shand, 1943). (c): AFM (A=Na_2O+K_2O, F=FeO_t, M=MgO) diagram (Irvine and Baragar, 1971). (d): Na_2O+K_2O-CaOxSiO_2 (wt%) diagram showing the approximate fields for the alkalic, alkali-calcic, calc-alkalic, and calcic rock series (Frost et al., 2001). (e): $FeO_t/(FeO_t+MgO)$xSiO_2 (wt%) diagram showing the approximate fields for ferroan and magnesian rock series (Frost et al., 2001). (f): RbxY+Nb geotectonic classification diagram for granitic rocks (Pearce et al., 1984).
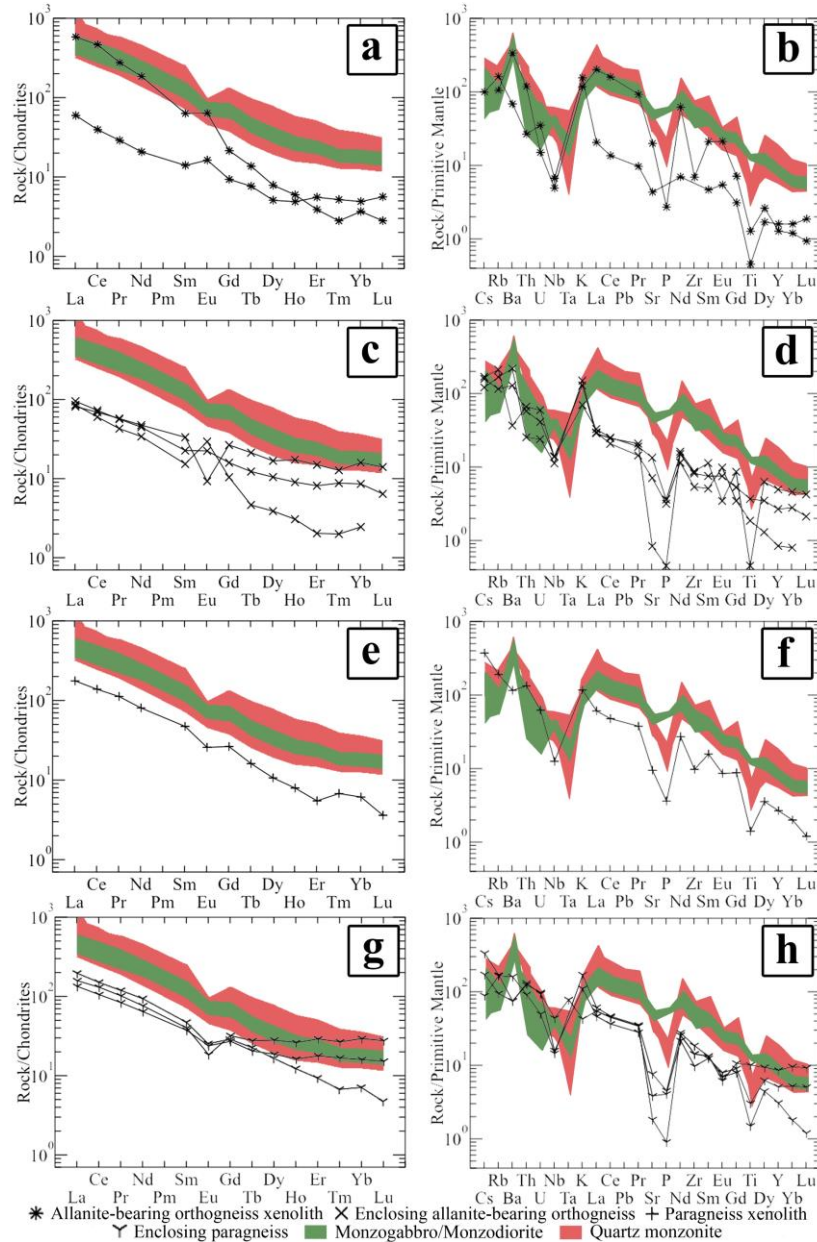
Figure 3.7: REE patterns normalized to chondrite (McDonough and Sun, 1995) and multi-elements spider diagrams normalized to the primitive mantle (Sun and McDonough, 1989) of the investigated rocks and the main ACIC rocks. (a): Allanite-bearing orthogneiss xenolith REE patterns normalized to chondrite. (b): Allanite-bearing orthogneiss xenolith multi-elements spider diagram normalized to the primitive mantle. (c): Enclosing allanite-bearing orthogneiss REE patterns normalized to chondrite. (d): Enclosing allanite-bearing orthogneiss multi-elements spider diagram normalized to the primitive mantle. (e): Paragneiss xenolith REE patterns normalized to chondrite. (f): Paragneiss xenolith multi-elements spider diagram normalized to the primitive mantle. (g): Enclosing paragneiss REE patterns normalized to chondrite. (h): Enclosing paragneiss multi-elements spider diagram normalized to the primitive mantle.

3.4.4. U-Th-Pb monazite geochronology

Monazite crystals from P111 (allanite-bearing orthogneiss xenolith) and P275-A (paragneiss xenolith) samples were analyzed for dating purposes. Fourteen crystals from sample P111 were analyzed with forty-seven analyses distributed between the crystals, while nine crystals from sample P275-A were investigated, with twenty-four analyzes distributed between the crystals. The full dataset of monazite analyzes is presented in supplementary material 3.

The monazite crystals from sample P111 were classified as Ce-monazites and are anhedral to occasionally subhedral showing angular to rounded terminations sometimes fractured and presenting corroded borders (Figure 3.8a). These crystals showed in general normal to diffuse zoning mainly due to ThO_2 variations, with minor Ce_2O_3, La_2O_3, Y_2O_3, SiO_2 and P_2O_3 differences, however some crystals did not show compositional zoning (Figure 3.8a). Two main mean age groups were found, 478.2±9.3 Ma (n=18) and 431±13 Ma (n=11) (Figures 3.9a and 3.9b). It is possible to note two additional crystal populations, one between 521 and 527 Ma (n=3) and another last one between 624 and 635 Ma (n=2). These oldest crystals have higher La_2O_3 contents and are similar to some analyzed crystals which did not produced confident ages due to very low PbO contents.

Monazite crystals from sample P275-A were also classified as Ce-monazites, however the crystals are totally anhedral with frequent rounded terminations and with some occasional crystals showing angular terminations (Figure 3.8b). Crystals showing fractures and corroded borders are more common than in sample P111 and the monazite crystals show absent to diffuse zoning, the later one mainly due to ThO_2 variations coupled with minor Ce_2O_3, La_2O_3, Nd_2O_3, Y_2O_3, SiO_2 and P_2O_3 variations (Figure 3.8b). Two main age groups were found, 477±14 Ma (n=11) and 427±19 Ma (n=7), with only one crystal showing an older age of 527 ± 51 Ma (n=1) (Figures 3.9c and 3.9d).
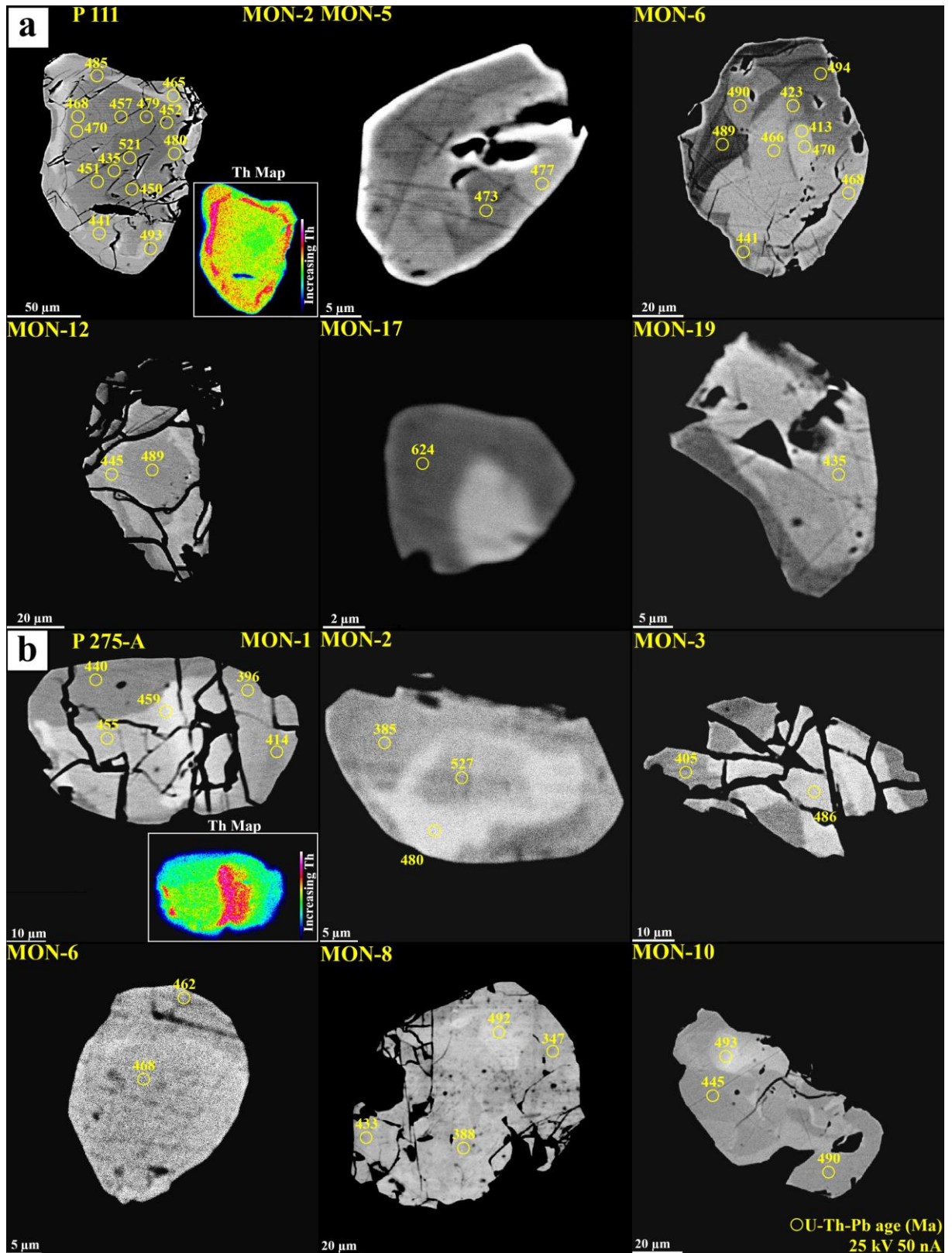
Figure 3.8: Backscattered electron images of some analyzed monazite crystals and Th chemical maps of two diffuse zoned monazites. (a): Monazite crystals from allanite-bearing orthogneiss xenolith (sample P111). (b): Monazite crystals from paragneiss xenolith (sample P275-A).
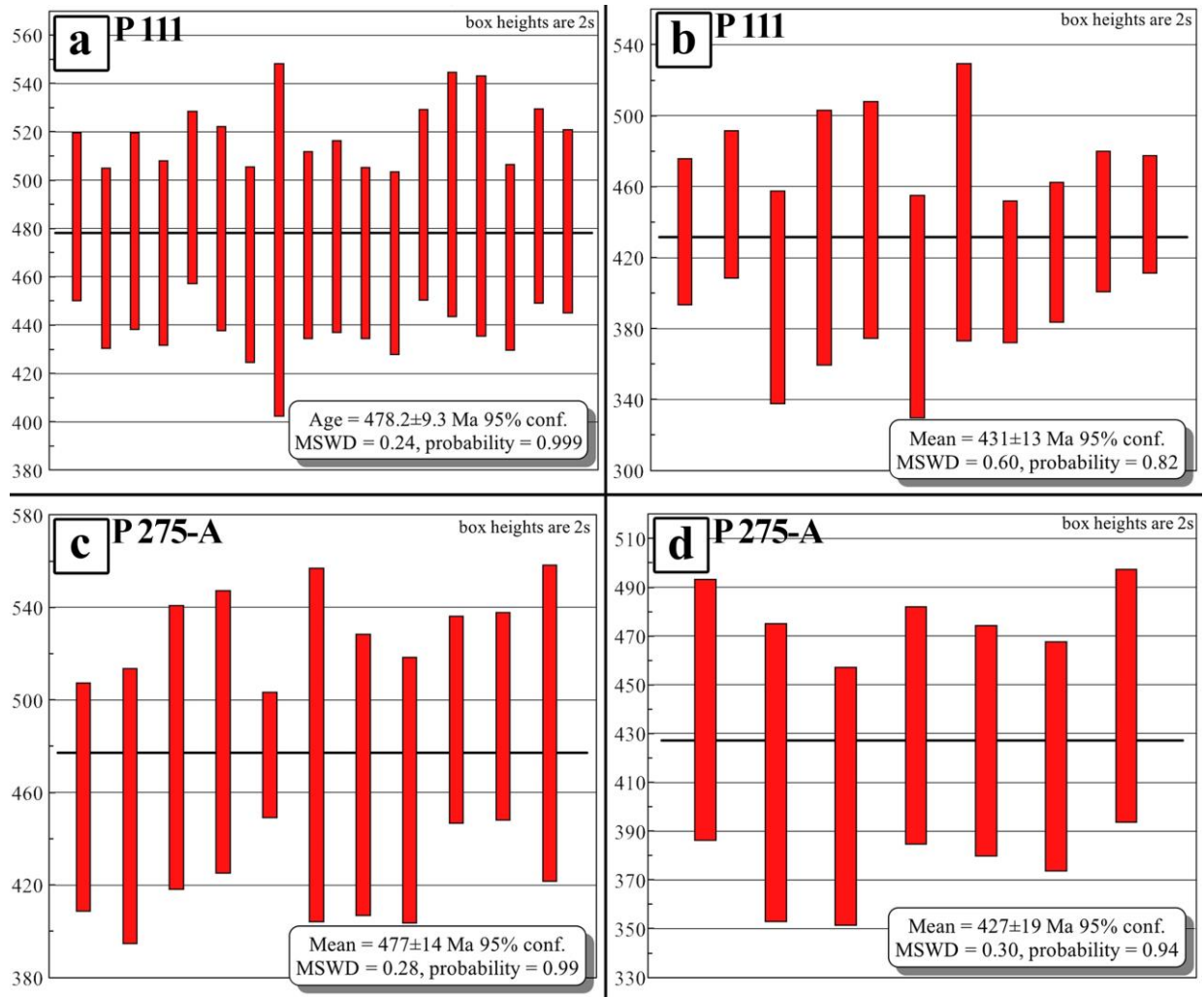
Figure 3.9: U-Th-Pb monazite average ages of the analyzed samples. (a): Older age group from allanite-bearing orthogneiss xenolith (sample P111). (b): Younger age group from allanite-bearing orthogneiss xenolith (sample P111). (c): Older age group from paragneiss xenolith (sample P275-A). (d): Younger age group from paragneiss xenolith (sample P275-A).

3.5. Discussion

3.5.1. Significance of U-Th-Pb monazite ages

Monazite is an LREE-bearing phosphate that can preserve since crystallization ages to a long time of geological events (Parrish, 1990; Williams et al., 1999, 2007, 2011). Investigation of this mineral phase has been applied with success to understand and track the evolution of diverse geological terranes worldwide (Dias et al., 1998; Terry et al., 2000; Dumond et al., 2008; Brandt et al., 2011; Ondrejka et al., 2012; Jiao et al., 2020; Skrzypek et

al., 2020) and it has been proved that the investigation of one single crystal can preserve a complex and long-time geological history (Parrish, 1990; Williams et al., 1999).

The monazite ages obtained in the analyzed samples are strongly concordant, while the allanite-bearing orthogneiss xenolith (sample P111) showed two main age groups of 478.2±9.3 Ma and 431±13 Ma, the main age groups preserved at monazite crystals from the paragneiss xenolith (sample P275A) are 477±14 Ma and 427±19 Ma (Figure 3.10).

The older ages (478.2±9.3 Ma and 477±14 Ma) are associated to the assimilation of the xenoliths by the host quartz monzonite magma and succeeding crystallization of the host, that shows U-Pb zircon crystallization age of 480±3.2 Ma (Aranda et al., 2020). These ages are strongly concordant with AWCO post-collisional magmatism (Wiedemann et al., 2002; De Campos et al., 2016; Araujo et al., 2020) and this event is accountable to partially reset the ages of monazite crystals found in both xenoliths (Figure 3.10). Monazite crystals submitted to thermal events that achieve 450°C have its U-Th-Pb systematic affected (Williams et al., 2011) and the crystallization temperatures associated to the host quartz monzonite range from near 909°C down to 623°C (Aranda et al., 2021). The average younger ages obtained in the xenoliths with comparison to the host quartz monzonite could be related to the time that the pluton remained heated, which could easily last 5 Ma (Spera, 1980; Coulson et al., 2002; Wagner et al., 2006; Barboni et al., 2013) and could be easier recorded in monazite than in zircon due to the capability of this LREE-bearing phosphate to register thermal events related to lower temperatures (Williams et al., 2011).

The younger ages (431±13 Ma and 427±19 Ma) obtained in monazite crystals from the analyzed xenoliths are similar to an age obtained to a leucocratic dyke which crosscuts the Castelo Intrusive Complex, that shows U-Pb zircon crystallization age of 426±15 Ma (Lopes de Macêdo et al., 2022). These authors interpreted that the thermal event responsible for the post-collisional magmatism remained active at least to this age, as well as the AWCO post-collisional stage. In ACIC, these ages are probably associated to the intrusion of the syenogranite dykes that crosscut this pluton (Aranda et al., 2020). As previously mentioned, the U-Th-Pb monazite systematics can be easily affected by thermal events that achieve 450°C and syenogranitic rocks worldwide show crystallization temperatures up to near 800°C (Yuguchi and Nishiyama, 2007; Zou et al., 2019). This thermal event registered in monazite crystals from xenoliths could represent a late stage of the AWCO post-collisional magmatism or a later unrelated thermal event (Figure 3.10). Post-collisional younger ages were also found at Ribeira orogen, which limits to south the Araçuaí orogen and shows similar tectonic

evolution (Da Silva Schmitt et al., 2004; Bongiolo et al., 2016; Vieira et al., 2022). Bongiolo et al. (2016) interpreted that these younger ages could represent an extension of the post-collisional magmatism in the region.

In addition to the two main age groups found at the analyzed xenoliths, two age populations were found. A set of ages of 527 to 521 Ma was found in both samples and it is concordant with the beginning of the AWCO post-collisional magmatism (Araujo et al., 2020; Potratz et al., 2022). Oldest ages ranging from 635 to 624 Ma were only found in two crystals from allanite-bearing orthogneiss xenolith and are probably associated to monazite unaffected areas by the post-collisional magmatism or later thermal events. These ages are concordant with the typical ages of the Rio Doce magmatic arc (Gonçalves et al., 2016; Tedeschi et al., 2016; Gouvêa et al., 2020; Araujo et al., 2023), which is associated to the AWCO pre-collisional magmatism, to which allanite-bearing orthogneiss from ACIC enclosing country rocks are related.
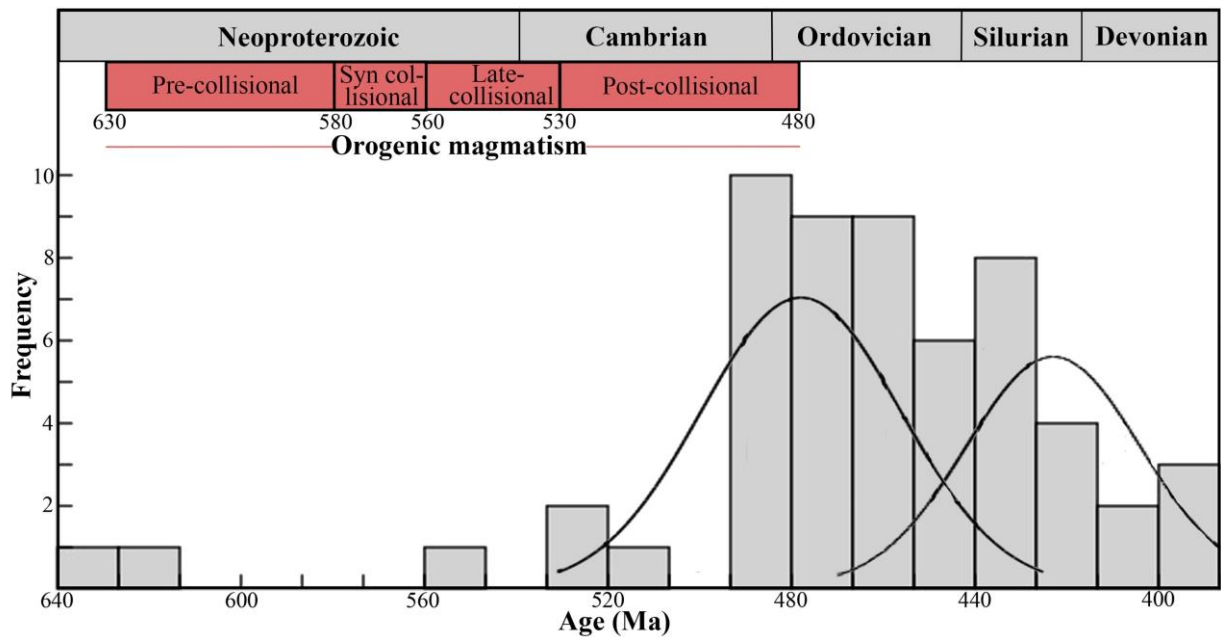
Figure 3.10: Histogram of ages obtained from the analyzed xenoliths in comparison the main AWCO orogenic magmatic events. The ages of AWCO magmatism are from Pedrosa-Soares et al. (2011), De Campos et al. (2016), and references therein.

3.5.2. Crustal assimilation and magma sources of ACIC

AWCO post-collisional magmatism has been extensively studied and it is largely known that at least mantle and crustal magmas interacted to generate the plutons crystalized in this tectonic stage (Medeiros et al., 2001; Wiedemann et al., 2002; De Campos et al., 2016). The most primitive gabbroic rocks from this geotectonic supersuite were found at Jacutinga and Itaoca (Mimoso do Sul) plutons and showed Ba, Sr and LREE enrichment, low contents of Rb and K, $\varepsilon Nd_{(t)}$ values of -14.10 to -3.83, and $^{87}Sr/^{86}Sr$ values ranging from 0.705394 to 0.70892, which supports a crustal component in these rocks (Ludka and Wiedemann-Leonardos, 2000; De Campos et al., 2016). Gabbroic rocks from Venda Nova Intrusive Complex also exhibited similar geochemical characteristics, however the enclosing country rocks showed similar to lower contents of Ba, Sr and LREE, suggesting that the neighboring rocks could not be the main crustal contamination source of these gabbroic rocks (Ludka et al., 1998). This crustal component has been associated to a gradual enrichment of a depleted mantle probably due to introduction of crustal material into mantle through subduction at AWCO collisional stage (Ludka et al., 1998; Ludka and Wiedemann-Leonardos, 2000; De Campos et al., 2016). Additional evidence of the crustal influence in the gabbroic rocks has been provided to recent investigations focused on Hf isotopes, which revealed common negative $\varepsilon Hf_{(t)}$ signatures in gabbroic to dioritic rocks from Afonso Cláudio, Castelo and Santa Angélica Intrusive Complexes (Aranda et al., 2020; Lopes de Macêdo et al., 2022; Potratz et al., 2022). Though, to explain the very negative $\varepsilon Nd_{(t)}$ and $\varepsilon Hf_{(t)}$ coupled to higher Ba and Sr values commonly found at mafic to intermediate rocks of AWCO post-collisional plutons it is necessary an additional crustal component in addition to the material introduced into mantle during crust subduction (De Campos et al., 2016).

The AWCO post-collisional stage is associated to the collapse of this orogenic system (Pedrosa-Soares et al., 2001, 2011). Gravitational forces due to the crustal thickening developed during the AWCO collisional stage associated to the hot asthenosphere up-flow after slab-break off and crustal delamination followed by the upwelling of a mantle plume could be the triggers of the intense AWCO post-collisional magma production (Pedrosa-Soares et al., 2001, 2011; De Campos et al., 2016; Serrano et al., 2018). An additional input of crustal material into mantle could had provided to the delamination of a Paleoproterozoic or older lower crust, which could explain the high negative $\varepsilon Nd_{(t)}$ and $\varepsilon Hf_{(t)}$ values found in post-collisional gabbroic rocks (De Campos et al., 2016). Decompression associated to the addition of heat and volatiles related to

the previously mentioned processes contributed to the melting of an enriched lithospheric mantle (Wiedemann et al., 2002; De Campos et al., 2016), generating a magma enriched in elements not commonly found in juvenile magmas (Sparks, 1986; Ludka and Wiedemann-Leonardos, 2000). The $\varepsilon Nd_{(t)}$ values found at AWCO gabbroic rocks associated to the crystallization of these magmas range from very negative to almost positive, with these higher values partially related to later and deeper juvenile mantle magma injections (De Campos et al., 2016). Gabbroic intrusions crosscutting previously crystalized or in sub-solidus state gabbroic rocks were found by Zanon et al. (2015) at Santa Angélica Intrusive Complex. Positive $\varepsilon Hf_{(t)}$ values recently found at gabbroic and dioritic rocks from Castelo and Santa Angélica Intrusive Complexes (Lopes de Macêdo et al., 2022; Potratz et al., 2022) provide further evidence of a juvenile component and mantle contribution in the AWCO post-collisional magmatism.

The mantle magmas mainly ascent by deep faults and shear zones generated or reactivated at AWCO post-collisional stage, where the decompression associated to the gravitational collapse and heat influx provided to the mantle magmas contributed to the melting of continental crust and generation of crustal magmas (Pedrosa-Soares and Wiedemann-Leonardos, 2000; Medeiros et al., 2001; Wiedemann et al., 2002; De Campos et al., 2004; Alkmim et al., 2006). Changes in CO_2/H_2O pressure have been attributed to control the generation of granitic to charnockitic magmas (De Campos et al., 2016). Coeval mantle and crustal magmas interacted at deep to mid crustal levels at different grades, and subtle to intense magma mixing and mingling took place (Wiedemann et al., 2002; De Campos et al., 2016; Aranda et al., 2021). Mafic to felsic rocks investigated at AWCO post-collisional intrusions showed similar high LILE and LREE values and general high-K calc-alkaline signature in addition to linear trends in bimodal element diagrams, providing evidences of an intense interaction of mantle and crustal magmas (Horn and Weber-Diefenbach, 1987; Ludka et al., 1998; Medeiros et al., 2000, 2001; Wiedemann et al., 2002; De Campos et al., 2004, 2016; Zanon et al., 2015; Aranda et al., 2020). In addition to the geochemical evidences, the typical AWCO post-collisional plutons have showed field, petrographic and isotopic evidences that support intense magma mingling and mixing (Medeiros et al., 2001; Wiedemann et al., 2002; Aranda et al., 2020; Araujo et al., 2020; Lopes de Macêdo et al., 2022; Potratz et al., 2022). Cotemporaneous magma crystallization associated to the activity of the deep shear zones where post-collisional plutons were emplaced could contribute to the effectiveness of the magma mingling and mixing (Wiedemann et al., 2002). Despite the common evidences of magmatic ductile deformation associated to the coeval crustal and mantle magmas (Medeiros et al., 2001;

Wiedemann et al., 2002; Mendes et al., 2005), intensely deformed quartz monzonite was found in the borders of the ACIC near a regional shear zone, providing evidences that these regional shear zones were active at least near the end of the plutons crystallization (Aranda et al., 2020, 2021).

In addition to the hypotheses of the interaction of crustal and mantle magmas from different sources, Aranda et al. (2020) based on investigation of the ACIC main rocks proposed that partially crystalized monzogabbroic mantle magma could have melted due to the continuation of the AWCO post-collisional extensional forces, followed by coupled crustal assimilation and fractional crystallization to generate a new contrasting quartz monzonitic magma, which mixed and mingled with the previous gabbroic magma.

In order to better track the ACIC evolution and to examine if monzogabbro and quartz monzonite are parental rocks or derived from different sources, the Lu-Hf zircon dataset from Aranda et al. (2020) was reevaluated. Quartz monzonite showed $^{176}Hf/^{177}Hf_{(t)}$ ranging from 0.28212 to 0.28218, $\epsilon Hf_{(t)}$ from -12.93 to -10.67 and $T_{DM(t)}$ ages from 1.73 up to 1.84 Ga, while monzogabbro revealed $^{176}Hf/^{177}Hf_{(t)}$ from 0.28213 to 0.28220, $\epsilon Hf_{(t)}$ ranging from -11.89 to -8.84 and $T_{DM(t)}$ ages from 1.67 to 1.81 Ga (Figures 3.11a, 3.11b and 3.11c). It is possible to note a clear overlapping between $^{176}Hf/^{177}Hf_{(t)}$ (from 0.28213 to 0.28218), $\epsilon Hf_{(t)}$ (from -11.89 to -10.67) and $T_{DM(t)}$ ages (from 1.81 to 1.73 Ga) between monzogabbro and quartz monzonite and a subtle linear trend mainly noted at $^{176}Hf/^{177}Hf_{(t)}$ and $\epsilon Hf_{(t)}$xU-Pb age diagrams (Figures 3.11a, 3.11b and 3.11c). These characteristics are typical of magma mixing between mantle and crustal magmas at different tectonic settings worldwide (Griffin et al., 2002; Shaw and Flood, 2009; Marangoanha et al., 2020; Ortiz et al., 2021), suggesting that at least two contrasting magmas were involved at the ACIC evolution. Monzogabbro showed a wider range of $^{176}Hf/^{177}Hf_{(t)}$ values, that is common of enriched mantle magmas (Spencer et al., 2020). Quartz monzonite also showed a general spread of $^{176}Hf/^{177}Hf_{(t)}$, however it is possible to note a main concentration between 0.28214 up to 0.28216, that is typical of magmas from crustal sources (Spencer et al., 2020). The quartz monzonite $^{176}Hf/^{177}Hf_{(t)}$ general spread values could suggest influence of mixing with a different magma or crustal contamination. Besides the overlapping between $T_{DM(t)}$ ages found at quartz monzonite and monzogabbro, it is possible to note older $T_{DM(t)}$ ages related to quartz monzonite (average 1.79 Ga) in comparison to the monzogabbro (average 1.67 Ga).
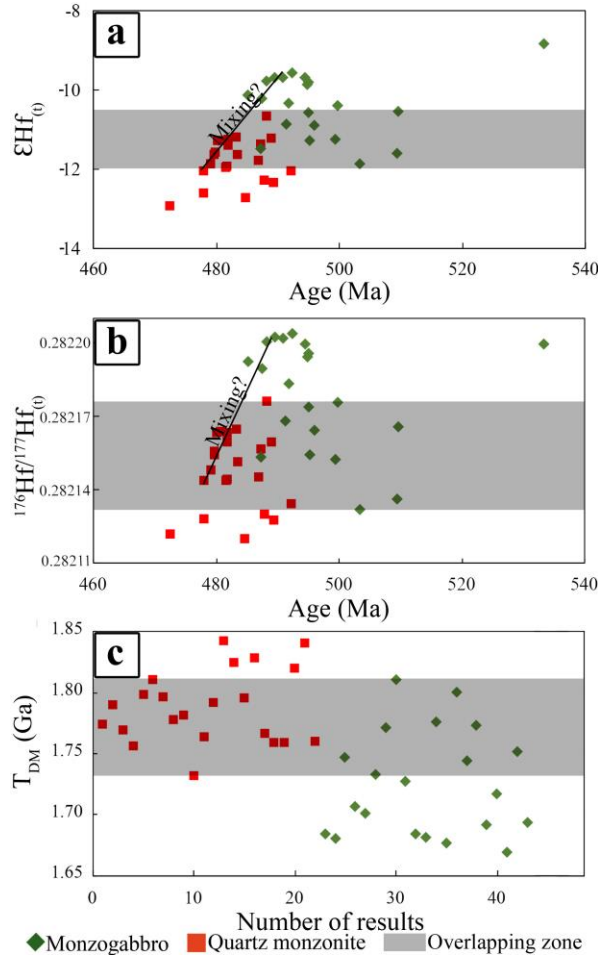
Figure 3.11: (a): ℰHf$_{(t)}$xU-Pb zircon age diagram. (b): ^{176}Hf/^{177}Hf$_{(t)}$xU-Pb zircon age diagram. (c): T$_{DM}$xU-Pb zircon age diagram. The dataset is from Aranda et al. (2020).

As previously stated, the mantle magmas associated to AWCO post-collisional magmatism have been associated to partial melting of an enriched lithospheric mantle (Ludka and Wiedemann-Leonardos, 2000; Wiedemann et al., 2002; De Campos et al., 2016). On the other hand, the source of crustal magmas remains uncertain. It has been proposed mainly based on zircon Hf isotopic investigations that at least two crustal sources are associated to AWCO post-collisional magmas, the first one showing Archean to Paleoproterozoic T$_{DM(t)}$ ages and the last one showing Paleoproterozoic to Neoproterozoic T$_{DM(t)}$ ages (De Campos et al., 2004; Araujo et al., 2020; Melo et al., 2020; Lopes de Macêdo et al., 2022; Potratz et al., 2022). The older T$_{DM(t)}$ ages are probably related to the AWCO basement rocks or lower crust units, while the younger T$_{DM(t)}$ ages are possibly associated to the country rocks.

Aranda et al. (2020) and Aranda et al. (2021) proposed that enclosing country rocks were important sources of AWCO post-collisional crustal magmas and the main accountable to mantle magmas contamination. The xenoliths investigated in this study showed similar

characteristics than ACIC enclosing rocks. Allanite-bearing orthogneiss xenoliths have been associated to enclosing pre-collisional rocks from G1 Supersuite, which represents rocks from Rio Doce arc, while the paragneiss xenoliths have been associated to enclosing Nova Venécia Complex (Aranda et al., 2020, 2021). Partially similar patterns between analogous xenoliths and enclosing country rocks in discrimination geochemical and REE and multi-elements normalized diagrams provide further evidences of the cogeneticity between these rocks (Figures 3.12a, 3.12b, 3.12c and 3.12d). Two monazite crystals from the analyzed allanite-bearing orthogneiss xenolith (sample P111) showed similar ages to the typical G1 Supersuite ages (Tedeschi et al., 2016), supporting that this xenolith is a rock from this geotectonic unit which monazite systematics was affected due to assimilation by the host magma.

The analyzed xenoliths and enclosing allanite-bearing orthogneiss showed similar affinity with calc-alkaline series, metaluminous to slightly peraluminous signature and plotted in volcanic arc field in granite tectonic discrimination diagrams (Figures 3.6b, 3.6c, 3.6d e 3.6f). One allanite-bearing orthogneiss xenolith (sample P111) show similar patterns than enclosing allanite-bearing orthogneisses in the both REE and multi-elements normalized diagrams (Figures 3.12a and 3.12b). On the other hand, the another analyzed allanite-bearing orthogneiss xenolith (sample P285-A) showed enriched LREE and LILE patterns when compared to enclosing allanite-bearing orthogneisses. However, the patterns presented in this sample are partially similar to the ACIC host quartz monzonite patterns (Figures 3.12a and 3.12b). The similarities in LREE and LILE between this xenolith and host quartz monzonite could be explained due to influences of host quartz monzonite by assimilation of this xenolith. In a first view, partial melting of the xenolith contributing to quartz monzonitic magma generation could be a reasonable way to explain this similarity, however the dissimilar REE and multi-elements normalized patterns between quartz monzonite and the other analyzed xenolith and enclosing allanite-bearing orthogneisses limits this hypothesis. In addition, rocks related to the Rio Doce arc showed a large geochemical signature range (Tedeschi et al., 2016), that also could explain these partial different patterns from this xenolith. The common Eu positive anomalies found in both xenoliths and enclosing allanite-bearing orthogneisses could represent a partial melting with absent to minor melting extraction on these rocks. This process has been reported by Rudnick (1992) and Terekhov and Shcherbakova (2006) as an effective way to generate these anomalies. Some AWCO post-collisional plutons showed agmatic titanite-bearing fine to medium grained granitic borders related to the melting of enclosing country rocks, with both rocks showing similar patterns in REE and multi-elements normalized diagrams (Bayer et al.,

1987; Wiedemann et al., 2002; De Campos et al., 2004; Zanon et al., 2015). This granite type has not been found at ACIC and probably it is generated when the melt is successfully extracted from enclosing country rocks or the melting is more intense.

The paragneiss xenolith and enclosing country rocks also showed similar patterns in both REE and multi-elements normalized diagrams (Figures 3.12c and 3.12d). Differences are mainly noted at HREE patterns, which could reflect garnet accumulation due to partial melting events related to AWCO syn to post-collisional stages. These patterns and melting evidences related to different AWCO tectonic stages have been regionally reported in Nova Venécia Complex rocks (Gradim et al., 2014; Richter et al., 2016; Wisniowski et al., 2021). Petrographic investigation of the analyzed paragneiss xenolith revealed that some plagioclase crystals show igneous appearance, which could represent ACIC magma injections associated to xenolith assimilation by the host magma or partial melting events previous or concomitant to xenolith assimilation by host magma. Visual injections of quartz monzonite in paragneiss xenoliths in some outcrops have been commonly noted at xenoliths hosted by quartz monzonite (Figure 3.4f).

The ACIC rocks in comparison to allanite-bearing orthogneisses and paragneiss xenoliths and enclosing rocks showed different patterns in REE and multi-elements normalized diagrams (Figures 3.12a, 3.12b, 3.12c and 3.12d). Furthermore, the ACIC rocks showed higher values of REE and incompatible elements than both xenoliths and enclosing rocks. These evidences suggest that the enclosing rocks are neither the main accountable to ACIC monzogabbroic magma contamination nor the main sources of the ACIC quartz monzonitic magma, since similar patterns have been reported between granites and their related crustal sources worldwide (Sawyer, 1998; Solar and Brown, 2001; Turkina and Sukhorukov, 2017).
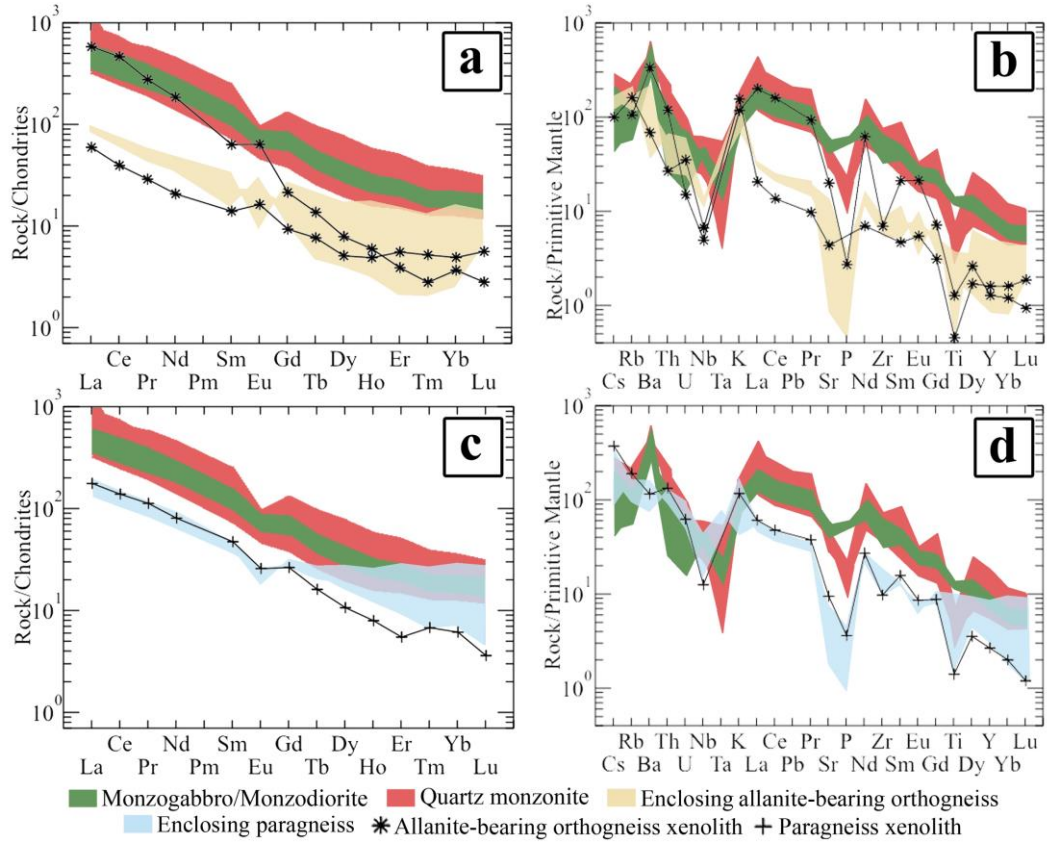
Figure 3.12: REE patterns normalized to chondrite (McDonough and Sun, 1995) and multi-elements spider diagrams normalized to the primitive mantle (Sun and McDonough, 1989) of the analyzed xenoliths in comparison to the analyzed enclosing rocks and ACIC main rocks. (a): Allanite-bearing orthgneiss xenolith REE patterns normalized to chondrite. (b): Allanite-bearing orthgneiss xenolith multi-elements spider diagram normalized to the primitive mantle. (c): Paragneiss xenolith REE patterns normalized to chondrite. (d): Paragneiss xenolith multi-elements spider diagram normalized to the primitive mantle.

Geochemical modeling of magmatic processes has been successfully applied in plutonic and volcanic rocks worldwide in order to track the magmatic processes which acted in these rocks (Borg and Clynne, 1998; Szilas et al., 2015; Etemadi et al., 2019; Costa et al., 2020). Previous igneous geochemical modeling of ACIC rocks was presented by Aranda et al. (2020), however the presented models considered general lower crust as main assimilant. In order to better track the major igneous process that acted in ACIC and the role of enclosing rocks, a more robust geochemical modeling is presented considering ACIC enclosing country rocks and xenoliths as main assimilant. FC-AFC-FCA and mixing modeler excel spreadsheet (Ersoy and Helvaci, 2010) was used to model the igneous processes following the suggestions of Cribb and Barton (1996). Petrographic and whole-rock dataset of ACIC main rocks from Aranda et al.

(2020) was used in the modeling, in addition to the whole-rock major and trace elements data of the xenoliths and enclosing country rocks presented in this paper. Partition coefficients used in the modeling was previously defined by Ersoy and Helvaci (2010). The modeling of monzogabbroic and monzodioritic rocks considered the partition coefficients of basic melt compositions, while the modeling of quartz monzonitic rocks considered the partition coefficients of intermediate melt compositions previously determined by FC-AFC-FCA and mixing modeler excel spreadsheet (Ersoy and Helvaci, 2010). Monzogabbroic and quartz monzonitic rocks with minor SiO_2 contents were the determined starting compositions. The fractionating phases of the monzogabbroic rock were plagioclase (47%), clinopyroxene (19%), biotite (15%), orthopyroxene (7%), K-feldspar (7%), ilmenite (2%), amphibole (1%), apatite (1%) and magnetite (1%), while the fractionating phases of quartz monzonite were K-feldspar (44%), plagioclase (43%), biotite (6%), amphibole (3%), apatite (1%), titanite (1%), magnetite (1%) and ilmenite (1%), in accordance to petrography presented by Aranda et al. (2020). All enclosing country rocks and xenoliths were tested as assimilant material and generated similar results to all similar samples. The samples used as assimilant in the presented igneous modeling were P89 (enclosing allanite-bearing orthogneiss) and P274-A (enclosing paragneiss). Due the chemical similarities between the xenolith and enclosing country rocks, these last ones were used in the modeling because the major and trace element concentrations of the xenoliths could be affected due to interactions with host magma, as previously noted in petrography and REE and multi-elements normalized patterns.

The best fit models of igneous processes revealed that fractional crystallization ruled the evolution of monzogabbroic to monzodioritic rocks with 10% of crustal assimilant material and crystallization concluded between 45 to 72% of fractionating, while the evolution of quartz monzonitic magma was mainly controlled to coupled assimilation and fractional crystallization with 30 to 50% of crustal assimilant material and conclusion of crystallization between 36 to 54% of fractionation (Figures 3.13a, 3.13b, 3.13c, 3.13d, 3.13e and 3.13f). Mixing linear trends between monzogabbroic and quartz monzonitic rocks were well noted in all presented models. Coupled assimilation and fractional crystallization of quartz monzonitic rocks trends are similar to the mixing trends in the models considering SrxTh and VxK systematics (Figures 3.13a, 3.13b, 3.13e and 3.13f). On other hand, igneous modeling considering SrxK systematic clearly showed the differences between mixing and coupled assimilation and fractional crystallization trends (Figures 3.13c and 3.13d).

The ACIC crustal contamination of quartz monzonitic magma by assimilation of enclosing country rocks is also supported by the melting evidences found in some xenoliths mainly hosted by quartz monzonite and the visual aspects of assimilation showed by some xenoliths. Evidences of assimilation of country rocks has been recently reported at Alto Chapéu, Barra de São Francisco, Vitória and Mestre Álvaro Plutons and Castelo, Pedra Azul-Arecê and Venda Nova Intrusive Complexes based on zircon Hf isotopic signatures and commonly found country rocks inherited zircons in intermediate to felsic rocks from these intrusions (Araujo et al., 2020; Melo et al., 2020; Teixeira et al., 2020; Bellon et al., 2022; Lopes de Macêdo et al., 2022; Potratz et al., 2022). In addition, the common occurrence of country rocks xenoliths in intermediate to granitic rocks of many AWCO post-collisional intrusions supports this process (see table 1 and references therein).

Aranda et al. (2021) attributed to the enclosing rocks as the possible main contamination sources of ACIC monzogabbroic magmas in ACIC. Considering that the igneous modeling of processes presented here has performed well, the monzogabbroic rocks show minor contamination by assimilation of enclosing rocks, suggesting that this magma is really derivate from a previously enriched mantle source. The few amounts of xenoliths found hosted by monzogabbro/monzodiorite domain in addition to the higher contents of LILE and LREE in monzogabbroic rocks than allanite-bearing orthogneiss and paragneiss xenoliths and enclosing rocks also indicate that these rocks are not the main source of crustal contamination of the ACIC monzogabbroic magma. The monzogabbro and monzodiorite showed higher or similar Ba and Sr coupled to lower K_2O and Rb contents than quartz monzonites from ACIC (see supplementary material 2), also suggesting that the contamination of the mantle magma which generated the monzogabbroic rocks was previous than the interaction with quartz monzonitic magma. The igneous modeling has also showed that is necessary at least 70% of assimilation of enclosing rocks to the monzogabbro evolve to quartz monzonite ruled by coupled assimilation and fractional crystallization, which is an unrealistic value of crustal assimilation and a further evidence of coexistence of two contrasting magmas to generate ACIC. Furthermore, to a monzogabbroic magma generate an intermediate magma with similar quartz monzonitic compositions it is necessary a huge volume of monzogabbroic magma (Neves, 2012 and references therein), which occurs in small volumes in ACIC.

The interpretation of the ACIC xenoliths and enclosing country rocks dataset presented in this investigation in addition to the previous dataset of ACIC main rocks from Aranda et al. (2020) and Aranda et al. (2021) provide evidences to support that quartz monzonitic magma is

related to the melting of some geological unit from lower to mid crust, probably from AWCO basement or more primitive units from Rio Doce arc. On the other hand, the monzogabbroic magma is related to partial melting of an enriched lithospheric mantle. Mixing between these magmas is accountable to generate the similar geochemical patterns between these rocks, which evolution was ruled by different magmatic processes. The monzogabbroic magma evolved mainly due to typical fractional crystallization with minor assimilation from enclosing country rocks, while the quartz monzonitic magma had an evolution controlled by coupled assimilation and fractional crystallization, with intense contamination by assimilation of enclosing country rocks.
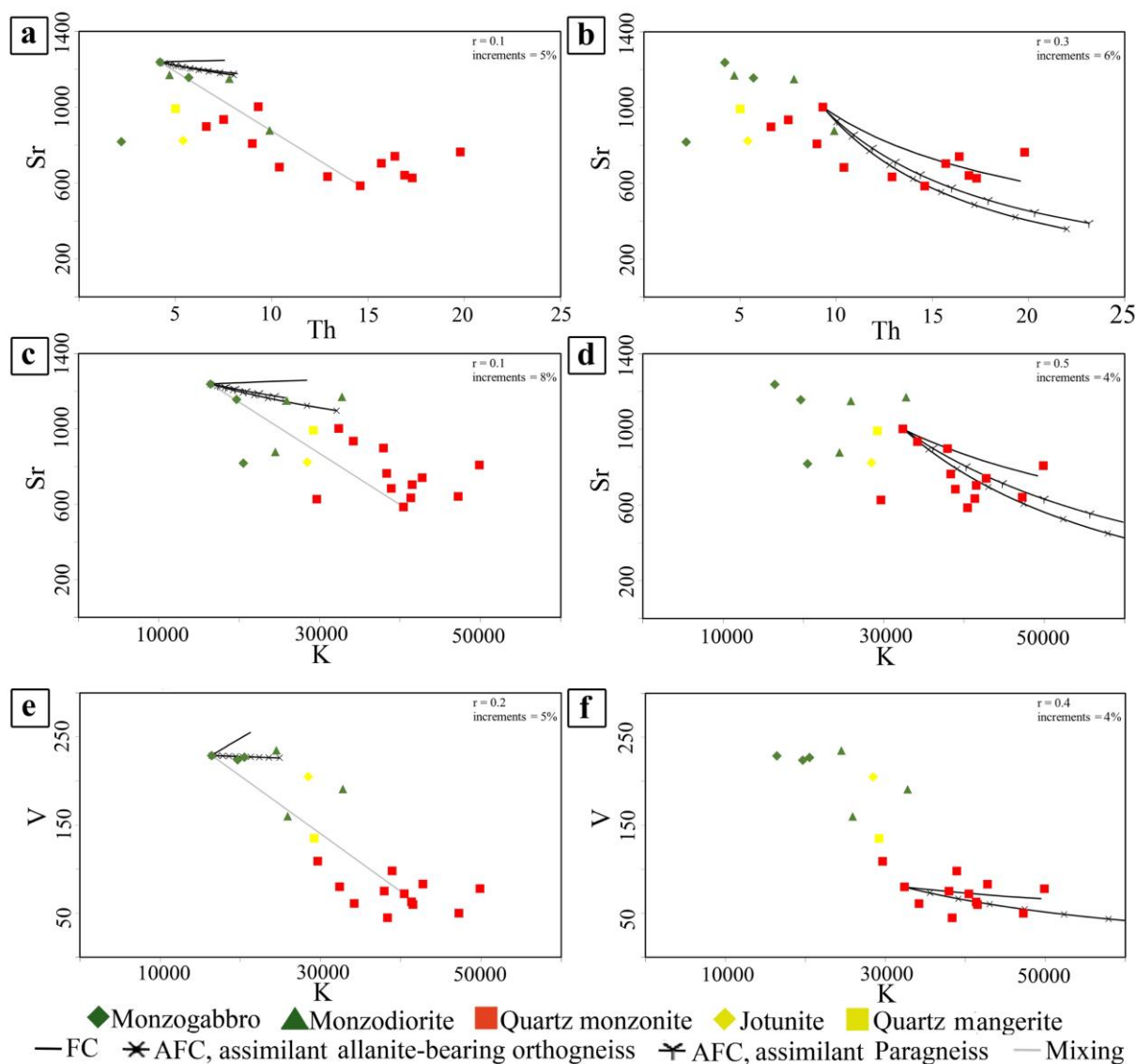
Figure 3.13: Diagrams of geochemical modeling of igneous processes. (a): SrxTh diagram showing the evolution trends of monzogabbro for different processes. (b): SrxTh diagram showing the evolution trends of quartz monzonite for different processes. (c): SrxK diagram showing the evolution trends of monzogabbro for different processes. (d): SrxK diagram showing the evolution trends of quartz monzonite for different processes. (e): VxK diagram showing the evolution trends of monzogabbro for different processes. (f): VxK diagram showing the evolution trends of monzogabbro for different processes. The abbreviations are: AFC: Coupled Fractional Crystallization; FC: Fractional Crystallization; r: Amount of assimilation.

3.5.3. ACIC magmatic evolution

Aranda et al. (2020) supported by field aspects, petrography, whole-rock geochemistry, and zircon U-Pb dating and Lu-Hf isotopes proposed two potential genetic models for ACIC evolution. The investigation of the xenoliths and enclosing country rocks brings new insights about the ACIC evolution and in addition to the previous dataset of Aranda et al. (2020) and Aranda et al. (2021), it is possible to propose a more accurate magmatic evolution model for ACIC.

As previously discussed, the interaction of at least two distinct magmas from different sources is required to generate the rocks found at ACIC. Extensional forces coupled to heat influx associated to mantle upwelling triggered the melting of an enriched lithospheric mantle and lower crust during the AWCO post-collisional stage (De Campos et al., 2016), generating respectively monzogabbroic and quartz monzonitic magmas. These magmas ascent to a magmatic chamber situated at lower to mid crustal level through a regional deep dextral shear zone with a transtensional component, which was generated or reactivated at AWCO post-collisional stage (Aranda et al., 2020, 2021). An intense interaction between monzogabbroic and quartz monzonitic magmas took place and magma mingling and mixing occurred (Aranda et al., 2020, 2021). Concomitant assimilation of crustal material during magma ascent and subsequent arrival at the magma chamber also took place (Figure 3.14a). The assimilation of crustal material from enclosing rocks was more intense in the quartz monzonitic magma, which shows younger crystallization ages and commonly found xenoliths of allanite-bearing orthogneiss from G1 Supersuite and paragneiss from Nova Venécia Complex, suggesting that the intense assimilation from crustal xenoliths was more intense at final stages of ACIC crystallization.

Fractional crystallization ruled the evolution of the monzogabbroic magma, which crystallization at 496±3.6 Ma (Aranda et al., 2020) generated the monzogabbro and monzodiorite, while coupled assimilation and fractional crystallization (AFC) was the ruling magmatic process associated to the evolution of the quartz monzonitic magma, which crystallized near 480±3.2 Ma (Aranda et al., 2020) generating the quartz monzonite (Figure 3.14b). Mixing magma process was responsible for the chemical and isotopic homogeneity between these rocks and the generation of jotunite and quartz monzonite. Intense mixing of two different magmas has been largely supported as an important process involved at ACIC evolution, supported by evidences found at field (plagioclase and K-feldspar xenocrysts in

monzogabbro and monzodiorite, injections of quartz monzonite into monzogabbro and monzodiorite, and monzogabbro and monzodiorite enclaves hosted at quartz monzonite), petrography (needle-shape apatite, poikilitic K-feldspar and feldspars strongly zoned sometimes showing rapakivi texture and oval terminations), whole-rock geochemistry (linear trends in bimodal diagrams and similar patterns at REE and multi-elements normalized diagrams), mineral chemistry (biotites and amphiboles showing sources related to the interaction of mantle and crustal magmas and oscillatory zoning in plagioclase crystals showing Ca spikes) and Lu-Hf isotopes (similar isotopic signatures) (Aranda et al., 2020, 2021).

The deep dextral shear zone which ACIC intruded probably was active until the end of ACIC crystallization, contributing to the elliptic shape of this intrusion and shear deformational evidences found at quartz monzonite from ACIC borders near this shear zone (Aranda et al., 2020, 2021). After these processes, syenogranite dykes intruded ACIC rocks probably at 431±13 Ma to 427 ±19 Ma (Figure 3.14c), with some of these dykes probably intruding in fractures generated due to intrusion cooling (Aranda et al., 2020).

Aranda et al. (2021) investigated the temperature and pressure conditions that ACIC main rocks crystallized. These authors found higher pressures associated to quartz monzonite than monzodiorite, suggesting that the higher pressures associated to quartz monzonite are associated to the activity of surrounding shear zone or that monzodioritic rocks crystallized at initial stages of AWCO post-collisional magmatism, whereas the quartz monzonite crystallized at a more advanced phase of this orogenic stage, which presented higher and more stable pressures than orogenic collapse initial stage. Melting of monzogabbro and monzodiorite suggested by Aranda et al. (2020) is not sustained due to lack of melting evidences in these rocks and the necessity of at least two contrasting magmas to generate the rocks found in ACIC.

Mafic microgranular enclaves found hosted at quartz monzonite show similar mineralogical characteristics than monzogabbro and monzodiorite from ACIC cores (Aranda et al., 2020) and probably represent blobs of the monzogabbroic magma into quartz monzonite. This genetic model of mafic microgranular enclaves has been proposed as a common process to generate these mafic enclaves (Barbarin and Didier 1992).

It is not possible to assert if the two monzogabbroic/monzodioritic cores found at ACIC represent two different mantle magma intrusions, a single mantle magma intrusion segmented due to deformational forces from enclosing shear zone or a consequence of the erosional level.
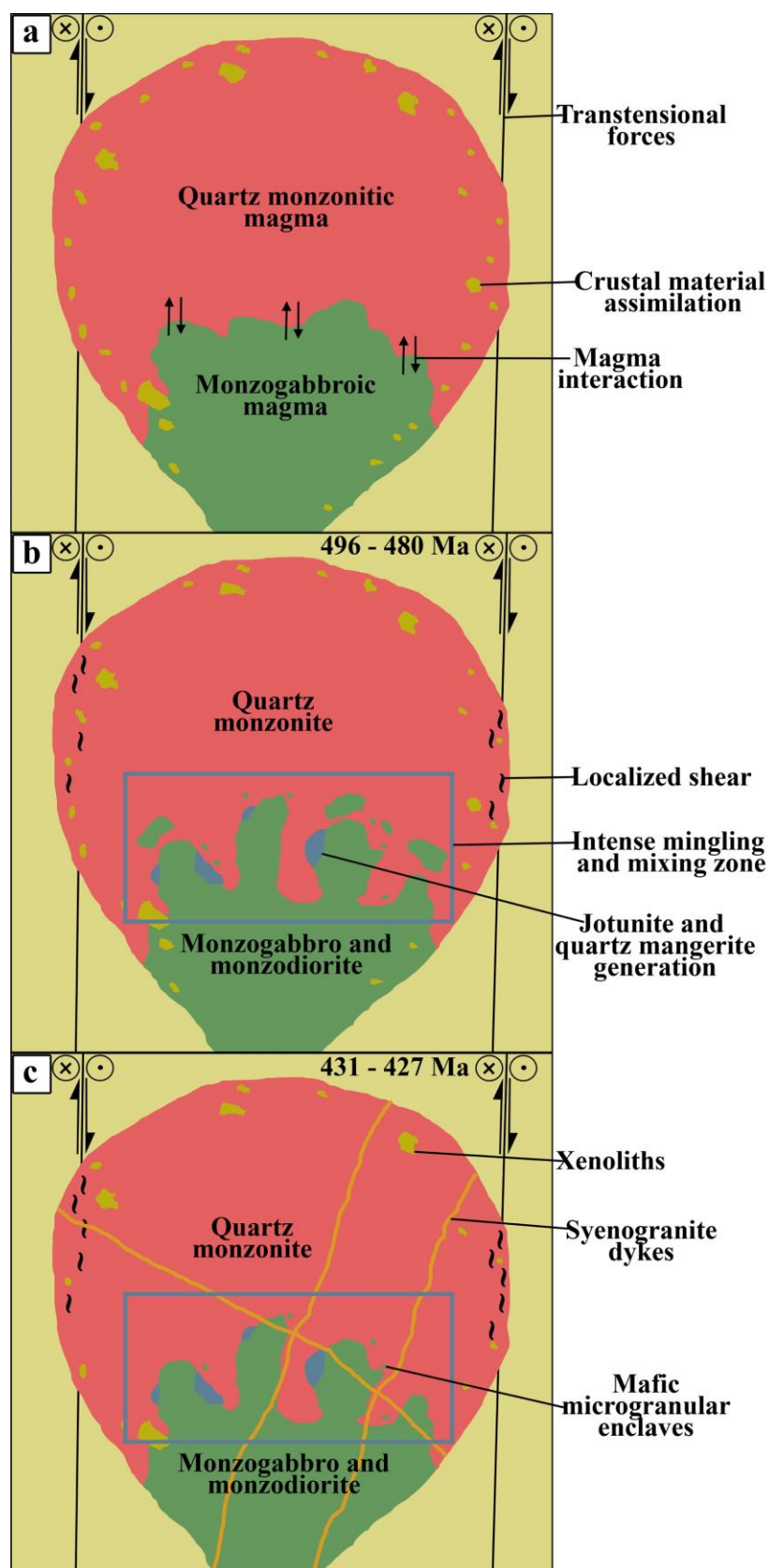
Figure 3.14: Model of ACIC magmatic evolution. (a): Interaction between mantle and crustal contrasting magmas, which assimilate enclosing rocks. (b): Generation of mingling and mixing zones and crystallization of the ACIC main rocks. (c): Intrusion of late syenogranite dykes.

3.5.4. Implications for the AWCO post-collisional magmatism

The ACIC is a typical pluton from AWCO post-collisional stage showing typical characteristics, such as more mafic cores surrounded by more felsic rocks and intense magma mingling and mixing between these rocks (Wiedemann et al., 2002; Aranda et al., 2020). Assuming the general similarities between the typical AWCO post-collisional intrusions, the inferences found in this investigation could bring new insights to the understanding about the evolution of the AWCO post-collisional magmatism.

It has been largely known that crustal and mantle magmas interacted to generate the AWCO post-collisional plutons (Medeiros et al., 2001; Wiedemann et al., 2002). Some authors have argued that at least two crustal magmas from different sources contributed to generate the intermediate to felsic rocks found at AWCO post-collisional intrusions (Lopes de Macêdo et al., 2022; Potratz et al., 2022). In the investigation of the xenoliths found at ACIC and enclosing country rocks, it was not possible to argue accurately about the crustal magma sources, however the important influence of assimilation by enclosing country rocks is noticeable. The assimilation of crustal material from enclosing rocks was more intense in intermediate to felsic rocks related to crustal magmas, in which coupled assimilation and fractional crystallization was the ruling magmatic evolution process. This argument has been sustained due to the commonly found crustal xenoliths in intermediate to felsic rocks from AWCO post-collisional plutons (Medeiros et al., 2001; Wiedemann et al., 2002; De Campos et al., 2004, 2016; Aranda et al., 2020). Geochemical and isotopic investigations of ACIC, Pedra Azul-Aracê Intrusive Complex and Vitória and Mestre Álvaro plutons have also pointed to an important role of assimilation of country rocks in the evolution of these intrusions (Aranda et al., 2020; Araujo et al., 2020). The influence of enclosing country rocks is highlighted in some intrusions, such as Santa Angélica, Pedra Azul-Aracê and Castelo Intrusive Complexes, due to the melting of enclosing country rocks during pluton emplacement, generating a magma which succeeding crystallization generates a titanite-bearing granite that sometimes surrounds the plutons (Bayer et al., 1987; Wiedemann et al., 2002; De Campos et al., 2004). On the other hand, the assimilation of enclosing country rocks is a minor process associated to the evolution of the AWCO post-collisional mafic to intermediate rocks related to mantle magmas. In these rocks, fractional crystallization of an previously enriched mantle magma is the dominant process, as previously discussed by Ludka and Wiedemann-Leonardos (2000) and Medeiros et al. (2001) and highlighted in the investigation of xenoliths and enclosing country rocks from ACIC. In

addition to these processes, it has been largely known that mixing and mingling are important processes associated to the evolution of AWCO post-collisional plutons (Medeiros et al., 2001; Wiedemann et al., 2002; De Campos et al., 2004, 2016; Zanon et al., 2015; Teixeira et al., 2020; Lopes de Macêdo et al., 2022).

Despite the common general features of the AWCO post-collisional plutons, there are differences between the plutons that could be mainly explained due to differences associated to emplacement levels, magma sources, intensity of magma mingling and mixing, erosional levels (Wiedemann et al., 2002), and diversity of enclosing country rocks and subsequent different grades of assimilation of the these rocks.

The AWCO post-collisional stage ranges from 530 to 480 Ma (Pedrosa-Soares et al., 1999, 2001; De Campos et al., 2016; Araujo et al., 2020; Potratz et al., 2022). Recently, Lopes de Macêdo et al. (2022) found a crystallization age of 426±15 Ma for a leucocratic dyke which crosscut the Castelo Intrusive Complex. This age is concordant with the younger ages (431±13 Ma and 427±19 Ma) found at xenoliths hosted by ACIC. More robust studies are necessary to understanding theses ages, however these ones could represent an extension of the post-collisional magmatism or a late thermal event in AWCO. Such younger ages have also been reported at Ribeira orogen and they have been interpreted as an extension of the post-collisional magmatism at this orogenic system (Bongiolo et al., 2016), which limits the AWCO to south.

3.6. Conclusions

The AWCO post-collisional intrusions have been extensively studied, however the common xenoliths hosted by these intrusions have never been investigated in detail. This investigation brings new and important insights about the ACIC and AWCO post-collisional magmatism evolution.

Geochemical investigation revealed that correlated xenoliths and enclosing country rocks of ACIC are cogenetic and that they are not the main sources of quartz monzonite found at ACIC. The quartz monzonite was probably derived from partial melting of the lower crust and was not the main accountable to the contamination of monzogabbroic rocks, which were related to the partial melting of a previous enriched lithospheric mantle. Similar geochemical patterns between ACIC main rocks are due to mixing between monzogabbroic and quartz monzonitic magmas, which the subsequent evolution was ruled by different magmatic processes. The monzogabbroic magma evolution was controlled by fractional crystallization

with minor assimilation of enclosing country rocks, while the evolution of quartz monzonitic magma was ruled by coupled assimilation and fractional crystallization with intense contribution of enclosing country rocks. Due to the similarities between the AWCO post-collisional plutons, the new insights about the ACIC could be applied to typical AWCO post-collisional magmatism, considering the differences between the plutons.

Monazite crystals found at analyzed xenoliths have preserved two main ages related to AWCO post-collisional stage. The older ages (478.2±9.3 Ma and 477±14 Ma) are related to typical AWCO post-collisional magmatism, however the younger ages (431±13 Ma and 427±19 Ma) could represent and extension of the post-collisional stage or a later unrelated thermal event associated to AWCO evolution.

This work shows that the investigation of the xenoliths commonly found hosted by an igneous intrusion could bring new and important insights about its evolution. Xenoliths have been usually found enclosed by AWCO pre to post-collisional magmatic rocks and its investigation may bring important insights over the AWCO evolution.

3.7. Acknowledgments

3.8. References

Alkmim, F. F., Marshak, S., Pedrosa-Soares, A. C., Peres, G. G., Cruz, S. C. P., Whittington, A. (2006). Kinematic evolution of the Araçuaí-West Congo orogen in Brazil and Africa: Nutcracker tectonics during the Neoproterozoic assembly of Gondwana. *Precambrian Research* **149**, 43–64.

Alkmim, F. F., Pedrosa-soares, A. C., Noce, C. M., Cerqueira, S., Cruz, P. (2007). Sobre a Evolução Tectônica Do Orógeno Araçuaí-Congo Ocidental. *Geonomos* **15**, 25–43.

Aranda, R. O., Horn, A. H., Medeiros Júnior, E. B., Venturini Junior, R. (2021).

Geothermobarometry of igneous rocks from Afonso Cláudio Intrusive Complex (Espírito Santo state, Southeastern Brazil), Araçuaí-West Congo Orogen: Further evidence for deep emplacement levels. *Journal of South American Earth Sciences* **110**, 1–16.

Aranda, R. O., Chaves, A. O., Medeiros Júnior, E. B., Venturini Junior, R. (2020). Petrology of the Afonso Cláudio Intrusive Complex: New insights for the Cambro-Ordovician post-collisional magmatism in the Araçuaí-West Congo Orogen, Southeast Brazil. *Journal of South American Earth Sciences* **98**, 1–19.

Araujo, C., Pedrosa-Soares, A., Lana, C., Dussin, I., Queiroga, G., Serrano, P., Medeiros-Júnior, E. (2020). Zircon in emplacement borders of post-collisional plutons compared to country rocks: A study on morphology, internal texture, U–Th–Pb geochronology and Hf isotopes (Araçuaí orogen, SE Brazil). *Lithos* **352**–**353**, 1–18.

Araujo, C., Pedrosa-Soares, A., Lana, C., Tedeschi, M., Roncato, J., Dussin, I., Serrano, P., Dantas, E. (2023). Tracking a magmatic arc within a confined orogen: New evidence from the Araçuaí orogen (SE Brazil). *Journal of South American Earth Sciences* **129**, 1–22.

Babazadeh, S., Furman, T., Cottle, J. M., Raeisi, D., Lima, I. (2019). Magma chamber evolution of the Ardestan pluton, Central Iran: evidence from mineral chemistry, zircon composition and crystal size distribution. *Mineralogical Magazine* **83**, 763–780.

Barbarin, B., Didier, J. (1992). Genesis and evolution of mafic microgranular enclaves through various types of interaction between coexisting felsic and mafic magmas. *Transactions of the Royal Society of Edinburgh: Earth Sciences* **83**, 145–153.

Barboni, M., Schoene, B., Ovtcharova, M., Bussy, F., Schaltegger, U., Gerdes, A. (2013). Timing of incremental pluton construction and magmatic activity in a back-arc setting revealed by ID-TIMS U/Pb and Hf isotopes on complex zircon grains. *Chemical Geology* **342**, 76–93.

Bayer, P., Schmidt-Thomé, R., Weber-Diefenbach, K., Horn, H. A. (1987). Complex concentric granitoid intrusions in the coastal mobile belt, Espírito Santo, Brazil: The Santa Angélica Pluton - an example. *Geologische Rundschau* **76**, 357–371.

Bellon, U. D., Souza Junior, G. F., Temporim, F. A., D'Agrella-Filho, M. S., Trindade, R. I. F. (2022). U-Pb geochronology of a reversely zoned pluton: Records of pre-to-post collisional magmatism of the Araçuaí belt (SE-Brazil)? *Journal of South American Earth Sciences* **119**, 1–15.

Bongiolo, E. M., Renac, C., Piza, P. D. A. T., Schmitt, R. S., Mexias, A. S. (2016). Origin of pegmatites and fluids at Ponta Negra (RJ, Brazil) during late- to post-collisional stages of the Gondwana Assembly. *Lithos* **240**–**243**, 259–275.

Borg, L. E., Clynne, M. A. (1998). The petrogenesis of felsic calc-alkaline magmas from the southernmost Cascades, California: origin by partial melting of basaltic lower crust. *Journal of Petrology* **39**, 1197–1222.

Brandt, S., Schenk, V., Raith, M. M., Appel, P., Gerdes, A., Srikantappa, C. (2011). Late neoproterozoic P-T evolution of HP-UHT granulites from the palni hills (south india): New constraints from phase diagram modelling, LA-ICP-MS zircon dating and in-situ EMP monazite dating. *Journal of Petrology* **52**, 1813–1856.

Brito Neves, B., Cordani, U. (1991). Tectonic evolution of South America during the late Proterozoic. *Precambrian Research* **53**, 23–40.

Carr, M. J., Gazel, E. (2017). Igpet software for modeling igneous processes: examples of application using the open educational version. *Mineralogy and Petrology* **111**, 283–289.

Chaves, A. O., Oliveira, E. K., Garcia, L. R. A. (2013). Desenvolvimneto do médodo de datação química U-Th-Pb de monazita por microssonda eletrônica na UFMG. *Geonomos* **21**, 13–18.

Chen, M., Sun, M., Buslov, M. M., Cai, K., Zhao, G., Kulikova, A. V., Rubanova, E. S. (2016). Crustal melting and magma mixing in a continental arc setting: Evidence from the Yaloman intrusive complex in the Gorny Altai terrane, Central Asian Orogenic Belt. *Lithos* **252**–**253**, 76–91.

Chen, Q., Sun, M., Zhao, G., Yang, F., Long, X., Li, J., Wang, J., Yu, Y. (2017). Origin of the mafic microgranular enclaves (MMEs) and their host granitoids from the Tagong pluton in Songpan–Ganze terrane: An igneous response to the closure of the Paleo-Tethys ocean. *Lithos* **290**–**291**, 1–17.

Costa, S., Masotta, M., Gioncada, A., Pistolesi, M., Bosch, D., Scarlato, P. (2020). Magma evolution at La Fossa volcano (Vulcano Island, Italy) in the last 1000 years: evidence from eruptive products and temperature gradient experiments. *Contributions to Mineralogy and Petrology* **175**, 1–22.

Coulson, I. M., Villeneuve, M. E., Dipple, G. M., Duncan, R. A., Russell, J. K., Mortensen, J. K. (2002). Time-scales of assembly and thermal history of a composite felsic pluton: Constraints from the Emerald Lake area, northern Canadian Cordillera, Yukon. *Journal of Volcanology and Geothermal Research* **114**, 331–356.

Cribb, J. W., Barton, M. (1996). Geochemical effects of decoupled fractional crystallization and crustal assimilation. *Lithos* **37**, 293–307.

De Campos, C. P., Cezar Mendes, J., Ludka, I. P., Medeiros, S. R., Moura, J. C., Wallfass, C. M. (2004). A review of the Brasiliano magmatism in southern Espírito Santo, Brazil, with

emphasis on post-collisional magmatism. *Journal of the Virtual Explorer* **17**, 1–39.

De Campos, C. P., Medeiros, S. R., Mendes, J. C., Pedrosa-Soares, A. C., Dussin, I., Ludka, I. P., Dantas, E. L. (2016). Cambro-Ordovician magmatism in the Araçuaí Belt (SE Brazil): Snapshots from a post-collisional event. *Journal of South American Earth Sciences* **68**, 248–268.

De Mello, F. M., Machado, R., Bilal, E. (2011). Petrography and geochemistry of the Aimorés charnockitic complex: An example of post-orogenic plutonism of the Araçuaí/Ribeira Belt. *Geologia USP - Serie Cientifica* **11**, 33–57.

Dias, G., Leterrier, J., Mendes, A., Simões, P. P., Bertrand, J. M. (1998). U-Pb zircon and monazite geochronology of post-collisional Hercynian granitoids from the Central Iberian Zone (Northern Portugal). *Lithos* **45**, 349–369.

dos Santos Dias, J. C., Gonçalves, L., Gonçalves, C. C. (2019). Contrasting oxygen fugacity of I- and S-type granites from the Araçuaí orogen, SE Brazil: an approach based on opaque mineral assemblages. *Mineralogy and Petrology* **113**, 667–686.

Dumond, G., McLean, N., Williams, M. L., Jercinovic, M. J., Bowring, S. A. (2008). High-resolution dating of granite petrogenesis and deformation in a lower crustal shear zone: Athabasca granulite terrane, western Canadian Shield. *Chemical Geology* **254**, 175–196.

Ersoy, Y., Helvaci, C. (2010). FC-AFC-FCA and mixing modeler: A Microsoft®Excel©spreadsheet program for modeling geochemical differentiation of magma by crystal fractionation, crustal assimilation and mixing. *Computers and Geosciences* **36**, 383–390.

Etemadi, A., Karimpour, M. H., Malekzadeh Shafaroudi, A., Santos, J. F., Mathur, R., Ribeiro, S. (2019). U-pb zircon geochronology, geochemistry, and petrogenesis of the hamech intrusions in the kuh-e-shah volcano-plutonic complex, Eastern Iran. *Turkish Journal of Earth Sciences* **28**, 38–59.

Fernandes, C. M., Duffles Teixeira, P. A., Mendes, J. C. (2021). Constraining crystallization conditions during the Cambro-Ordovician post-collisional magmatism at Araçuaí belt (SE Brazil): Zircon as key petrologic witness. *Journal of South American Earth Sciences* **108**, 103235.

Fourny, A., Weis, D., Scoates, J. S. (2019). Isotopic and Trace Element Geochemistry of the Kiglapait Intrusion, Labrador: Deciphering the Mantle Source, Crustal Contributions and Processes Preserved in Mafic Layered Intrusions. *Journal of Petrology* **60**, 553–590.

Frost, B. R., Barnes, C. G., Collins, W. J., Arculus, R. J., Ellis, D. J., Frost, C. D. (2001). A

Geochemical Classification for Granitic Rocks. *Journal of Petrology* **42**, 2033–2048.

Gonçalves, L., Alkmim, F. F., Pedrosa-Soares, A. C., Dussin, I. A., Valeriano, C. M., Lana, C., Tedeschi, M. (2016). Granites of the intracontinental termination of a magmatic arc: an example from the Ediacaran Araçuaí orogen, southeastern Brazil. *Gondwana Research* **36**, 439–458.

Gonçalves, L., Alkmim, F. F., Pedrosa-Soares, A., Gonçalves, C. C., Vieira, V. (2018). From the plutonic root to the volcanic roof of a continental magmatic arc: a review of the Neoproterozoic Araçuaí orogen, southeastern Brazil. *International Journal of Earth Sciences* **107**, 337–358.

Gonçalves, L., Farina, F., Lana, C., Pedrosa-Soares, A. Ô. C., Alkmim, F., Nalini, H. A. (2014). New U-Pb ages and lithochemical attributes of the Ediacaran Rio Doce magmatic arc, Araçuaí confined orogen, southeastern Brazil. *Journal of South American Earth Sciences* **52**, 129–148.

Gouvêa, L. P., Medeiros, S. R., Mendes, J. C., Soares, C., Marques, R., Melo, M. (2020). Magmatic activity period and estimation of P-T metamorphic conditions of pre-collisional opx-metatonalite from Araçuaí-Ribeira orogens boundary, SE Brazil. *Journal of South American Earth Sciences* **99**, 1–22.

Gradim, C., Roncato, J., Pedrosa-Soares, A.P., Cordani, U., Dussin, I., Alkmim, F.F., Queirogra, G., Jacobsohn, T., Silva, L.C., Babinski. (2014). The hot back-arc zone of the Araçuaí orogen, Eastern Brazil: from sedimentation to granite generation. *Brazilian Journal of Geology* **44**, 155–180.

Griffin, W. L., Wang, X., Jackson, S. E., Pearson, N. J., O'Reilly, S. Y., Xu, X., Zhou, X. (2002). Zircon chemistry and magma mixing, SE China: In-situ analysis of Hf isotopes, Tonglu and Pingtan igneous complexes. *Lithos* **61**, 237–269.

Horn, H. A., Weber-Diefenbach, W. (1987). Geochemical and genetic studies of three invers zoned intrusive bodies of both alkaline and calc-alkaline composition in the Ribeira Mobile Belt (Espírito Santo, Brazil). *Revista Brasileira de Geociências* **17**, 488–497.

Irvine, T. N., Baragar, W. R. A. (1971). A Guide to the Chemical Classification of the Common Volcanic Rocks. *Canadian Journal of Earth Sciences* **8**, 523–548.

Janousek, V., Bowes, D. R., Colin, J. R., Braithwaite, Rogers, G. (2000). Microstructural and minaralogical evidence for limited involvement of magma mixing in the petrogenesis of a Hercynian high-K calc-alkaline intrusion: the Kozarovice granodiorite, Central Bohemian Pluton, Czech Republic. *Transactions of the Royal Society of Edinburgh: Earth Sciences* **91**, 15–26.

Jiao, S., Fitzsimons, I. C. W., Zi, J. W., Evans, N. J., McDonald, B. J., Guo, J. (2020). Texturally

Controlled U-Th-Pb Monazite Geochronology Reveals Paleoproterozoic UHT Metamorphic Evolution in the Khondalite Belt, North China Craton. *Journal of Petrology* **61**, 1–20.

Lamarque, G., Bascou, J., Ménot, R. P., Paquette, J. L., Couzinié, S., Rolland, Y., Cottin, J. Y. (2018). Ediacaran to lower Cambrian basement in eastern George V Land (Antarctica): Evidence from U–Pb dating of gneiss xenoliths and implications for the South Australia- East Antarctica connection. *Lithos* **318**–**319**, 219–229.

Le Bas, M. J., Le Maitre, R. W., Streckeisen, A., Zanettin, B. (1986). A chemical classification of volcanic rocks based on the total alkali silica diagram. *Journal of Petrology* **27**, 745–750.

Lopes de Macêdo, I. M., Geraldes, M. C., Marques, R. A., Melo, M. G., Tavares, A. D., Alves Martins, M. V., Oliveira, H. C., Rodrigues, R. D. (2022). New clues for magma-mixing processes using petrological and geochronological evidence from the Castelo Intrusive Complex, Araçuaí Orogen (SE Brazil). *Journal of South American Earth Sciences* **115,** 1–21.

Lu, L., Zhang, K.-J., Jin, X., Zeng, L., Yan, L.-L., Santosh, M. (2019). Crustal Thickening of the Central Tibetan Plateau prior to India–Asia Collision: Evidence from Petrology, Geochronology, Geochemistry and Sr–Nd–Hf Isotopes of a K-rich Charnockite–Granite Suite in Eastern Qiangtang. *Journal of Petrology* **60**, 827–854.

Ludka, I. P., Wiedemann-Leonardos, C. M. (2000). Further Signs of an Enriched Mantle Source Under the Neoproterozoic Araçuaí-Ribeira Mobile Belt. *Revista Brasileira de Geociências* **30**, 95–98.

Ludka, I. P., Wiedemann, C. M., Töpfner, C. (1998). On the origin of incompatible element enrichment in the Venda Nova pluton, State of Espirito Santo, southeast Brazil. *Journal of South American Earth Sciences* **11**, 473–486.

Ludwig, K. R. (2003). *User's Manual for Isoplot 3.75, a geochronological toolkit for Microsoft Excel. Berkeley Geochronology Center Special Publication*. Berkeley.

Ma, X., Meert, J. G., Xu, Z., Zhao, Z. (2017). Evidence of magma mixing identified in the Early Eocene Caina pluton from the Gangdese Batholith, southern Tibet. *Lithos* **278**–**281**, 126–139.

Marangoanha, B., Oliveira, D. C., Galarza, M. A., Marques, G. T. (2020). Crustal anatexis and mantle-derived magmas forming Neoarchean A-type granitoids in Carajás Province, northern Brazil: Petrological evidence and tectonic control. *Precambrian Research* **338**, 1–22.

Martins, V. T. d. S., Teixeira, W., Noce, C. M., Pedrosa-Soares, A. C. (2004). Sr and Nd characteristics of Brasiliano/Pan-African granitoid plutons of the Araçuaí Orogen, Southeastern Brazil: Tectonic implications. *Gondwana Research* **7**, 75–89.

McDonough, W. F., Sun, S. S. (1995). The composition of the Earth. *Chemical Geology* **120**,

223–253.

Medeiros, S. R., Wiedeman-Leonardos, C. M., Mendes, J. C. (2000). Post-collisional multistage magmatism in the Ribeira mobile belt; geochemical and isotopic study of the Varzea Alegre Intrusive Complex, Espírito Santo, Brazil. *Revista Brasileira de Geociencias* **30**, 30–34.

Medeiros, S. R., Wiedemann-Leonardos, C. M., Vriend, S. (2001). Evidence of mingling between contrasting magmas in a deep plutonic environment: The example of Várzea Alegre, in the Ribeira Mobile Belt, Espírito Santo, Brazil. *Anais da Academia Brasileira de Ciencias* **73**, 99–119.

Melekhova, E., Camejo-Harry, M., Blundy, J., Wallis, S. R., Annen, C., Kunz, B. E., Jenner, F. E., Thirlwall, M. (2022). Arc Crust Formation of Lesser Antilles Revealed by Crustal Xenoliths from Petit St. Vincent. *Journal of Petrology* **63**, 1–29.

Melo, M. G., Lana, C., Stevens, G., Hartwig, M. E., Pimenta, M. S., Nalini, H. A. (2020). Deciphering the source of multiple U–Pb ages and complex Hf isotope composition in zircon from post-collisional charnockite-granite associations from the Araçuaí orogen (southeastern Brazil). *Journal of South American Earth Sciences* **103**, 1–22.

Melo, M. G., Lana, C., Stevens, G., Pedrosa-Soares, A. C., Gerdes, A., Alkmin, L. A., Nalini, H. A., Alkmim, F. F. (2017a). Assessing the isotopic evolution of S-type granites of the Carlos Chagas Batholith, SE Brazil: Clues from U–Pb, Hf isotopes, Ti geothermometry and trace element composition of zircon. *Lithos* **284**–**285**, 730–750.

Melo, M. G., Stevens, G., Lana, C., Pedrosa-Soares, A. C., Frei, D., Alkmim, F. F., Alkmin, L. A. (2017b). Two cryptic anatectic events within a syn-collisional granitoid from the Araçuaí orogen (southeastern Brazil): Evidence from the polymetamorphic Carlos Chagas batholith. *Lithos* **277**, 51–71.

Mendes, J. C., De Campos, C. M. P. (2012). Norite and charnockites from the Venda Nova Pluton, SE Brazil: Intensive parameters and some petrogenetic constraints. *Geoscience Frontiers* **3**, 789–800.

Mendes, J. C., Medeiros, S. R., McReath, I., De Campos, C. M. P. (2005). Cambro-Ordovician magmatism in SE Brazil: U-Pb and Rb-Sr ages, combined with Sr and Nd isotopic data of Charnockitic rocks from the Varzea Alegre Complex. *Gondwana Research* **8**, 337–345.

Mendes, J. C., Wiedemann, C. M., McRearth, I. (1999). Conditions of Formation of Charnockitic Magmatic Rocks From the Várzea Alegre Massif, Espírito Santo, Southeastern Brazil. *Revista Brasileira de Geociências* **29**, 47–54.

Middlemost, E. A. K. (1994). Naming Materials in the Magma/Igneous Rock System. *Earth-Science Reviews* **37**, 215–224.

Neves, S. P. (2012). *Granitos Orogênicos: Da Geração dos Magmas à Intrusão e Deformação. Synergia Editora*. Rio de Janeiro: Synergia Editora.

Ondrejka, M., Uher, P., Putiš, M., Broska, I., Bačík, P., Konečný, P., Schmiedt, I. (2012). Two-stage breakdown of monazite by post-magmatic and metamorphic fluids: An example from the Veporic orthogneiss, Western Carpathians, Slovakia. *Lithos* **142**–**143**, 245–255.

Ortiz, A., Becchio, R., Juárez, S., Suzaño, N., Hauser, N., Sola, A., Bardelli, L., Simón, V., Quiroga, M., Bordese, S. (2021). Magma mixing, zircon U–Pb ages and Hf isotopes: Insights for the Miocene magmatic plumbing system in the Soroche Porphyry, Puna Argentina, Central Andes. *Journal of South American Earth Sciences* **109**, 1–25.

Paradella, W. R., Liu, C. C., Meneses, P. R. (1978). Caracterização de maciços ácidos e diferenciados do sul do Espírito Santo através de técnicas de realces automáticos de dados do Landsat. *I Simpósio Brasileiro de Sensoriamento Remoto*. São José dos Campos: INPE, 582–596.

Parrish, R. R. (1990). U-Pb dating of monazite and its application to geological problems. *Canadian Journal of Earth Sciences* **27**, 1431–1450.

Pearce, J. A., Harris, N. B. W., Tindle, A. G. (1984). Trace-Element Discrimination Diagrams for the Tectonic Interpretation of Granitic-Rocks. *Journal of Petrology* **25**, 956–983.

Pedrosa-Soares, A. C., De Campos, C.P., Noce, C., Silva, L.C., Novo, T., Roncato, J., Medeiros, S., Castañeda, C., Queiroga, G., Dantas, E., Dussin, I., Alkmim, F. (2011). Late Neoproterozoic – Cambrian granitic magmatism in the Araçuaí orogen (Brazil), the Eastern Brazilian Pegmatite Province and related mineral resources. *Geological Society, London, Special Publications* **350**, 25–51.

Pedrosa-Soares, A. C., Alkmim, F. F., Tack, L., Noce, C. M., Babinski, M., Silva, L. C., Martins-Neto, M. A. (2008). Similarities and differences between the Brazilian and African counterparts of the Neoproterozoic Araçuaí-West Congo orogen. *Geological Society, London, Special Publications* **294**, 153–172.

Pedrosa-Soares, A. C., Noce, C. M., Alkmim, F. F., da Silva, L. C., Babinski, M., Cordani, U., Castañeda, C. (2007). Orógeno Araçuaí : Síntese do conhecimento 30 anos após Almeida 1977. *Geonomos* **15**, 1–16.

Pedrosa-Soares, A. C., Noce, C. M., Wiedemann, C. M., Pinto, C. P. (2001). The Araçuaí-West-Congo Orogen in Brazil: An overview of a confined orogen formed during Gondwanaland

assembly. *Precambrian Research* **110**, 307–323.

Pedrosa-Soares, A. C., Wiedemann-Leonardos, C. M. (2000). Evolution of Araçuaí Belt and its connection to the Ribeira Belt, eastern Brazil. In: Cordani, U. G., Milani, E. J., Filho, A. T., Campos, D. A. (eds) *Tectonic evolution of South America*. Rio de Janeiro: Sociedade Brasileira de Geologia, 265–285.

Pedrosa-Soares, A. C., Wiedemann, C. M., Fernandes, M. L. S., Faria, L. F., Ferreira, J. C. H. (1999). Geotectonic Significance of the Neoproterozoic Granitic Magmatism in the Araçuaí Belt, Eastern Brazil: a Model and Pertinent Questions. *Revista Brasileira de Geociências* **29**, 59–66.

Pommier, A., Cocherie, A., Legendre, O. (2004). EPMA Dating User' Manual, V.1.01: Age Calculation from Electron Probe Microanalyser Measurements of U–Th–Pb. *BRGM*. Orleans.

Porada, H. (1989). Pan-African rifting and orogenesis in southern to equatorial Africa and eastern Brazil. *Precambrian Research* **44**, 103–136.

Potratz, G. L., Geraldes, M. C., Martins, M. V. A., Almeida, B. S. (2021). Sana Granite, a post-collisional S-type magmatic suite of the Ribeira Belt (Rio de Janeiro, SE Brazil). *Lithos* **388–389**, 1–14.

Potratz, G. L., Geraldes, M. C., Medeiros Júnior, E. B., Temporim, F. A., Martins, M. V. A. (2022). A Juvenile Component in the Pre- and Post-Collisional Magmatism in the Transition Zone between the Araçuaí and Ribeira Orogens (SE Brazil). *Minerals* **12**, 1–22.

Quek, L. X., Ghani, A.A., Chung, S.L., Li, S., Lai, Y.M., Saidin, M., Hassan, M.H.A., Ali, M.A.M., Badruldin, M.H., Bakar, A.F.A. (2017). Mafic microgranular enclaves (MMEs) in amphibole-bearing granites of the Bintang batholith, Main Range granite province: Evidence for a meta-igneous basement in Western Peninsular Malaysia. *Journal of Asian Earth Sciences* **143**, 11–29.

Ratajeski, K., Glazner, A. F., Miller, B. V. (2001). Geology and geochemistry of mafic to felsic plutonic rocks in the Cretaceous intrusive suite of Yosemite Valley , California. *Geological Society of America Bulletin* **113**, 1486–1502.

Richter, F., Lana, C., Stevens, G., Buick, I., Pedrosa-Soares, A. C., Alkmim, F. F., Cutts, K. (2016). Sedimentation, metamorphism and granite generation in a back-arc region: Records from the Ediacaran Nova Venécia Complex (Araçuaí Orogen, Southeastern Brazil). *Precambrian Research* **272**, 78–100.

Rudnick, R. L. (1992). Restites, Eu anomalies and the lower continental crust. *Geochimica et Cosmochimica Acta* **56**, 963–970.

Sami, M., Ntaflos, T., Farahat, E. S., Mohamed, H. A., Hauzenberger, C., Ahmed, A. F. (2018). Petrogenesis and geodynamic implications of Ediacaran highly fractionated A-type granitoids in the north Arabian-Nubian Shield (Egypt): Constraints from whole-rock geochemistry and Sr-Nd isotopes. *Lithos* **304–307**, 329–346.

Sawyer, E. W. (1998). Formation and evolution of granite magmas during crustal reworking: the significance of diatexites. *Journal of Petrology* **39**, 1147–1167.

Schmitt, R.S., Trouw, R. A. J., Van Schmus, W. R., Pimentel, M. M. (2004). Late amalgamation in the central part of West Gondwana: New geochronological data and the characterization of a Cambrian collisional orogeny in the Ribeira Belt (SE Brazil). *Precambrian Research* **133**, 29–61.

Schmidt-Thome, R., Weber-Diefenbach, K. (1987). Evidence for "frozen-in" magma mixing in Brasiliano calc-alkaline intrusions: the Santa Angelica Pluton, southern Espirito Santo, Brazil. *Revista Brasileira de Geociencias* **17**, 498–506.

Serrano, P., Pedrosa-Soares, A., Medeiros-Júnior, E., Fonte-Boa, T., Araujo, C., Dussin, I., Queiroga, G., Lana, C. (2018). A-type Medina batholith and post-collisional anatexis in the Araçuaí orogen (SE Brazil). *Lithos* **320–321**, 515–536.

Shand, S. J. (1943). *Eruptive Rocks: Their Genesis, Composition, Classification and their Relation to Ore Deposits with a Chapter on Meteorites.* New York: John Wiley & Sons.

Shaw, S. E., Flood, R. H. (2009). Zircon Hf isotopic evidence for mixing of crustal and silicic mantle-derived magmas in a zoned granite pluton, Eastern Australia. *Journal of Petrology* **50**, 147–168.

Signorelli, N., Drumind, J. B. V., Raposo, F. O., Souza, E. C., Heineck, C. A. (1993). Afonso Cláudio, folha SF.24-V-A-II: estados do Espírito Santo e Minas Gerais. Escala: 1:100.000. In: Signorelli, N. (ed.) *Afonso Cláudio, folha SF.24-V-A-II: estados do Espírito Santo e Minas Gerais. Escala: 1:100.000.* Brasília: DNPM/CPRM, 86–86.

Skrzypek, E., Sakata, S., Sorger, D. (2020). Alteration of magmatic monazite in granitoids from the Ryoke belt (SW Japan): Processes and consequences. *American Mineralogist* **105**, 538–554.

Solar, G. S., Brown, M. (2001). Petrogenesis of migmatites in Maine, USA: Possible source of perluminous leucogranite in Plutons? *Journal of Petrology* **42**, 789–823.

Sparks, R. S. J. (1986). The role of crustal contamination in magma evolution through geological time. *Earth and Planetary Science Letters* **78**, 211–223.

Spencer, C. J., Kirkland, C. L., Roberts, N. M. W., Evans, N. J., Liebmann, J. (2020). Strategies

towards robust interpretations of in situ zircon Lu–Hf isotope analyses. *Geoscience Frontiers* **11**, 843–853.

Spera, F. (1980). Thermal evolution of plutons: A parameterized approach. *Science* **207**, 299–301.

Sun, S. S., McDonough, W. F. (1989). Chemical and isotopic systematics of oceanic basalts: Implications for mantle composition and processes. *Geological Society Special Publication* **42**, 313–345.

Szilas, K., Hoffmann, J. E., Hansmeier, C., Hollis, J. A., Münker, C., Viehmann, S., Kasper, H. U. (2015). Sm-Nd and Lu-Hf isotope and trace-element systematics of Mesoarchaean amphibolites, inner Ameralik fjord, southern West Greenland. *Mineralogical Magazine* **79**, 857–876.

Tedeschi, M., Novo, T., Pedrosa-Soares, A., Dussin, I., Tassinari, C., Silva, L.C., Gonçalves, L., Alkmim, F., Lana, C, Figueiredo, C., Dantas, E., Medeiros, S., De Campos, C., Corrales, F., Heilbron, M. (2016). The Ediacaran Rio Doce magmatic arc revisited (Araçuaí-Ribeira orogenic system, SE Brazil). *Journal of South American Earth Sciences* **68**, 167–186.

Teixeira, P. A. D., Fernandes, C. M., Mendes, J. C., Medeiros, S.R., Rocha, I. S. A. (2020). U-PB LA-ICP-MS and geochemical data of the Alto Chapéu Pluton: Contributions on bimodal post-collisional magmatism in the Araçuaí belt (SE Brazil). *Journal of South American Earth Sciences* **103**, 1–18.

Temporim, F. A., Trindade, R.I.F., Egydio-Silva, M., Angelo, T.V., Tohver, E., Soares, C.C., Gouvêa, L.P., Mendes, J.C., Medeiros, S.R., Pedrosa-Soares, A.C., Silva, G.G. (2022). Vertical deformation partitioning across a collapsing large and hot orogen. *Terra Nova*, 1–9.

Terekhov, E. N., Shcherbakova, T. F. (2006). Genesis of positive Eu anomalies in acid rocks from the eastern Baltic Shield. *Geochemistry International* **44**, 439–455.

Terry, M. P., Robinson, P., Hamilton, M. A., Jercinovic, M. J. (2000). Monazite geochronology of UHP and HP metamorphism, deformation, and exhumation Nordøyane, Western Gneiss Region, Norway. *American Mineralogist* **85**, 1651–1664.

Thakurdin, Y., Bolhar, R., Horváth, P., Rocholl, A., Collerson, K. (2019). Characterization of crustal xenoliths from the Bearpaw Mountains, Montana (USA), using U-Pb geochronology, whole-rock geochemistry and thermobarometry, with implications for lower crustal processes and evolution of the Wyoming Craton. *Chemical Geology* **524**, 295–322.

Trompette, R. (1994). *Geology of western Gondwana (2000-500 Ma): Pan-African-Brasiliano aggregation of South America and Africa. Geology of western Gondwana (2000-500 Ma): Pan-*

African-Brasiliano aggregation of South America and Africa. London: CRC Press.

Turkina, O. M., Sukhorukov, V. P. (2017). Composition and genesis of garnet in the rocks of Paleoproterozoic gneiss-migmatite complex (Sharyzhalgai uplift, southwestern Siberian craton). *Russian Geology and Geophysics* **58**, 674–691.

Vieira, T. A. T., Schmitt, R. S., Mendes, J. C., Moraes, R., Luvizotto, G. L., Andrade Silva, R. L., Vinagre, R., Medeiros, S. R. (2022). Contrasting P-T-t paths of basement and cover within the Búzios Orogen, SE Brazil – Tracking Ediacaran-Cambrian subduction zones. *Precambrian Research* **368**, 1–29.

Vieira, V. S. (2015). *Geologia e Recursos Minerais do Estado do Espírito Santo: texto explicativo do mapa geológico e de recursos minerais. Geologia e Recursos Minerais do Estado do Espírito Santo: texto explicativo do mapa geológico e de recursos minerais.* Belo Horizonte: CPRM.

Wagner, R., Rosenberg, C. L., Handy, M. R., Möbus, C., Albertz, M. (2006). Fracture-driven intrusion and upwelling of a mid-crustal pluton fed from a transpressive shear zone - The Rieserferner Pluton (Eastern Alps). *Bulletin of the Geological Society of America* **118**, 219–237.

Wang, R. Q., Qiu, J. S., Yu, S. Bin, Lin, L., Xu, H. (2019). Magma mixing origin for the Quxu intrusive complex in southern Tibet: insights into the early Eocene magmatism and geodynamics of the southern Lhasa subterrane. *Lithos* **328**–**329**, 14–32.

Wiedemann, C. M., Medeiros, S. R., Ludka, I. P., Mendes, J. C., Costa-de-Moura, J. (2002). Architecture of Late Orogenic Plutons in the Araçuaí-Ribeira Fold Belt, Southeast Brazil. *Gondwana Research* **5**, 381–399.

Williams, M. L., Jercinovic, M. J., Harlov, D. E., Budzyń, B., Hetherington, C. J. (2011). Resetting monazite ages during fluid-related alteration. *Chemical Geology* **283**, 218–225.

Williams, M. L., Jercinovic, M. J., Hetherington, C. J. (2007). Microprobe monazite geochronology: Understanding geologic processes by integrating composition and chronology. *Annual Review of Earth and Planetary Sciences* **35**, 137–175.

Williams, M. L., Jercinovic, M. J., Terry, M. P. (1999). Age mapping and dating of monazite on the electron microprobe: Deconvoluting multistage tectonic histories. *Geology* **27**, 1023–1026.

Wisniowski, L., Pedrosa-Soares, A., Medeiros-Junior, E., Belém, J., Dussin, I., Queiroga, G. (2021). Ultra-high temperature, mid-crustal level, contact metamorphism imprinted on granulite facies paragneisses by a norite intrusion (São Gabriel da Baunilha, Araçuaí orogen,

southeast Brazil). *Journal of Metamorphic Geology* **39**, 867–895.

Yang, H., Ge, W. C., Zhao, G. C., Dong, Y., Xu, W. L., Ji, Z., Yu, J. J. (2015). Late triassic intrusive complex in the Jidong region, Jiamusi-Khanka Block, NE China: Geochemistry, zircon U-Pb ages, Lu-Hf isotopes, and implications for magma mingling and mixing. *Lithos* **224**–**225**, 143–159.

Yuguchi, T., Nishiyama, T. (2007). Cooling process of a granitic body deduced from the extents of exsolution and deuteric sub-solidus reactions: Case study of the Okueyama granitic body, Kyushu, Japan. *Lithos* **97**, 395–421.

Zanon, M. L., Chaves, A. O., Rangel, C. V. G. T., Gaburo, L., Pires, C. R. (2015). Os aspectos geológicos do Maciço Santa Angélica (ES): uma nova abordagem. *Brazilian Journal of Geology* **45**, 609–633.

Zhang, C., Yu, J., O'Reilly, S. Y., Griffin, W. L., Qian, J., Liu, Q., Lou, F., Zhou, X., Shen, L. (2016). Granulite facies xenoliths from the Yuhuashan complex, central Jiangxi, South China: Constraints on Late Palaeozoic orogeny and middle-lower crust components. *Journal of Metamorphic Geology* **34**, 45–61.

Zhang, S. H., Zhao, Y. (2017). Cogenetic origin of mafic microgranular enclaves in calc-alkaline granitoids: The permian plutons in the northern north China block. *Geosphere* **13**, 1–36.

Zhou, X., Zheng, J. P., Xiong, Q., Yang, J. S., Wu, Y. B., Zhao, J. H., Griffin, W. L., Dai, H. K. (2017). Early Mesozoic deep-crust reworking beneath the central Lhasa terrane (South Tibet): Evidence from intermediate gneiss xenoliths in granites. *Lithos* **274**–**275**, 225–239.

Zhu, K. Y., Shen, Z. Y., Li, M. Y., Yu, Y. H. (2018). Interaction between mingling mafic and felsic magmas: Its roles in differentiation of a quartz monzonite and MMEs from eastern South China. *Lithos* **318**–**319**, 60–77.

Zou, H., Cao, H. W., Bagas, L., Zhang, Y. H., Zhang, S. T., Zhang, Q., Liu, H., Li, Y. (2019). Origin of the Mo-bearing Xiaoshuijing Syenogranite in the Tengchong Terrane, SW China. *Ore Geology Reviews* **105**, 258–272.

4. CONCLUSIONS

The AWCO post-collisional magmatism has been extensively studied in the last years, however the investigations have been mainly focused at field aspects, petrography, whole-rock geochemistry, geochronology and isotopic features of the intrusions (Bayer et al., 1987; Schmidt-Thome and Weber-Diefenbach, 1987; Horn and Weber-Diefenbach, 1987; Ludka et al., 1998; Mendes et al., 1999, 2005; Pedrosa-Soares et al., 1999, 2011; Ludka and Wiedemann-Leonardos, 2000; Medeiros et al., 2000, 2001; Noce et al., 2000; Wiedemann et al., 2002; Martins et al., 2004; De Campos et al., 2004, 2016; De Mello et al., 2011; Mendes and De Campos, 2012; Gradim et al., 2014; Zanon et al., 2015; Słaby et al., 2017; Serrano et al., 2018; Aranda et al., 2020; Araujo et al., 2020; Melo et al., 2020; Temporim et al., 2020; Wisniowski et al., 2021; Fernandes et al., 2021; Lopes de Macêdo et al., 2022; Potratz et al., 2022; Bellon et al., 2022). Crystallization conditions of the plutons have been occasionally investigated (Mendes et al., 1999; Ludka and Wiedemann-Leonardos, 2000; Medeiros et al., 2001; Wiedemann et al., 2002; Mendes and De Campos, 2012; Serrano et al., 2018; Araujo et al., 2020), while the commonly found crustal xenoliths hosted by the intrusions have never been studied in such detail.

The typical AWCO post-collisional plutons are mainly composed of mafic to intermediate off-centered cores surrounded by intermediate to felsic rocks, with mingling and mixing zones between these domains and some plutons showing an external charnockitic ring (De Campos et al., 2004, 2016). These intrusions have evolution associated to the interaction between mantle magmas related to the partial melting of an previously enriched mantle and crustal magmas derived from the melting of the lower crust (Medeiros et al., 2001; Wiedemann et al., 2002).

The focus of the thesis was the ACIC, a typical AWCO post-collisional pluton that intruded at homonymous town at Espírito Santo state. The first paper of this thesis focused on understanding of the crystallization conditions of the ACIC main rocks. The results provided evidences that the ACIC intruded between middle to deep crustal levels. In addition, the chemical compositions of the minerals that compound ACIC main rocks revealed additional evidences to support mixing between two contrasting magmas.

The sources of crustal magmas and the role of enclosing rocks were some remained questions about ACIC evolution that the first paper could not faithfully answer. The investigation of the commonly found xenoliths hosted by ACIC rocks and enclosing country

rocks may bring some insights about these questions. These topics are the focus of the second paper, that brings new and important insights about the ACIC evolution. It is proved that the similar xenoliths and enclosing country rocks are related and that these ones are neither the main sources of crustal magmas associated to ACIC evolution nor the main contamination source of monzograbbroic and monzodioritic rocks. Geochemical modeling of igneous processes showed that the ACIC rocks are formed due to interaction between at least two contrasting magmas, which evolved ruled by different processes. The monzogabroic magma is related to partial melting of an enriched mantle source, which has evolution associated to fractional crystallization with minor assimilation from enclosing rocks and the crystallization of this magma generated the monzogabbro and monzodiorite. On the other hand, quartz monzonitic magma is related to lower crust melting and has evolution related to coeval assimilation and fractional crystallization, with intense contributions from enclosing rocks. The similarities in geochemical signatures between the contrasting magmas is due to mixing processes. In addition, U-Th-Pb monazite geochronology of the main xenoliths found hosted by ACIC revealed two main ages. The older ages (478.2 ± 9.3 Ma and 477 ± 14 Ma) are related to typical AWCO post-collisional magmatism, however the younger ages (431 ± 13 Ma and 427 ± 19 Ma) could represent an extension of the AWCO post-collisional stage or a later unrelated thermal event.

The typical AWCO post-collisional intrusions are similar, permitting that the detailed investigations of one single pluton brings insights to AWCO post-collisional magmatism. Due to this it is possible to argue based on this investigation about ACIC that the typical AWCO post-collisional intrusions have evolution associated to interaction between previously-enriched mantle magmas and crustal magmas at mid to deep crustal levels. The interaction between the magmas by mixing processes generated the geochemical and isotopic similarities between these contrasting magmas, which evolved ruled by different processes. Typical fractional crystallization with minor enclosing country rocks contributions controlled the evolution of the mantle magmas, while coeval assimilation and fractional crystallization with intense contamination by enclosing country rocks ruled the evolution of crustal magmas. The minor differences noted at intrusions could be due to emplacement levels, crustal magma sources, intensity of magma mingling and mixing, erosional levels and grade of contamination from different enclosing rocks (Wiedemann et al., 2002). Differences are mainly noted at post-collisional intrusions related to northern part of the AWCO, where the typical circular to elongated post-collisional plutons became large batholiths related to shallower crustal levels

(De Campos et al., 2016; Temporim et al., 2022).

The younger ages (431±13 Ma and 427±19 Ma) found at monazite crystals associated to xenoliths could represent an extension of the AWCO post-collisional magmatism or a later unrelated thermal event. The dykes that crosscut the AWCO post-collisional intrusions have been occasionally investigated and detailed examination of these dykes could better elucidate these newer ages.

4.1. References

Aranda, R. O., Chaves, A. O., Medeiros Júnior, E. B., Venturini Junior, R. (2020). Petrology of the Afonso Cláudio Intrusive Complex: New insights for the Cambro-Ordovician post-collisional magmatism in the Araçuaí-West Congo Orogen, Southeast Brazil. *Journal of South American Earth Sciences* **98**, 1–19.

Araujo, C., Pedrosa-Soares, A., Lana, C., Dussin, I., Queiroga, G., Serrano, P., Medeiros-Júnior, E. (2020). Zircon in emplacement borders of post-collisional plutons compared to country rocks: A study on morphology, internal texture, U–Th–Pb geochronology and Hf isotopes (Araçuaí orogen, SE Brazil). *Lithos* **352–353**, 1–18.

Bayer, P., Schmidt-Thomé, R., Weber-Diefenbach, K., Horn, H. A. (1987). Complex concentric granitoid intrusions in the coastal mobile belt, Espírito Santo, Brazil: The Santa Angélica Pluton - an example. *Geologische Rundschau* **76**, 357–371.

Bellon, U. D., Souza Junior, G. F., Temporim, F. A., D'Agrella-Filho, M. S., Trindade, R. I. F. (2022). U-Pb geochronology of a reversely zoned pluton: Records of pre-to-post collisional magmatism of the Araçuaí belt (SE-Brazil)? *Journal of South American Earth Sciences* **119**, 1–15.

De Campos, C. P., Cezar Mendes, J., Ludka, I. P., Medeiros, S. R., Moura, J. C., Wallfass, C. M. (2004). A review of the Brasiliano magmatism in southern Espírito Santo, Brazil, with emphasis on post-collisional magmatism. *Journal of the Virtual Explorer* **17**, 1–39.

De Campos, C. P., Medeiros, S. R., Mendes, J. C., Pedrosa-Soares, A. C., Dussin, I., Ludka, I. P., Dantas, E. L. (2016). Cambro-Ordovician magmatism in the Araçuaí Belt (SE Brazil): Snapshots from a post-collisional event. *Journal of South American Earth Sciences* **68**, 248–268.

De Mello, F. M., Machado, R., Bilal, E. (2011). Petrography and geochemistry of the Aimorés charnockitic complex: An example of post-orogenic plutonism of the Araçuaí/Ribeira Belt.

Geologia USP - Serie Cientifica **11**, 33–57.

Fernandes, C. M., Duffles Teixeira, P. A., Mendes, J. C. (2021). Constraining crystallization conditions during the Cambro-Ordovician post-collisional magmatism at Araçuaí belt (SE Brazil): Zircon as key petrologic witness. *Journal of South American Earth Sciences* **108**, 103235.

Gradim, C., Roncato, J., Pedrosa-Soares, A.P., Cordani, U., Dussin, I., Alkmim, F.F., Queirogra, G., Jacobsohn, T., Silva, L.C., Babinski. (2014). The hot back-arc zone of the Araçuaí orogen, Eastern Brazil: from sedimentation to granite generation. *Brazilian Journal of Geology* **44**, 155–180.

Horn, H. A., Weber-Diefenbach, W. (1987). Geochemical and genetic studies of three invers zoned intrusive bodies of both alkaline and calc-alkaline composition in the Ribeira Mobile Belt (Espírito Santo, Brazil). *Revista Brasileira de Geociências* **17**, 488–497.

Lopes de Macêdo, I. M., Geraldes, M. C., Marques, R. A., Melo, M. G., Tavares, A. D., Alves Martins, M. V., Oliveira, H. C., Rodrigues, R. D. (2022). New clues for magma-mixing processes using petrological and geochronological evidence from the Castelo Intrusive Complex, Araçuaí Orogen (SE Brazil). *Journal of South American Earth Sciences* **115**, 1–21.

Ludka, I. P., Wiedemann-Leonardos, C. M. (2000). Further Signs of an Enriched Mantle Source Under the Neoproterozoic Araçuaí-Ribeira Mobile Belt. *Revista Brasileira de Geociências* **30**, 95–98.

Ludka, I. P., Wiedemann, C. M., Töpfner, C. (1998). On the origin of incompatible element enrichment in the Venda Nova pluton, State of Espirito Santo, southeast Brazil. *Journal of South American Earth Sciences* **11**, 473–486.

Martins, V. T. d. S., Teixeira, W., Noce, C. M., Pedrosa-Soares, A. C. (2004). Sr and Nd characteristics of Brasiliano/Pan-African granitoid plutons of the Araçuaí Orogen, Southeastern Brazil: Tectonic implications. *Gondwana Research* **7**, 75–89.

Medeiros, S. R., Wiedeman-Leonardos, C. M., Mendes, J. C. (2000). Post-collisional multistage magmatism in the Ribeira mobile belt; geochemical and isotopic study of the Varzea Alegre Intrusive Complex, Espírito Santo, Brazil. *Revista Brasileira de Geociencias* **30**, 30–34.

Medeiros, S. R., Wiedemann-Leonardos, C. M., Vriend, S. (2001). Evidence of mingling between contrasting magmas in a deep plutonic environment: The example of Várzea Alegre, in the Ribeira Mobile Belt, Espírito Santo, Brazil. *Anais da Academia Brasileira de Ciencias* **73**, 99–119.

Melo, M. G., Lana, C., Stevens, G., Hartwig, M. E., Pimenta, M. S., Nalini, H. A. (2020). Deciphering the source of multiple U–Pb ages and complex Hf isotope composition in zircon from post-collisional charnockite-granite associations from the Araçuaí orogen (southeastern Brazil). *Journal of South American Earth Sciences* **103**, 1–22.

Mendes, J. C., De Campos, C. M. P. (2012). Norite and charnockites from the Venda Nova Pluton, SE Brazil: Intensive parameters and some petrogenetic constraints. *Geoscience Frontiers* **3**, 789–800.

Mendes, J. C., Medeiros, S. R., McReath, I., De Campos, C. M. P. (2005). Cambro-Ordovician magmatism in SE Brazil: U-Pb and Rb-Sr ages, combined with Sr and Nd isotopic data of Charnockitic rocks from the Varzea Alegre Complex. *Gondwana Research* **8**, 337–345.

Mendes, J. C., Wiedemann, C. M., McRearth, I. (1999). Conditions of Formation of Charnockitic Magmatic Rocks From the Várzea Alegre Massif, Espírito Santo, Southeastern Brazil. *Revista Brasileira de Geociências* **29**, 47–54.

Noce, C. M., José, M., Macambira, B., Carlos, A., Soares, P. (2000). Chronology of Neoproterozoic-Cambrian granitic magmatism in the Araçuaí Belt, Eastern Brazil, based on single zircon evaporation dating. *Revista Brasileira de Geociências* **30**, 25–29.

Pedrosa-Soares, A. C., De Campos, C.P., Noce, C., Silva, L.C., Novo, T., Roncato, J., Medeiros, S., Castañeda, C., Queiroga, G., Dantas, E., Dussin, I., Alkmim, F. (2011). Late Neoproterozoic – Cambrian granitic magmatism in the Araçuaí orogen (Brazil), the Eastern Brazilian Pegmatite Province and related mineral resources. *Geological Society, London, Special Publications* **350**, 25–51.

Pedrosa-Soares, A. C., Wiedemann, C. M., Fernandes, M. L. S., Faria, L. F., Ferreira, J. C. H. (1999). Geotectonic Significance of the Neoproterozoic Granitic Magmatism in the Araçuaí Belt, Eastern Brazil: a Model and Pertinent Questions. *Revista Brasileira de Geociências* **29**, 59–66.

Potratz, G. L., Geraldes, M. C., Medeiros Júnior, E. B., Temporim, F. A., Martins, M. V. A. (2022). A Juvenile Component in the Pre- and Post-Collisional Magmatism in the Transition Zone between the Araçuaí and Ribeira Orogens (SE Brazil). *Minerals* **12**, 1–22.

Schmidt-Thome, R., Weber-Diefenbach, K. (1987). Evidence for "frozen-in" magma mixing in Brasiliano calc-alkaline intrusions: the Santa Angelica Pluton, southern Espirito Santo, Brazil. *Revista Brasileira de Geociencias* **17**, 498–506.

Serrano, P., Pedrosa-Soares, A., Medeiros-Júnior, E., Fonte-Boa, T., Araujo, C., Dussin, I., Queiroga, G., Lana, C. (2018). A-type Medina batholith and post-collisional anatexis in the

Araçuaí orogen (SE Brazil). *Lithos* **320**–**321**, 515–536.

Słaby, E., De Campos, C. P., Majzner, K., Simon, K., Gros, K., Moszumańska, I., Jokubauskas, P. (2017). Feldspar megacrysts from the Santa Angélica composite pluton — Formation/transformation path revealed by combined CL, Raman and LA-ICP-MS data. *Lithos* **277**, 269–283.

Temporim, F. A., Trindade, R.I.F., Egydio-Silva, M., Angelo, T.V., Tohver, E., Soares, C.C., Gouvêa, L.P., Mendes, J.C., Medeiros, S.R., Pedrosa-Soares, A.C., Silva, G.G. (2022). Vertical deformation partitioning across a collapsing large and hot orogen. *Terra Nova*, 1–9.

Temporim, F. A., Trindade, R. I. F., Tohver, E., Soares, C. C., Gouvêa, L. P., Egydio-Silva, M., Amaral, C. A. D., Souza, G. F. (2020). Magnetic Fabric and Geochronology of a Cambrian "Isotropic" Pluton in the Neoproterozoic Araçuaí Orogen. *Tectonics* **39**, 1–21.

Wiedemann, C. M., Medeiros, S. R., Ludka, I. P., Mendes, J. C., Costa-de-Moura, J. (2002). Architecture of Late Orogenic Plutons in the Araçuaí-Ribeira Fold Belt, Southeast Brazil. *Gondwana Research* **5**, 381–399.

Wisniowski, L., Pedrosa-Soares, A., Medeiros-Junior, E., Belém, J., Dussin, I., Queiroga, G. (2021). Ultra-high temperature, mid-crustal level, contact metamorphism imprinted on granulite facies paragneisses by a norite intrusion (São Gabriel da Baunilha, Araçuaí orogen, southeast Brazil). *Journal of Metamorphic Geology* **39**, 867–895.

Zanon, M. L., Chaves, A. O., Rangel, C. V. G. T., Gaburo, L., Pires, C. R. (2015). Os aspectos geológicos do Maciço Santa Angélica (ES): uma nova abordagem. *Brazilian Journal of Geology* **45**, 609–633.

5. SUPPLEMENTARY MATERIAL

5.1. SUPPLEMENTARY MATERIAL 1 - Microprobe analyses

Table S1.1: K-feldspar microprobe analyses.

Rock	Quartz Monzonite					Monzodiorite	Monzogabbro					
Crystal id	1		2	3		1	1	2	3	4	5	6
Comment	Mc core	Mc rim	Mc	Mc core	Mc rim	Kfs	Kfs	Kfs inclusion in Pl	Kfs	Kfs	Kfs	Kfs
SiO$_2$	64.76	63.96	65.02	65.01	64.50	63.59	62.13	58.28	61.64	61.70	63.55	63.17
TiO$_2$	0.02	0.00	0.05	0.03	0.00	0.03	0.00	0.05	0.00	0.01	0.03	0.10
Al$_2$O$_3$	18.71	19.16	18.89	18.68	18.56	19.36	19.43	19.81	19.75	19.44	19.37	19.37
FeO	0.10	0.07	0.04	0.01	0.09	0.01	0.05	0.01	0.06	0.11	0.03	0.01
CaO	0.01	0.00	0.03	0.01	0.02	0.01	0.04	0.10	0.07	0.01	0.08	0.03
Na$_2$O	0.72	0.75	1.09	1.45	1.07	1.27	0.93	0.87	1.17	1.13	0.84	1.02
K$_2$O	15.39	15.35	14.72	13.67	15.15	13.99	14.20	13.79	14.38	14.20	14.57	14.50
BaO	0.39	1.14	1.08	1.21	0.97	3.23	2.52	4.38	2.19	2.14	2.16	2.13
SrO	0.00	0.08	0.00	0.00	0.05	0.03	0.05	0.00	0.15	0.00	0.00	0.03
MgO	0.00	0.00	0.01	0.01	0.00	0.02	0.00	0.00	0.02	0.02	0.00	0.02
MnO	0.02	0.00	0.00	0.00	0.05	0.03	0.00	0.02	0.00	0.00	0.02	0.00
Total	100.12	100.50	100.94	100.08	100.46	101.56	99.36	97.30	99.42	98.75	100.65	100.38
Oxygen number: 32												
Si	11.95	11.84	11.93	11.98	11.93	11.77	11.72	11.43	11.64	11.69	11.79	11.76
Ti	0.00	0.00	0.01	0.00	0.00	0.00	0.00	0.01	0.00	0.00	0.00	0.01
Al	4.07	4.18	4.08	4.06	4.05	4.22	4.32	4.58	4.39	4.34	4.24	4.25
Fe^{2+}	0.02	0.01	0.01	0.00	0.01	0.00	0.01	0.00	0.01	0.02	0.00	0.00
Ca	0.00	0.00	0.01	0.00	0.00	0.00	0.01	0.02	0.01	0.00	0.02	0.01
Na	0.26	0.27	0.39	0.52	0.38	0.46	0.34	0.33	0.43	0.42	0.30	0.37
K	3.62	3.63	3.45	3.21	3.57	3.30	3.42	3.45	3.46	3.43	3.45	3.45
Ba	0.03	0.08	0.08	0.09	0.07	0.23	0.19	0.34	0.16	0.16	0.16	0.16
Endmembers												
An	0.07	0.02	0.15	0.06	0.08	0.06	0.20	0.54	0.34	0.04	0.42	0.17
Ab	6.65	6.89	10.13	13.87	9.65	12.11	9.06	8.66	10.99	10.82	8.00	9.66
Or	93.28	93.09	89.72	86.07	90.27	87.83	90.74	90.80	88.66	89.14	91.58	90.17

Table S1.2: Plagioclase microprobe analyses.

Rock	Quartz monzonite														
Crystal id	1		2		3	4	5	6	7		8		9	10	11
Comment	Pl rim	Pl core	Pl rim	Pl core	Pl	Pl	Pl	Pl	Pl core	Pl rim	Pl core	Pl rim	Pl	Pl	Pl inclusion in Mc porphyry
SiO_2	62.75	59.38	60.59	61.52	61.90	60.19	61.93	62.29	60.59	61.22	61.23	67.74	62.20	63.04	66.85
TiO_2	0.00	0.00	0.00	0.00	0.00	0.00	0.00	0.00	0.00	0.00	0.09	0.00	0.00	0.00	0.00
Al_2O_3	23.54	22.22	23.05	23.28	23.11	23.23	23.69	23.78	24.44	23.83	23.96	19.64	23.93	24.41	19.55
FeO	0.01	0.08	0.04	0.12	0.10	0.04	0.11	0.13	0.06	0.06	0.07	0.00	0.06	0.04	0.02
CaO	5.14	5.54	5.61	5.54	5.74	6.01	5.47	5.57	6.50	6.28	5.92	0.43	5.37	5.57	0.38
Na_2O	8.31	8.48	8.27	8.17	8.16	7.74	8.20	8.06	7.49	7.69	8.13	10.43	6.27	5.03	7.74
K_2O	0.08	0.14	0.11	0.27	0.12	0.14	0.11	0.15	0.13	0.21	0.18	0.12	0.13	0.07	3.09
BaO	0.00	0.00	0.05	0.02	0.05	0.00	0.09	0.04	0.08	0.03	0.00	0.01	0.00	0.09	0.39
SrO	0.00	0.00	0.00	0.00	0.00	0.00	0.03	0.02	0.06	0.03	0.00	0.00	0.04	0.01	0.00
MgO	0.02	0.00	0.00	0.01	0.00	0.00	0.00	0.00	0.00	0.00	0.00	0.00	0.00	0.00	0.00
MnO	0.00	0.03	0.00	0.02	0.01	0.01	0.03	0.00	0.01	0.00	0.00	0.00	0.00	0.03	0.00
Total	99.84	95.87	97.71	98.96	99.19	97.34	99.66	100.03	99.36	99.34	99.57	98.38	98.00	98.29	98.03
Oxygen number: 32															
Si	11.11	11.02	11.01	11.04	11.07	10.97	11.03	11.04	10.85	10.95	10.93	11.99	11.14	11.20	12.01
Ti	0.00	0.00	0.00	0.00	0.00	0.00	0.00	0.00	0.00	0.00	0.01	0.00	0.00	0.00	0.00
Al	4.91	4.86	4.94	4.92	4.87	4.99	4.97	4.97	5.16	5.02	5.04	4.10	5.05	5.11	4.14
Fe^{2+}	0.00	0.01	0.01	0.02	0.01	0.01	0.02	0.02	0.01	0.01	0.01	0.00	0.01	0.01	0.00
Ca	0.98	1.10	1.09	1.07	1.10	1.17	1.04	1.06	1.25	1.20	1.13	0.08	1.03	1.06	0.07
Na	2.85	3.05	2.91	2.84	2.83	2.73	2.83	2.77	2.60	2.67	2.81	3.58	2.18	1.73	2.70
K	0.02	0.03	0.02	0.06	0.03	0.03	0.02	0.03	0.03	0.05	0.04	0.03	0.03	0.01	0.71
Total	19.87	20.09	19.99	19.95	19.92	19.91	19.91	19.88	19.89	19.90	19.97	19.77	19.44	19.12	19.63
Endmembers															
An	25.38	26.29	27.11	26.84	27.80	29.78	26.77	27.42	32.18	30.73	28.41	2.20	31.84	37.79	2.10
Ab	74.15	72.94	72.29	71.58	71.49	69.39	72.59	71.72	67.08	68.05	70.55	97.05	67.23	61.68	77.52
Or	0.46	0.77	0.60	1.58	0.71	0.83	0.64	0.86	0.75	1.23	1.04	0.75	0.93	0.53	20.38

Table S1.2: Plagioclase microprobe analyses (continuation).

Rock	Quartz Monzonite										Monzodiorite				
Crystal id	12		13		14			15			1			2	3
Comment	Pl rim	Pl core	Pl rim	Pl core	Pl porphyry rim	Pl porphyry core	Pl porphyry core	Pl inclusion core in Mc	Pl inclusion mantle in Mc	Pl inclusion rim in Mc	Pl porphyry core	Pl porphyry mantle	Pl porphyry rim	Pl	Pl inclusion in Mag
SiO_2	60.36	60.55	61.48	61.08	60.31	58.16	60.69	61.35	61.63	68.61	60.93	60.48	58.65	60.19	60.50
TiO_2	0.07	0.00	0.03	0.05	0.00	0.00	0.00	0.00	0.04	0.00	0.00	0.00	0.00	0.05	0.02
Al_2O_3	24.70	24.79	24.56	24.74	25.53	26.03	25.61	24.81	24.90	20.13	26.02	25.62	27.80	25.47	23.88
FeO	0.13	0.08	0.13	0.15	0.05	0.10	0.11	0.10	0.11	0.02	0.78	0.06	0.08	0.12	0.54
CaO	6.86	6.70	6.18	6.39	6.18	6.79	6.80	6.55	6.07	0.58	1.31	7.17	8.97	6.97	6.33
Na_2O	7.48	7.63	7.71	7.71	8.03	7.40	7.19	7.87	7.90	11.05	7.04	7.08	6.29	7.18	7.45
K_2O	0.33	0.32	0.18	0.29	0.24	0.31	0.32	0.20	0.18	0.11	3.97	0.26	0.19	0.16	0.20
BaO	0.14	0.08	0.00	0.00	0.05	0.13	0.05	0.00	0.00	0.00	0.22	0.00	0.02	0.03	0.24
SrO	0.00	0.00	0.01	0.00	0.00	0.00	0.03	0.00	0.07	0.00	0.08	0.12	0.14	0.18	0.16
MgO	0.01	0.00	0.02	0.00	0.00	0.00	0.00	0.00	0.01	0.00	0.17	0.00	0.02	0.00	0.01
MnO	0.00	0.03	0.02	0.00	0.00	0.01	0.02	0.02	0.00	0.00	0.03	0.00	0.00	0.00	0.00
Total	100.06	100.17	100.31	100.40	100.39	98.94	100.82	100.89	100.91	100.50	100.56	100.79	102.15	100.34	99.31
Oxygen number: 32															
Si	10.77	10.78	10.89	10.82	10.70	10.51	10.72	10.82	10.85	11.92	10.88	10.69	10.29	10.69	10.89
Ti	0.01	0.00	0.00	0.01	0.00	0.00	0.00	0.00	0.01	0.00	0.00	0.00	0.00	0.01	0.00
Al	5.19	5.20	5.13	5.17	5.34	5.54	5.33	5.16	5.17	4.12	5.47	5.34	5.75	5.33	5.07
Fe^{2+}	0.02	0.01	0.02	0.02	0.01	0.01	0.02	0.01	0.02	0.00	0.12	0.01	0.01	0.02	0.08
Ca	1.31	1.28	1.17	1.21	1.18	1.31	1.29	1.24	1.15	0.11	0.25	1.36	1.69	1.33	1.22
Na	2.59	2.63	2.65	2.65	2.76	2.59	2.46	2.69	2.70	3.72	2.44	2.43	2.14	2.47	2.60
K	0.07	0.07	0.04	0.06	0.06	0.07	0.07	0.05	0.04	0.02	0.90	0.06	0.04	0.04	0.04
Total	19.96	19.97	19.89	19.94	20.04	20.05	19.88	19.97	19.93	19.90	20.06	19.88	19.92	19.89	19.90
Endmembers															
An	33.00	32.06	30.34	30.91	29.44	33.03	33.68	31.13	29.48	2.78	6.98	35.33	43.61	34.57	31.57
Ab	65.14	66.11	68.60	67.45	69.19	65.18	64.44	67.72	69.48	96.58	67.82	63.13	55.29	64.47	67.26
Or	1.86	1.84	1.06	1.64	1.38	1.80	1.89	1.15	1.04	0.64	25.19	1.54	1.10	0.96	1.16

Table S1.2: Plagioclase microprobe analyses (continuation).

Rock	Monzodiorite																			
Crystal id	4	5	6		7	8			9	10	11	12			13	14				15
Comment	Pl	Pl	Pl porphyry core	Pl porphyry rim	Pl	Pl core	Pl mantle	Pl rim	Pl	Pl	Pl	Pl rim	Pl mantle	Pl core	Pl	Pl rim	Pl mantle	Pl core	Pl rim	Pl
SiO_2	60.93	61.70	61.02	57.26	60.27	49.78	56.34	62.03	60.65	61.39	61.09	60.57	59.54	59.41	59.74	60.94	58.93	62.55	59.88	60.50
TiO_2	0.00	0.01	0.02	0.04	0.00	0.00	0.01	0.00	0.07	0.01	0.00	0.00	0.00	0.01	0.04	0.00	0.03	0.03	0.00	0.06
Al_2O_3	24.56	24.65	24.18	27.35	25.54	25.05	28.75	25.33	25.54	25.82	25.73	25.40	26.77	25.80	25.89	25.24	25.84	23.02	24.80	24.99
FeO	0.20	0.24	0.11	0.10	0.29	0.03	0.12	0.03	0.13	0.10	0.16	0.07	0.10	0.01	0.08	0.06	0.07	0.24	0.15	0.16
CaO	6.58	6.14	6.60	9.17	6.38	21.25	10.22	6.55	6.52	6.71	6.65	6.32	8.05	6.91	6.67	6.54	7.59	3.76	6.37	6.56
Na_2O	7.55	7.73	7.34	6.06	7.38	2.15	5.25	7.42	7.51	7.26	7.58	7.64	6.62	7.31	7.28	7.26	6.75	9.32	7.47	7.48
K_2O	0.25	0.13	0.31	0.30	0.18	0.08	0.22	0.33	0.12	0.18	0.15	0.11	0.23	0.23	0.17	0.31	0.31	0.07	0.25	0.21
BaO	0.10	0.00	0.00	0.14	0.13	0.03	0.08	0.06	0.08	0.06	0.08	0.11	0.00	0.00	0.00	0.18	0.09	0.07	0.04	0.12
SrO	0.11	0.11	0.06	0.12	0.16	0.21	0.10	0.16	0.03	0.10	0.19	0.04	0.14	0.06	0.06	0.13	0.10	0.11	0.12	0.13
MgO	0.02	0.00	0.02	0.00	0.02	0.01	0.00	0.00	0.00	0.00	0.01	0.00	0.00	0.00	0.00	0.02	0.00	0.01	0.01	0.00
MnO	0.00	0.00	0.00	0.00	0.00	0.00	0.00	0.00	0.00	0.00	0.00	0.00	0.00	0.01	0.00	0.01	0.04	0.01	0.03	0.02
Total	100.29	100.70	99.66	100.53	100.34	98.60	101.10	101.92	100.65	101.62	101.64	100.24	101.44	99.74	99.91	100.67	99.74	99.19	99.11	100.24
Oxygen number: 32																				
Si	10.83	10.89	10.89	10.24	10.71	9.44	10.03	10.83	10.72	10.74	10.72	10.75	10.49	10.62	10.64	10.79	10.56	11.17	10.77	10.77
Ti	0.00	0.00	0.00	0.00	0.00	0.00	0.00	0.00	0.01	0.00	0.00	0.00	0.00	0.00	0.01	0.00	0.00	0.00	0.00	0.01
Al	5.15	5.13	5.09	5.76	5.35	5.60	6.03	5.21	5.32	5.33	5.32	5.31	5.56	5.43	5.43	5.26	5.46	4.85	5.26	5.24
Fe^{2+}	0.03	0.04	0.02	0.01	0.04	0.00	0.02	0.00	0.02	0.01	0.02	0.01	0.01	0.00	0.01	0.01	0.01	0.04	0.02	0.02
Ca	1.25	1.16	1.26	1.76	1.22	4.32	1.95	1.22	1.23	1.26	1.25	1.20	1.52	1.32	1.27	1.24	1.46	0.72	1.23	1.25
Na	2.60	2.65	2.54	2.10	2.54	0.79	1.81	2.51	2.57	2.46	2.58	2.63	2.26	2.53	2.52	2.49	2.35	3.23	2.60	2.58
K	0.06	0.03	0.07	0.07	0.04	0.02	0.05	0.07	0.03	0.04	0.03	0.02	0.05	0.05	0.04	0.07	0.07	0.02	0.06	0.05
Total	19.92	19.88	19.87	19.96	19.90	20.17	19.89	19.86	19.91	19.85	19.93	19.92	19.89	19.96	19.91	19.86	19.91	20.02	19.93	19.92
Endmembers																				
An	32.05	30.27	32.60	44.73	31.99	84.18	51.15	32.14	32.17	33.45	32.36	31.19	39.63	33.83	33.16	32.62	37.62	18.14	31.55	32.24
Ab	66.49	68.99	65.57	53.51	66.93	15.42	47.56	65.93	67.10	65.51	66.75	68.19	59.03	64.80	65.81	65.56	60.57	81.48	67.00	66.51
Or	1.46	0.74	1.83	1.77	1.08	0.40	1.29	1.92	0.73	1.04	0.89	0.62	1.34	1.37	1.03	1.81	1.80	0.39	1.45	1.25

Table S1.2: Plagioclase microprobe analyses (continuation).

Rock	Monzogabbro																	
Crystal id	1	2	3		4	5	6	7		8		9	10	11		12		13
Comment	Pl	Pl	Pl	Pl	Pl	Pl	Pl	Pl rim	Pl core	Pl rim	Pl core	Pl	Pl	Pl core	Pl rim	Pl rim	Pl core	Pl
SiO_2	55.33	55.42	57.48	58.02	53.81	58.87	56.76	56.31	55.54	55.37	59.16	58.33	57.00	55.48	54.52	57.37	54.50	57.58
TiO_2	0.00	0.04	0.02	0.05	0.04	0.00	0.01	0.00	0.00	0.02	0.00	0.05	0.00	0.00	0.00	0.01	0.03	0.00
Al_2O_3	27.59	27.39	26.14	26.60	27.64	26.56	27.29	27.77	29.10	27.70	26.35	26.29	26.46	28.85	29.19	27.73	28.93	27.00
FeO	0.24	0.10	0.14	0.06	0.00	0.11	0.17	0.06	0.09	0.05	0.10	0.14	0.04	0.11	0.10	0.14	0.16	0.09
CaO	9.71	9.74	7.87	8.19	9.18	8.11	8.33	9.83	10.89	8.96	8.10	7.60	6.51	10.43	10.99	9.42	10.77	8.26
Na_2O	5.62	5.58	6.39	6.40	6.11	6.30	6.05	5.54	4.92	5.90	6.45	6.56	6.74	5.12	4.96	5.60	4.91	6.36
K_2O	0.25	0.21	0.31	0.28	0.14	0.33	0.12	0.24	0.20	0.30	0.31	0.28	0.88	0.18	0.23	0.25	0.21	0.16
BaO	0.00	0.00	0.00	0.28	0.00	0.02	0.05	0.05	0.11	0.00	0.17	0.06	0.00	0.17	0.10	0.00	0.08	0.09
SrO	0.07	0.02	0.07	0.11	0.19	0.10	0.07	0.05	0.09	0.13	0.03	0.10	0.09	0.08	0.07	0.02	0.01	0.08
MgO	0.01	0.02	0.01	0.01	0.00	0.00	0.02	0.01	0.01	0.01	0.00	0.00	0.01	0.00	0.00	0.00	0.00	0.02
MnO	0.10	0.03	0.01	0.00	0.02	0.00	0.02	0.02	0.05	0.00	0.03	0.00	0.02	0.00	0.00	0.00	0.05	0.00
Total	98.93	98.55	98.44	100.00	97.12	100.41	98.89	99.86	100.99	98.44	100.70	99.41	97.74	100.42	100.15	100.52	99.65	99.64
Oxygen number: 32																		
Si	10.08	10.11	10.44	10.41	9.99	10.48	10.27	10.13	9.92	10.11	10.51	10.49	10.43	9.96	9.83	10.22	9.87	10.35
Ti	0.00	0.00	0.00	0.01	0.01	0.00	0.00	0.00	0.00	0.00	0.00	0.01	0.00	0.00	0.00	0.00	0.00	0.00
Al	5.92	5.89	5.60	5.62	6.05	5.57	5.82	5.89	6.13	5.96	5.52	5.57	5.71	6.10	6.20	5.82	6.17	5.72
Fe^{2+}	0.04	0.02	0.02	0.01	0.00	0.02	0.02	0.01	0.01	0.01	0.01	0.02	0.01	0.02	0.01	0.02	0.02	0.01
Ca	1.90	1.90	1.53	1.57	1.82	1.55	1.62	1.89	2.08	1.75	1.54	1.46	1.28	2.01	2.12	1.80	2.09	1.59
Na	1.99	1.97	2.25	2.23	2.20	2.18	2.12	1.93	1.70	2.09	2.22	2.29	2.39	1.78	1.73	1.93	1.72	2.21
K	0.06	0.05	0.07	0.07	0.03	0.08	0.03	0.05	0.05	0.07	0.07	0.06	0.20	0.04	0.05	0.06	0.05	0.04
Total	19.98	19.95	19.92	19.92	20.10	19.86	19.89	19.91	19.89	19.99	19.88	19.90	20.01	19.90	19.96	19.86	19.93	19.92
Endmembers																		
An	48.12	48.47	39.74	40.73	44.98	40.74	42.89	48.81	54.35	44.79	40.19	38.37	32.96	52.38	54.33	47.45	54.12	41.41
Ab	50.41	50.28	58.40	57.59	54.23	57.28	56.36	49.78	44.45	53.43	57.99	59.95	61.77	46.55	44.33	51.06	44.61	57.63
Or	1.47	1.26	1.86	1.68	0.79	1.98	0.75	1.40	1.20	1.79	1.81	1.68	5.28	1.07	1.34	1.49	1.27	0.97

Table S1.3: Clinopyroxene microprobe analyses.

Rock	Monzodiorite												
Crystal id	1		2	3	4	5	6	7	8	9	10	11	12
Comment	Cpx core with Hbl rim	Cpx core with Hbl rim (closer Hbl than last analysis)	Cpx core with Hbl rim	Cpx	Cpx core with Hbl rim	Cpx core with Hbl rim	Cpx core with Hbl rim	Cpx associated with Hbl and Bt	Cpx replaced by Hbl	Cpx replaced by Hbl	Cpx replaced by Hbl	Cpx associated with Hbl and Bt	Cpx associated with Hbl and Bt
SiO_2	54.07	52.49	53.45	51.86	51.90	53.80	53.75	52.48	53.80	53.72	51.74	54.10	52.69
TiO_2	0.19	0.12	0.17	0.22	0.25	0.30	0.26	0.39	0.08	0.19	0.34	0.18	0.52
Al_2O_3	1.14	1.61	1.15	5.22	5.20	3.50	3.76	3.53	1.04	1.09	2.40	1.31	4.33
FeO	9.07	9.60	8.77	11.45	11.43	12.77	12.34	11.86	8.86	9.35	10.08	9.23	12.25
MnO	0.55	0.69	0.59	0.44	0.40	0.43	0.28	0.35	0.76	0.73	0.48	0.78	0.48
MgO	13.45	12.57	13.09	15.94	16.02	16.11	16.12	16.46	13.71	13.54	13.62	13.39	15.76
CaO	23.43	22.45	23.27	12.21	12.14	12.70	12.87	12.87	23.68	23.08	22.11	23.26	13.01
Na_2O	0.48	0.62	0.51	0.59	0.66	0.29	0.37	0.32	0.49	0.52	0.60	0.57	0.63
K_2O	0.00	0.02	0.00	0.23	0.20	0.21	0.25	0.30	0.01	0.02	0.15	0.01	0.37
BaO	0.09	0.00	0.05	0.00	0.02	0.00	0.08	0.08	0.00	0.06	0.09	0.00	0.09
SrO	0.00	0.00	0.00	0.00	0.00	0.00	0.00	0.00	0.00	0.00	0.00	0.00	0.00
Total	102.47	100.18	101.04	98.15	98.22	100.10	100.09	98.65	102.42	102.29	101.63	102.83	100.11
Oxygen number: 6													
Si	1.97	1.96	1.98	1.95	1.95	2.00	1.99	1.97	1.96	1.96	1.90	1.96	1.95
Ti	0.01	0.00	0.00	0.01	0.01	0.01	0.01	0.01	0.00	0.01	0.01	0.00	0.01
Al	0.05	0.07	0.05	0.23	0.23	0.15	0.16	0.16	0.04	0.05	0.10	0.06	0.19
Fe^t	0.28	0.30	0.27	0.36	0.36	0.40	0.38	0.37	0.27	0.29	0.31	0.28	0.38
Mn	0.02	0.02	0.02	0.01	0.01	0.01	0.01	0.01	0.02	0.02	0.01	0.02	0.01
Mg	0.73	0.70	0.72	0.89	0.90	0.89	0.89	0.92	0.74	0.74	0.75	0.72	0.87
Ca	0.92	0.90	0.92	0.49	0.49	0.51	0.51	0.52	0.92	0.90	0.87	0.90	0.52
Na	0.03	0.04	0.04	0.04	0.05	0.02	0.03	0.02	0.03	0.04	0.04	0.04	0.05
K	0.00	0.00	0.00	0.01	0.01	0.01	0.01	0.01	0.00	0.00	0.01	0.00	0.02
Total	4.00	4.00	4.00	4.00	4.00	4.00	4.00	4.00	4.00	4.00	4.00	4.00	4.00
Fe^{2+}	0.25	0.25	0.25	0.45	0.44	0.53	0.51	0.46	0.20	0.23	0.18	0.23	0.44
Fe^{3+}	0.03	0.05	0.02	-0.09	-0.08	-0.14	-0.13	-0.08	0.07	0.06	0.13	0.05	-0.06
$Fe^{2+}/(Fe^{2+}+Fe^{3+})$	0.89	0.84	0.91	1.25	1.23	1.35	1.34	1.22	0.74	0.80	0.58	0.84	1.16
$Fe^{3+}/(Fe^{3+}+Fe^{2+})$	0.11	0.16	0.09	-0.25	-0.23	-0.35	-0.34	-0.22	0.26	0.20	0.42	0.16	-0.16
Endmembers													
Wo	47.20	46.82	47.70	27.92	27.76	27.90	28.44	28.35	47.15	46.39	44.91	46.81	28.95
En	37.70	36.47	37.35	50.71	50.97	49.22	49.56	50.48	37.97	37.86	38.51	37.50	48.82
Fs	15.10	16.71	14.95	21.38	21.27	22.88	22.00	21.16	14.88	15.76	16.58	15.69	22.23

Table S1.3: Clinopyroxene microprobe analyses (continuation).

Rock	Monzodiorite					Monzogabbro							
Crystal id	**13**	**14**	**15**	**16**	**17**	**1**	**2**	**3**	**4**	**5**	**6**	**7**	**8**
Comment	Cpx associated with Hbl and Bt	Cpx associated with Hbl and Bt	Cpx associated with Hbl and Bt	Cpx associated with Hbl and Bt	Cpx with Hbl rim	Cpx inclusion in Opx	Cpx	Cpx	Cpx	Apparently Cpx is replacing Opx and replaced by Hbl	Cpx	Cpx replacing Opx	Cpx
SiO₂	54.66	52.09	54.05	50.32	53.00	51.76	52.97	52.32	51.67	50.66	51.86	52.40	53.07
TiO₂	0.04	0.03	0.11	0.70	0.14	0.19	0.14	0.16	0.16	0.09	0.08	0.20	0.11
Al₂O₃	1.27	0.91	1.07	5.98	0.67	1.68	1.43	1.41	1.60	2.89	1.68	1.65	1.74
FeO	8.96	8.92	8.91	13.70	9.67	9.18	9.02	8.68	9.39	13.04	8.76	8.64	9.38
MnO	0.41	0.62	0.64	0.43	0.57	0.38	0.25	0.41	0.42	0.22	0.28	0.31	0.34
MgO	13.70	13.48	13.23	13.95	13.57	14.20	13.90	14.13	14.02	15.15	13.70	13.73	13.86
CaO	23.36	24.14	23.48	13.74	22.86	23.42	22.76	23.36	22.95	15.31	22.55	22.61	22.44
Na₂O	0.52	0.47	0.52	0.79	0.39	0.43	0.39	0.37	0.42	0.19	0.40	0.48	0.46
K₂O	0.00	0.00	0.01	0.29	0.02	0.00	0.00	0.01	0.00	0.04	0.02	0.02	0.00
BaO	0.15	0.11	0.15	0.00	0.00	0.02	0.00	0.00	0.00	0.12	0.00	0.00	0.05
SrO	0.00	0.00	0.00	0.00	0.00	0.00	0.00	0.00	0.00	0.00	0.00	0.00	0.00
Total	103.07	100.77	102.17	99.90	100.90	101.25	100.85	100.84	100.63	97.69	99.34	100.02	101.45
Oxygen number: 6													
Si	1.98	1.93	1.98	1.88	1.96	1.90	1.96	1.93	1.91	1.94	1.94	1.95	1.95
Ti	0.00	0.00	0.00	0.02	0.00	0.01	0.00	0.00	0.00	0.00	0.00	0.01	0.00
Al	0.05	0.04	0.05	0.26	0.03	0.07	0.06	0.06	0.07	0.13	0.07	0.07	0.08
Feᵗ	0.27	0.28	0.27	0.43	0.30	0.28	0.28	0.27	0.29	0.42	0.27	0.27	0.29
Mn	0.01	0.02	0.02	0.01	0.02	0.01	0.01	0.01	0.01	0.01	0.01	0.01	0.01
Mg	0.74	0.74	0.72	0.78	0.75	0.78	0.76	0.78	0.77	0.86	0.76	0.76	0.76
Ca	0.91	0.96	0.92	0.55	0.91	0.92	0.90	0.92	0.91	0.63	0.90	0.90	0.88
Na	0.04	0.03	0.04	0.06	0.03	0.03	0.03	0.03	0.03	0.01	0.03	0.03	0.03
K	0.00	0.00	0.00	0.01	0.00	0.00	0.00	0.00	0.00	0.00	0.00	0.00	0.00
Total	4.00	4.00	4.00	4.00	4.00	4.00	4.00	4.00	4.00	4.00	4.00	4.00	4.00
Fe²⁺	0.25	0.14	0.24	0.42	0.23	0.13	0.23	0.17	0.16	0.41	0.21	0.21	0.23
Fe³⁺	0.02	0.13	0.03	0.01	0.07	0.15	0.05	0.10	0.13	0.01	0.07	0.06	0.05
Fe²⁺/(Fe²⁺+Fe³⁺)	0.92	0.51	0.89	0.97	0.78	0.48	0.83	0.63	0.55	0.98	0.75	0.79	0.81
Fe³⁺/(Fe³⁺+Fe²⁺)	0.08	0.49	0.11	0.03	0.22	0.52	0.17	0.37	0.45	0.02	0.25	0.21	0.19
Endmembers													
Wo	46.98	48.03	47.59	31.10	46.00	46.32	46.16	46.68	45.86	32.76	46.38	46.46	45.53
En	38.34	37.30	37.32	43.95	37.99	39.09	39.22	39.27	38.98	45.11	39.19	39.26	39.13
Fs	14.68	14.67	15.08	24.95	16.01	14.59	14.62	14.06	15.16	22.13	14.43	14.28	15.34

Table S1.4: Orthopyroxene microprobe analyses.

Rock	Monzogabbro												
Crystal id	1	2	3	4	5	6	7	8	9	10	11	12	13
Comment	Opx	Opx	Opx	Opx	Opx	Opx replaced by Cpx	Opx replaced by Cpx	Opx	Opx	Opx	Opx replaced by Cpx	Opx	Opx
SiO_2	47.63	51.19	51.01	51.76	51.98	50.32	48.12	50.53	52.50	52.69	50.48	52.98	52.03
TiO_2	0.09	0.08	0.13	0.12	0.09	0.13	0.10	0.01	0.08	0.16	0.10	0.11	0.12
Al_2O_3	0.93	0.91	0.92	0.92	0.86	0.93	0.86	1.02	1.02	0.88	0.81	1.04	1.05
FeO	29.16	27.34	27.18	27.10	25.84	26.30	30.71	26.13	25.11	24.19	25.07	26.30	24.98
MnO	0.89	0.76	0.79	0.91	0.79	0.75	0.76	0.87	0.92	0.77	0.75	0.79	0.69
MgO	19.39	20.82	20.93	20.86	20.78	20.30	18.62	19.83	19.90	19.31	19.37	20.98	20.55
CaO	2.29	1.11	0.49	0.51	0.45	0.59	0.50	0.49	0.50	3.07	0.50	0.54	1.04
Na_2O	0.04	0.08	0.03	0.00	0.00	0.00	0.00	0.02	0.02	0.06	0.02	0.05	0.03
K_2O	0.00	0.02	0.01	0.00	0.01	0.00	0.03	0.01	0.02	0.02	0.02	0.00	0.00
BaO	0.00	0.00	0.06	0.00	0.03	0.00	0.00	0.00	0.01	0.15	0.03	0.00	0.00
SrO	0.00	0.00	0.00	0.00	0.00	0.00	0.00	0.00	0.00	0.00	0.00	0.00	0.00
Total	100.43	102.30	101.55	102.19	100.83	99.32	99.71	98.91	100.06	101.29	97.15	102.78	100.48
Oxygen number: 6													
Si	1.81	1.89	1.90	1.92	1.95	1.92	1.85	1.93	1.99	1.97	1.97	1.95	1.95
Ti	0.00	0.00	0.00	0.00	0.00	0.00	0.00	0.00	0.00	0.00	0.00	0.00	0.00
Al	0.04	0.04	0.04	0.04	0.04	0.04	0.04	0.05	0.05	0.04	0.04	0.04	0.05
Fe^t	0.93	0.84	0.85	0.84	0.81	0.84	0.99	0.84	0.79	0.76	0.82	0.81	0.78
Mn	0.03	0.02	0.02	0.03	0.03	0.02	0.02	0.03	0.03	0.02	0.02	0.02	0.02
Mg	1.10	1.15	1.16	1.15	1.16	1.15	1.07	1.13	1.12	1.08	1.13	1.15	1.15
Ca	0.09	0.04	0.02	0.02	0.02	0.02	0.02	0.02	0.02	0.12	0.02	0.02	0.04
Na	0.00	0.01	0.00	0.00	0.00	0.00	0.00	0.00	0.00	0.00	0.00	0.00	0.00
K	0.00	0.00	0.00	0.00	0.00	0.00	0.00	0.00	0.00	0.00	0.00	0.00	0.00
Total	4.00	4.00	4.00	4.00	4.00	4.00	4.00	4.00	4.00	4.00	4.00	4.00	4.00
Fe^{2+}	0.59	0.67	0.69	0.72	0.75	0.72	0.74	0.75	0.81	0.74	0.80	0.75	0.74
Fe^{3+}	0.34	0.18	0.15	0.12	0.06	0.12	0.25	0.09	-0.02	0.02	0.02	0.06	0.05
$Fe^{2+}/(Fe^{2+}+Fe^{3+})$	0.63	0.79	0.82	0.86	0.92	0.86	0.75	0.90	1.02	0.98	0.97	0.93	0.94
$Fe^{3+}/(Fe^{3+}+Fe^{2+})$	0.37	0.21	0.18	0.14	0.08	0.14	0.25	0.10	-0.02	0.02	0.03	0.07	0.06
Endmembers													
Wo	4.39	2.14	0.96	1.00	0.90	1.18	1.00	1.01	1.02	6.21	1.05	1.06	2.10
En	51.81	56.04	56.90	56.69	57.76	56.77	51.33	56.29	57.05	54.39	56.65	57.48	57.65
Fs	43.81	41.82	42.14	42.30	41.34	42.05	47.67	42.70	41.93	39.40	42.30	41.46	40.25

Table S1.5: Hornblende microprobe analyses.

Rock	Quartz monzonite								Monzodiorite			
Cryst al id	1	2	3	4	5	6	7	8	1	2	3	4
Com ment	Hbl	Small Hbl	Hbl	Hbl	Hbl	Hbl	Hbl	Hbl	Hbl rim in Cpx	Hbl rim in Cpx	Hbl rim in Cpx	Hbl
SiO_2	41.96	41.91	42.16	42.89	41.37	42.26	41.76	42.47	45.70	45.36	45.12	45.38
TiO_2	0.72	0.87	1.06	1.16	1.16	1.21	0.79	1.36	1.63	1.33	1.14	1.24
Al_2O_3	10.49	10.13	9.94	10.06	11.23	10.23	11.42	10.60	9.58	9.84	9.73	9.66
FeO	20.41	19.93	18.96	19.17	19.06	18.78	19.88	19.51	15.92	15.55	15.91	16.18
MnO	0.70	0.67	0.80	0.75	0.78	0.70	0.81	0.70	0.37	0.34	0.36	0.34
MgO	8.93	9.37	9.54	9.55	8.80	9.33	8.50	8.99	11.76	11.71	11.53	11.70
CaO	11.66	11.86	11.82	11.62	11.82	11.91	11.89	11.58	12.12	12.38	11.91	12.09
Na_2O	1.41	1.50	1.45	1.45	1.60	1.56	1.53	1.66	1.31	1.21	1.28	1.04
K_2O	1.56	1.50	1.50	1.42	1.60	1.56	1.60	1.55	1.09	1.10	1.07	1.06
BaO	0.00	0.00	0.03	0.10	0.03	0.00	0.10	0.00	0.03	0.11	0.08	0.00
SrO	0.00	0.00	0.00	0.00	0.00	0.00	0.00	0.00	0.00	0.00	0.00	0.00
Total	97.83	97.75	97.26	98.17	97.44	97.53	98.26	98.42	99.50	98.91	98.12	98.70
Oxygen number: 23												
Si	6.36	6.36	6.42	6.44	6.31	6.43	6.33	6.40	6.65	6.65	6.65	6.63
Al^{iv}	1.64	1.64	1.58	1.56	1.69	1.57	1.67	1.60	1.35	1.35	1.35	1.37
T	8.00	8.00	8.00	8.00	8.00	8.00	8.00	8.00	8.00	8.00	8.00	8.00
Al^{vi}	0.23	0.17	0.20	0.23	0.33	0.27	0.37	0.28	0.29	0.35	0.34	0.29
Ti	0.08	0.10	0.12	0.13	0.13	0.14	0.09	0.15	0.18	0.15	0.13	0.14
Cr	0.00	0.00	0.00	0.00	0.00	0.00	0.00	0.00	0.00	0.00	0.00	0.00
Fe^{3+}	0.75	0.69	0.57	0.63	0.44	0.38	0.51	0.49	0.36	0.28	0.44	0.53
Fe^{2+}	1.83	1.84	1.84	1.78	1.99	2.01	2.01	1.96	1.58	1.63	1.52	1.45
Mn	0.09	0.09	0.10	0.10	0.10	0.09	0.10	0.09	0.04	0.04	0.04	0.04
Mg	2.02	2.12	2.16	2.14	2.00	2.12	1.92	2.02	2.55	2.56	2.53	2.55
C	5.00	5.00	5.00	5.00	5.00	5.00	5.00	5.00	5.00	5.00	5.00	5.00
Ca	1.89	1.93	1.93	1.87	1.93	1.94	1.93	1.87	1.89	1.94	1.88	1.89
Na	0.11	0.07	0.07	0.13	0.07	0.06	0.07	0.13	0.11	0.06	0.12	0.11
B	2.00	2.00	2.00	2.00	2.00	2.00	2.00	2.00	2.00	2.00	2.00	2.00
Na	0.30	0.37	0.35	0.29	0.40	0.40	0.38	0.35	0.26	0.29	0.25	0.19
K	0.30	0.29	0.29	0.27	0.31	0.30	0.31	0.30	0.20	0.21	0.20	0.20
A	0.61	0.66	0.65	0.57	0.72	0.71	0.69	0.65	0.46	0.49	0.45	0.38
$Fe^{2+}/(Fe^{2+}+Fe^{3+})$	0.71	0.73	0.76	0.74	0.82	0.84	0.80	0.80	0.82	0.86	0.78	0.73
$Fe^{3+}/(Fe^{3+}+Fe^{2+})$	0.29	0.27	0.24	0.26	0.18	0.16	0.20	0.20	0.18	0.14	0.22	0.27
$Mg/(Mg+Fe^{2+})$	0.52	0.54	0.54	0.55	0.50	0.51	0.49	0.51	0.62	0.61	0.62	0.64
$Fe^{3+}/(Fe^{3+}+Al^{vi})$	0.77	0.80	0.74	0.74	0.57	0.59	0.58	0.64	0.55	0.44	0.57	0.64
Name	Magnesio-hastingsite	Magnesio-hastingsite	Magnesio-hastingsite	Magnesio-hastingsite	Magnesio-hastingsite	Magnesio-hastingsite	Hastingsite	Magnesio-hastingsite	Magnesio-hornblende	Magnesio-hornblende	Magnesio-hornblende	Magnesio-hornblende

Reference: Leake, B.E., Woolley, A.R., Arps, C.E.S., Birch, W.D., Gilbert, M.C., Grice, J.D., Hawthorne, F.C., Kato, A., Kisch, H.J., Krivovichev, V.G., Linthout, K., Laird, J., Mandarino, J., Maresch,W.V., Nickel, E.H., Schumacher, J.C., Smith, D.C., Stephenson, N.C.N., Ungaretti, L.,Whittaker, E.J.W., Youzhi, G. (1978). Nomenclature of amphiboles: report of the subcommittee on amphiboles of the International Mineralogical Association, Commission on New Minerals and Mineral Names. *The Canadian Mineralogist* **35**, 219-246;

Table S1.5: Hornblende microprobe analyses (continuation).

Rock	Monzodiorite													
Crystal id	5	6	7	8	9	10	11	12	13	14	15	16	17	18
Comment	Hbl	Hbl rim in Cpx	Hbl associated with Cpx and Bt	Hbl associated with Cpx and Bt	Hbl associated with Cpx and Bt	Hbl associated with Cpx and Bt	Hbl associated with Cpx and Bt	Hbl associated with Cpx and Bt	Hbl associated with Cpx and Bt	Hbl associated with Cpx and Bt	Hbl associated with Cpx and Bt	Hbl replacing Cpx	Hbl rim in Cpx	Hbl
SiO_2	44.80	45.47	46.00	46.08	44.27	45.71	45.25	45.13	44.87	44.98	46.09	45.75	44.08	43.88
TiO_2	1.38	1.56	1.13	1.40	1.56	1.62	1.48	1.58	1.77	1.56	1.29	1.51	1.34	1.48
Al_2O_3	9.89	10.18	9.53	8.96	9.72	9.85	9.91	9.81	10.41	9.52	9.40	9.56	9.93	10.11
FeO	15.95	16.36	15.98	16.73	15.87	16.58	16.36	15.92	16.28	16.09	16.00	16.35	16.69	16.23
MnO	0.30	0.36	0.34	0.33	0.26	0.33	0.24	0.27	0.32	0.25	0.29	0.46	0.29	0.31
MgO	11.45	11.55	12.07	11.86	11.97	11.81	11.92	11.73	11.57	11.97	12.22	11.96	11.92	11.94
CaO	12.06	12.33	12.48	12.11	12.40	12.08	12.09	12.22	12.19	12.28	12.01	12.28	12.22	12.17
Na_2O	1.29	1.17	1.17	1.08	1.25	1.24	1.27	1.29	1.39	1.20	1.19	1.13	1.22	1.27
K_2O	1.17	1.23	1.07	1.09	1.06	1.20	1.15	1.19	1.19	1.08	1.06	1.08	1.09	1.12
BaO	0.06	0.00	0.00	0.00	0.00	0.00	0.05	0.03	0.00	0.04	0.12	0.00	0.05	0.00
SrO	0.00	0.00	0.00	0.00	0.00	0.00	0.00	0.00	0.00	0.00	0.00	0.00	0.00	0.00
Total	98.35	100.20	99.76	99.63	98.36	100.42	99.71	99.16	99.98	98.95	99.67	100.08	98.82	98.50
Oxygen number: 23														
Si	6.61	6.58	6.66	6.68	6.52	6.58	6.56	6.60	6.51	6.58	6.66	6.61	6.46	6.44
Al^{iv}	1.39	1.42	1.34	1.32	1.48	1.42	1.44	1.40	1.49	1.42	1.34	1.39	1.54	1.56
T	8.00	8.00	8.00	8.00	8.00	8.00	8.00	8.00	8.00	8.00	8.00	8.00	8.00	8.00
Al^{vi}	0.33	0.31	0.29	0.21	0.21	0.25	0.25	0.29	0.29	0.22	0.26	0.23	0.17	0.19
Ti	0.15	0.17	0.12	0.15	0.17	0.18	0.16	0.17	0.19	0.17	0.14	0.16	0.15	0.16
Cr	0.00	0.00	0.00	0.00	0.00	0.00	0.00	0.00	0.00	0.00	0.00	0.00	0.00	0.00
Fe^{3+}	0.36	0.39	0.40	0.53	0.45	0.52	0.55	0.34	0.42	0.47	0.56	0.52	0.69	0.63
Fe^{2+}	1.61	1.59	1.54	1.50	1.50	1.48	1.44	1.60	1.56	1.50	1.38	1.45	1.35	1.36
Mn	0.04	0.04	0.04	0.04	0.03	0.04	0.03	0.03	0.04	0.03	0.04	0.06	0.04	0.04
Mg	2.52	2.49	2.61	2.56	2.63	2.54	2.58	2.56	2.50	2.61	2.63	2.57	2.60	2.61
C	5.00	5.00	5.00	5.00	5.00	5.00	5.00	5.00	5.00	5.00	5.00	5.00	5.00	5.00
Ca	1.91	1.91	1.94	1.88	1.96	1.86	1.88	1.91	1.89	1.92	1.86	1.90	1.92	1.91
Na	0.09	0.09	0.06	0.12	0.04	0.14	0.12	0.09	0.11	0.08	0.14	0.10	0.08	0.09
B	2.00	2.00	2.00	2.00	2.00	2.00	2.00	2.00	2.00	2.00	2.00	2.00	2.00	2.00
Na	0.28	0.24	0.26	0.18	0.31	0.21	0.23	0.28	0.28	0.26	0.19	0.22	0.26	0.28
K	0.22	0.23	0.20	0.20	0.20	0.22	0.21	0.22	0.22	0.20	0.19	0.20	0.20	0.21
A	0.50	0.47	0.46	0.39	0.51	0.43	0.45	0.50	0.50	0.46	0.39	0.42	0.47	0.49
$Fe^{2+}/(Fe^{2+}+Fe^{3+})$	0.82	0.80	0.80	0.74	0.77	0.74	0.72	0.82	0.79	0.76	0.71	0.74	0.66	0.68
$Fe^{3+}/(Fe^{3+}+Fe^{2+})$	0.18	0.20	0.20	0.26	0.23	0.26	0.28	0.18	0.21	0.24	0.29	0.26	0.34	0.32
$Mg/(Mg+Fe^{2+})$	0.61	0.61	0.63	0.63	0.64	0.63	0.64	0.61	0.62	0.64	0.66	0.64	0.66	0.66
$Fe^{3+}/(Fe^{3+}+Al^{vi})$	0.53	0.55	0.58	0.71	0.68	0.67	0.69	0.54	0.59	0.68	0.68	0.69	0.80	0.77
Name	Magnesio-hornblende	Magnesio-hornblende	Magnesio-hornblende	Magnesio-hornblende	Edenite	Magnesio-hornblende	Magnesio-hornblende	Edenite	Edenite	Magnesio-hornblende	Magnesio-hornblende	Magnesio-hornblende	Tschermakite	Tschermakite

Reference: Leake, B.E., Woolley, A.R., Arps, C.E.S., Birch, W.D., Gilbert, M.C., Grice, J.D., Hawthorne, F.C., Kato, A., Kisch, H.J., Krivovichev, V.G., Linthout, K., Laird, J., Mandarino, J., Maresch,W.V., Nickel, E.H., Schumacher, J.C., Smith, D.C., Stephenson, N.C.N., Ungaretti, L.,Whittaker, E.J.W., Youzhi, G. (1978). Nomenclature of amphiboles: report of the subcommittee on amphiboles of the International Mineralogical Association, Commission on New Minerals and Mineral Names. *The Canadian Mineralogist* 35, 219–246;

Table S1.5: Hornblende microprobe analyses (continuation).

Rock	Monzodiorite										
Crystal id	19	20	21	22	23	24	25	26	27	28	29
Comment	Hbl rim in Cpx	Hbl rim in Cpx	Hbl associated with Cpx and Bt	Hbl associated with Cpx and Bt	Hbl associated with Cpx and Bt	Hbl associated with Cpx and Bt	Hbl associated with Cpx and Bt	Hbl associated with Cpx and Bt	Hbl associated with Cpx and Bt	Hbl	Hbl
SiO₂	45.30	44.77	45.80	45.70	44.13	44.23	45.07	49.75	43.65	43.96	44.69
TiO₂	1.40	1.64	1.54	1.61	1.18	1.61	1.52	0.86	1.60	1.71	1.08
Al₂O₃	9.76	10.32	9.86	9.55	9.56	10.05	9.95	5.64	9.62	10.56	9.63
FeO	15.82	16.95	15.99	16.19	15.70	16.48	16.44	13.16	15.89	16.74	15.18
MnO	0.33	0.28	0.37	0.31	0.34	0.32	0.31	0.39	0.30	0.42	0.41
MgO	11.79	11.59	11.81	11.95	11.79	11.51	11.83	13.05	11.69	11.37	12.41
CaO	12.11	12.36	12.20	12.17	12.30	12.14	12.20	16.54	12.27	12.20	11.92
Na₂O	1.40	1.21	1.31	1.34	1.02	1.34	1.26	0.87	1.35	1.24	1.10
K₂O	1.06	1.16	1.11	1.13	1.01	1.11	1.13	0.59	1.06	1.17	1.01
BaO	0.00	0.00	0.14	0.12	0.00	0.05	0.00	0.00	0.14	0.00	0.14
SrO	0.00	0.00	0.00	0.00	0.00	0.00	0.00	0.00	0.00	0.00	0.00
Total	98.96	100.28	100.12	100.08	97.02	98.84	99.71	100.84	97.56	99.34	97.54
Oxygen number: 23											
Si	6.62	6.48	6.62	6.62	6.57	6.50	6.54	7.13	6.51	6.42	6.57
Alⁱᵛ	1.38	1.52	1.38	1.38	1.43	1.50	1.46	0.87	1.49	1.58	1.43
T	8.00	8.00	8.00	8.00	8.00	8.00	8.00	8.00	8.00	8.00	8.00
Alᵛⁱ	0.30	0.24	0.31	0.25	0.25	0.24	0.24	0.08	0.20	0.24	0.24
Ti	0.15	0.18	0.17	0.18	0.13	0.18	0.17	0.09	0.18	0.19	0.12
Cr	0.00	0.00	0.00	0.00	0.00	0.00	0.00	0.00	0.00	0.00	0.00
Fe³⁺	0.38	0.54	0.38	0.43	0.50	0.50	0.53	0.00	0.42	0.58	0.69
Fe²⁺	1.55	1.51	1.55	1.53	1.46	1.53	1.47	1.58	1.56	1.47	1.18
Mn	0.04	0.03	0.05	0.04	0.04	0.04	0.04	0.05	0.04	0.05	0.05
Mg	2.57	2.50	2.55	2.58	2.62	2.52	2.56	2.79	2.60	2.48	2.72
C	5.00	5.00	5.00	5.00	5.00	5.00	5.00	4.59	5.00	5.00	5.00
Ca	1.90	1.92	1.89	1.89	1.96	1.91	1.90	2.54	1.96	1.91	1.88
Na	0.10	0.08	0.11	0.11	0.04	0.09	0.10	-0.54	0.04	0.09	0.12
B	2.00	2.00	2.00	2.00	2.00	2.00	2.00	2.00	2.00	2.00	2.00
Na	0.29	0.25	0.26	0.26	0.26	0.29	0.25	0.78	0.35	0.26	0.19
K	0.20	0.21	0.20	0.21	0.19	0.21	0.21	0.11	0.20	0.22	0.19
A	0.49	0.47	0.46	0.47	0.45	0.50	0.46	0.89	0.55	0.48	0.38
Fe²⁺/(Fe²⁺+Fe³⁺)	0.80	0.73	0.80	0.78	0.74	0.75	0.74	1.93	0.79	0.72	0.63
Fe³⁺/(Fe³⁺+Fe²⁺)	0.20	0.27	0.20	0.22	0.26	0.25	0.26	-0.93	0.21	0.28	0.37
Mg/(Mg+Fe²⁺)	0.62	0.62	0.62	0.63	0.64	0.62	0.64	0.64	0.62	0.63	0.70
Fe³⁺/(Fe³⁺+Alᵛⁱ)	0.56	0.70	0.56	0.63	0.66	0.68	0.69	0.00	0.67	0.71	0.74
Name	Magnesio-hornblende	Tscher makite	Magnesio-hornblende	Magnesio-hornblende	Magnesio-hornblende	Tscher makite	Magnesio-hornblende	Edeni te	Edeni te	Tscher makite	Magnesio-hornblende

Reference: Leake, B.E., Woolley, A.R., Arps, C.E.S., Birch, W.D., Gilbert, M.C., Grice, J.D., Hawthorne, F.C., Kato, A., Kisch, H.J., Krivovichev, V.G., Linthout, K., Laird, J., Mandarino, J., Maresch,W.V., Nickel, E.H., Schumacher, J.C., Smith, D.C., Stephenson, N.C.N., Ungaretti, L.,Whittaker, E.J.W., Youzhi, G. (1978). Nomenclature of amphiboles: report of the subcommittee on amphiboles of the International Mineralogical Association, Commission on New Minerals and Mineral Names. *The Canadian Mineralogist* **35**, 219–246;

Table S1.6: Biotite microprobe analyses.

Rock	Quartz monzonite																
Crystal id	1	2	3	4	5	6	7	8	9	10	11	12	13	14	15	16	17
Comment	Bt core	Bt rim	Bt rim	Darker Bt	Lighter Bt	Lighter Bt	Bt	Bt	Bt	Bt	Bt	Bt	Bt	Bt	Bt	Lighter Bt	Darker Bt
SiO_2	37.28	37.37	37.93	37.59	37.09	37.82	36.51	37.39	37.61	37.71	37.04	37.69	37.28	37.29	38.18	37.42	37.91
TiO_2	1.80	1.90	1.41	2.01	2.70	2.47	1.79	2.10	2.53	2.03	2.13	2.14	2.29	2.05	2.24	2.46	1.86
Al_2O_3	13.87	13.87	14.00	14.20	14.31	14.63	13.88	14.43	14.13	14.60	14.43	14.51	14.24	14.36	14.66	14.71	14.84
FeO	17.94	18.29	17.83	18.51	19.23	18.53	18.75	19.35	19.31	18.79	18.78	18.71	18.67	19.32	18.79	19.26	19.24
MnO	0.55	0.57	0.52	0.55	0.60	0.48	0.55	0.51	0.52	0.46	0.52	0.55	0.51	0.50	0.49	0.56	0.49
MgO	12.95	13.02	12.94	12.80	12.41	12.42	12.83	12.37	12.39	12.76	12.60	13.04	12.60	12.42	12.48	11.86	12.14
CaO	0.04	0.02	0.16	0.04	0.03	0.00	0.03	0.04	0.04	0.05	0.01	0.02	0.03	0.04	0.02	0.05	0.06
Na_2O	0.07	0.05	0.04	0.08	0.08	0.08	0.10	0.08	0.10	0.05	0.10	0.07	0.04	0.11	0.08	0.07	0.13
K_2O	9.73	9.49	9.19	9.57	9.72	9.70	9.52	9.55	9.35	9.47	9.31	9.74	8.98	9.35	9.77	9.50	9.28
BaO	0.08	0.19	0.39	0.42	0.34	0.15	0.48	0.27	0.38	0.32	0.32	0.14	0.07	0.27	0.30	0.34	0.34
SrO	0.00	0.00	0.00	0.00	0.00	0.00	0.00	0.00	0.00	0.00	0.00	0.00	0.00	0.00	0.00	0.00	0.00
Total	94.33	94.76	94.40	95.78	96.50	96.28	94.43	96.09	96.40	96.25	95.23	96.61	94.71	95.70	97.01	96.24	96.28
Oxygen number: 22																	
Si	5.74	5.73	5.82	5.72	5.63	5.70	5.67	5.68	5.70	5.70	5.67	5.68	5.70	5.69	5.73	5.68	5.73
Al^{iv}	2.26	2.27	2.18	2.28	2.37	2.30	2.33	2.32	2.30	2.30	2.33	2.32	2.30	2.31	2.27	2.32	2.27
Al^{vi}	0.26	0.24	0.35	0.27	0.19	0.30	0.21	0.27	0.22	0.30	0.27	0.25	0.27	0.27	0.32	0.31	0.37
Ti	0.21	0.22	0.16	0.23	0.31	0.28	0.21	0.24	0.29	0.23	0.25	0.24	0.26	0.24	0.25	0.28	0.21
Fe^{2+}	2.31	2.35	2.29	2.36	2.44	2.34	2.43	2.46	2.45	2.37	2.40	2.36	2.39	2.46	2.36	2.44	2.43
Mn	0.07	0.07	0.07	0.07	0.08	0.06	0.07	0.07	0.07	0.06	0.07	0.07	0.07	0.07	0.06	0.07	0.06
Mg	2.97	2.98	2.96	2.90	2.81	2.79	2.97	2.80	2.80	2.88	2.87	2.93	2.87	2.82	2.79	2.68	2.74
Ca	0.01	0.00	0.03	0.01	0.00	0.00	0.01	0.01	0.01	0.01	0.00	0.00	0.00	0.01	0.00	0.01	0.01
Na	0.02	0.02	0.01	0.02	0.02	0.02	0.03	0.02	0.04	0.02	0.03	0.02	0.01	0.03	0.02	0.02	0.04
K	1.91	1.86	1.80	1.86	1.88	1.87	1.88	1.81	1.81	1.83	1.82	1.87	1.75	1.82	1.87	1.84	1.79
Total	15.76	15.73	15.66	15.72	15.73	15.66	15.81	15.72	15.67	15.69	15.71	15.74	15.63	15.71	15.67	15.66	15.65
Mg	2.97	2.98	2.96	2.90	2.81	2.79	2.97	2.80	2.80	2.88	2.87	2.93	2.87	2.82	2.79	2.68	2.74
Fe+Mg	2.38	2.42	2.35	2.43	2.52	2.40	2.51	2.53	2.51	2.43	2.47	2.43	2.45	2.53	2.42	2.52	2.49
$Al^{vi}+Fe^{3+}+Ti$	0.46	0.46	0.51	0.50	0.50	0.58	0.42	0.51	0.51	0.53	0.52	0.49	0.53	0.50	0.57	0.59	0.58

Table S1.6: Biotite microprobe analyses (continuation).

Rock	Monzodiorite														
Crystal id	1	2	3	4	5	6	7	8	9	10	11	12	13	14	15
Comment	Bt	Bt	Bt	Bt	Bt	Bt Inclusion in other Bt	Bt	Bt associated with Cpx and Hbl	Bt	Bt	Bt	Bt associated with Cpx and Hbl	Bt associated with Cpx and Hbl	Bt	Bt
SiO_2	36.50	36.65	35.86	37.09	37.02	37.01	37.13	37.56	37.52	36.62	36.61	35.76	37.92	36.08	36.76
TiO_2	4.49	4.44	4.89	4.56	4.32	4.85	4.91	4.68	5.49	4.39	4.67	4.72	4.56	5.02	4.85
Al_2O_3	14.84	14.45	14.07	14.14	14.21	14.21	14.49	14.59	14.79	14.89	14.43	14.38	14.81	14.47	14.72
FeO	17.41	17.85	18.29	17.60	18.13	17.58	18.04	17.88	17.82	19.48	17.77	17.37	17.95	17.73	18.07
MnO	0.20	0.10	0.09	0.12	0.06	0.16	0.17	0.12	0.12	0.22	0.14	0.16	0.07	0.14	0.19
MgO	12.44	12.68	12.75	12.72	12.56	12.42	12.80	12.77	13.02	13.24	13.33	13.25	13.06	12.87	12.78
CaO	0.00	0.02	0.74	0.04	0.04	0.00	0.07	0.11	0.01	0.09	0.03	0.06	0.02	0.05	0.12
Na_2O	0.12	0.05	0.17	0.09	0.10	0.11	0.11	0.11	0.06	0.10	0.11	0.09	0.09	0.09	0.10
K_2O	9.43	9.43	7.05	9.38	9.41	9.29	9.52	9.45	9.30	7.99	9.00	8.89	9.20	9.39	9.10
BaO	0.68	0.78	0.66	0.55	0.80	0.79	1.03	0.87	1.27	0.73	1.05	0.98	1.04	1.06	1.11
SrO	0.00	0.00	0.00	0.00	0.00	0.00	0.00	0.00	0.00	0.00	0.00	0.00	0.00	0.00	0.00
Total	96.10	96.43	94.58	96.29	96.65	96.43	98.26	98.15	99.39	97.74	97.14	95.65	98.71	96.89	97.78
Oxygen number: 22															
Si	5.52	5.54	5.49	5.59	5.59	5.58	5.53	5.57	5.51	5.46	5.50	5.45	5.58	5.45	5.50
Al^{iv}	2.48	2.46	2.51	2.41	2.41	2.42	2.47	2.43	2.49	2.54	2.50	2.55	2.42	2.55	2.50
Al^{vi}	0.17	0.12	0.02	0.10	0.12	0.11	0.07	0.12	0.07	0.07	0.05	0.04	0.15	0.03	0.09
Ti	0.51	0.50	0.56	0.52	0.49	0.55	0.55	0.52	0.61	0.49	0.53	0.54	0.51	0.57	0.54
Fe^{2+}	2.20	2.26	2.34	2.22	2.29	2.22	2.25	2.22	2.19	2.43	2.23	2.21	2.21	2.24	2.26
Mn	0.03	0.01	0.01	0.02	0.01	0.02	0.02	0.02	0.02	0.03	0.02	0.02	0.01	0.02	0.02
Mg	2.81	2.86	2.91	2.86	2.83	2.79	2.84	2.82	2.85	2.94	2.98	3.01	2.87	2.90	2.85
Ca	0.00	0.00	0.12	0.01	0.01	0.00	0.01	0.02	0.00	0.01	0.00	0.01	0.00	0.01	0.02
Na	0.04	0.01	0.05	0.03	0.03	0.03	0.03	0.03	0.02	0.03	0.03	0.03	0.03	0.03	0.03
K	1.82	1.82	1.38	1.80	1.81	1.79	1.81	1.79	1.74	1.52	1.73	1.73	1.73	1.81	1.74
Total	15.57	15.58	15.39	15.55	15.58	15.51	15.57	15.54	15.48	15.52	15.58	15.59	15.50	15.60	15.54
Mg	2.81	2.86	2.91	2.86	2.83	2.79	2.84	2.82	2.85	2.94	2.98	3.01	2.87	2.90	2.85
Fe+Mg	2.23	2.27	2.35	2.23	2.30	2.24	2.27	2.23	2.20	2.46	2.25	2.24	2.22	2.26	2.28
$Al^{vi}+Fe^{3+}+Ti$	0.68	0.62	0.59	0.62	0.61	0.66	0.62	0.65	0.67	0.56	0.58	0.58	0.66	0.60	0.63

Table S1.6: Biotite microprobe analyses (continuation).

Rock	Monzogabbro										
Crystal id	1	2	3	4	5	6	7	8	9	10	11
Comment	Bt	Bt replacing Cpx and Opx	Bt	Bt	Bt replacing Cpx and Opx	Bt	Bt	Bt associated with Opx and Cpx	Bt associated with Opx and Cpx	Bt	Bt
SiO_2	36.62	37.22	37.00	37.21	37.65	37.25	37.46	37.11	36.88	36.39	38.49
TiO_2	5.07	4.45	4.76	4.82	5.00	4.84	4.41	4.83	4.96	5.06	4.05
Al_2O_3	14.37	14.45	14.43	15.48	14.52	14.61	15.06	14.57	14.36	14.04	15.03
FeO	16.51	16.27	15.58	16.01	15.90	16.28	15.14	15.85	16.06	16.08	14.04
MnO	0.11	0.11	0.11	0.02	0.18	0.05	0.03	0.09	0.09	0.09	0.06
MgO	14.01	14.52	14.62	12.28	14.14	13.97	15.23	14.14	14.00	13.89	14.94
CaO	0.02	0.13	0.07	0.22	0.06	0.10	0.07	0.05	0.05	0.05	0.01
Na_2O	0.03	0.03	0.05	0.04	0.03	0.04	0.03	0.07	0.05	0.05	0.04
K_2O	9.26	9.24	9.63	9.66	9.70	9.48	9.79	9.77	9.87	9.79	10.03
BaO	0.85	0.67	0.84	0.64	0.46	0.80	0.74	0.91	0.74	0.74	0.24
SrO	0.00	0.00	0.00	0.00	0.00	0.00	0.00	0.00	0.00	0.00	0.00
Total	96.84	97.09	97.08	96.37	97.62	97.41	97.95	97.38	97.06	96.17	96.93
Oxygen number: 22											
Si	5.48	5.53	5.51	5.56	5.55	5.53	5.50	5.52	5.51	5.49	5.64
Al^{iv}	2.52	2.47	2.49	2.44	2.45	2.47	2.50	2.48	2.49	2.50	2.36
Al^{vi}	0.02	0.06	0.04	0.29	0.07	0.08	0.10	0.07	0.03	0.00	0.24
Ti	0.57	0.50	0.53	0.54	0.55	0.54	0.49	0.54	0.56	0.57	0.45
Fe^{2+}	2.07	2.02	1.94	2.00	1.96	2.02	1.86	1.97	2.00	2.03	1.72
Mn	0.01	0.01	0.01	0.00	0.02	0.01	0.00	0.01	0.01	0.01	0.01
Mg	3.13	3.21	3.24	2.74	3.11	3.09	3.33	3.13	3.12	3.13	3.26
Ca	0.00	0.02	0.01	0.04	0.01	0.02	0.01	0.01	0.01	0.01	0.00
Na	0.01	0.01	0.01	0.01	0.01	0.01	0.01	0.02	0.01	0.02	0.01
K	1.77	1.75	1.83	1.84	1.82	1.79	1.83	1.85	1.88	1.88	1.87
Total	15.57	15.59	15.62	15.46	15.55	15.56	15.63	15.60	15.62	15.63	15.56
Mg	3.13	3.21	3.24	2.74	3.11	3.09	3.33	3.13	3.12	3.13	3.26
Fe+Mg	2.08	2.03	1.95	2.00	1.98	2.03	1.86	1.98	2.02	2.04	1.73
$Al^{vi}+Fe^{3+}+Ti$	0.59	0.56	0.57	0.83	0.62	0.62	0.59	0.61	0.59	0.57	0.68

Table S1.7: Magnetite and ilmenite microprobe analyses.

Rock	Quartz monzonite								Monzodiorite			
Crystal id	1	2	3	4	1	2	5	6	1	2	1	3
Comment			Surrounded by Ttn	Surrounded by Ttn and associated with Ilm	Surrounded by Ttn and associated with Mag	Surrounded by Ttn	Surrounded by Ttn	Surrounded by Ttn		Inclusion in Cpx	Inclusion in Bt	Associated with Mag
Mineral	Mag	Mag	Mag	Mag	Ilm	Ilm	Mag	Mag	Ilm	Ilm	Mag	Ilm
SiO_2	0.01	0.02	0.03	0.11	0.05	0.03	0.03	0.06	0.05	3.73	0.06	0.14
TiO_2	0.06	0.01	0.11	4.04	51.57	47.66	0.31	0.22	47.84	45.64	0.00	51.46
Al_2O_3	0.10	0.13	0.09	0.00	0.00	0.01	0.23	0.22	0.00	0.06	0.09	0.03
FeO	91.26	91.60	89.44	83.53	41.32	46.74	90.68	90.51	49.04	45.88	92.59	47.87
MnO	0.18	0.20	0.11	0.04	7.06	3.93	0.15	0.22	2.02	1.47	0.01	2.67
MgO	0.02	0.00	0.00	0.02	0.01	0.03	0.04	0.05	0.06	1.34	0.01	0.04
CaO	0.00	0.03	0.04	0.31	0.25	0.31	0.21	0.08	0.00	1.90	0.00	0.21
K_2O	0.01	0.02	0.01	0.00	0.01	0.01	0.01	0.00	0.00	0.01	0.00	0.01
Na_2O	0.02	0.00	0.10	0.03	0.00	0.00	0.00	0.00	0.00	0.00	0.05	0.00
BaO	0.04	0.00	0.00	0.22	0.08	0.09	0.00	0.15	0.05	0.00	0.04	0.00
SrO	0.04	0.00	0.00	0.00	0.00	0.02	0.00	0.00	0.01	0.00	0.00	0.04
Total	91.74	92.01	89.93	88.30	100.35	98.82	91.65	91.51	99.07	100.03	92.84	102.47
Oxygen number: 32 for magnetite and 6 for ilmenite												
Si	0.00	0.01	0.01	0.04	0.00	0.00	0.01	0.02	0.00	0.18	0.02	0.01
Ti	0.01	0.00	0.03	0.99	1.95	1.82	0.07	0.05	1.83	1.68	0.00	1.90
Al	0.04	0.05	0.03	0.00	0.00	0.00	0.08	0.08	0.00	0.00	0.03	0.00
Fe^{3+}	15.93	15.93	15.89	13.94	0.10	0.35	15.75	15.78	0.34	0.27	15.93	0.18
Fe^{2+}	7.96	7.95	7.99	8.90	1.64	1.64	7.96	7.96	1.74	1.60	8.01	1.78
Mn	0.05	0.05	0.03	0.01	0.30	0.17	0.04	0.06	0.09	0.06	0.00	0.11
Mg	0.01	0.00	0.00	0.01	0.00	0.00	0.02	0.03	0.00	0.10	0.01	0.00
Ca	0.00	0.01	0.01	0.11	0.01	0.02	0.07	0.03	0.00	0.10	0.00	0.01
Total	24	24	24	24	4	4	24	24	4	4	24	4
$Fe^{2+}/(Fe^{2+}+Fe^{3+})$	0.33	0.33	0.33	0.39	0.94	0.82	0.34	0.34	0.83	0.85	0.33	0.91
$Fe^{3+}/(Fe^{3+}+Fe^{2+})$	0.67	0.67	0.67	0.61	0.06	0.18	0.66	0.66	0.17	0.15	0.67	0.09

Table S1.7: Magnetite and ilmenite microprobe analyses (continuation).

Rock	Monzodiorite					Monzogabbro								
Crystal id	2	4	5	3	6	1	2	3	1	2	4	3	5	4
Comment	Associated with Ilm		Associated with Mag	Associated with Ilm		Inclusion in Opx	Inclusion in Opx	Inclusion in Opx			Associated with Ilm	Associated with Mag	Associated with Ilm	Associated with Mag
Mineral	Mag	Ilm	Ilm	Mag	Ilm	Mag	Mag	Mag	Ilm	Ilm	Mag	Ilm	Mag	Ilm
SiO_2	0.10	0.04	0.15	0.05	0.01	4.00	3.10	2.02	0.01	0.02	0.08	0.05	0.07	0.02
TiO_2	0.21	48.98	51.14	0.14	45.02	3.16	4.12	1.21	47.19	47.71	0.50	49.12	0.32	50.02
Al_2O_3	0.16	0.02	0.01	0.00	0.01	0.63	2.01	2.62	0.03	0.04	0.09	0.03	0.26	0.03
FeO	94.05	52.01	49.35	94.42	53.98	84.24	79.32	84.18	53.01	51.61	92.48	49.19	91.30	49.11
MnO	0.07	1.81	2.35	0.00	1.94	0.41	0.51	0.14	0.58	0.73	0.05	0.98	0.00	0.65
MgO	0.00	0.03	0.05	0.01	0.09	1.86	1.08	1.32	0.40	0.46	0.03	0.34	0.05	0.58
CaO	0.01	0.04	0.02	0.00	0.01	0.11	2.08	0.15	0.01	0.02	0.01	0.02	0.00	0.00
K_2O	0.00	0.00	0.03	0.00	0.00	0.01	0.00	0.01	0.01	0.01	0.02	0.02	0.02	0.00
Na_2O	0.00	0.02	0.00	0.02	0.00	0.00	0.06	0.00	0.00	0.02	0.03	0.00	0.02	0.00
BaO	0.00	0.16	0.26	0.01	0.31	0.07	0.12	0.08	0.21	0.08	0.00	0.11	0.10	0.00
SrO	0.00	0.00	0.01	0.00	0.00	0.00	0.02	0.02	0.00	0.02	0.01	0.00	0.00	0.02
Total	94.60	103.10	103.36	94.65	101.36	94.49	92.39	91.74	101.46	100.72	93.31	99.86	92.14	100.43
Oxygen number: 32 for magnetite and 6 for ilmenite														
Si	0.03	0.00	0.01	0.01	0.00	1.19	0.94	0.62	0.00	0.00	0.03	0.00	0.02	0.00
Ti	0.05	1.80	1.88	0.03	1.68	0.71	0.94	0.28	1.75	1.78	0.12	1.86	0.08	1.88
Al	0.06	0.00	0.00	0.00	0.00	0.22	0.72	0.94	0.00	0.00	0.03	0.00	0.10	0.00
Fe^{3+}	15.78	0.40	0.23	15.91	0.65	11.99	11.52	13.27	0.49	0.43	15.68	0.28	15.71	0.24
Fe^{2+}	8.06	1.72	1.78	8.04	1.59	8.94	8.59	8.21	1.70	1.72	8.11	1.79	8.07	1.81
Mn	0.02	0.07	0.10	0.00	0.08	0.10	0.13	0.04	0.02	0.03	0.01	0.04	0.00	0.03
Mg	0.00	0.00	0.00	0.00	0.01	0.82	0.49	0.60	0.03	0.03	0.01	0.03	0.02	0.04
Ca	0.00	0.00	0.00	0.00	0.00	0.04	0.67	0.05	0.00	0.00	0.00	0.00	0.00	0.00
Total	24	4	4	24	4	24	24	24	4	4	24	4	24	4
$Fe^{2+}/(Fe^{2+}+Fe^{3+})$	0.34	0.81	0.89	0.34	0.71	0.43	0.43	0.38	0.78	0.80	0.34	0.87	0.34	0.88
$Fe^{3+}/(Fe^{3+}/Fe^{2+})$	0.66	0.19	0.11	0.66	0.29	0.57	0.57	0.62	0.22	0.20	0.66	0.13	0.66	0.12

5.2. SUPPLEMENTARY MATERIAL 2 - Whole-rock geochemistry

Table S2.1: Whole-rock analyses from ACIC main rocks (Aranda et al. 2020).

Sample	P 246-A	P 276-A	P 292-B	P 292-A	P 277-A	P 193-B	P 156-A	P 197-C	P 288
Rock	Mzg	Mzg	Mzd	Mzg	Mzd	Jot	Mzd	Q Mag	Q Moz
Major Elements									
SiO$_2$	49.4	50.42	51.17	51.36	52.35	53.29	54.99	55.7	59.68
TiO$_2$	2.6	2.97	2.71	2.97	2.34	2.43	2.53	1.67	1.18
Fe$_2$O$_3$	11.59	12.42	11.92	11.22	10.06	10.89	10.73	9.09	7.07
Al$_2$O$_3$	15.33	15.31	16.8	14.51	16.13	13.79	14.96	15.92	15.76
MgO	6.3	3.71	3.38	4.68	3.05	2.66	3.93	2.04	1.41
MnO	0.17	0.19	0.18	0.17	0.15	0.2	0.15	0.08	0.12
CaO	8.46	7.33	6.49	7.76	6.34	5.78	6.59	4.91	4.11
K$_2$O	1.98	2.47	3.95	2.37	3.12	3.43	2.95	3.52	3.9
Na$_2$O	3.16	3.21	3.85	3.14	3.4	2.9	2.94	3.76	3.43
P$_2$O$_5$	1.15	1.36	1.18	1.32	1.07	1.12	1.11	0.71	0.49
Cr$_2$O$_3$	0.02	<0,01	<0,01	<0,01	<0,01	<0,01	<0,01	<0,01	<0,01
LOI	0.2	0.14	0.14	0.64	1.48	0.26	0.33	1.08	0.09
Sum	100.36	99.53	101.77	100.14	99.49	96.75	101.21	98.48	97.24
Trace Elements									
Ni	88	36	12	50	21	10	30	11	10
Co	36.3	30.3	24.4	70.7	21.4	23.9	22	16.4	9.5
Rb	39.6	36.5	77.5	52.5	77.2	78.8	78	81	80.3
Ba	1980	2482	4081	2435	2960	2609	1964	2875	4492
Sr	1238	818	1171	1156	1150	824	879	993	1003
Zr	352	556	701	595	628	489	446	1019	837
Nb	21.47	33.16	34.61	29.06	26.96	31.32	23.69	14.73	20.54
Y	30.76	45.24	42.86	36.55	31.52	37.94	31.74	26.23	30.48
Ta	0.6	0.88	0.92	1.02	0.81	0.91	0.64	<0,05	0.18
Hf	7.48	11.81	13.94	15.2	13.21	11.59	9.94	21.91	18.41
Th	4.2	2.2	4.7	5.7	7.8	5.4	9.9	5	9.3
U	0.77	0.33	0.8	0.92	1.48	0.6	1.32	0.99	0.76
Zn	130	174	168	148	138	149	131	139	156
V	229	227	191	224	160	205	235	135	80
Cs	0.52	0.39	0.6	0.34	1.69	0.43	1.37	0.91	0.69
Cu	33	19	20	29	21	18	17	17	16
Ga	18.5	21.3	24	21.5	21	21.2	20.9	25	22.8
Mo	<2	<2	<2	2	<2	<2	<2	<2	<2
Sn	<0,3	<0,3	<0,3	<0,3	<0,3	<0,3	<0,3	<0,3	<0,3
Tl	<0,5	<0,5	<0,5	<0,5	<0,5	<0,5	<0,5	<0,5	<0,5
W	1.4	1.6	2.9	213	2.2	1.4	1.3	1.3	3
Rare-earth Elements									
La	93.3	113.4	145.3	130.1	109.2	110.3	86.7	121.8	150.2
Ce	191.1	250.4	297	265	228.9	230.3	178.7	241.6	299.4
Pr	22.59	31.22	35.66	30.87	27.05	27.76	21.71	27.11	34.48
Nd	87.3	128	135.7	120.6	102.3	110.7	86.5	100.3	128.2
Sm	15.2	22.8	21.9	19.7	17.4	18.6	15.3	15.5	19.8
Eu	3.52	4.52	5.08	4.51	4.02	4.33	3.53	3.88	4.95
Gd	11.53	16.93	16.05	13.98	12.24	13.72	11.66	10.51	13.01
Tb	1.36	2.02	1.88	1.66	1.44	1.71	1.41	1.21	1.45
Dy	6.94	10.58	9.82	8.22	7.05	8.73	7.22	5.9	7.16
Ho	1.2	1.8	1.69	1.39	1.21	1.43	1.24	0.97	1.18
Er	3.16	4.62	4.31	3.67	3.24	3.88	3.3	2.59	3.09
Tm	0.4	0.56	0.55	0.46	0.4	0.52	0.41	0.33	0.38
Yb	2.5	3.5	3.3	3	2.5	3.1	2.5	2.1	2.3
Lu	0.36	0.5	0.48	0.42	0.35	0.44	0.36	0.31	0.34

Table S2.1: Whole-rock analyses from ACIC main rocks (Aranda et al. 2020) (continuation).

Sample	P 295-B	P 285-B	P 206-D	P 98	P 297	P 296	P 146-B	P 291	P 298	P 90-A	P 102
Rock	Q Moz	Q Moz	Q Moz	Q Moz	Q Moz	Q Moz	Q Moz	Q Moz	Q Moz	Q Moz	Q Moz
Major Elements											
SiO$_2$	62.28	62.37	62.81	63.65	65.27	65.43	66.65	66.71	66.77	66.86	69.08
TiO$_2$	1.55	1.15	0.9	1.07	0.86	1.33	0.94	1.07	0.6	0.69	1.01
Fe$_2$O$_3$	7.96	6.62	5.21	5.24	4.13	6.86	5.36	5.35	4.05	3.97	5.3
Al$_2$O$_3$	14.32	15.09	15.8	14.96	16.06	14.58	14.39	14.5	16.29	14.44	13.79
MgO	1.73	1.4	1.02	1.33	1	1.53	1.17	1.22	0.72	0.77	1.2
MnO	0.12	0.12	0.1	0.08	0.06	0.11	0.09	0.09	0.07	0.08	0.09
CaO	4.05	3.69	4.07	3.36	2.67	3.6	2.98	3.07	2.87	2.17	2.67
K$_2$O	3.57	4.57	4.12	5.15	6.01	4.69	5	4.98	4.62	5.69	4.87
Na$_2$O	3.45	3.17	3.37	3.21	3.43	3.05	3.11	3.25	3.78	3.19	3.13
P$_2$O$_5$	0.52	0.47	0.35	0.41	0.31	0.49	0.37	0.39	0.21	0.26	0.34
Cr$_2$O$_3$	<0,01	<0,01	<0,01	<0,01	<0,01	<0,01	<0,01	<0,01	<0,01	<0,01	<0,01
LOI	0.56	0.14	0.32	0.87	0.21	0.59	0.51	0.14	0.32	0.22	0.36
Sum	100.11	98.79	98.07	99.33	100.01	102.26	100.57	100.77	100.3	98.34	101.84
Trace Elements											
Ni	12	9	10	13	10	12	12	10	11	8	10
Co	13.1	9.9	7.2	10.5	8	12.8	7.9	9.7	5.3	5.5	8.7
Rb	103.2	89.2	82.6	134.7	144	116.7	117	131.1	113.9	138.8	130.4
Ba	1966	4735	4307	3059	3635	2798	2999	2772	3327	2926	2545
Sr	627	898	935	741	809	685	705	635	764	641	586
Zr	832	854	806	458	413	647	555	586	529	412	533
Nb	43.52	17.32	20.59	19.78	18.69	27.98	22.54	26.75	15.9	16.75	27.32
Y	85.34	38.03	30.45	24.61	26.22	38.64	38.9	36.99	30.65	30.38	37.16
Ta	2.23	0.2	0.16	1.39	0.42	0.64	1.17	0.5	0.34	0.26	0.67
Hf	20.36	18.13	18.97	11.95	8.29	14.62	13.41	12.67	11.64	9.96	13.14
Th	17.3	6.6	7.5	16.4	9	10.4	15.7	12.9	19.8	16.9	14.6
U	1.29	0.6	0.62	2.11	1.92	1.02	1.1	1.2	1.26	1.86	1.45
Zn	142	115	102	82	68	106	104	98	84	79	98
V	109	75	61	83	78	98	60	63	45	50	72
Cs	0.49	0.44	0.42	2.2	2.22	0.69	0.59	1.14	1.88	1.25	1.13
Cu	13	8	8	9	7	18	5	16	6	11	11
Ga	24.4	22.4	24.1	21.7	23.1	22.2	21.8	22.8	20.8	20.5	21.5
Mo	<2	<2	<2	<2	<2	<2	<2	<2	<2	<2	<2
Sn	<0,3	<0,3	<0,3	<0,3	<0,3	<0,3	<0,3	<0,3	<0,3	<0,3	1.5
Tl	<0,5	<0,5	<0,5	1	<0,5	<0,5	0.7	<0,5	<0,5	<0,5	<0,5
W	1.3	1.2	1.7	1.8	1.5	0.8	1.1	1.7	1.6	1.4	1.6
Rare-earth Elements											
La	184.5	129.7	132.1	113.7	79.8	128.8	152.9	135.2	221.4	302.6	141.5
Ce	415.5	267.7	264.1	225.2	157.2	262.5	316	274.6	457	303.2	281.2
Pr	52.64	31.54	30.59	25	18.71	30.96	36.4	30.95	46.61	50.32	31.62
Nd	212.4	122.1	116.6	88.8	66.7	116.4	130.4	113.2	159.9	166	113.8
Sm	39	19.5	18.5	13.6	11.2	18.7	20.5	19.1	22	20.6	18.7
Eu	5.38	4.73	5.16	2.91	2.74	3.65	3.81	3.5	4.31	4.73	3.38
Gd	26.73	13.53	12.69	9.41	7.92	13.74	14.16	12.71	13.43	12.87	12.89
Tb	3.55	1.58	1.47	1.09	0.99	1.63	1.64	1.57	1.51	1.38	1.57
Dy	19.14	7.98	7.2	5.48	5.11	8.51	8.48	8.15	7.42	6.22	7.87
Ho	3.23	1.38	1.21	0.97	0.92	1.37	1.47	1.36	1.24	1.06	1.37
Er	8.21	3.81	3.31	2.46	2.45	3.67	3.64	3.52	3.16	2.58	3.69
Tm	0.98	0.44	0.4	0.34	0.33	0.49	0.48	0.47	0.41	0.35	0.47
Yb	5.8	2.7	2.5	2.1	2.1	2.9	3.1	2.9	2.5	2.2	3
Lu	0.77	0.39	0.35	0.34	0.31	0.41	0.44	0.4	0.38	0.33	0.4

The major elements concentration is showed as wt%, while the traces and REE content is showed as ppm;

Detection limits are 0.01% for oxides and 0.1 ppm for most traces and REE elements;

a=REE ratios normalized after Mc Donough and Sun (1995);

b=Eu/Eu* = Eu$_N$/[(Sm$_N$) + (Gd$_N$)]$^{1/2}$;

References: McDonough, W. F., Sun, S. S., (1995). The composition of the Earth. *Chemical Geology* 120, 223-253;

Aranda, R. O., Chaves, A. O., Medeiros Júnior, E. B., Venturini Junior, R. (2020). Petrology of the Afonso Cláudio Intrusive Complex: New insights for the Cambro-Ordovician post-collisional magmatism in the Araçuaí-West Congo Orogen, Southeast Brazil. *Journal of South American Earth Sciences* 98, 1-19;

Table S2.1: Whole-rock analyses from ACIC main rocks (Aranda et al. 2020) (continuation).

Sample	P 246-A	P 276-A	P 292-B	P 292-A	P 277-A	P 193-B	P 156-A	P 197-C	P 288	P 295-B	P 285-B	P 206-D	P 98	P 297	P 296	P 146-B	P 291	P 298	P 90-A	P 102
Rock	Mzg	Mzg	Mzd	Mzg	Mzd	Jot	Mzd	QMag	QMoz	QMoz	QMoz	QMoz	QMoz	QMoz	QMoz	QMoz	QMoz	QMoz	QMoz	QMoz
Rare-earth Elements Normalized[a]																				
La_N	393.67	478.48	613.08	548.95	460.76	465.40	365.82	513.92	633.76	778.48	547.26	557.38	479.75	336.71	543.46	645.15	570.46	934.18	1276.79	597.05
Ce_N	311.75	408.48	484.50	432.30	373.41	375.69	291.52	394.13	488.42	677.81	436.70	430.83	367.37	256.44	428.22	515.50	447.96	745.51	494.62	458.73
Pr_N	243.43	336.42	384.27	332.49	291.49	299.14	233.94	292.13	371.55	567.24	339.87	329.63	269.40	201.62	333.62	392.24	333.51	502.26	542.24	340.73
Nd_N	191.03	280.09	296.94	263.89	223.85	242.23	189.28	219.47	280.53	464.77	267.18	255.14	194.31	145.95	254.70	285.34	247.70	349.89	363.24	249.02
Sm_N	102.70	154.05	147.97	133.11	117.57	125.68	103.73	104.78	133.51	263.76	131.00	125.00	91.69	75.68	126.35	138.51	129.05	148.65	139.19	126.35
Eu_N	62.52	80.28	90.23	80.11	71.40	76.91	62.70	68.92	87.92	95.56	84.01	91.65	51.69	48.67	64.83	67.67	62.17	76.55	84.01	60.04
Gd_N	57.94	85.08	80.65	70.25	61.51	68.94	58.59	52.81	65.38	134.32	67.99	63.77	47.29	39.80	69.05	71.16	63.87	67.49	64.67	64.77
Tb_N	37.67	55.96	52.08	45.98	39.89	47.36	39.06	33.52	40.17	98.34	43.77	40.79	30.19	27.42	45.15	45.43	43.49	41.83	38.23	43.49
Dy_N	28.21	43.01	39.92	33.41	28.66	35.49	29.35	23.98	29.11	77.80	32.44	29.27	22.28	20.77	34.59	34.47	33.13	30.16	25.28	31.99
Ho_N	21.98	32.97	30.95	25.46	22.16	26.19	22.71	17.77	21.61	59.16	25.27	22.16	17.77	16.85	25.09	26.92	24.91	22.71	19.41	25.09
Er_N	19.75	28.88	26.94	22.94	20.25	24.25	20.63	16.19	19.31	51.31	23.81	20.69	15.38	15.31	22.94	22.75	22.00	19.75	16.13	23.06
Tm_N	16.19	22.67	22.27	18.62	16.19	21.05	16.60	13.36	15.38	39.68	17.81	16.19	13.77	13.36	19.84	19.43	19.03	16.60	14.17	19.03
Yb_N	15.53	21.74	20.50	18.63	15.53	19.25	15.54	13.04	14.29	36.02	16.77	15.53	13.04	13.04	18.01	19.25	18.01	15.53	13.66	18.63
Lu_N	14.63	20.33	19.51	17.07	14.23	17.89	14.63	12.60	13.82	31.30	15.85	14.23	13.82	12.60	16.67	17.89	16.26	15.45	13.41	16.26
Eu/Eu^b	0.81	0.70	0.83	0.83	0.84	0.83	0.81	0.93	0.94	0.51	0.89	1.03	0.78	0.89	0.69	0.68	0.68	0.76	0.89	0.66
La_N/Yb_N	25.35	22.01	29.96	29.47	29.67	24.17	23.56	39.40	44.36	21.61	32.63	35.90	36.78	25.81	30.17	33.51	31.67	60.16	93.44	32.04
La_N/Sm_N	3.83	3.11	4.14	4.12	3.92	3.70	3.54	4.91	4.74	2.95	4.15	4.46	5.22	4.45	4.30	4.66	4.42	6.28	9.17	4.73
Ce_N/Yb_N	20.08	18.79	23.64	23.20	24.05	19.51	18.77	30.22	34.19	18.82	26.04	27.75	28.17	19.66	23.77	26.77	24.87	48.01	36.20	24.62
Ce_N/Sm_N	3.04	2.65	3.27	3.25	3.18	2.99	2.82	3.76	3.65	2.57	3.31	3.45	4.00	3.39	3.33	3.72	3.47	5.02	3.55	3.63
Eu_N/Yb_N	4.03	3.69	4.40	4.30	4.60	3.99	4.04	5.28	6.15	2.65	5.01	5.90	3.96	3.73	3.60	3.51	3.45	4.93	6.15	3.22
Gd_N/Yb_N	3.73	3.91	3.93	3.77	3.96	3.58	3.77	4.05	4.58	3.73	4.05	4.11	3.63	3.05	3.83	3.70	3.55	4.35	4.73	3.48

Table S2.2: Whole-rock analyses from xenoliths and enclosing country rocks.

Sample	P 285-A	P 111	P 52	P 268	P 89	P 275-A	P 117	P 23	P 274-A
Rock	Allanite-bearing orthogneiss xenolith	Allanite-bearing orthogneiss xenolith	Enclosing allanite-bearing orthogneiss	Enclosing allanite-bearing orthogneiss	Enclosing allanite-bearing orthogneiss	Paragneiss xenolith	Enclosing paragneiss	Enclosing paragneiss	Enclosing paragneiss
Major elements									
SiO_2	68.11	75.45	67.54	70.55	74.47	70.3	79.93	71.31	73.88
TiO_2	0.28	0.1	0.81	0.41	0.09	0.31	2.22	0.67	0.33
Fe_2O_3	2.86	1.55	6.87	3.24	2.65	2.34	7.53	4.79	2.15
Al_2O_3	13.83	12.94	13.76	14.16	11.42	13.69	7.8	10.66	14.06
MgO	0.67	0.26	2.62	1.07	0.17	0.59	1.02	2.01	0.41
MnO	0.04	0.04	0.1	0.03	0.05	0.03	0.15	0.05	0.04
CaO	2.46	1.5	3.88	2.24	0.54	2.03	0.3	0.45	1.56
K_2O	3.59	4.77	2.13	4.6	3.97	3.58	1.31	3.38	5.21
Na_2O	3.13	3.41	2.38	2.77	3.36	2.62	0.29	1.11	2.88
P_2O_5	0.06	<0,01	0.08	0.07	<0,01	0.08	0.02	0.09	0.1
Cr_2O_3	0.02	<0,01	0.03	<0,01	0.02	0.02	0.03	0.03	<0,01
LOI	0.05	-0.02	0.36	0.34	0.18	0.43	0.24	0.63	0.2
Sum	95.1	100	100.56	99.48	96.92	96.02	100.84	95.18	100.82
Trace elements									
Ni	11	11	42	17	17	9	25	39	9
Co	3.1	1.9	17.8	7.1	1.7	2.6	11.4	13.1	1.7
Rb	67.5	104	74.1	108.1	133.7	122.9	61.1	109.2	106.2
Ba	2394	487	914	1554	259	820	530	534	1139
Sr	427	93	287	152	19	203	39	82	163
Zr	79	<10	93	61	88	111	162	110	211
Nb	3.56	4.83	10.1	8.13	11.06	9.09	31.74	11.47	10.52
Y	5.9	7.39	12.36	3.89	23.18	12.33	39.64	23.54	14.24
Ta	<0,05	<0,05	<0,05	<0,05	<0,05	<0,05	3.23	<0,05	<0,05
Hf	4.24	1.72	6.64	3.98	4.23	4.94	7.95	5.32	4.91
Th	10.2	2.3	5	2.2	5.5	11.5	11.3	10.7	7.9
U	0.32	0.75	0.88	0.51	1.2	1.33	2	2.08	1.06
Zn	57	16	86	18	56	47	51	66	25
V	24	<5	91	23	6	<5	86	69	<5
Cs	<0,05	0.8	1.27	0.97	1.24	2.99	1.38	2.68	0.71
Cu	11	6	37	11	14	13	22	24	8
Ga	16.5	14.2	18.5	16.8	17.8	19.6	11	13.9	13.7
Mo	9	9	9	9	10	9	10	9	8
Sn	3.1	2.5	3.5	2.5	3.7	5.6	3.7	3.6	3.6
Tl	<0,5	<0,5	<0,5	<0,5	<0,5	<0,5	<0,5	<0,5	<0,5
W	13.8	8	6.8	11.1	13.7	6.8	20.7	6.2	1.3
Rare-earth Elements									
La	139.6	14.3	22.9	20.6	19.6	42.4	38	32.2	42.8
Ce	288	24.5	45.4	37.4	42.9	86	81.1	65.5	83.9
Pr	26.02	2.72	5.31	4.03	5.42	10.56	9.56	7.85	9.93
Nd	85.6	9.6	20.7	15.8	22	37.3	35.3	29.8	38.1
Sm	9.5	2.1	3.4	2.3	5	7.1	6	5.6	6
Eu	3.63	0.93	1.28	1.68	0.53	1.47	1.05	1.36	1.19
Gd	4.32	1.88	3.21	2.1	5.37	5.32	6.46	5.48	4.8
Tb	0.5	0.28	0.45	0.17	0.78	0.59	1.01	0.75	0.68
Dy	1.96	1.27	2.61	0.97	4.19	2.66	7.03	4.66	3.33
Ho	0.33	0.27	0.5	0.17	0.96	0.44	1.45	0.9	0.54
Er	0.63	0.9	1.32	0.33	2.43	0.89	4.72	2.89	1.19
Tm	0.07	0.13	0.22	0.05	0.32	0.17	0.67	0.42	0.13
Yb	0.6	0.8	1.4	0.4	2.6	1	4.8	2.6	0.9
Lu	0.07	0.14	0.16	<0,05	0.35	0.09	0.69	0.38	0.09

The major elements concentration is showed as wt%, while the traces and REE content is showed as ppm;

Detection limits are 0.01% for oxides and 0.1 ppm for most traces and REE elements;

a=REE ratios normalized after Mc Donough and Sun (1995);

b=Eu/Eu* = $Eu_N/[(Sm_N) + (Gd_N)]^{1/2}$;

References: McDonough, W. F., Sun, S. S., (1995). The composition of the Earth. *Chemical Geology* 120, 223-253;

Table S2.2: Whole-rock analyses from xenoliths and enclosing country rocks (continuation).

Sample	P 285-A	P 111	P 52	P 268	P 89	P 275-A	P 117	P 23	P 274-A
Rock	Allanite-bearing orthogneiss xenolith	Allanite-bearing orthogneiss xenolith	Enclosing allanite-bearing orthogneiss	Enclosing allanite-bearing orthogneiss	Enclosing allanite-bearing orthogneiss	Paragneiss xenolith	Enclosing paragneiss	Enclosing paragneiss	Enclosing paragneiss
Rare-earth Elements Normalized[a]									
La_N	589.03	60.34	96.62	86.92	82.70	178.90	160.34	135.86	180.59
Ce_N	469.82	39.97	74.06	61.01	69.98	140.29	132.30	106.85	136.87
Pr_N	280.39	29.31	57.22	43.43	58.41	113.79	103.02	84.59	107.00
Nd_N	187.31	21.01	45.30	34.57	48.14	81.62	77.24	65.21	83.37
Sm_N	64.19	14.19	22.97	15.54	33.78	47.97	40.54	37.84	40.54
Eu_N	64.48	16.52	22.74	29.84	9.41	26.11	18.65	24.16	21.14
Gd_N	21.71	9.45	16.13	10.55	26.98	26.73	32.46	27.54	24.12
Tb_N	13.85	7.76	12.47	4.71	21.61	16.34	27.98	20.78	18.84
Dy_N	7.97	5.16	10.61	3.94	17.03	10.81	28.58	18.94	13.54
Ho_N	6.04	4.95	9.16	3.11	17.58	8.06	26.56	16.48	9.89
Er_N	3.94	5.63	8.25	2.06	15.19	5.56	29.50	18.06	7.44
Tm_N	2.83	5.26	8.91	2.02	12.96	6.88	27.13	17.00	5.26
Yb_N	3.73	4.97	8.70	2.48	16.15	6.21	29.81	16.15	5.59
Lu_N	2.85	5.69	6.50	<2	14.23	3.66	28.05	15.45	3.66
Eu/Eu_b	1.73	1.43	1.18	2.33	0.31	0.73	0.51	0.75	0.68
La_N/Yb_N	158.06	12.14	11.11	34.99	5.12	28.80	5.38	8.41	32.31
La_N/Sm_N	9.18	4.25	4.21	5.59	2.45	3.73	3.95	3.59	4.45
Ce_N/Yb_N	126.07	8.04	8.52	24.56	4.33	22.59	4.44	6.62	24.48
Ce_N/Sm_N	7.32	2.82	3.22	3.93	2.07	2.92	3.26	2.82	3.38
Eu_N/Yb_N	17.30	3.32	2.61	12.01	0.58	4.20	0.63	1.50	3.78
Gd_N/Yb_N	5.83	1.90	1.86	4.25	1.67	4.30	1.09	1.71	4.31

The major elements concentration is showed as wt%, while the traces and REE content is showed as ppm;

Detection limits are 0.01% for oxides and 0.1 ppm for most traces and REE elements;

a=REE ratios normalized after Mc Donough and Sun (1995);

b=Eu/Eu* = $Eu_N/[(Sm_N) + (Gd_N)]^{1/2}$;

References: McDonough, W. F., Sun, S. S., (1995). The composition of the Earth. *Chemical Geology* 120, 223-253;

5.3. SUPPLEMENTARY MATERIAL 3 - U-Th-Pb monazite geochronology

Table S3.1: Monazite microprobe analyses and obtained U-Th-Pb ages.

Sample	Id	P_2O_5	SiO_2	ThO_2	UO_2	Y_2O_3	La_2O_3	Ce_2O_3	Pr_2O_3	Nd_2O_3	Sm_2O_3	Gd_2O_3	Dy_2O_3	CaO	PbO	Total
P 111	Monazite 01 - 01	28.87	7.53	0.27	0.30	1.49	17.41	30.56	2.70	9.36	1.33	0.87	0.32	0.53	0.01	101.54
P 111	Monazite 02 - 01	26.50	1.95	9.73	0.28	2.20	10.19	24.90	3.42	14.01	2.90	1.64	0.54	0.76	0.22	99.22
P 111	Monazite 02 - 02	27.62	1.37	8.52	0.29	2.96	10.08	25.54	3.18	13.50	2.78	1.86	0.63	0.92	0.19	99.43
P 111	Monazite 02 - 03	27.83	1.14	7.37	0.27	2.92	10.45	26.70	3.27	13.32	2.57	1.65	0.71	0.91	0.16	99.26
P 111	Monazite 02 - 04	27.75	1.19	7.52	0.30	2.78	11.14	26.75	3.07	12.71	2.75	1.76	0.66	0.94	0.17	99.49
P 111	Monazite 02 - 05	27.89	1.23	7.49	0.29	2.82	10.93	26.21	3.24	12.90	2.70	1.83	0.66	0.91	0.16	99.26
P 111	Monazite 02 - 06	28.10	1.32	8.28	0.29	3.07	10.53	26.28	3.21	12.50	2.67	1.90	0.74	0.93	0.18	99.98
P 111	Monazite 02 - 07	28.30	1.23	7.45	0.32	3.04	10.94	25.98	3.09	12.76	2.70	1.84	0.75	0.92	0.16	99.48
P 111	Monazite 02 - 08	27.78	1.11	6.98	0.27	2.72	11.00	27.96	2.97	12.44	2.58	1.73	0.77	0.89	0.17	99.36
P 111	Monazite 02 - 09	27.10	1.70	8.22	0.19	2.39	11.27	27.76	3.27	12.79	2.55	1.25	0.44	0.60	0.16	99.69
P 111	Monazite 02 - 10	27.05	1.88	9.63	0.24	2.04	10.27	25.63	3.19	13.16	2.71	1.61	0.55	0.86	0.22	99.04
P 111	Monazite 02 - 11	27.89	1.14	7.27	0.27	2.50	11.12	27.26	3.26	12.72	2.67	1.58	0.58	0.92	0.17	99.34
P 111	Monazite 02 - 12	27.96	1.21	7.47	0.31	2.84	10.78	27.10	3.18	12.82	2.62	1.73	0.66	0.91	0.17	99.76
P 111	Monazite 02 - 13	27.52	1.23	7.26	0.31	2.84	11.04	26.92	3.05	12.73	2.63	1.88	0.69	0.90	0.15	99.17
P 111	Monazite 02 - 14	27.75	1.33	7.26	0.30	2.87	11.00	26.71	3.07	12.74	2.70	1.70	0.61	0.89	0.16	99.10
P 111	Monazite 03 - 01	27.34	3.04	4.05	0.31	1.92	12.98	29.38	3.24	11.95	2.56	1.53	0.50	0.39	0.09	99.28
P 111	Monazite 03 - 02	27.29	3.05	3.24	0.28	1.78	13.11	29.31	3.93	12.74	2.34	1.33	0.54	0.34	0.08	99.34
P 111	Monazite 03 - 03	26.87	3.63	4.79	0.29	1.42	12.36	29.52	3.30	12.49	2.58	1.51	0.44	0.42	0.13	99.74
P 111	Monazite 04 - 01	27.02	2.23	3.21	0.38	1.56	13.00	31.22	3.34	12.56	2.60	1.50	0.40	0.32	0.09	99.42
P 111	Monazite 04 - 02	27.58	1.59	2.96	0.33	1.88	12.85	31.36	3.21	12.69	2.62	1.41	0.44	0.33	0.10	99.34
P 111	Monazite 04 - 03	27.29	2.79	2.90	0.34	1.00	13.30	31.03	3.22	12.63	2.52	1.42	0.52	0.33	0.08	99.40
P 111	Monazite 04 - 04	27.86	1.09	3.62	0.34	1.82	12.57	31.44	3.22	12.90	2.54	1.48	0.42	0.36	0.08	99.75
P 111	Monazite 04 - 05	28.12	1.97	2.47	0.38	1.89	13.60	31.18	3.32	12.03	2.24	1.31	0.55	0.30	0.07	99.41
P 111	Monazite 05 - 01	27.57	2.35	8.64	0.19	1.63	10.49	26.78	3.29	12.96	2.73	1.48	0.39	0.61	0.18	99.30
P 111	Monazite 05 - 02	26.93	2.13	8.44	0.17	1.66	10.61	27.21	3.30	13.26	2.76	1.50	0.41	0.59	0.18	99.18
P 111	Monazite 06 - 01	27.07	1.63	9.54	0.24	1.90	10.29	25.77	3.21	13.43	2.92	1.73	0.45	0.85	0.20	99.24
P 111	Monazite 06 - 02	27.75	1.57	7.42	0.31	2.19	11.24	27.08	3.14	13.01	2.69	1.69	0.45	0.60	0.15	99.29
P 111	Monazite 06 - 03	27.48	1.72	8.71	0.23	1.64	10.94	26.97	3.35	13.47	2.35	1.36	0.35	0.68	0.19	99.43
P 111	Monazite 06 - 04	28.01	1.48	8.33	0.23	1.77	10.92	26.54	3.40	13.02	2.46	1.35	0.44	0.86	0.19	99.00
P 111	Monazite 06 - 05	28.12	1.48	7.96	0.25	2.15	10.95	26.42	3.26	13.15	2.54	1.51	0.59	0.80	0.16	99.34
P 111	Monazite 06 - 06	28.16	1.32	5.38	0.32	1.84	12.48	29.12	3.54	12.77	2.52	1.49	0.37	0.39	0.14	99.84
P 111	Monazite 06 - 07	28.40	1.05	4.45	0.41	2.01	12.87	29.50	3.44	12.56	2.56	1.47	0.49	0.37	0.12	99.69
P 111	Monazite 06 - 08	27.17	1.83	7.89	0.35	1.75	11.59	28.07	3.24	12.84	2.45	1.47	0.49	0.48	0.18	99.81
P 111	Monazite 06 - 09	27.56	1.59	8.39	0.17	1.16	11.24	28.01	3.34	12.90	2.38	1.22	0.32	0.56	0.17	99.00
P 111	Monazite 07 - 01	30.24	0.65	1.26	0.38	1.76	14.20	32.41	3.22	11.77	2.18	1.25	0.41	0.14	0.04	99.93
P 111	Monazite 07 - 02	30.54	0.94	0.89	0.29	1.73	15.93	31.86	3.15	10.80	1.93	1.15	0.36	0.14	0.04	99.75

Table S3.1: Monazite microprobe analyses and obtained U-Th-Pb ages (continuation).

Sample	Id	P2O5	SiO2	ThO2	UO2	Y2O3	La2O3	Ce2O3	Pr2O3	Nd2O3	Sm2O3	Gd2O3	Dy2O3	CaO	PbO	Total
P 111	Monazite 08 - 01	30.22	0.57	0.51	0.21	1.78	19.20	32.17	2.89	9.21	1.60	0.99	0.41	0.19	0.03	99.97
P 111	Monazite 08 - 02	30.90	0.70	0.51	0.27	1.77	18.70	31.84	2.83	9.08	1.52	1.01	0.41	0.20	0.04	99.77
P 111	Monazite 09 - 01	28.70	1.46	0.32	0.20	4.03	16.16	30.45	2.68	9.53	1.94	1.89	0.96	1.22	0.04	99.58
P 111	Monazite 12 - 01	27.05	1.54	8.37	0.17	1.39	11.09	28.14	3.30	13.80	2.40	1.23	0.34	0.66	0.18	99.65
P 111	Monazite 12 - 02	26.15	1.86	10.30	0.28	1.96	10.48	26.68	3.40	13.68	2.44	1.42	0.45	0.76	0.21	100.05
P 111	Monazite 13 - 01	29.37	0.83	0.60	0.24	1.62	18.26	32.19	3.01	10.37	1.62	1.00	0.32	0.14	0.04	99.59
P 111	Monazite 17 - 01	27.29	1.72	6.14	0.34	2.22	13.27	28.78	3.17	12.55	2.45	1.50	0.56	0.68	0.12	100.78
P 111	Monazite 17 - 02	27.55	1.85	3.39	0.31	2.23	14.30	29.18	2.81	12.61	2.46	1.48	0.46	0.74	0.12	99.48
P 111	Monazite 18 - 01	27.68	1.28	8.35	0.31	2.82	10.95	26.35	3.12	12.69	2.72	1.87	0.63	0.96	0.19	99.87
P 111	Monazite 19 - 01	28.88	2.42	1.35	0.22	1.67	17.39	30.60	3.00	10.55	1.64	1.14	0.47	0.19	0.04	99.54
P 111	Monazite 19 - 02	29.15	2.00	1.28	0.22	2.05	17.56	31.53	2.80	9.08	1.53	1.05	0.59	0.22	0.01	99.07
P 275 A	Monazite 01 - 01	29.68	0.51	6.07	0.22	0.17	12.91	27.57	3.35	14.07	2.81	1.34	0.17	1.18	0.13	100.16
P 275 A	Monazite 01 - 02	29.75	0.23	3.80	0.56	3.01	13.28	28.30	3.15	12.60	2.63	1.68	0.68	0.94	0.11	100.71
P 275 A	Monazite 01 - 03	29.51	0.35	3.68	0.87	2.71	12.77	28.61	3.26	12.72	2.76	1.88	0.69	1.00	0.11	100.92
P 275 A	Monazite 01 - 04	29.41	0.45	4.59	0.23	0.42	12.70	29.79	3.43	14.22	3.01	1.33	0.24	1.04	0.10	100.96
P 275 A	Monazite 01 - 05	29.64	0.32	2.59	0.64	1.97	15.47	28.75	3.41	12.59	2.42	1.65	0.60	0.69	0.09	100.82
P 275 A	Monazite 02 - 01	28.93	0.46	5.18	0.38	2.09	13.38	29.02	3.28	11.96	2.33	1.46	0.56	1.10	0.15	100.26
P 275 A	Monazite 02 - 02	29.34	0.68	4.79	0.16	0.16	13.90	30.23	3.51	13.20	2.65	1.16	0.10	0.90	0.11	100.86
P 275 A	Monazite 02 - 03	29.15	0.35	3.92	0.89	2.49	13.84	29.96	3.18	11.72	2.41	1.34	0.56	0.98	0.12	100.9
P 275 A	Monazite 03-01	28.58	0.36	4.45	0.24	0.75	13.71	30.60	3.34	13.17	2.73	1.49	0.24	0.89	0.11	100.63
P 275 A	Monazite 03-02	28.07	0.28	3.63	0.60	2.38	13.14	29.48	3.32	12.58	3.19	1.99	0.74	0.98	0.10	100.45
P 275 A	Monazite 04 - 01	26.82	1.75	12.65	0.64	1.88	12.03	26.63	2.70	9.96	2.01	1.39	0.51	1.47	0.30	100.74
P 275 A	Monazite 04 - 02	27.64	0.30	2.51	0.40	1.69	14.89	30.38	3.33	12.38	2.70	1.64	0.55	0.58	0.06	99.03
P 275 A	Monazite 05 - 01	28.23	0.29	1.77	0.58	2.42	15.90	31.00	3.14	11.51	2.37	1.48	0.61	0.66	0.08	100.03
P 275 A	Monazite 06 - 01	28.29	0.44	4.56	0.21	0.20	13.97	31.29	3.27	13.43	2.69	1.15	0.17	0.87	0.10	100.64
P 275 A	Monazite 06 - 02	28.02	0.44	4.77	0.24	0.17	14.06	31.94	3.41	12.97	2.57	1.10	0.17	0.87	0.11	100.84
P 275 A	Monazite 08 - 01	29.15	0.68	7.26	0.18	0.33	12.11	28.11	3.41	13.73	2.89	1.25	0.25	1.31	0.16	100.82
P 275 A	Monazite 08 - 02	30.23	0.33	4.31	0.41	2.30	13.20	28.47	3.11	12.33	2.61	1.74	0.73	0.94	0.08	100.79
P 275 A	Monazite 08 - 03	29.57	0.33	4.43	0.38	0.64	13.95	29.97	3.42	12.98	2.65	1.34	0.26	0.97	0.09	100.99
P 275 A	Monazite 08 - 04	29.68	0.32	3.51	0.82	2.38	13.22	28.63	3.26	11.68	2.81	1.84	0.81	0.94	0.12	100.01
P 275 A	Monazite 09 - 01	30.27	0.48	5.41	0.41	1.19	11.38	28.28	3.18	13.47	2.97	1.81	0.31	1.19	0.12	100.45
P 275 A	Monazite 09 - 02	30.87	0.54	3.91	0.79	2.61	12.14	27.69	3.06	12.47	2.73	1.79	0.60	1.10	0.12	100.39
P 275 A	Monazite 10 - 01	27.91	0.56	6.90	0.26	0.43	11.53	29.47	3.32	13.78	3.09	1.45	0.11	1.28	0.16	100.24
P 275 A	Monazite 10 - 02	28.41	0.16	3.30	0.76	2.46	13.57	30.42	3.13	12.37	2.63	1.74	0.81	0.87	0.11	100.73
P 275 A	Monazite 10 - 03	28.22	0.21	2.90	0.44	2.17	15.28	30.70	3.20	11.96	2.50	1.41	0.59	0.69	0.09	100.37

Table S3.1: Monazite microprobe analyses and obtained U-Th-Pb ages (continuation).

Sample	Id	Age (Ma)	Error Age (Ma)	U (ppm)	Error U (%)	Th (ppm)	Error Th (%)	Pb (ppm)	Error Pb (%)	MPb
P 111	Monazite 01 - 01	125	129	2943	3.40	2346	4.26	65	100.00	206.414
P 111	Monazite 02 - 01	485	35	2151	4.65	85525	2.00	2014	4.96	207.829
P 111	Monazite 02 - 02	468	37	2387	4.19	74909	2.00	1736	5.76	207.793
P 111	Monazite 02 - 03	457	41	2241	4.46	64750	2.00	1476	6.78	207.779
P 111	Monazite 02 - 04	479	41	2522	3.97	66051	2.00	1597	6.26	207.761
P 111	Monazite 02 - 05	452	40	2424	4.13	65787	2.00	1495	6.69	207.768
P 111	Monazite 02 - 06	470	38	2383	4.20	72800	2.00	1699	5.89	207.789
P 111	Monazite 02 - 07	451	40	2736	3.66	65488	2.00	1504	6.65	207.744
P 111	Monazite 02 - 08	521	44	2226	4.49	61349	2.00	1606	6.23	207.770
P 111	Monazite 02 - 09	441	39	1327	7.54	72211	2.00	1513	6.61	207.867
P 111	Monazite 02 - 10	493	36	1827	5.47	84637	2.00	2005	4.99	207.848
P 111	Monazite 02 - 11	480	42	2207	4.53	63889	2.00	1532	6.53	207.779
P 111	Monazite 02 - 12	465	40	2644	3.78	65664	2.00	1550	6.45	207.751
P 111	Monazite 02 - 13	435	40	2648	3.78	63783	2.00	1411	7.09	207.745
P 111	Monazite 02 - 14	450	41	2578	3.88	63836	2.00	1457	6.86	207.750
P 111	Monazite 03 - 01	398	59	2832	3.53	35574	2.00	798	12.53	207.577
P 111	Monazite 03 - 02	432	71	2614	3.83	28456	2.00	715	13.99	207.529
P 111	Monazite 03 - 03	526	56	2625	3.81	42086	2.00	1198	8.35	207.647
P 111	Monazite 04 - 01	441	66	3586	2.79	28218	2.00	789	12.67	207.407
P 111	Monazite 04 - 02	550	75	3072	3.26	25986	2.00	891	11.22	207.433
P 111	Monazite 04 - 03	475	73	3255	3.07	25503	2.00	770	12.98	207.404
P 111	Monazite 04 - 04	393	62	3200	3.13	31813	2.00	743	13.47	207.498
P 111	Monazite 04 - 05	451	77	3633	2.75	21671	2.00	678	14.76	207.289
P 111	Monazite 05 - 01	473	39	1390	7.19	75884	2.00	1708	5.85	207.867
P 111	Monazite 05 - 02	477	40	1203	8.31	74153	2.00	1671	5.98	207.879
P 111	Monazite 06 - 01	470	35	1823	5.49	83855	2.00	1894	5.28	207.848
P 111	Monazite 06 - 02	413	39	2658	3.76	65216	2.00	1365	7.33	207.749
P 111	Monazite 06 - 03	466	38	1715	5.83	76570	2.00	1717	5.82	207.844
P 111	Monazite 06 - 04	490	39	1760	5.68	73186	2.00	1736	5.76	207.835
P 111	Monazite 06 - 05	423	39	1963	5.09	69961	2.00	1448	6.91	207.814
P 111	Monazite 06 - 06	494	51	2807	3.56	47315	2.00	1253	7.98	207.661
P 111	Monazite 06 - 07	489	54	3817	2.62	39098	2.00	1133	8.83	207.506
P 111	Monazite 06 - 08	468	38	2988	3.35	69355	2.00	1662	6.02	207.737
P 111	Monazite 06 - 09	441	39	1186	8.43	73705	2.00	1532	6.53	207.880
P 111	Monazite 07 - 01	369	106	3700	2.70	11090	2.00	381	26.27	206.965
P 111	Monazite 07 - 02	457	142	2883	3.47	7830	2.00	353	28.35	206.915
P 111	Monazite 08 - 01	556	221	2038	4.91	4464	2.24	278	35.91	206.810
P 111	Monazite 08 - 02	568	188	2628	3.81	4456	2.24	334	29.92	206.694
P 111	Monazite 09 - 01	933	271	2009	4.98	2847	3.51	408	24.48	206.612
P 111	Monazite 12 - 01	489	40	1168	8.56	73512	2.00	1699	5.89	207.881
P 111	Monazite 12 - 02	445	33	2094	4.77	90534	2.00	1940	5.15	207.840
P 111	Monazite 13 - 01	635	192	2342	4.27	5255	2.00	371	26.93	206.819
P 111	Monazite 17 - 01	375	43	2989	3.35	53967	2.00	1068	9.37	207.680
P 111	Monazite 17 - 02	624	71	2884	3.47	29809	2.00	1105	9.05	207.506
P 111	Monazite 18 - 01	483	38	2558	3.91	73406	2.00	1773	5.64	207.778
P 111	Monazite 19 - 01	435	133	2064	4.84	11846	2.00	362	27.62	207.272
P 111	Monazite 19 - 02	162	130	2119	4.72	11222	2.00	130	76.95	207.243
P 275 A	Monazite 01 - 01	459	48	1784	5.61	53308	2.00	1216	8.22	207.785
P 275 A	Monazite 01 - 02	440	53	5368	2.00	33412	2.00	1003	9.97	207.308
P 275 A	Monazite 01 - 03	396	45	8416	2.00	32349	2.00	1058	9.45	207.085
P 275 A	Monazite 01 - 04	455	58	2008	4.98	40354	2.00	956	10.46	207.705
P 275 A	Monazite 01 - 05	414	60	6235	2.00	22778	2.00	798	12.53	207.060
P 275 A	Monazite 02 - 01	527	51	3450	2.90	45513	2.00	1346	7.43	207.590
P 275 A	Monazite 02 - 02	480	60	1245	8.03	42077	2.00	993	10.07	207.805
P 275 A	Monazite 02 - 03	385	43	8670	2.00	34458	2.00	1077	9.29	207.101
P 275 A	Monazite 03- 01	486	60	2087	4.79	39115	2.00	1003	9.97	207.688
P 275 A	Monazite 03- 02	405	52	5809	2.00	31857	2.00	919	10.88	207.252
P 275 A	Monazite 04 - 01	477	27	5595	2.00	111124	2.00	2766	3.61	207.702
P 275 A	Monazite 04 - 02	351	73	3791	2.64	22014	2.00	538	18.57	207.280
P 275 A	Monazite 05 - 01	481	75	5657	2.00	15537	2.00	733	13.64	206.919
P 275 A	Monazite 06 - 01	468	60	1810	5.53	40091	2.00	965	10.36	207.727
P 275 A	Monazite 06 - 02	462	57	2126	4.70	41945	2.00	1012	9.88	207.701
P 275 A	Monazite 08 - 01	492	44	1348	7.42	63757	2.00	1504	6.65	207.851
P 275 A	Monazite 08 - 02	347	52	3816	2.62	37894	2.00	780	12.82	207.498
P 275 A	Monazite 08 - 03	388	53	3498	2.86	38913	2.00	873	11.46	207.537
P 275 A	Monazite 08 - 04	433	48	8017	2.00	30820	2.00	1105	9.05	207.084
P 275 A	Monazite 09 - 01	427	47	3716	2.69	47561	2.00	1142	8.76	207.582
P 275 A	Monazite 09 - 02	421	46	7601	2.00	34379	2.00	1114	8.98	207.162
P 275 A	Monazite 10 - 01	493	44	2121	4.71	60602	2.00	1495	6.69	207.777
P 275 A	Monazite 10 - 02	445	51	7380	2.00	28983	2.00	1058	9.45	207.094
P 275 A	Monazite 10 - 03	490	67	4205	2.38	25520	2.00	863	11.58	207.296

Red ages were discarded

Figure S3.1: Monazite crystals and analyzed spots associated to U-Th-Pb ages from sample P 111 (allanite-bearing orthogneiss xenolith).
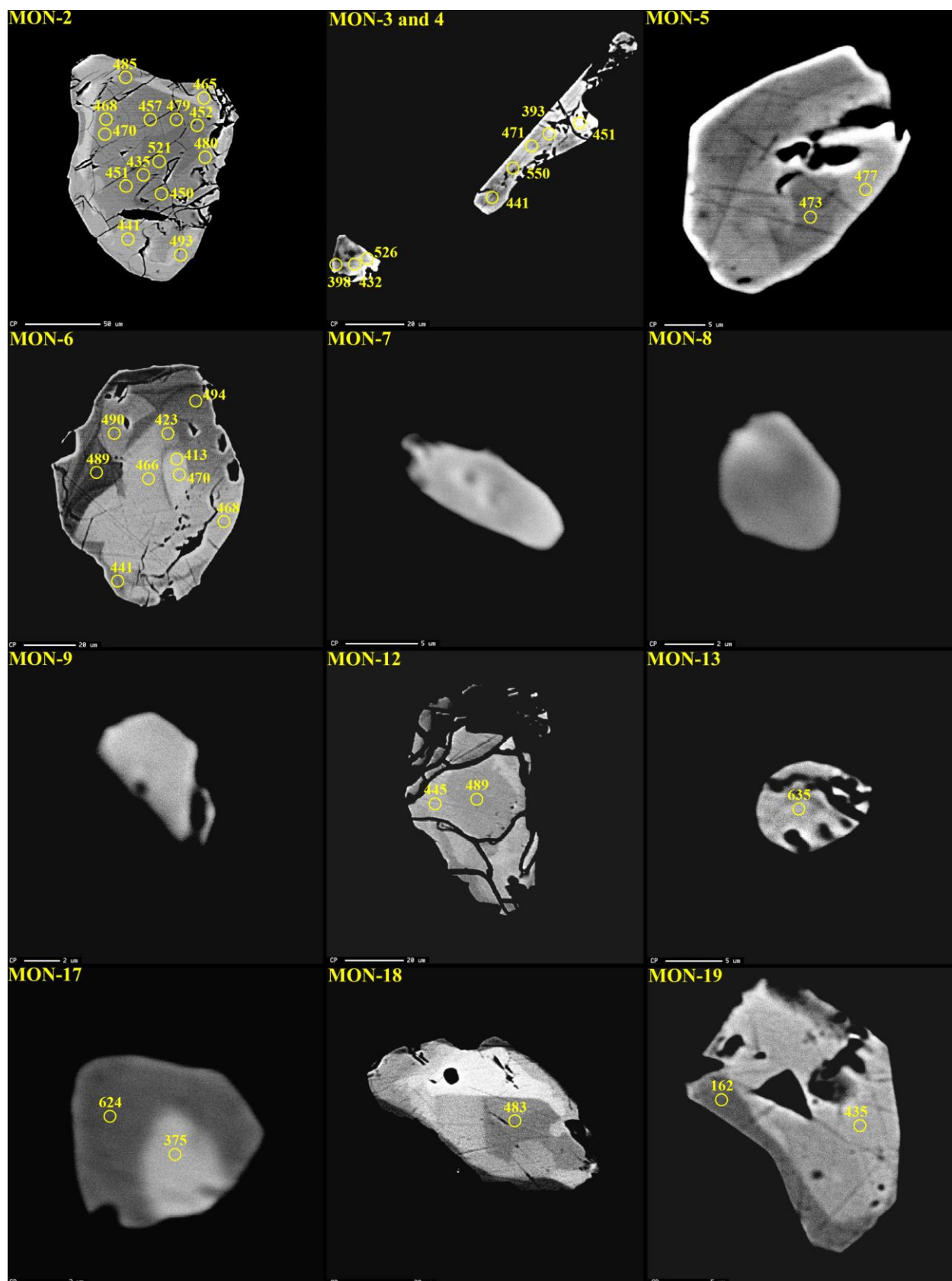
Figure S3.2: Monazite crystals and analyzed spots associated to U-Th-Pb ages from sample P 275-A (paragneiss xenolith).